UNIVERSITÉ DE STRASBOURG

ÉCOLE DOCTORALE PHYSIQUE ET CHEMIE-PHYSIQUE

Institut de Physique et Chimie des Matériaux de Strasbourg

THÈSE présentée par :

Ilias Nikolinakos

soutenue le : **25 Mars 2022**

pour obtenir le grade de : **Docteur de l'université de Strasbourg**

Discipline/ Spécialité : Physique

Ultrafast Spectroscopy of Transparent Dye Sensitized Solar Cells designed for the near-Infrared

THÈSE dirigée par :

Prof. Stefan Haacke	Professeur, Université de Strasbourg

RAPPORTEURS :

Prof. Natalie Banerji	Professeur, Université de Berne
Prof. Marcin Ziółek	Professeur, Université Adam-Mickiewicz de Poznań

AUTRES MEMBRES DU JURY :

Prof. Jaques-E. Moser	Professeur, École polytechnique fédérale de Lausanne
Prof. Thomas Heiser	Professeur, Université de Strasbourg

Στους γονείς μου και την αδερφή μου,
για όλη την υπομονή και τη στήριξη που μου έδειξαν από την αρχή.
Γιατί παρά τις δυσκολίες δεν σταμάτησαν ποτέ να είναι δίπλα μου.
Χωρίς εκείνους δεν θα είχα φτάσει μέχρι εδώ.
Το ευχαριστώ δεν είναι αρκετό, είναι όμως η αρχή!

Acknowledgements

First and foremost, I would like to express my gratitude towards my supervisor, Prof. Stefan Haacke, for all of his invaluable guidance and help throughout the entire project. I would like to thank him for trusting me with this exciting project, for the countless fruitful conversations we had and the freedom he granted me in my research. I thank him for his patience, his encouragement to move forward and even his active assistance in the laboratory. During the last three and a half years I learned a lot on his side and this thesis would not have been possible without him.

I would like to extend my sincere thanks to the members of the Thesis advisory committee. To the research director Prof. Natalie Banerjee (Université de Bern), as well as Prof. Jacques Edouard Moser (École polytechnique fédérale de Lausanne), Prof. Marcin Ziolek (Adam Mickiewicz University) and Prof. Thomas Heiser (Université de Strasbourg) for the time they invested to the evaluation of the PhD work and their valuable feedback, as experts in the field.

I gratefully acknowledge the French National Research Agency (ANR) for the financial support. I'm also very grateful to my collaborators, in the framework of the VISION-NIR project, at the University of Amiens, Nantes and Paris. I am especially thankful to the coordinator of the project Dr. Frédéric Sauvage (LRCS) for his consultation and fruitful exchange of ideas through regular online meetings, as well as to Prof. Fabrice Odobel (CEISAM), for the pioneering work on the synthesis of novel dyes and the excellent collaboration. Many thanks to Dr. Yann Pellegrin for his thoughtful suggestions, relative to the device preparation, along with Prof. Sophie Cassaignon, Dr. Capucine Sassoye and Dr. Tsou Hsi Camille Chan Chang of the LCMCP laboratory, for the carried out studies on titanium dioxide. I would like to express my thanks to my ANR colleagues, Waad Naim and Thibaut Baron for the great work and collaboration we had, wishing them all the best for their future career.

I would also like to thank all the members of the Biodyn Group and especially Dr. Jeremie Leonard, for his useful feedback and insightful comments and suggestions, contributing to my scientific progress, as well as Olivier Cregut for his time and significant help and guidance in the laboratory. Many thanks to Amira, Bogdan, Robin, Mathew and Samiul for their support and contributing to a warm and friendly atmosphere, whether during lab work or coffee breaks, as well as to Natalia and Lena, who became dear friends of mine here in Strasbourg.

I would like to offer my special thanks to my friends Georgios and Apostolos for their help and support throughout my PhD. Last but certainly not least, I would like to thank Nikoletta, for her patience and unwavering support all these years and my family for their unconditional support and belief in me.

Abstract

Dye sensitized solar cells or DSSCs belong to the next generation of photovoltaic technologies. They are advantageous compared to the conventional ones, because in DSSCs both photon harvesting and charge separation and collection occur in the active area of the cell. In addition, the wavelength-selective absorption flexibility of the dye extends into the near infrared, leading to transparent applications. Therefore, the effort of the study is to focus on the use of near-IR organic dyes with minimized absorption in the visible.

Chapter 1, includes the general introduction and motivation of the current work and Chapter 2 consists of the general description of the various transparent photovoltaic technologies, the photovoltaic parameters and the state of the art means of time-resolved characterization. A glance on the essential theoretical background has been made is Chapter 3, presenting in detail the important photophysical processes and species that is made in and investigated in the Thesis. The in-detail experimental instrumentation, is laid out/introduced in Chapter 4, as well as the fundamentals of non-linear optics.

The dyes under study, as well as the experimental results are presented in Chapter 5, with the conclusions and perspectives to be shown in Chapter 6. We have introduced and characterized using the fs-Transient Absorption technique, the near-infrared cyanine sensitizer **VG20** which strongly absorbs at 830 nm (154000 M^1cm^1), when adsorbed on TiO_2. After optimization and use of the de-aggregating agent CDCA, as well as electrolyte additives to adjust the conduction band level of the SC, the **VG20** displayed the record, at the time, of the product of PCE efficiency (3.1 %) and average visible transmission (AVT) of 75 % with injection occurring in 2-4 ps. The kinetic competition with energy transfer (ET) from the monomers to the aggregates limits the injection efficiency to 30 %. Data reproducibility and standard error due to DSSC surface inhomogeneity are investigated on a large number of samples prepared under similar conditions. Finally, a complete photophysical scheme was constructed, including the interaction of monomers

and aggregates and highlighting the electron injection of monomers into the TiO_2 conduction band, as well as the ET of monomers into the lowest electronic aggregates state.

In the second part of the presentation of the experimental results, the two novel pyrrolopyrrole cyanine dyes (**TB207**, **TB423**) are shown. They are designed to absorb strongly in the near infrared and impede aggregate formation upon sensitization by introducing bulkier side groups. Both absorb at 760 nm ($\varepsilon \sim$ 138000 M^1cm^1) in solution, possess long excited-state lifetimes ($\sim$ 3.2 ns) and when incorporated into real DSSCs span the 650- 850 nm, range of absorption. This makes them attractive candidates for transparent DSSC applications. We also identify the absorption spectrum of the TB cations that form after photoinjection into the SC to be maximum at 640-650 nm. Through the successful combined use of fs-fluorescence and fs-transient techniques the dyes were studied in solution and in non-injecting DSSC Al_2O_3 and injecting DSSC TiO_2. It has been reported for **TB207** that injection and ET occur in a time distribution (2 -23 ps), due to the system's inhomogeneity. More precisely, ET and injection are extremely sensitive to intermolecular distances and thus, the nm variations of the distances between neighboring dyes lead to a wide distribution of ET and injection times. The total PCE reached 4.0 % for **TB207**, with an AVT of 74 % and an injection efficiency of 40-60 %, while for **TB423** the injection efficiency reached 80 %. For the **TB** dyes we combined used two fs set-ups and identified the injection efficiency via two approaches. Interestingly, for **TB423**, no pronounced dependence on aggregate concentrations was recorded, indicating a possible high-yield secondary injection from aggregates.

Finally, the next experiments focus on promising new dyes designed to overcome aggregation problems and tune the absorption spectrum towards the near-IR with weak contribution in the visible, in order to increase the average visible transmittance of the DSSC devices.

Résumé

Les cellules solaires à colorant ou DSSC (de Dye sensitized solar cells en Anglais) appartiennent à la prochaine génération de technologies photovoltaïques. Ils sont avantageux par rapport aux systèmes conventionnels, car dans les DSSCs, à la fois la récolte des photons ainsi que la séparation et la collecte des charges se produisent dans la zone active de la cellule. De plus, la flexibilité d'absorption sélective de la longueur d'onde du colorant s'étend jusqu'au proche infrarouge, conduisant à des applications transparentes. Par conséquent, l'effort de l'étude est de se concentrer sur l'utilisation de colorants organiques proche de l'IR avec une absorption minimisée dans le visible.

Le chapitre 1, comprend l'introduction générale et la motivation du travail actuel et le chapitre 2 consiste en la description générale des différentes technologies photovoltaïques transparentes, des paramètres photovoltaïques et de l'état de l'art des moyens de caractérisation résolus en temps. Le chapitre 3 donne un aperçu du contexte théorique essentiel et présente en détail les processus et espèces photophysiques importants qui ont été rencontrés et étudiés durant la thèse. La description détaillée de l'instrumentation expérimentale est présentée au chapitre 4, ainsi que les principes fondamentaux de l'optique non linéaire.

Les colorants étudiés et les résultats expérimentaux sont présentés au chapitre 5, les conclusions et les perspectives étant exposées au chapitre 6. Nous avons déjà introduit et caractérisé à l'aide de la technique d'absorption transitoire à l'échelle fs, le sensibilisateur à la cyanine proche infrarouge **VG20** qui absorbe fortement à 830 nm ($154'000 M^{-1} cm^{-1}$) lorsqu'il est adsorbé sur du TiO_2. Après optimisation et utilisation de l'agent de désagrégation CDCA, ainsi que d'additifs électrolytiques pour ajuster l'énergie du semi-conducteur, le **VG20** atteind le record, à l'époque, du produit, d'efficacité PCE (3.1 %) et de la transmission visible moyenne (AVT) de 75 % avec une injection survenant en 2-4 ps. La compétition temporelle du transfert d'énergie des monomères aux agrégats limite l'efficacité d'injection à 30 %. La reproductibilité des données et l'erreur

standard due à l'inhomogénéité des DSSC sont étudiés démontrée sur un grand nombre d'échantillons préparés dans des conditions similaires. Enfin, un schéma photophysique complet a été construit, incluant l'interaction des monomères et des agrégats et mettant en évidence l'injection d'électrons des monomères à la bande de conduction de TiO_2, ainsi que le transfert d'énergie des monomères à l'état électronique le plus bas des agrégats.

Dans la deuxième partie de la présentation des résultats expérimentaux, les deux colorants cyanine nouveaux de type pyrrolopyrrole (**TB207**,**TB423**) sont montrés. Ils sont conçus pour absorber fortement dans le proche infrarouge et empêcher la formation d'agrégats lors de la sensibilisation en introduisant des groupes latéraux plus volumineux. Ils absorbent tous les deux à 760 nm ($\varepsilon \sim$ 138000 M^1cm^1), possèdent de longues durées de vie des états excités (∼3.2 ns) et, lorsqu'ils sont incorporés dans des DSSC réels, couvrent la plage de 650 à 850 nm, ce qui en fait des candidats attrayants pour les applications de DSSC transparents. Nous identifions également le spectre d'absorption des cations TB qui se forment après la photoinjection dans le semi-conducteur pour être maximum à 640-650 nm. Grâce à l'utilisation combinée réussie de la fluorescence fs et de l' absorption transitoire fs en solution, dans le DSSC Al_2O_3 et le DSSC TiO_2 sans et avec injection, il a été signalé pour le **TB207** que l'injection et le transfert d'énergie se produisent dans une distribution temporelle (2 -23 ps), en raison de l'inhomogénéité structuelle du système. Plus précisément, le transfert d'énergie et l'injection sont extrêmement sensibles aux distances intermoléculaires et donc, les variations en nm des distances entre les colorants voisins conduisent à l'obtention d'une large distribution du transfert d'énergie et du temps d'injection. Le PCE total a atteint 4.0 % pour le **TB207**, avec un AVT de 74 % et une efficacité d'injection de 40-60 %, tandis que pour le **TB423** l'efficacité d'injection a atteint 80 %. Pour les colorant TB, nous avons combiné deux configurations fs et identifié l'efficacité de l'injection par deux approches. Il est intéressant de noter que pour le **TB423**, nous n'avons pas observé de dépendance marquée aux concentrations d'agrégats, ce qui indique la possibilité d'une injection secondaire à haut rendement à partir d'agrégats.

Enfin, les expériences suivantes se concentrent sur de nouveaux colorants prometteurs conçus pour surmonter les problèmes d'agrégation et régler le spectre d'absorption vers le proche IR avec une faible contribution dans le visible, afin d'augmenter la transmittance visible moyenne des dispositifs DSSC.

List of Publications

Journal papers

1. W. Naim, V. Novelli, I. Nikolinakos, N. Barbero, I. Dzeba, F. Grifoni, Y. Ren, T.Alnasser, A. Velardo, R. Borrelli, et al., "Transparent and colorless dye-sensitized solar cells exceeding 75 % average visible transmittance," Jacs Au, vol. 1, no. 4,pp. 409–426, 2021.

2. T. Baron, W. Naim, I. Nikolinakos, Yann Pellegrin, Denis Jacquemin, Stefan Haacke, Frédéric Sauvage, and Fabrice Odobel, "Transparent and colorless dye sensitized solar cells based on pyrrolopyrrole cyanine sensitizers," recently submitted (contribution equal to the first author).

Conference proceedings

1. I. Nikolinakos, N. Waad, V. Novelli, N. Barbero, I. Dzeba, F. Grifoni, C. Barolo, F. Sauvage, and S. Haacke, "Ultrafast spectroscopy of transparent dye-sensitized solar cells designed for the near-infrared," in International Conference on Ultrafast Phenomena, Optical Society of America, 2020,Tu4A–26 (Poster presentation).

2. I. Nikolinakos, W. Naim, N. Barbero, C. Barolo, F. Sauvage, and S. Haacke, "Ultrafast spectroscopy of transparent dye-sensitized solar cells designed for the near-infrared," in Advances in Ultrafast Condensed Phase Physics II, International Society for Optics and Photonics, vol. 11346, 2020, 113460P. (Oral presentation)

3. I. Nikolinakos, W. Naim, N. Barbero, C. Barolo, F. Sauvage, S. Haacke, "Ultrafast Spectroscopy of Transparent Dye-sensitized Solar Cells (DSSCs) Designed for the Near-infrared," in Karlsruhe School of Optics Photonics Summer School, 2020. (Poster presentation)

4. I. Nikolinakos, T. Baron, W. Naim, T. Alnasser, Y. Pellegrin, F. Sauvage, F. Odobel, S. Haacke, "Photoinduced Charge Transfer Dynamics in novel Diketopyrrolopyrrole Transparent Dye-Sensitized Solar Cells," in International Conference on Photochemistry - 30th Edition, 2021. (Poster presentation)

5. I. Nikolinakos, T. Baron, W. Naim, T. Alnasser, Y. Pellegrin, F. Sauvage, F. Odobel, S. Haacke, "Photoinduced Charge and Energy Transfer Dynamics in novel Diketopyrrolopyrrole Transparent Dye-Sensitized Solar Cells," in 17èmes journées de la matière condensée, 2021. (Oral presentation)

6. I. Nikolinakos, W. Naim, N. Barbero, C. Barolo, F. Sauvage, S. Haacke, "Ultrafast spectroscopy of transparent dye-sensitized solar cells (DSSCs) designed for the near-infrared," in International Chemical Congress of Pacific Basin Societies, Pacifichem, 2021. (Poster Presentation)

7. I. Nikolinakos, T. Baron, W. Naim, T. Alnasser, Y. Pellegrin, F. Sauvagec, F. Odobel, S. Haacke, "Ultrafast Charge and Energy Transfer dynamics of novel pyrrolopyrrole cyanine sensitizers for Transparent and Colorless Dye Sensitized Solar Cells (conference presentation)," in Advances in Ultrafast Condensed Phase Physics II, International Society for Optics and Photonics, Paper No. 12132-20 (Oral presentation).

8. W. Naim, F. Grifoni, N. Barbero, I. Nikolinakos, I. Dzeba, S. Haacke, C. Barolo, F. Sauvage, "Selective NIR-Conversion in Dye-Sensitized Solar Cells: A New Generation of Fully Transparent and Colorless Photovoltaic," in CI(G)S, CdTe and Related Thin Films / Organic and Dye-Sensitised Devices / II-V and Related Compound Semiconductors / Tandems, European PV Solar Energy Conference and Exhibition, 2021.

9. C. Barolo, F. Grifoni, N. Barbero, R. Borrelli, M. Bonomo, Y. Ren, S. M. Zakeeruddin, W. Naim, T. Alnasser, M. Giordano, F. Matteocci, A. Di Carlo, M. Graetzel, G. Viscardi, I. Nikolinakos, S. Haacke, F. Sauvage, "Synthetic strategies in functional NIR dyes towards transparent and colorless Dye-sensitized Solar Cells," in International Conference on Electronic Materials and XIX Brazilian Materials Research Society Meeting, 2021.

10. Participation in the VIII Ciamician Photochemistry School, Bologna, 2019.

Abbreviations and acronyms

A	Acceptor
AGG	Aggregates
AM1.5G	1.5 times length of air mass
AVT	Average Visible Transmittance
BBO	Beta Barium Borate
CB	Conduction Band
CCD	Charge Coupled Device
CIE	Commission Internationale de l'éclairage
CRI	Color Rendering Index
CT	Charge Transfer
D	Donor
DADS	Decay Associated Difference Spectra
DEE	Dexter Electron Exchange
DFM	Difference Frequency Mixing
DOS	Density Of States
DSSC	Dye Sensitized Solar Cells
EADS	Evolution Associated Difference Spectra
ESA	Excited State Absorption
ET	Energy Transfer
FC	Franck-Condon
FF	Fill Factor
FLUPS	Fluorescence Up-Conversion spectroscopy (or Set-up)
FRET	Förster Resonance Energy Transfer

FTO	Fluorine doped Tin Oxide
FWHM	Full Width Half Maximum
GA	Global Analysis
GS	Ground State
GSB	Ground State Bleaching
GVD	Group Velocity Dispersion
HOMO	Highest Occupied Molecular Orbital
IC	Internal Conversion
ICT	Intramolecular Charge Transfer
IPCE	Incident Photon to Current Efficiency
IR	Infrared
IRF	Instrument's Response Function
ISC	Intersystem Crossing
LE	Locally Excited
LSC	Luminescent solar concentrator
LUE	Light Utilization efficiency
LUMO	Lower Unoccupied Molecular Orbital
MA	Magic Angle
MCP	Micro-Channel Plate
MONO	Monomers
NIR	Near-Infrared
NL	Non-Linear
NOPA	Non-Linear Optical Amplifier
NP	Nanoparticle
OD	Optical Density
OLED	Organic Light Emitted Diodes
OPA	Optical Parameter Amplifier (or Amplification)
OPV	Organic Photovoltaic Devices
OX	Oxidant

PM	Phase Matching
PA	Photoproduct Absorption
PCE	Power Conversion Efficiency
PV	Photovoltaic
RE	Reactant
SADS	Species Associated Difference Spectra
SE	Stimulated Emission
SFG	Sum Frequency Generation
SH	Second Harmonic
SPM	Self Phase Modulation
SSA	Steady State Absorption
SSE	Steady State Absorption
SVD	Singular Value Decomposition
TA	Transient Absorption
TAS	Transient Absorption Spectroscopy (or Set-up)
TCSPC	Time Correlated Single Photon Counting
UV	Ultra Violet
VR	Vibronic Relaxation
Vis	Visible
Voc	Voltage Open Circuit
WL	White Light
WLG	White Light Generation
XPM	Cross-Phase Modulation
ΔA	Different Absorption

Contents

Acknowledgements i

Abstract iii

Résumé v

List of Publications vi

Abbreviations and acronyms viii

List of Figures xv

List of Tables xxi

1 General Introduction 1

2 Transparent photovoltaics 5

2.1 Theory of Dye Sensitized Solar Cells 5

2.1.1 Components of Dye Sensitized Solar Cells 6

2.1.2 Dynamic processes in Dye-Sensitized-Solar-Cells 7

2.1.3 Photovoltaic parameters 13

2.2 Transparent DSSCs 15

2.2.1 Determination of the degree of Transparency 15

2.2.2 Wavelength selective and non-selective transparent solar cells . . . 18

2.2.3 Dyes for Dye-Sensitized-Solar-Cells designed for the near-infrared 22

2.3 Ultrafast Spectroscopy on DSSCs 24

3 Photophysics 43

3.1 Basic Photophysical Processes 43

3.2 Theories of Energy and Electron Transfer 46

3.2.1 Excitation Energy Transfer . . . 46
3.2.2 Electron transfer . . . 49
3.3 Exciton Theory of molecular aggregates . . . 51
3.3.1 Kasha's classic theory . . . 52
3.3.2 Beyond Kasha's approach . . . 54

4 Experimental Methods **61**
4.1 Steady-State spectroscopy . . . 61
4.2 Non-linear Optics . . . 62
4.2.1 Non-linear optical processes (SFG, SHG, DFM, WLG) . . . 62
4.2.2 (Non-Collinear) Optical Parametric Amplification . . . 66
4.3 Streak Camera set-up . . . 68
4.4 Broadband Fluorescence Up-Conversion . . . 69
4.5 fs-Transient Absorption . . . 73
4.6 Data analysis . . . 76
4.6.1 Background and artifact corrections . . . 76
4.6.2 Fitting functions . . . 79
4.6.3 Global and spectro-temporal analysis . . . 81
4.6.4 Sample preparation . . . 84

5 Experimental results **91**
5.1 Dye molecules under investigation . . . 91
5.2 Steady-state absorption/fluorescence . . . 95
5.2.1 Dyes in solution . . . 95
5.2.2 Dyes in complete DSSCs . . . 97
5.3 PV performances and dye regeneration . . . 109
5.4 Time resolved spectroscopy on VG20 . . . 114
5.4.1 Ultrafast spectroscopy of VG20 in solution . . . 114
5.4.2 Ultrafast spectroscopy of VG20 in complete ZrO_2 and TiO_2 DSSCs 116
5.4.3 The effect of CDCA on VG20 ZrO_2 and TiO_2 DSSCs . . . 124
5.4.4 The effect of Li^+ concentration in the electrolyte on VG20 TiO_2 DSSCs . . . 133
5.4.5 The excitation wavelength effects . . . 136
5.5 Time resolved spectroscopy on TB-dyes . . . 141
5.5.1 Excited state reaction scheme of TB207 and TB423 . . . 142
5.5.2 Detailed determination of the injection and FRET rates and yields 153

5.6 Summary and conclusions 162

6 Conclusions and perspectives **169**

Appendix A Supporting information **A.1**

Appendix B Thèse résumée en français **B.1**

Appendix Thèse résumée en français **B.1**

B.1 Introduction générale B.1
B.2 Photovoltaïque transparente B.3
B.3 Photophysique B.5
B.4 Méthodes expérimentales B.7
B.5 Résultats expérimentaux B.10

Appendix C Conclusions et perspectives **B.19**

List of Figures

1.1 Best Research-Cell Efficiencies 2

2.1 The DSSC principle and the various device components 8
2.2 Standard J-V curve for a DSSC 14
2.3 The CIE 1931 uniform chromaticity diagram 17
2.4 CRI images and the CIELAB colour space 18
2.5 Diagram of main TPV technologies 19
2.6 Luminescence solar concentrators 20
2.7 Solar spectral irradiance and DSSC energy levels 23
2.8 Photon energies, frequencies, and wavelength from X-rays to THz 25
2.9 X-ray pump-probe spectroscopy 28

3.1 Perrin-Jablonski diagram 44
3.2 Excitation energy transfer (FRET, Dexter) 47
3.3 Marcus theory of electron transfer 50
3.4 Types of excitons 52
3.5 Energy levels of aggregates following the Kasha model 54
3.6 Possible aggregate configurations according to Spano's model 56

4.1 Sum frequency generation wavectors and spectral overlap 64
4.2 White light generation and relative RMS noise 65
4.3 Collinear and non-collinear interaction geometry for optical parametric amplification 66
4.4 Streak camera set-up 69
4.5 Broadband fluorescence up-conversion set-up 70
4.6 Schematic diagram showing the basic principles of the fluorescence up-conversion technique 71
4.7 Fluorescence and gate beam profiles at the overlap position 72
4.8 fs-Transient absorption set-up 73

4.9 Major electronic processes probed with TAS 75
4.10 2D profile of Chirp corrected 78
4.11 Parallel, sequential and target analysis models for TAS data analysis . . 83
4.12 DSSC assemble procedure 86

5.1 Dyes under investigation: VG20, TB207 and TB423 92
5.2 SSA and SSE of solutions: VG20, TB207 and TB423 96
5.3 SSA in ZrO_2, Al_2O_3 and TiO_2 DSSCs: VG20, TB207 and TB423 98
5.4 Schematic illustration of CDCA:dye effect on a SC layer 99
5.5 Normalized SSA spectra of DSSCs increasing CDCA concentration: VG20, TB207 and TB423 101
5.6 Peak ratio of H-aggregate band/Monomer band for different DSSCs, increasing CDCA for all dyes 102
5.7 Aggregates absorption spectra 103
5.8 SSE spectra of DSSCs: VG20, TB207 and TB423 106
5.9 Spectral features of VG20, TB207 and TB423 in the cationic form 110
5.10 PCE versus AVT for various TPV technologies 113
5.11 TCSPC AND TAS of VG20 in solution 115
5.12 TA kinetic profiles of VG20 in solution 116
5.13 Wavelength-dependent amplitudes of VG20 in solution 117
5.14 Transient spectra of VG20 dye in non-injecting ZrO_2 and injecting TiO_2 DSSCs 118
5.15 TAS averaged kinetic profiles for VG20 in non-injecting ZrO_2 and injecting TiO_2 DSSCs and the relative standard error 121
5.16 Wavelength-dependent decay amplitudes of VG20 in non-injecting ZrO_2 and injecting TiO_2 DSSCs and photophysical scheme 122
5.17 Excited state reaction schemes 124
5.18 TAS spectra of VG20 ZrO_2 DSSCs for different CDCA concentrations . . 126
5.19 Kinetic traces of VG20 ZrO_2 DSSCs of different CDCA concentrations in the visible spectral region 127
5.20 Kinetic traces of VG20 ZrO_2 DSSCs of different CDCA concentrations in the near-IR spectral region 128
5.21 TAS spectra of VG20 TiO_2 DSSCs for different CDCA concentrations . . 130
5.22 Kinetic traces of VG20 TiO_2 DSSCs of different CDCA concentrations in the near-IR spectral region 131
5.23 TAS spectra of VG20 TiO_2 DSSCs for different CDCA concentrations . . 132

5.24 TAS spectra of VG20 TiO_2 DSSCs for different Li^+ concentrations . . . 134
5.25 SE kinetics of VG20 TiO_2 1:500 dye:CDCA DSSC, increasing the Li^+ concentration . . . 135
5.26 TAS spectra of a VG20 TiO_2 DSSCs, excited at different wavelengths . . 138
5.27 TAS spectra at 2 ns, of VG20 TiO_2 DSSC, excited at different energies . 139
5.28 SE and GSB kinetics of VG20 TiO_2 DSSC excited at three different wavelengths . . . 139
5.29 TAS spectra at 0.1 and 10 ps of VG20 TiO_2 DSSC, exciting at 880 nm . 141
5.30 Streak camera 2D spectro-temporal profiles of TB207 and TB423 in EtOH solutions . . . 142
5.31 TAS of TB207 and TB423 in EtOH solutions . . . 144
5.32 TAS of TB207 and TB423 $Al2_O3$ DSSCs of different CDCA concentration 145
5.33 FLUPS 2D spectro-temporal profile of TB207 Al_2O_3 DSSC of zero CDCA 147
5.34 Kinetics of TB207 Al_2O_3 1:0 DSSC obtained by TAS and FLUPS 147
5.35 FLUPS kinetics of TB423 Al_2O_3 DSSCs of different CDCA concentrations 149
5.36 TAS of TB207 and TB423 TiO_2 DSSCs, increasing CDCA concentration 151
5.37 FLUPS kinetics with fits, of TB207 in solution, in Al_2O_3 and TiO_2 DSSCs, in the standard conditions . . . 153
5.38 FLUPS kinetics with fits, of TB423 in solution, in Al_2O_3 and TiO_2 DSSCs, in the standard conditions . . . 155
5.39 DADS of TB207 of Al_2O_3 and TiO_2 DSSCs, in the standard conditions . 156
5.40 Excited state reaction scheme of TB207 TiO_2 DSSCs . . . 159
5.41 DADS of TB423 of Al_2O_3 and TiO_2 DSSCs, in the standard conditions . 159
5.42 Excited state reaction scheme of TB423 TiO_2 DSSCs . . . 160

6.1 Image of a TB207 TiO_2 DSSC . . . 171

A.1 HOMO, LUMO and EDD ($S_0 - S_1$) representation for TB207 . . . A.1
A.2 2D streak camera-TAS profiles for TB207 TiO_2 DSSC with inert or iodide based electrolyte . . . A.2
A.3 Powertests of VG20, TB207 and TB423, both solution and DSSC samples A.4
A.4 TA kinetics of VG20 ZrO_2 1:500 DSSC at different wavelengths . . . A.5
A.5 TA kinetics of VG20 TiO_2 dye:CDCA DSSC at different wavelengths . . A.5
A.6 TA kinetics with 3, 4 and 5 exponential fits, of VG20 TiO_2 1:500 dye:CDCA DSSC at different wavelengths . . . A.6
A.7 DADS of VG20 ZrO_2 DSSCs, of various dye:CDCA concentration ratios A.9

A.8 DADS of VG20 TiO_2 DSSCs, of various dye:CDCA concentration ratios . A.9
A.9 SSA VG20 TiO_2 1:500 dye:CDCA DSSCs, of different Li^+ concentration in the electrolyte A.10
A.10 DADS of VG20 TiO_2 DSSCs, of different Li^+ concentration A.10
A.11 TAS of a VG20 ZrO_2 1:1000 DSSC, at different excitation wavelengths . A.12
A.12 DADS of VG20 ZrO_2 and TiO_2 1:1000 DSSCs, at different excitation wavelengths A.12
A.13 FLUPS 2D spectro-temporal map of TB207 and TB423 TiO_2 DSSCs . . A.15
A.14 TAS kinetics at different wavelengths and fittings, of TB207 in solution . A.16
A.15 DADS and EADS of TB207 and TB423 in solution A.16
A.16 DADS of TB207 Al_2O_3 DSSCs, with different CDCA concentration . . . A.17
A.17 Streak camera fluorescence kinetics of TB207 Al_2O_3 DSSCs, increasing the CDCA concentration A.18
A.18 TA spectra of TB207 TiO_2 DSSCs, increasing the CDCA concentration . A.19
A.19 DADS of TB207 TiO_2 DSSCs, increasing the CDCA concentration A.19
A.20 FLUPS kinetics of TB207 TiO_2 DSSCs, increasing the CDCA concentration A.20
A.21 TA spectra of TB423 TiO_2 DSSCs, increasing the CDCA concentration . A.21
A.22 DADS of TB423 TiO_2 DSSCs, increasing the CDCA concentration A.21
A.23 FLUPS kinetics of TB423 TiO_2 DSSCs, increasing the CDCA concentration A.22
A.24 TA spectra of a TB423 TiO_2 DSSC 1:0, excited at different wavelengths . A.23

B.1 Meilleure efficacité des cellules de recherche B.2
B.2 Le principe des DSSC et les différents composants du dispositif B.4
B.3 Niveaux d'énergie des agrégats selon le modèle de Kasha B.6
B.4 Configuration de la caméra Streak B.8
B.5 Dispositif de conversion ascendante de la fluorescence à large bande . . . B.9
B.6 fs-Configuration d'absorption transitoire B.10
B.7 Colorants à l'étude : VG20, TB207 et TB423 . . . . . B.12
B.8 SSA dans les DSSC de ZrO_2, Al_2O_3 et TiO_2 : VG20, TB207 et TB423 . B.13
B.9 Illustration schématique de l'effet du colorant CDCA:dye sur une couche SC B.14
B.10 Amplitudes de décroissance du VG20 en fonction de la longueur d'onde dans des DSSC de type ZrO_2 sans injection et TiO_2 avec injection, et schéma photophysique B.15
B.11 Diagramme simplifié des états excités photophysiques pour les monomères et les agrégats dans l'interface colorant-SC B.16
B.12 DADS de TB207 de DSSCs de Al_2O_3 et TiO_2, dans les conditions standards B.17

B.13 Cinétique FLUPS avec ajustements, de TB207 et TB423 en solution, dans des DSSCs de Al_2O_3 et TiO_2, dans les conditions standards B.18

List of Tables

5.1 Spectroscopic properties of VG20, TB207 and TB423 in solution. 96
5.2 Aggregate comparison of TB207 and TB423 99
5.3 Aggregate properties of VG20, TB207 and TB423 in TiO_2 DSSCs 105
5.4 Spectroscopic properties of VG20, TB207 and TB423 in non-injecting DSSCs, increasing the CDCA concentration 108
5.5 Spectroscopic properties of VG20, TB207 and TB423 in TiO_2 DSSCs, increasing the CDCA concentration 108
5.6 Regeneration and recombination times and efficiency for VG20 and TB207 TiO_2 regenerating DSSCs with I_3^-/I redox couple in the electrolyte . . . 111
5.7 Photovoltaic performances of VG20, TB207 and TB423 increasing CDCA concentration for TiO_2 DSSCs 111
5.8 Photovoltaic performances of VG20 and TB207, increasing Li^+ concentration for TiO_2 DSSCs 112
5.9 TA kinetic parameters for VG20 in EtOH:DMSO (9:1) solvent mixture obtained by femtosecond transient absorption spectroscopy 115
5.10 TA kinetic parameters of VG20 in non-injecting ZrO_2 and injecting TiO_2 DSSCs obtained by femtosecond transient absorption spectroscopy. . . . 123
5.11 Fitting values of VG20 ZrO_2 DSSCs of different CDCA concentrations . 129
5.12 Fitting values of VG20 TiO_2 DSSCs of different CDCA concentrations . 131
5.13 Aggregate comparison of TB207 and TB423 132
5.14 Injection efficiency as a function of the Li^+ concentration 135
5.15 Fitting values of VG20 TiO_2 DSSCs of different Li^+ concentrations . . . 136
5.16 Peak ratio of the monomer, early time ESA, against the long time PA . . 138
5.17 Fitting values of a VG20 TiO_2 1:1000 DSSC at different excitation wavelengths 140
5.18 Luminescence decay fit values of TB207 and TB423 in EtOH 143

5.19 Fitting values of TB207 Al_2O_3 DSSC TAS/FLUPS kinetics, of different CDCA concentrations . . . 148
5.20 Fitting values TB423 Al_2O_3 DSSC FLUPS kinetics of different CDCA concentrations . . . 150
5.21 Fitting values, of the FLUPS kinetics, of TB207 in Al_2O_3 and TiO_2 DSSCs, prepared in the standard conditions . . . 154
5.22 Fitting values, of the FLUPS kinetics, of TB423 in Al_2O_3 and TiO_2 DSSCs, prepared under in standard conditions . . . 155
5.23 Injection efficiencies of TB207 and TB423 TiO_2 DSSCs, increasing CDCA concentration . . . 161

A.1 Fitting values of VG20 ZrO_2 DSSCs of different CDCA concentrations . A.7
A.2 Fitting values of VG20 TiO_2 DSSCs of different CDCA concentrations . A.8
A.3 Fitting values of VG20 TiO_2 DSSCs of different Li^+ concentrations . . . A.11
A.4 Fitting values of VG20 ZrO_2 DSSCs at different excitation wavelengths . A.13
A.5 Fitting values of VG20 TiO_2 DSSCs of different excitation wavelength concentrations . . . A.14
A.6 Fitting values of TB207 and TB423 in solution, measured with TAS and FLUPS . . . A.15
A.7 Fitting values of TB207 Al_2O_3 DSSC TAS kinetics, of different CDCA concentrations . . . A.17
A.8 Fitting values of TB207 Al_2O_3 DSSC fluorescence kinetics, of different CDCA concentrations, obtained by streak camera measurements . . . A.18
A.9 Fitting values of TB207 TiO_2 DSSC TAS and FLUPS kinetics, of different CDCA concentrations . . . A.20
A.10 Fitting values of TB423 TiO_2 DSSCs of different CDCA concentrations . A.22
A.11 Fitting values of TB423 TiO_2 DSSCs at different excitation wavelengths . A.23

Chapter 1

General Introduction

The increasing global energy consumption demands a greater variety of clean and sustainable power sources. In this context, photovoltaic technology is undoubtedly an attractive and applicable response to this challenge, as solar energy can meet the increasing global energy needs. According to recent statistical surveys, since 2010, the generation rate of new and renewable energy has grown rapidly from 1.24 %, to 8.88 % in 2018, and during the same period, solar energy production presented an impressive 1200 % growth [1]. Today, silicon based solar cells account for more than 90 % of the current installations, represent ca. 4 % of the energy production in Europe [2] and they accomplished the impressive achievement to produce several tenths of GW of electricity. Drawbacks of the silica photovoltaics such as the high production and conservation cost, the low efficiency and the bulkier non-flexible design can be overcome with even "greener" solutions such as the 3rd generation photovoltaics. In this category belong the Organic Photovoltaic Devices (OPVs), the Perovkite Photovoltaics, the Quantum Dot Photovoltaics and the Dye-Sensitized-Solar-Cells (DSSCs). All of them present advantages and disadvantages mostly centered around the photovoltaic performances in terms of efficiency [2], long-term stability, environmentally and human friendly properties, low-cost production and thus, production sustainability. The increasing multidisciplinary research interest on these promising technologies leading to one-after-another efficiency records directing many companies (Great Cell Energy, Ubiquitous Energy, Solaronix et al.) to commercialize them.

Our collaborating study is focused on the DSSCs' technology recognizing their unique advantages for various applications. These belong in the framework of the technology of transparent devices that can be integrated from buildings to electronic displays, autonomously powered electronic-glazing, etc. Our target is the creation, characterization

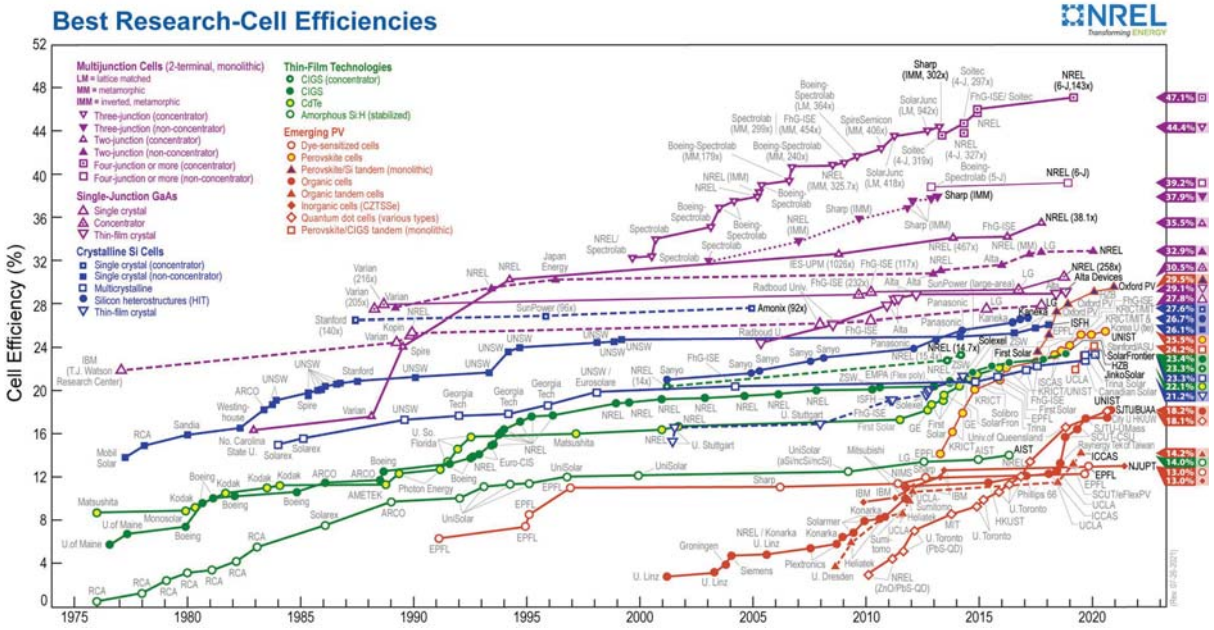

Figure 1.1: Summary of the different cell technologies best results by year (source: www.nrel.gov/pv/cell-efficiency). Impressively, new solutions PV applications emerged the last decades (red graphs) with cell efficiencies reaching 26 %.

and optimization of such novel transparent or semi-transparent DSSC devices. The effort includes four groups in the framework of the VISION-NIR project and additional collaborating international groups. The design of the synthesis of the first dye under investigation (cyanine -**VG20**) in this thesis were made by C. Barolo's group at the University of Torino and the last two (pyrrolopyrrole cyanines - **TB207**,**TB423**) by F. Odobel's group in CEISAM laboratory at the University of Nantes. The thorough optimization of the solar cells and the measurements of the photovoltaic performances took place by F Sauvage's group in the LRCS group at the University of Picardie Jules Verne in Amiens. The growth and characterization of the semiconductor (SC) nanoparticles is the field of study of the group of C. Sassoye at the University of Sorbonne in Paris.

This PhD work took place in the BIODYN group of the Department of Ultrafast Optics and Nanophotonics (DON) at the Institute of Physics and Chemistry of Materials (IPCMS) part of the National Center for Scientific Research (CNRS) in France in the framework of the University of Strasbourg. Our study is focused on the identification of the ultrafast processes occurring in a DSSC upon photoexcitation up to the photoemission in the fs-ps and ns timescale. Utilizing state-of-the-art experimental fs time-resolved techniques exciting and probing from the near-UV, through the Visible up to the near-IR we are able to determine the kinetics rates of the radiative and non-radiative processes

that limit or enhance the photovoltaic performances of the solar cells, with most important the injection efficiency from the dyes to the semiconductor conduction band, which occurs in the ps time scale. Detailed description of the experimental set-ups is presented in chapter 4 and the demonstration, analysis and discussion of the experimental results and foundlings in chapter 5.

References

[1] J.-H. Kim and S.-H. Han, "Energy generation performance of window-type dye-sensitized solar cells by color and transmittance," *Sustainability*, vol. 12, no. 21, p. 8961, 2020.

[2] E. C. of Auditors, "Electricity production from wind and solar photovoltaic power in the eu," *Background paper*, 2018.

Chapter 2

Transparent photovoltaics

2.1 Theory of Dye Sensitized Solar Cells

Bringing our attention to the third generation photovoltaic devices, along with the organic heterojunction photovoltaics (OPV), the quantum dots solar cells and the organic-inorganic halide perovskite solar cells, Dye-Sensitized-Solar-Cells (DSSCs) constitute a very prominent technology. DSSCs were initially invented in 1991 by B. O'Regan and M. Grätzel back in 1991 [1]. They introduced in a pioneering way an assembly of transparent thin films of anatase TiO2 nanoparticles sensitized with trimeric ruthenium (Ru) complexes acting as a solar light, energy harvesting antenna. The overall light-to-electricity energy conversion yield was 7.1 % in simulated solar light and 12 % in diffuse daylight, with exceptional stability realizing the concept of a breakthrough low-cost technology feasible for real world applications. Aftermath developments led very fast to higher efficiencies up tp 10.3 % by Nazeeruddin et al. using the Ru dye (N3 dye) as sensitizer with an iodine-based redox liquid electrolyte [2] and in 2005, with the improved Ru (N179) dye the efficiency of 11.2 % was achieved [3].In 2013-2014 the efficiency was further improved more than 13 % using this time organic dyes and utilizing cobalt(II/III) electrolyte. In 2014 porphyrin rings as dye molecules were utilized by Grätzel et al. achieving the remarkable efficiency of 13 % [4] and Hanaya et al. in 2015 prepared cells by co-sensitized an alkoxysilyl-anchor dye with a carboxy-anchor organic dye accomplishing impressively 14 % efficiency [5]. Finally the most recent high efficiency development has been reported early in 2021 by Grätzel et al. [6] using an organic Donor-Acceptor dye and cobalt(II/III) electrolyte determining efficiency of 13.5 % under standard conditions.

At this point it is important to highlight that the unique advantage of DSSCs is the flexibility for optical tuning depending on the dye that acts as sensitizer. Some sensitizers

among others that can be utilized for DSSC applications are organic dyes (Porphyrin, Rhodamine, D-A dyes et al.) [7, 8], scarce expensive metal complexes (Ru complexes et al.), mordant dyes (yellow mordant et al. [8, 9]) and finally natural dyes (Polyene dye, Coumarin and merocyanine derivatives et al [8]). Quantum dot and perovskite based sensitizers [8] have also widely been reviewed in the literature, as well as solid-state DSSCs [10–12], in which the liquid electrolyte is replaced by an electron-transport material (e.g. Spiro-OMeTAD) [13].

2.1.1 Components of Dye Sensitized Solar Cells

The elementary architecture of DSSCs contains the following components, as they are illustrated in Figure 2.1. Apart from the dye sensitizers on the semiconductor nanoparticles, described above, additional elements are the two electrodes, referring to the photoanode and photocathode, which are essentially glass films, whose connection parts are coated on a transparent conducting oxide (TCO). What's more, the semiconductor (SC) nanoparticles are coated in a transparent layer to the conduction side of the photoanode, and finally the electrolyte in between the two films. In detail:

- **The photoanode essentially acts as the working electrode for the device.** In the conductive TCO side, which mostly the fluorine-doped tin oxide (FTO) is used, there is the coated SC material. Various structural phases exist, such as the anatase (Eg = 3.20 eV), the rutile (Eg = 3.00 eV) and the brookite (Eg = 3.13 eV). The standard case, which gives the best Power Conversion Efficiencies (PCE) and is also in the scope of this Thesis, refers to the anatase-phase SC nanoparticles forming a film of 7 to 10 μm thickness. Essentially, the characteristic conduction band level of each material determines greatly its choice. For efficient devices, the classic case is TiO_2 and apart from this other materials have been used like ZnO for efficient devices. Other oxide semiconducting materials are SnO_2, Nb_2O_5 (n-type), and NiO (p-type). Additionally and in a different approach oxides such as ZrO_2 and Al_2O_3, have been used as references. Specifically, their conduction band level is energetically very high, higher than the dye's LUMO and thus, the driving force for injection is zero. This kind of inert device is usually used as reference for studying all photo-induced processes other than electron injection. Last, it should be mentioned that in order to suppress possible recombination mechanisms on the part of the conducting substrate that is exposed to the electrolyte a compact blocking metal oxide layer is used [14].

- **The photocathode acts as the counter electrode in the system.** It "closes" the system by completing the final process. The ultimate role of the photocathode is to collect electrons from the outer circuit and transfer them to the electrolyte therefore contributing to the reduction of the electrolyte.

- **The electrolyte** is yet another significant component with a significant role in the device operation. The presence of the reduction-oxidation (redox) couple in the electrolyte serves as a charge transport medium between the photocathode and the photoanode. Furthermore, it regenerates the dye, which had been altered to its cationic form after injection to the SC, before the next photon is absorbed. Electrolyte's role is finally essential and can define the stability of the device. Several general requirements are needed for a successful electrolyte, such as the physical and chemical stability, the high ionic conductivity to promote the charge transfer, low vapor pressure to avoid leakage and low volatility to avoid long term evaporation. Liquid electrolytes are most common, offering good efficiencies and stability with the most classic to contain the I_3^-/I^- redox couple. In modern DSSCs the electrolyte contains additives which boost the performance and improve the stability. Alternative electrolytes that have been introduced in bibliography contain Fc^+/Fc or Co^{3+}/Co^{2+} complexes [6], as well as ones with Cu redox pairs that have crossed efficiency of 14 % [15] For applications referring to transparent devices, colourless electrolytes are proposed with minimum absorption in the visible part of the solar spectrum, such as the sulfur based electrolytes [16].

2.1.2 Dynamic processes in Dye-Sensitized-Solar-Cells

The DSSC technology is unique and simple, taking into consideration the fact that energy harvesting and charge carrier separation occurs in the same layer. The principle of DSSCs is based on various dynamic and correlated photophysical and electrochemical processes. They take place and interact in a complementary way and finally define the photovoltaic performances. Accordingly, the understanding and individual study of each "section" is crucial for optimization.

The plain principle, step-by-step is illustrated in Figure 2.1 and described as follows. The dye, chemically-absorbed to the semiconductor, absorbs a photon and instantaneously is promoted to its excited state. Electron injection to the SC is a fast process, faster than the deactivation rate of the dye to its ground state and leaves the dye in its

cationic form. Continuing, the electrons transport through the nanostructured layer of the anode and finally is extracted in the external circuit. After injection the dye is regenerated by the electrolyte and in between charge recombination processes are possible to occur, limiting the efficiency. The temporal scheme of these processes extends from fs to ms.

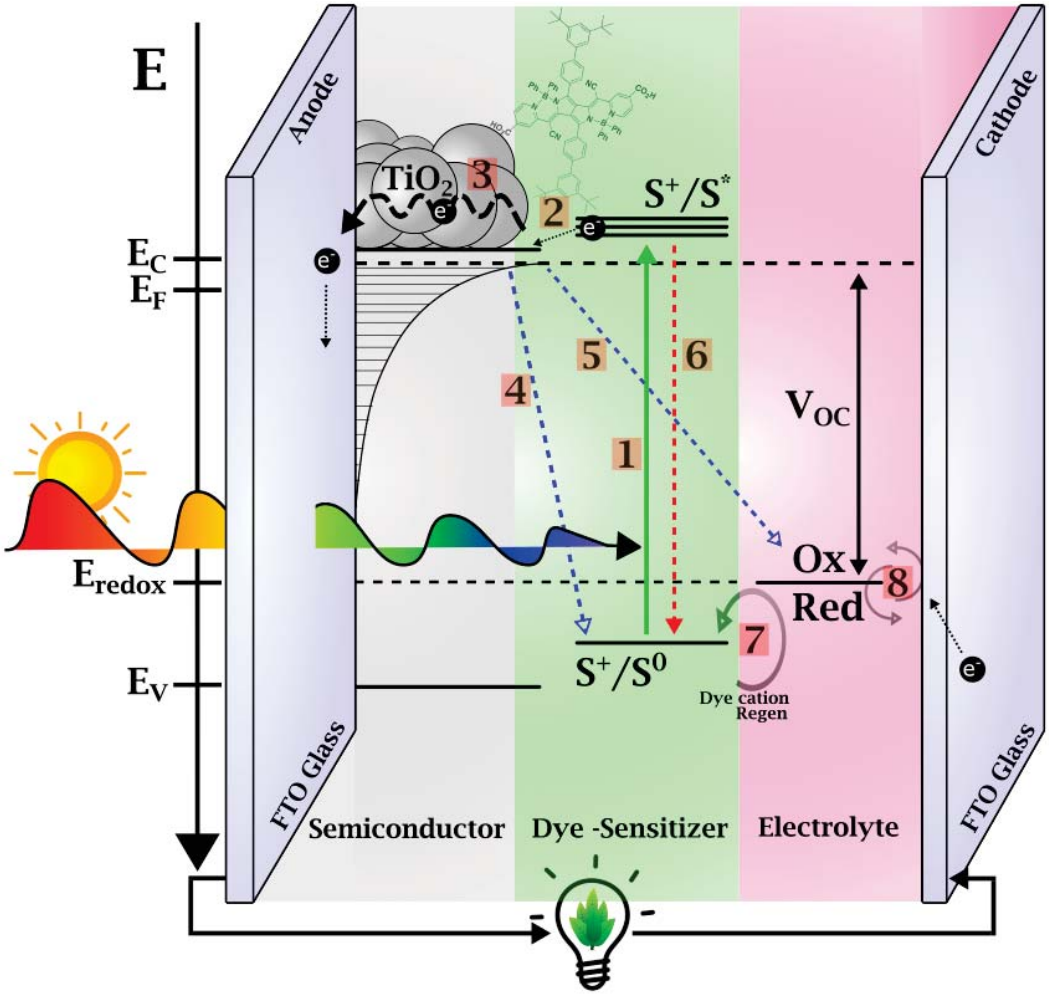

Figure 2.1: The DSSC principle and the various device components. (1) Dye-absorption. (2) Injection to the SC. (3) Charge transport. (4) Recombination from SC-dye cation (back electron-transfer). (5) Recombination from SC-electrolyte (Indirect recombination). (6) First excited-state deactivation (7) Dye regeneration. (8) Redox couple regeneration

In this Thesis, for the DSSCs under study thorough optimization has been performed by our collaborators in all different individual "sections" and our studies are precisely focused on the ultrafast processes. These includes the identification of the injection rate(s) and yield(s), as well as more specific interactions between different molecular species and

in general the photophysical study of the system.

More in detail:

- **Dye-sensitizer's photo-excitation.**

$$S_0|SC + h\nu \rightarrow S^*|SC \tag{2.1}$$

The photons incident on the DSSC, with minimum power losses (e.g. due to reflection on the glass and SC substrate) will be absorbed by the dye. The photoabsorption essentially refers to the promotion of an electron from the Highest Occupied Molecular Orbital (HOMO) to the Lowest Unoccupied Molecular Orbital (LUMO) and occurs very fast in $\sim 10-20fs$, faster than the vibrational relaxation in 10^{-13}-10^{-14} s [17, 18], in agreement with the Born Oppenheimer approximation.

- **Electron injection from the dye-sensitizer to the semiconductor acceptor.**

$$S^*|SC \rightarrow e^-_{cb}(SC) + S^+|SC \tag{2.2}$$

Possibly the most crucial parameter for achieving higher efficiencies [19]. A requirement for competitive electron transfer from the dye in the excited state to the SC manifold of states is the conduction band level to be energetically lower in energy than the LUMO of the dye. In this manner the overlap is considerable and the driving force for injection is enhanced. Also, the number of density states (DOS), at the surface of the semiconductor layer, in which the dye is attached is crucial [20–22]. In this manner the more dense the distribution of energy levels in the conduction band, the higher the injection rate. Therefore, electron transfer from a molecular donor d to a single band k of acceptor states can in an approximation be considered by Fermi's golden rule and in this manner the injection rate can be expressed as [23]:

$$k_{inj} = \frac{2\pi}{\hbar}\sum_k |V_{dk}|^2 \rho(\varepsilon_k) \tag{2.3}$$

where V_{dk} is the electronic coupling matrix element and $\rho(\varepsilon_k)$ the DOS. Relative to the dyes properties, another important requirement is the excited state lifetime. In principle the lifetimes must be significantly longer than the injection time, so as to avoid kinetic competition. For most sensitizers the excited state lifetimes extend from hundreds of ps to tens of ns, indicating that under this major condition the

potential injection efficiency could reach 100 %. Moreover, the electron density in LUMO, mainly determined by to the type and the specific structure of the dye, as well as the dye conformation on the SC surface [24] and the anchoring spacer groups that provide either a barrier, or a channel for surface electron transfer [25] are weighty parameters affecting the electron injection through the matrix element. It is worthy to be mentioned that in such densely populated systems, such as in the dye-SC solid state interface, the dyes tend to electrostatically interact and form bulkier conformations, such as molecular aggregates. These kinds of systems can drastically reduce the total efficiency and their role will be analytically described in the next chapter. It is significant to highlight that electron injection has essentially been observed to be strongly non-exponential [26]. An explanation could be the fact that in a real DSSC there is a distribution of dye-sensitizer conformations on the SC, which by its turn owns a degree of in-homogeneity that affects the CB manifold and the injection rate, which parameters in equation 2.3 changes as a function of the dye conformation. Single-exponential kinetic rates cannot be identified and if so, in order to obtain physical meaning, the rate should be accompanied by a distribution factor that describes the system best. An example of this should be a Stretched exponential or Kohlrausch function that will be described in Chapter 4.

- **Charge transport**

  After injection the charge is transported through the SC film to finally get collected at the external circuit. The precise mechanism of the transport is based on the random-walk principle [27] and it is hinged on the fact that at the surface of the SC nanoparticles there are many trap states and thus the trapping-detrapping process drives the electrons. The main driving force of charge transport is the gradient in electron concentration and it is not induced by the external electric field [28–30]. The electron can undergo an average of 10^6 trapping events until being collected, when they are generated far from the collecting electrode [27]. Because, the collection of injected electrons competes with recombination, slow transport can lead to a low charge-collection efficiency [31] and consequently to a low device's efficiency. It is a slow process which takes place in the ms time range.

- **Back electron transfer**

$$e_{cb}^{-}(SC) + S^{+}|SC \rightarrow S|SC \tag{2.4}$$

Back electron transfer or Electron-Cation recombination is an additional mecha-

nism that refers to the e^- recombination of e^- injected in the SC surface with the dye-sensitizer cation. This mechanism occurs before the regeneration due to the electrolyte and affects the efficiency negatively, because even though the initial electron has been efficiently injected to the SC, it isn't collected by to the external circuit. A sufficient timescale for the electron-hole recombination to occur, not to affect the DSSC performance is in hundreds of ns, but has been broadly observed occurring from ps to ms [23]. Both e^- injection and back e^- transfer rates, for the same in-homogeneity reasons are presented essentially as a distribution. Moreover, for the back e^--transfer yields and rates, the trapping-detrapping from a wide distribution of trap-state energies is crucial [23, 32–34]. In addition, both mechanisms are greatly affected by the dye's structure and geometry upon attachment on the SC, which could be either the spacer length between the dye and the SC, or the rigidity of the bonds and the degree of localization. Fundamentally, these parameters can affect the conformation of the dye upon the SC in a tilted or parallel conformation affecting also the pathway of charge transfer [23]. Last, the basis for the study of the charge transfer process in DSSCs in the last 3 decades was constituted by the Marcus theory [35–37]. Experimental discrepancies relative to the relation of the e^--transfer rate and the free energy driving force displayed signs of Marcus inverted region behavior [38, 39] and also gave rise to adjustments and modifications to the theory [40, 41].

- **Indirect recombination**

$$OX^+ + e^-_{cb}(SC) \rightarrow RED^- \tag{2.5}$$

The indirect recombination refers to the charge-hole recombination between the injected e^- that transports onto the SC with the oxidant of the redox mediator [42]. This mechanism is also non-beneficial for the total efficiency, because the injected electron wouldn't be driven to the external circuit, but reacts with the oxidant (OX) component promoting it to the reductant (RE) one. Relative to the reactions' kinetics scheme, this kind of indirect recombination can be minimized, when the dye-regeneration is sufficiently fast and the reduction of the oxidant in the electrolyte satisfactory slow.

- **Dye and Redox couple regeneration**

$$S^+|SC + RED^- \rightarrow S|SC + OX^+ \tag{2.6}$$

For a complete and long-term function of the DSSC the role of the electrolyte is essential. Indeed, the electrolyte can be described as a hole conductor. As it was mentioned above and demonstrated in the eq. 2.2, the dye radical cation S^+, formed after injection, receives an e^- from the reductant component and recovers to its initial neutral form. The rate should be fast enough to avoid direct recombination of the SC's e^- with the radical cation. In parallel, the reductant is converted to the oxidant and in the meantime the injected e^- that have been diffused on the SC, transits to the external circuit and finally is driven to the counter electrode (cathode). By its turn the previously formed oxidant will accept this e^- and re-form a reduced component. The above mentioned two-charge transfer mechanisms complete the circuit. In our systems under study the electrolyte of use is iodide based and therefore it contains I^-/I_3^- couples as reductant and oxidant components, respectively. It is suitable as a first candidate, because it offers sufficient redox potential, fast rapid regeneration and slow recombination. It is a broadly studied electrolyte [42] with high conductivity and good solubility. For developing transparent DSSCs its absorption in the visible spectral region prevents it to be a suitable candidate. However, our research focuses on the photophysics of the sensitizer and the interface's (dye-SC) interaction in the ultrafast time scale and not the electrolyte properties and consequently the iodine electrolyte is applicable. Therefore, for the iodide based electrolyte, the eq. 2.6 for the regeneration can be re-written as:

$$2S^+ + 3I^- \rightarrow 2S + I_3^- \tag{2.7}$$

and finally the oxidant component I_3^- reacts with two e^- at the counter electrode side producing the initial reductant component according to the following equation:

$$I_3^- + 2e^- \leftrightarrow 3I^- \tag{2.8}$$

Lastly, the regeneration process in the electrolyte is a rather complicated process with many experimental and theoretical works indicating that the reaction contains a series of subsequent reactions [43–46]. The predominately accepted scenario, includes in the sequence of reactions the formation of a physical-complex [S...I] and the contribution of the radical bi-iodide $I_2^{-\cdot}$. The insertion of $I_2^{-\cdot}$ in the chemical scheme converts the eq.2.8 to a one-electron reaction. Additional scenarios have been introduced, but the exact interpretation of regeneration is still debatable[44, 45].

- **Excited-state deactivation**

$$S^*|SC \rightarrow S|SC + (h\nu') \qquad , \nu' < \nu \tag{2.9}$$

The excited state deactivation can essentially have radiative character and reflect the luminescence, with the emission of photons of lower energy than the absorption or be non-radiative. Depending on the dye properties the excited-state lifetime varies and depending on the nature of the radiative process with values from hundred of ps up to tens of ns for fluorescence and up to μs or ms for phosphorescence. Finally, the excited state lifetime constitutes a decisive criterion for achieving high power-conversion efficiencies and should be orders of magnitude higher than the injection time. In this manner undesirable competition between them is avoided.

2.1.3 Photovoltaic parameters

The characteristic parameters describing the basic photovoltaic parameters are the short circuit (in zero voltage) current density (J_{SC}), the open circuit voltage (V_{OC}) and the fill factor (FF). The overall photoelectric conversion efficiency (PCE) for a DSSC is given by the product of the open-circuit (with zero-current density) voltage (V_{OC}), the fill factor of the cell (FF),the intensity of the incident light (P_{in}) and the short circuit Photocurrent Density (J_{SC}), according to the following equation.

$$PCE = \frac{P_{max}}{P_{in}} = \frac{J_{SC} \times V_{OC} \times FF}{P_{in}} \tag{2.10}$$

where P_{max} the maximum obtainable power. More detailed, J_{SC} is an important quantity derived from the measured I_{SC} divided by the incident surface. As it is presented in figure 2.2, J_{SC} depends on the quantum yield of electron generation by the incoming solar photons and essentially describes both the ability of the dye to absorb light and the yield for injection to the SC and collection to the external circuit. (V_{OC}) typically expresses the total output voltage when there is no current density and it is equal to the difference of the SC's Fermi level and the redox's couple potential (Figure 2.1). Last the FF is an important parameter that determines the photovoltaic quality by accounting for Ohmic losses (e.g. dark current in the SC), which must be minimized. From Figure 2.2 it is defined as the ratio of the maximum power from the solar cell P_{max} to the product

of V_{OC} and J_{SC} or the ratio between the two rectangules (eq. 2.11).

$$FF = \frac{P_{max}}{J_{SC} \times V_{OC}} = \frac{area\ B}{area\ A} \tag{2.11}$$

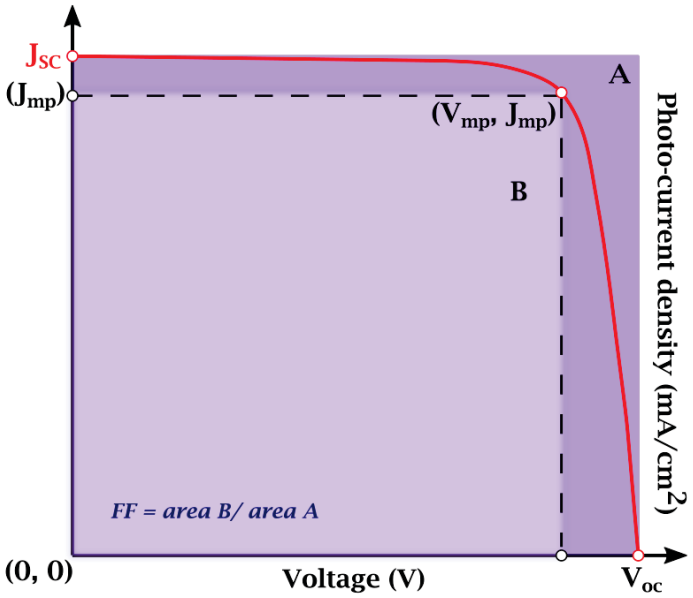

Figure 2.2: Standard J-V curve for a DSSC.

Another way of evaluating the performance of the photovoltaic cell is the external quantum efficiency or Incident Photon to Current Efficiency (IPCE). IPCE is commonly used for describing the spectral response of the DSSCs and its value corresponds to the photocurrent density produced in the external circuit under monochromatic illumination of the cell divided by the photon flux that strikes the cell. Analytically it is related to the J_{SC},

$$J_{SC} = \int IPCE(\lambda) \times e \times Photon\ Flux(\lambda)\ d\lambda \tag{2.12}$$

where e is the elementary charge. The IPCE can be expressed as:

$$IPCE(\lambda) = LHE(\lambda) \times \varphi_{inj}(\lambda) \times \varphi_{reg}(\lambda) \times n_{cc} \tag{2.13}$$

where, LHE(λ) is the light-harvesting efficiency at a given wavelength, $\varphi_{inj}(\lambda)$ and $\varphi_{reg}(\lambda)$ are the quantum yields for electron injection and dye regeneration, respectively, and η_{cc} is the charge collection efficiency.

For specific applications the term of efficiency can be modified taking into consideration relationships between additional parameters. For example for transparent photo-

voltaics (TPVs) meaning like Average Visible Transmittance (AVT) and Color Rendering Index (CRI), as well as the relationship between the PCE to AVT is important. Taking the above into consideration, an analytical description of these "colouring" parameters will be presented in the next paragraph.

2.2 Transparent DSSCs

Transparent technologies with partial light transmission is a field of study for the last three decades. They can be integrated in the space of the surrounding in which the bulkier conventional photovoltaics cannot and the efficient use of architectural space make them perfect candidates for integrated building-windows, in automotive applications, in electronic displays and in urban-street infrastructures et al. They require less space, offering more active surface to use and consequently increase the total gain.

2.2.1 Determination of the degree of Transparency

In the framework of transparent applications the degree of transparency and the aesthetic assessment are as important parameters as the determination of the efficiency of the photovoltaic device. There are various approaches to determine the level of transparency for transparent photovoltaics (TPVs). A general approach, accepted by industry is introducing the Average Visible Transmittance (AVT). It is defined as the ratio of the integration of the transmission spectrum against the phototopic human's eye response as follows:

$$AVT = \frac{\int T(\lambda)P(\lambda)S(\lambda)d(\lambda)}{\int P(\lambda)S(\lambda)d(\lambda)} \tag{2.14}$$

where λ is the wavelength, T is the transmission, P is the phototopic eye's response and S is the solar photon flux (AM1.5G). AVT is a direct way of determining the degree of transparency and for the theoretical value of 100 % AVT the thermodynamically limited efficiency, has been calculated to be 20.6 % [47], by the Shockley diode equation [48] for a single junction selective TPV and for the entire absorption of the near-UV ($<$435 nm) and near-IR part ($>$ 670 nm) of the solar spectrum. Also, it is commonly observed that AVT and PCE have often inversely relationship. Lunt et al. proposed as a new metric, the Light Utilization efficiency (LUE). This metric represents the overall system's efficiency rationalizing AVT and PCE as such:

$$LUE = PCE \times AVT \tag{2.15}$$

Ultimately, LUE is a useful quantity to compare different TPV technologies, beyond the theoretical limitations.

Last, but not least, the degree of transparency is one important metric for the aesthetic assessment of the TPV technologies, but there is an additional metric commonly used, relative to the coloration of the device. This is the Color Rendering Index (CRI). CRI was introduced by the International Commission on Illumination (Commission International de l'Eclairage-CIE) and is defined as a metric to quantify how accurately the color of a given object is rendered either from a light source, or through a transparent medium with respect to an "ideal" illumination source (a blackbody radiator under specific-standard conditions) [49, 50]. The idea behind the CRI introduction is that colouration is an abstract concept and colors can be perceived differently under different illuminations and therefore comparing with a universal reference is useful [51]. CRI takes values from 0 to 100 and it is self-evident that the higher the CRI the better the image's quality (Figure 2.4.a) or the "seen-through the TPV" colour compared to the initial colour. Usually, a TPV with a CRI $>$ 70 % is generally considered of very good quality [47, 49, 52] and greater than 90 % excellent. Mallick et al. [53] introduced CRI metric to assess the visual comfort of DSSC and they reported values between 83 and 93 % for coloured semitransparent DSSCs.

The derivation of the final equation for CRI is a rather complicated procedure and has been revised many times taking into account additional parameters and correct for them, such as the chromatic adaptation of the human eye etc. The CRI is calculated within an evolution of functions as an average score of eight different test colour samples [50]. Taking into consideration that the human eye possesses trichromacy, the CIE in 1931 [50, 54, 55] introduced the tristimulus values (X, Y, Z) as parameters to visually match a colour under standardized conditions against the three primary colours (red, green, and blue). Continuing, by adding the transmittance curve $\tau(\lambda)$ of the TPV device and the spectral reflectively $\beta_i(\lambda)$ the tristimulus chromaticity coordinates (x, y, z) can be evaluated by their relative magnitude as:

$$x = \frac{X}{X+Y+Z}, \quad y = \frac{Y}{X+Y+Z}, \quad z = \frac{Z}{X+Y+Z} \tag{2.16}$$

Subsequently, only the (x, y) coordinates are needed to describe the 2D chromaticity diagram or CIE1931 colour space (Figure 2.3).

An issue of CIE1931 is that the three dimension colour space in the rectangular coordinates is not visually uniform. Therefore, CIE1976 (or CIELUV) was created. The colour space was altered and the (x,y) coordinates, after mathematical transformation

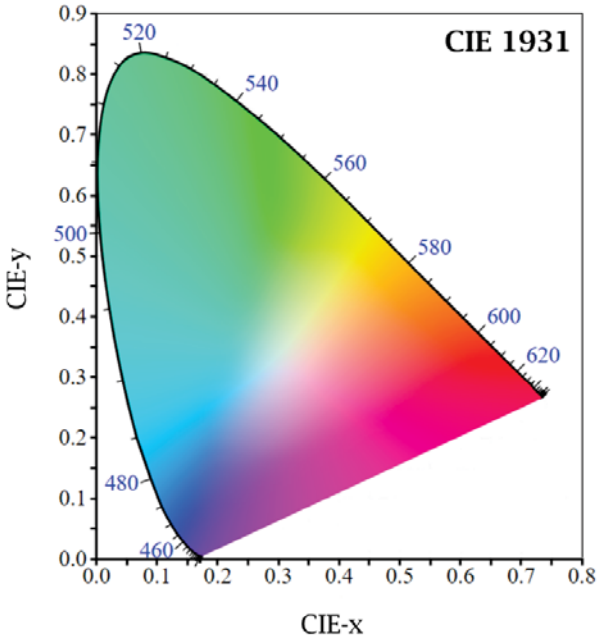

Figure 2.3: The CIE 1931 uniform chromaticity diagram with x-y chromaticity coordinates.

are expressed as (u, v), again as a function of the tristimulus coordinates.

For the CRI calculation there is need for some additional parameters to be taken into consideration. One is the adaptive colour shift that refers to the human's eye ability for chromatic adaptation to certain ambient conditions and second, the introduction of the brightness of an object as factors that affect the colour that will be seen. By summarizing, this new brightness/lightness coordinate W^* is introduced and the above mentioned chromatic coordinates, corrected for the distortion by chromatic adaptation, will be expressed as a function of it and finally the updated CIE1964 uniform colour space is derived. Nowadays, both CIE1931 and CIE1976 colour spaces are widely used.

An alternative color metric, based on CIE1976 is the CEILAB. CEILAB is useful in applications, in which the chromaticity coordinates are described directly, typically as a^* and b^* within the 3D CEILAB space (Figure 2.4.b). Precisely, a^* and b^* (latitude, altitude in the colour sphere) represent the transmission and reflection, respectively and they are also calculated by the tristimulus coordinates [56, 57]. A colour measurement in the $+a$ direction represents a shift from green towards red and a colour measurement in the $+b$ direction represents a shift from blue to yellow colour. In the 3D map the third chromaticity coordinate is L^* (longitude in the colour sphere) and it indicates lightness, which essentially reflects the human perception of contrast for given (a^*, b^*) and take values from 0 (black) to 100 (white).

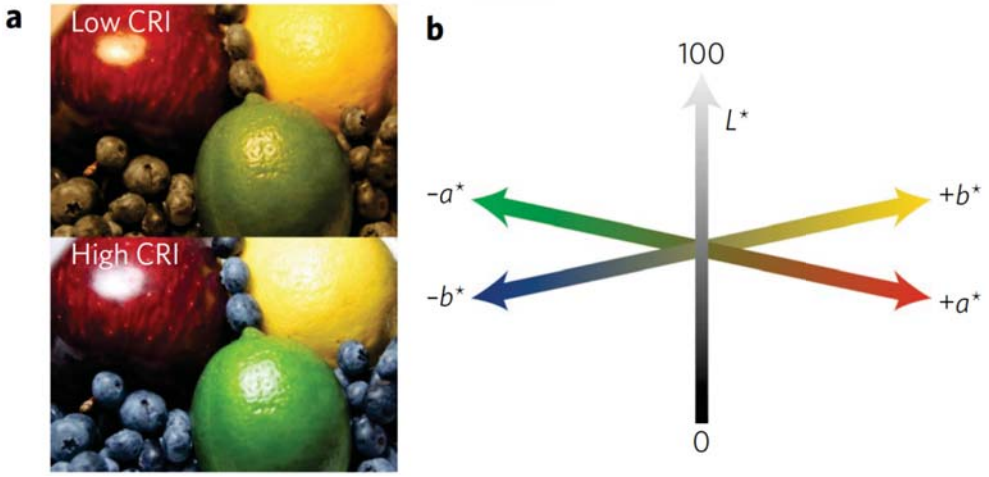

Figure 2.4: Images of (a) low (up) and high (down) CRI and (b) The 3D colour space CIELAB. [49]

2.2.2 Wavelength selective and non-selective transparent solar cells

Relative to the application of transparent technologies, there are many requirements and difficulties. The TPVs must exhibit high efficiencies, low fabrication cost, long operating lifetimes that at the same time maintain high level of transparency. Currently, there are various TPV technologies and can be categorized to wavelength-selective and non-selective [49] (Figure 2.5). As non-wavelength selective TPVs, we define all those photovoltaic technologies, of which the operating principle is based on photon harvesting through the solar (or other source's) spectrum targeting the maximization of the efficiency and the level of transparency is defined by structural modifications and adjustments of the device material. On the other side, the wavelength-selective TPVs, achieve high levels of transparency, by selectively collecting photons of energy lower (Infrared-IR) or higher (Ultra Violet-UV) than the visible (Vis) part at 350-750 nm of the electromagnetic spectrum. In Figure 2.5, the most important TPV technologies are categorized by type, as they have been distinguished elsewhere [49].

Starting from the "non-selective wavelength" TPVS, a great amount of research has been adapted to the previous conventional PV technologies, such as the silicon ones [58]. The conventional PVs, use material of bandgap 1.1-1.7 eV and have essentially an opaque structure, but present the higher efficiencies, close to the theoretical limit/max value for p-n junction PVs [59]. Therefore, in order to increase the transparency level, effort has been focused on either the thin-film technology, or on the spatially segmentation of the

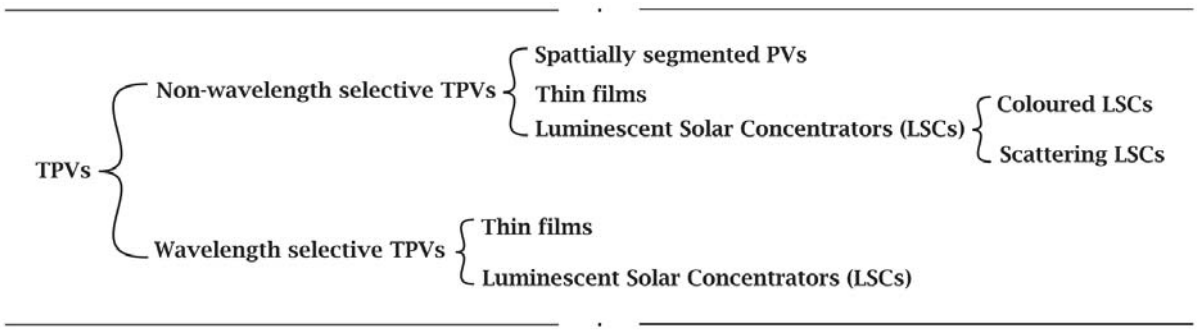

Figure 2.5: Diagram of main TPV technologies

PV's active area. The idea is to reduce the active area's surface allowing in this way visible light to pass through the structure. It is self-evident that for these broadband-absorbing devices when the AVT advances to 100 % the PCE approaches zero, due to the inherent trade-off between transmission and efficiency. Therefore, the PVs of this type are often called semi or quasi-transparent. The spatially segmented TPVs essentially own patterned active areas or pinholes in the cell with with the gaps or holes to be only the transparent substrate. Thus, by reducing the active area the transparency increases. Despite the conventional PVs, also 3rd generation PVs, such as perovskites have been tests in this category, utilizing micro-slices on the surface [60, 61]. In the same line, thin-film technology is based on the perception of reducing the thickness of the active area and vice-versa increasing the transmission. The performance and transparency of a thin film depends on various mechanisms such as the the material used and its micro-architecture (nanoparticles, nanotubes et al.), the thickness, the manufacturing procedure (e.g. porosity control) and the deposition method. Typical thickness for a thin-film ranges in the nm-μm scale and the most well-known deposition methods are screen-printing [62, 63], electrophoretic deposition [64] and sputtering deposition for nanotube deposition [65] and dip-coater [66]. Each method has advantages depending on the application's characteristics. Typical materials for thin films are perovskites [67], quantum dots [68], single-junction organic PVs (OPVs) [69] or hererojunctions with bulkier components [70] and even Dye-Sensitized Solar Cells (DSSCs) [71]. Essentially, for the DSSCs, the contact conductive anode-cathode layer thickness, as well as the SC (e.g TiO_2 nanoparticles) are in the nm scale.

Luminescent Solar concentrator (LSC) technology is another category for feasible transparent energy-harvesting devices [72] (Figure 2.6). It contains a transparent substrate doped with either dyes, or scattering nanoparticles. The incident light is either absorbed (coloured SCs [73]), then emitted and driven towards the edges (the glass sub-

strates acts as a waveguide plate), or it is directly driven (scattering LSCs [74]) to the perimeter's sides sides due to multiple scattering. There it is harvested by conventional PVS of high efficiency. The glass substrate acts as a waveguide plate. Scattering LSCs have the disadvantage that upon operation the optical losses are significant for wide effective areas (>5 cm), due to multiple scattering events that out-drive the waveguided photons outside the device's defined pathway. In terms of colouration they own a more blurred surface than the coloured ones. The molecules that are used for doping can be organic [73] or in-organic [75] and owns partial absorption in the visible, offering them a variety of colours, but affecting negatively the AVT with PCE less than 7 % [73].

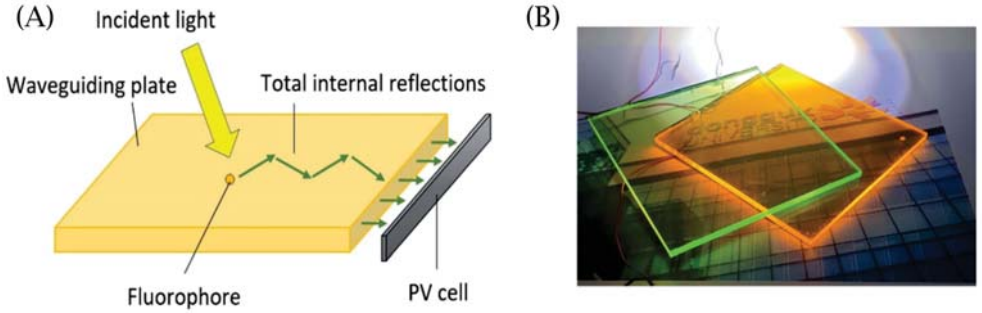

Figure 2.6: (A) A schematic illustration of a LSC device doped with chromosomes. The glass substrate works as the waveguide plate drive the fluorescence to the PV cell incorporated at the edges. (B) Picture of real LSCs of chomophores emitting at different wavelengths. *The figure was taken from reference [76].

The second category of interesting TPV technologies is the "wavelength selective one [77]. The basic principle is that the photon trapping material must be designed and tuned to absorb in the "non-visible" part of the spectrum with reference the human's eye phototopic response, which will be the UV and IR. Continuing with the LSCs, two tactics have been established. The first is to use dyes absorbing in the UV and emitting in the IR, minimizing in this way re-absorption phenomena and the second is to absorbing and emitting in the IR. In the first case the devices managed to exhibit the impressive AVT of 84 %, CRI of 94 %, but with very low PCE, less than 2 % [78], which is due to the low UV percentage that can be harvest in the solar spectrum, compare to the Vis and IR. As for the second case, of IR-selective solar concentrators, the record up-today AVT of 88 %, CRI of 94 % was achieved by using organic salt derivatives by Lunt et al. [79], but with efficiency less than 0.4 %, due to re-absorption mechanisms.

Last but equally important case, is the "UV/IR wavelength-selective PVs". The major candidates of this category are the Organic PVs (OPVs) or Polymer PVs (PVs), the DSSCs, as well as the Quantum dot PVs (QPVs). Broadband research has been focused

on each component achieving high levels of transparency and defining the limitations, with most important the dyes of selective absorption, which essentially defines the final AVT. Relative to OPVs, Lunt first introduced in 2011 an organic heterojunction consisting of a phalocyanine dye as donor and a C_{60} moiety as acceptor, achieving in this way AVT of 65 % with PCE of 1.7 %, when using back-positioned NIR reflecting mirrors [80]. Later in 2012, PCE of 4 % were reached, with AVT of 64 % utilizing the polymers PBDTT-DPP and PCBM and the top electrode consisted of a merge of ITO nanoparticles and Ag nanowires [81]. In terms of PCE, a record value of 5.1 % was achieved by the company Ubiquitous Energy, but with a modest AVT value of 52 % [49]. It was based on a single junction device of a NIR-selective excitonic semiconductor, converting in the range of 650-950 nm. Adding to the previous, there are various works relative to donor-acceptor PVs, that reached PCEs close to 10 %, but the AVT is pronounced low, below 35 % [82, 83]. Another very promising UV/NIR wavelength-selective technology are the DSSCs. They are advantageous due to the relative simplicity of the device, in which both photon collection and carrier separation occurs on the same layer. They exhibit high level of AVT and CRI that can be adjusted simply by finely tuning the dye's absorption and electrodes thickness. A notable DSSC example, with the higher PCE and AVT was published in 2014 by Han et al [84]. It was based on a squaraine dye with a peak maximum transmittance value of 60 % at 560 nm, attributing a "greenish" color to the DSSC and a PCE of 3.66 %. Another, example, referring to semi-transparent DSSCs, was proposed by Demadrille et al. [85]. They reported the high AVT of 59 %, but in the dark and under illumination the transparency decreases, but the PCE reaches the high value of 3.7 %.

In conclusion, all PV technologies present advantages and disadvantages. When the selection criteria narrow to TPVs, parameters like AVT and CRI et al. become crucial for transparency characterization and aesthetic assignment. Therefore, and taking the above progress of the various, up-to-date, technologies into consideration the TPVs that will most likely dominate, will contain molecular absorbers, as their discrete absorption bands allow more selective light harvesting. For this reason the current PhD study focuses on the investigation of wavelength-selective DSSC TPVs. Important findings will be presented relative to three dyes cyanine (**VG20**) [86] and pyrrollo-cyanine dyes (**TB207**, **TB423**) that harvest photons exclusively in NIR and exhibit unprecedented and record efficiencies ($>$ 4 %), with regard to their transparency (AVT=75 %). In the following section, we will present the major dyes that can be used as sensitizers in operation DSSCs and belong in the family of NIR molecules, promising for see-through applications.

2.2.3 Dyes for Dye-Sensitized-Solar-Cells designed for the near-infrared

NIR selective sensitizers are possibly the most important components related to the transparency of the DSSC device. Their fine tuning relative to their HOMO-LUMO energy band-gap is essential with respect to the conduction band (CB) of the semiconductor (SC), as it defines both the optical properties and colouration of the dye, as well as the well function of the device. For the NIR dyes' design there are some limitations that must be overcome and will be discussed below.

While the visible radiation (350-700 nm) includes the 45 % of the total solar energy (Figure 2.7 left), the red/NIR (600-1000 nm) accounts only for the 25 % of the solar energy flux [87, 88]. For this reason, it is essential that all photons below the threshold of 920 nm [89] be harvested by the device. The majority of the studies on DSSCs have been focused on sensitizers that absorb in the visible, with upper limit the 700 nm (1.7 eV). One of the main drawbacks of NIR dyes, is that the HOMO-LUMO bandgap is relative low (1.3 eV), due to the absorption at longer wavelengths. In this manner and with respect to the energy correlation described in previous sections, the LUMO energy level must be higher than the SC's CB, which for the case of the standard TiO_2 is around $E_{CB} = -0.2\ eV$ ($E_g = 3.2$). This restriction is difficult to be satisfied with dyes that have been synthesized to absorb at low energies and therefore when the LUMO is at equal or lower level, compared to the CB, the driving force for injection is very low or zero (Figure 2.7 right). LUMO should be typically 0.2 eV higher then the CB. This issue couldn't be satisfied by changing the SC material to one with lower CB level relative to TiO_2. Reducing the CB's level could possible increase the yield for undesirable geminate (back) and non-geminate (indirect) recombination mechanisms to occur, reducing the electron collection and finally the PCE. One way of finely tuning this interplay between the energy levels is the electrolyte composition. As in the original work of Graetzel et al. that influenced the majority up to date of researches in the field, the TiO_2 has been matched with the I_3^-/I^- redox couple [1]. However, alternative combinations could be used, such as metal-based electrolytes (eg. Co^{2+}/Co^{3+}) for successful regeneration and sensitizers with appropriate bandgap could be synthesized for these applications [5, 6]. An alternative that it is also used in the framework of this Thesis work, is the use of additives in the electrolyte, such as Li^+ in the I_3^-/I^- based electrolyte. The Li^+ atoms adsorb deep into the SC's layer and after thermodynamic equilibrium the CB position downshifts. In the same manner the concentration of additives is important to be examined with respect to

the photovoltaic performances.

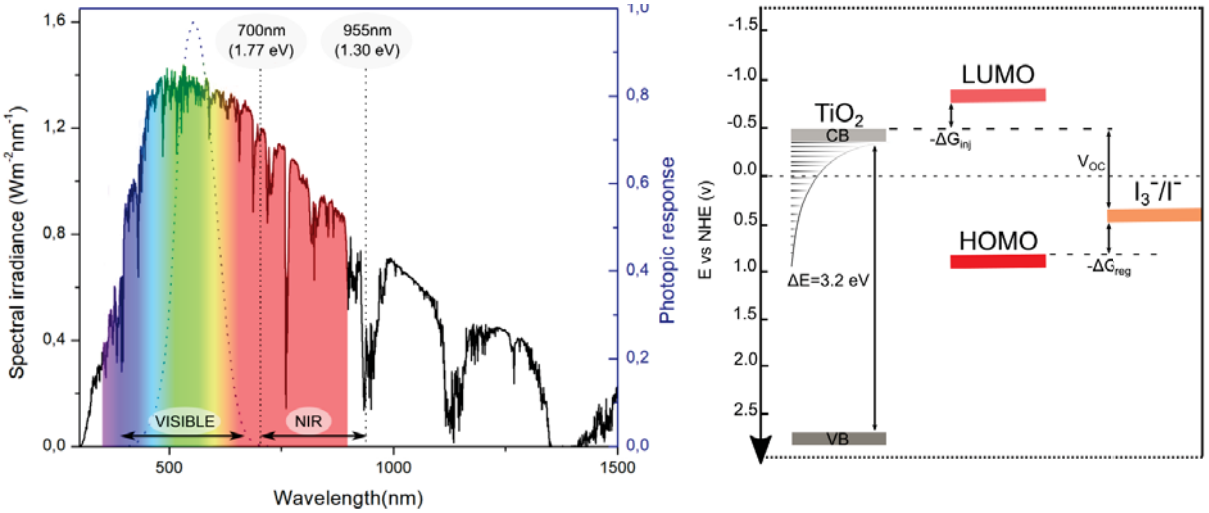

Figure 2.7: (Left) Standard solar spectral irradiance at A.M.1.5 G conditions at the sea level and the eyes' photopic response (blue-dotted). (Right) Dye's HOMO-LUMO (red) band positions, TiO_2 VB-CB energy gap (gray) and I_3^-/I^- couple redox potential energy level (orange). $-\Delta G_{inj}$ corresponds to the driving force for injection and equals the difference between the SC's CB and the dye's LUMO. $-\Delta G_{reg}$ corresponds to the driving force for regeneration and is equal to the potential difference between the dye's HOMO level and the redox couple potential of I_3^-/I^-.

In addition to the energy level interplay and positions, fundamental requirement for the choice of dye is the high molar absorption coefficient in the NIR region, but not in the visible. Therefore, transitions located in the near-UV ($S_0 \rightarrow S_2$, $S_0 \rightarrow S_3$ etc) should own very low extinction coefficient and only the transition to the first singlet-excited state ($S_0 \rightarrow S_1$) should be boosted, resulting in strong and narrow (selective) NIR absorption. Good physical, chemical and thermal stability of the dyes are equally important parameters [90], as well as the low-fabrication cost and the environmental and human friendly properties (e.g. no-toxicity). Another drawback of all dyes attached on DSSCs is the formation of aggregates [91–93]. Energy transfer from monomers to aggregates and inefficient injection to the SC from the aggregates strongly reduces the PCE. This energy transfer interaction depends on the spectral overlap of monomers' emission and aggregates' absorption, which by its turn scales with λ^4, indicating a greater effect for NIR dyes [90]. A more detailed and analytical description of the "aggregate issue", in terms of photophysics and on real DSSC devices will be given in Chapter 3 of the thesis.

The main categories of NIR dyes can be divided in those containing metal or non-metal sensitizers [88]. Relative to the NIR-metal-free dyes, this category includes poly-

methine dyes such as cyanines [87, 92, 94], squaraines [84, 90], croconites [95] and diketopyrrolopyrrole (DPP) dyes [96]. As for metal NIR complexes these can be Porphyrins [97–100], after proper structural engineering and Phthalocyanine dyes [101–103]. To conclude and taking the above into consideration, there are numerous cases of NIR dyes that have been used and explored for DSSC applications. Narrowing the interest to selective NIR wavelength applications the choices reduce further and careful selection and synthesis strategy must be adopted. In the context of the following PhD study the dyes of choice belong in the family of polymethine dyes (cyanines and pyrrolopyrrole-cyanines).

2.3 Ultrafast Spectroscopy on DSSCs

In DSSCs, as well as in all energy-harvesting applications, all photophysical processes are energetically coupled. Multi-step electron transfer and transport mechanisms take place from time zero, which essentially refers to the interaction of the solar photons with the collection antenna of the device, up to the final conversion to electrons and collection from the external circuit. The relative dynamics of each process are well aligned and principally defines the final PCE efficiency. Therefore, the temporal identification and analysis of the charge transfer processes is significant and numerous techniques have been developed forming the field of study for time-resolved spectroscopy.

The concept of time-resolved spectroscopy introduced since 1950 with flash-photolysis offering timescales in the range of μs and ms [104]. Later, the conception of lasers and advance of mode-locking techniques offered even shorter resolutions in the fs-ps and ns time scale. In the framework of our study we perform optical ultrafast spectroscopy, commonly referring to the fs-ps time domain. More advanced ultrafast spectroscopic techniques include laser beams with frequencies tuned to THz and X-ray and can be currently offered by modern high laser power facilities and free-electron lasers (e.g. THz FEL, XFEL). In their most classic form, ultrafast time-resolved experiments are based on a two-beam interaction and hence this kind of spectroscopy is commonly named Pump-Probe [105, 106]. The pump beam excites the sample under investigation and photoinduces all the measured kinetics. The probe is essentially a broadband pulse and arrives at the sample after a series of increment delay times. A recent development of these set-ups refers to the field of multi-dimensional spectroscopy [107–111], which fundamentally utilizes multipulse pump-probe beams by creating and probing, respectively, coherences associated with vibrations or coupling of electronic transitions.

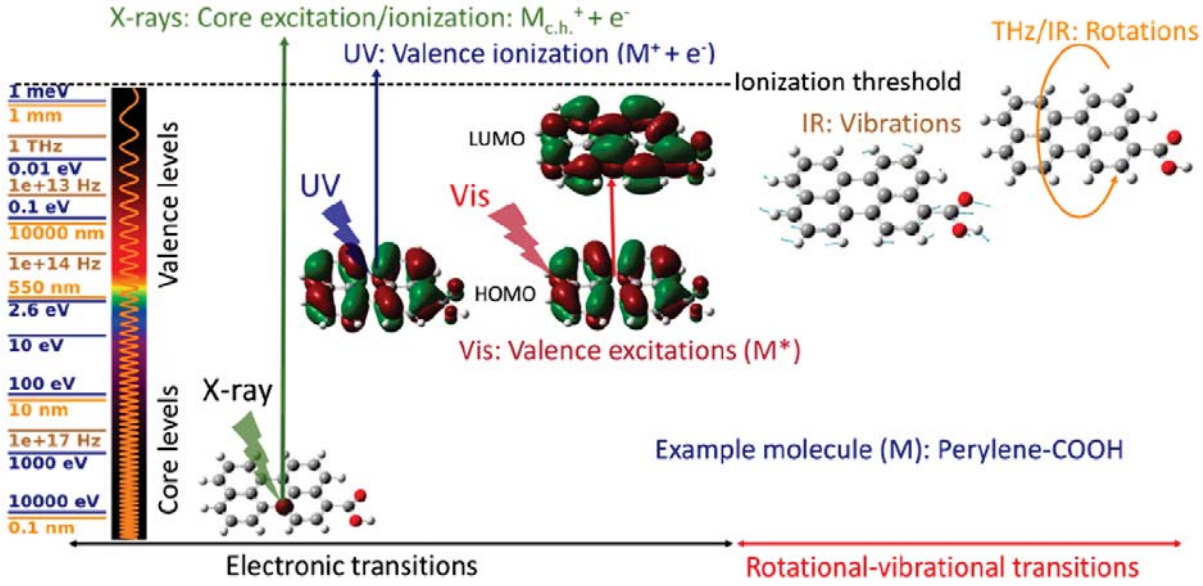

Figure 2.8: Typical molecular excitation processes at various excitation energies, wavelengths and frequencies from X-ray to THz. $M_{c.h.}^{+}$, stands for the ionized molecule with a core hole, M^+ for the ionized molecules with a valence hole and M^* for an excited molecule. *The figure was taken from the reference [69]

- **Time-resolved optical spectroscopy**

  One of the most widespread means of time-resolved spectroscopy on energy-harvesting systems is optical spectroscopy. This includes fs transmission (or scattering) and fluorescence spectroscopy and will be the main spectral region for our study. Detailed analysis of the photophysical mechanisms occurring in this spectral and time domain will be reminded and introduced in chapter 3 of the thesis and a detailed demonstration of these techniques in chapter 4. For energy-harvesting systems, such as the DSSCs, the experimental conditions should be close to the real-life operation ones of 1 sun solar radiation or 100 $mW \cdot cm^{-2}$. For visible excitation wavelengths the photon energy is the same as for the solar radiation. The energy density can be different, but typical fs pulsed lasers have repetition rates of 1-5 kHz and in this manner the number of $photons/cm^2/s$ can be comparable with the sun's irradiation [69]. Additional attention must be given to the excitation energies for realistic DSSC operational settings. If the pulse energies exceed a threshold point non-linear processes can occur, for instance Exciton-Exciton annihilation or Two-Photon absorption. Nonetheless, the exact value of the threshold depends greatly on the dye's properties. For DSSCs it is possible that the sensitiser molar absorption coefficient is large, especially for NIR selective dyes for TPV

applications ($> 100'000\ M^{-1}cm^{-1}$). Therefore, even in real-life operation under standard illumination conditions multi-exciton generation can take place. Hence, time-resolved investigation of the ultrafast processes by increasing the pump flux could be of great interest. Various works e.g. from A. Douhal, M. Ziolek et al.[112] and J. Moser et al.[113, 114] indicated the effect of the competition of intermolecular processes, such as self-quenching through e.g. singlet-singlet annihilation, to the population kinetics and charge-carrier injection.

- **Time-resolved THz spectroscopy**

  THz refers to the far infrared frequencies, typically from 0.1 to 10 THz. In semiconductor systems inside solar cells, time-resolved THz spectroscopy directly monitors the charge carrier dynamics [115, 116]. Specifically it monitors the transient conductivity in the fs-ps-ns timescale revealing indirectly both intra and interparticle transport mechanisms [117]. If the pump beam is in the UV the photoexcitation generates electrons in the SC via interband photoexcitation, while Vis photoexcitation results in electron injection from the dye to the SC. In addition to the pump beam, there are the probe (collected THz radiation) and the gate (800 nm). By controlling the delay pump-probe the change in photoconductivity can be measured and by varying the delay of the gate if is feasible to record the map of the THz electric field probe. The change in photoconductivity ($\Delta\sigma$) can be expressed with the following equation [69, 118]:

$$\frac{\Delta\sigma}{n_{exc}e_0} = \xi(\mu_e + \mu_h) = -\frac{E_{exc}(\omega) - E_{gs}(\omega)}{E_{gs}(\omega)} \frac{\varepsilon_0 c}{F e_0} \frac{1}{1 - e^{-\alpha D}} \tag{2.17}$$

  where, $n_{exc}e_0$ is the product of charge density with the elementary charge, ξ is the quantum yield of photoexcited carriers, μ_e and μ_h the mobilities of electrons and holes. $E_{exc}(\omega)$ is the THz electric field through the sample in its excited and $E_{gs}(\omega)$ ground state. c is the speed of light, ε_0 is the permittivity of vacuum, D the sample thickness, F the light fluence at the pump wavelength and α the absorption coefficient. Noteworthy, after the excitation from the pump, in order to detect charge carriers with this technique, they must 1) be created (e.g. after electron injection from the dye to the SC) and also their mobility must not be too low. Rise of the photoconductivity kinetics indicates the generation of the charge carriers on the SC and/or the increase of their mobility.

- **Time-resolved X-ray spectroscopy**

  There are various time resolved-X-ray spectroscopic techniques. X-ray scattering already offers unique structural information and when time-resolved, X-ray diffuse scattering (XDS) is able to monitor structural changes in the dye or the interacting media [119]. Additional useful techniques are based on the function "photon-in, electron-out" such as the X-ray photoelectron spectroscopy (XPS) or Auger electron spectroscopy (AES) [120] and X-ray emission spectroscopy (XES) [121, 122]. X-Ray emission probes weak and sensitive emission lines, rises experimental challenges to measure e.g. valence to core transitions (VTC) (Figure 2.9) and essentially is a complementary spectroscopic technique to the X-ray absorption spectroscopy.

  X-rays are, originally, ionization radiation, offering enough energy to eject a core electron from an atom. In Figure 2.9.A the low-resolution X-ray absorption spectrum for Pb is presented, revealing the three major transitions of K, L and M edges corresponding to the excitation of an electron from n=1, 2 and 3 atomic shells, respectively (Figure 2.9.D), where n are the principle quantum numbers [123, 124]. For example, excitation of an 1s electron occurs at the K-edge, while excitation of a 2s or 2p electron occurs at an L-edge. On its turn, X-ray absorption spectroscopy (XAS) is based on this principle, of tuning the photon energy to a range where the core electrons are excited and presents a powerful tool to identify the local geometric and electronic structure of the sample. Originating from XAS, the plot of the absorption against the photon energy (eV) exhibits a specific structure (Figure 2.9.C), which is named Extended X-ray absorption fine structure (EXAFS). Different "structure" regions are shown, such as the edge and near-edge (XANES), referring to the manifold of empty bound states at the pre-edge, which position and features refer to possible transition into LUMO and bound states [22]. Towards higher photon energies there is the extended X-ray absorption fine structure (EXAFS) that refers to the continuum that can be populated with excitations at energies higher than that for the bound states. The modulations in EXAFS right after the XANES can contain information relative to the structural dynamics. In general, EXAFS was one of the first techniques in which sub-ps resolution was achieved [125]. Relative to the time-resolved framework, X-ray Transient Absorption (XTA) spectroscopy is advantageous and has been established as a common tool to monitor molecular structures in chemical reactions and the structural parameters that influence the reaction pathways [126]. As a pump-probe technique

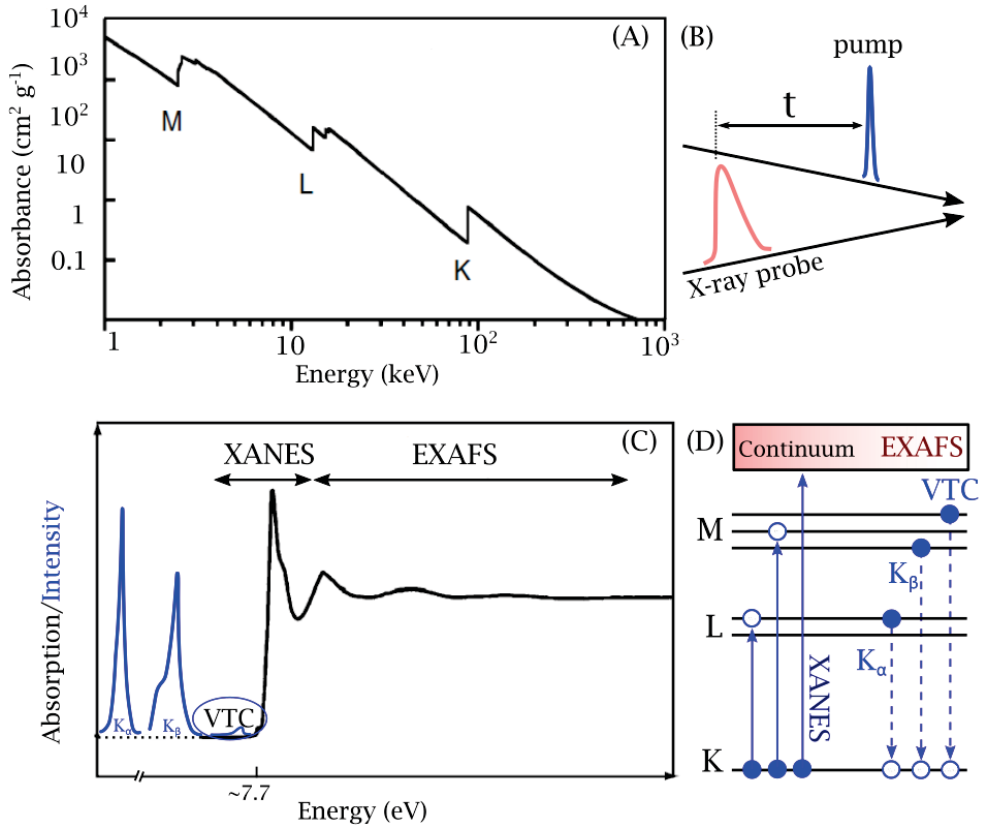

Figure 2.9: (A) The Absorbance to the incident photon energy low-resolution spectrum for Pb with the three indicating major transitions K, L and M. (B) Schematic principle of the X-ray pump-probe spectroscopy. (C) Representation of the X-ray absorption spectrum distinguish the pre-edge, edge, near- edge (XANES) and above edge (EXAFS) "structural" regions and (D) the atomic electronic levels from the core K to the higher L and M, up to the continuum. *Figures (A) and (C) were modified based on figures in reference [76].

XTA is based on the idea of optically exciting the sample and initiating the chemical reactions and the probe beam coming at a delay time (t) with respect to the pump, (Figure 2.9.B) is replaced with X-ray pulses at specific energies. Thus, a unique advantage of XTA is the ability of simultaneously resolving both transient electronic and local (around the probed atom) nuclear structures in photoexcited systems utilizing one single set-up [126]. XTA can be used for any kind of samples including energy harvesting applications, such as the DSSCs [127–130]. A well illustrated study has been made for DSSCs containing metal complexes such as RuN3 [127]. Upon photo-injection the Ru-N(dcbpy) bond length remains nearly unchanged, while the Ru-NCS bond length reduces, indicating the different structural response upon charge separation. This work demonstrated the great potential

of XTA in studying fundamental structural-functional correlations in an operative interfacial and heterogeneous DSSC system.

- **Infrared time-resolved spectroscopy**

  An important technique among many types of time-resolved spectroscopies uses the Infrared wavelength region [131]. Two ultrafast techniques in this region can be utilized for DSSC applications. First, the fs Time-Resolved Infrared Vibrational Spectroscopy (TR-IR) and the fs-Stimulated Raman Spectroscopy (FSRS). The substance of TR-IR is the investigation of the interplay between the vibrational (or structural) processes with the photoinduced electron injection and the intra-charge separation of the system (the dye-sensitizer for DSSCs). Many groups, such as Vauthey and co-workers investigated intramolecular effects relative to the charge separation upon photoexcitation by monitoring the time evolution in the ps timescale of the π-bridges of a series of symmetric organic molecules with Donor and Acceptor groups [132–134]. They experimentally utilized in this manner the TR-IR technique and identified that the symmetry breaking of these dyes occurs in times similar to fast solvation and it is highly driven by the solvent polarity. This insight in the fundamental photophysics of the sensitizer could be applied in real DSSCs and monitor the effect of carrier injection in the dye structure, as well as identify possible competitive channels to the injection. Current examples for DSSC applications involve the study of metal oxides and interfaces [135, 136]. FSRS and fs inverse Raman spectroscopy (FIRS) have also been applied to metal complexes [137] with potency for DSSC applications. These techniques have led to more advanced configurations such as the fs-stimulated Raman microscopy and naturally multi-dimensional spectroscopy [137]. Finally, visible-pump mid-IR probe techniques have been frequently used to monitor electrons in metal oxide conduction bands and thus the electron injection dynamics [138].

There are many ultrafast time-resolved experimental techniques that can be utilized to investigate various physical and chemical photo-induced processes taking place in DSSCs. In this section the most important and widely used were quoted, starting from the optical/visible spectroscopy, which is our field of interest and continue with Photoconductivity THz spectroscopy, X-ray and Infrared. More advanced techniques, such as two or multi-dimensional spectroscopy constitutes the physical extensions of the above

mentioned techniques offering advanced capabilities, such as the coupling of the electronic dynamics with vibronic coupling and make feasible to explore fundamental phenomena in detail.

References

[1] B. O'Regan and M. Grätzel, "A low-cost, high-efficiency solar cell based on dye-sensitized colloidal tio2 films," in *Renewable Energy*, Routledge, 2018, pp. 208–213.

[2] M. K. Nazeeruddin *et al.*, "Conversion of light to electricity by cis-x2bis (2, 2'-bipyridyl-4, 4'-dicarboxylate) ruthenium (ii) charge-transfer sensitizers (x= cl-, br-, i-, cn-, and scn-) on nanocrystalline titanium dioxide electrodes," *Journal of the American Chemical Society*, vol. 115, no. 14, pp. 6382–6390, 1993.

[3] M. K. Nazeeruddin *et al.*, "Combined experimental and dft-tddft computational study of photoelectrochemical cell ruthenium sensitizers," *Journal of the American Chemical Society*, vol. 127, no. 48, pp. 16 835–16 847, 2005.

[4] S. Mathew *et al.*, "Dye-sensitized solar cells with 13% efficiency achieved through the molecular engineering of porphyrin sensitizers," *Nature chemistry*, vol. 6, no. 3, pp. 242–247, 2014.

[5] K. Kakiage, Y. Aoyama, T. Yano, K. Oya, J.-i. Fujisawa, and M. Hanaya, "Highly-efficient dye-sensitized solar cells with collaborative sensitization by silyl-anchor and carboxy-anchor dyes," *Chemical communications*, vol. 51, no. 88, pp. 15 894–15 897, 2015.

[6] D. Zhang *et al.*, "A molecular photosensitizer achieves a v oc of 1.24 v enabling highly efficient and stable dye-sensitized solar cells with copper (ii/i)-based electrolyte," *Nature communications*, vol. 12, no. 1, pp. 1–10, 2021.

[7] T. Higashino and H. Imahori, "Porphyrins as excellent dyes for dye-sensitized solar cells: Recent developments and insights," *Dalton Transactions*, vol. 44, no. 2, pp. 448–463, 2015.

[8] S. Shalini, R. Balasundaraprabhu, T. S. Kumar, N. Prabavathy, S. Senthilarasu, and S. Prasanna, "Status and outlook of sensitizers/dyes used in dye sensitized solar cells (dssc): A review," *International journal of energy research*, vol. 40, no. 10, pp. 1303–1320, 2016.

[9] K. R. Millington, K. W. Fincher, and A. L. King, "Mordant dyes as sensitisers in dye-sensitised solar cells," *Solar energy materials and solar cells*, vol. 91, no. 17, pp. 1618–1630, 2007.

[10] A. S. Karmakar and J. P. Ruparelia, "A critical review on dye sensitized solar cells," in *Internation Conference on Current Trends in Technology*, 2011.

[11] I. A. Howard *et al.*, "Two channels of charge generation in perylene monoimide solid-state dye-sensitized solar cells," *Advanced Energy Materials*, vol. 4, no. 2, p. 1 300 640, 2014.

[12] U. B. Cappel *et al.*, "Characterization of the interface properties and processes in solid state dye-sensitized solar cells employing a perylene sensitizer," *The Journal of Physical Chemistry C*, vol. 115, no. 10, pp. 4345–4358, 2011.

[13] C.-Y. Hsu, Y.-C. Chen, R. Y.-Y. Lin, K.-C. Ho, and J. T. Lin, "Solid-state dye-sensitized solar cells based on spirofluorene (spiro-ometad) and arylamines as hole transporting materials," *Physical Chemistry Chemical Physics*, vol. 14, no. 41, pp. 14 099–14 109, 2012.

[14] G. S. Selopal, N. Memarian, R. Milan, I. Concina, G. Sberveglieri, and A. Vomiero, "Effect of blocking layer to boost photoconversion efficiency in zno dye-sensitized solar cells," *ACS applied materials & interfaces*, vol. 6, no. 14, pp. 11 236–11 244, 2014.

[15] K. Srivishnu, S. Prasanthkumar, and L. Giribabu, "Cu (ii/i) redox couples: Potential alternatives to traditional electrolytes for dye-sensitized solar cells," *Materials Advances*, vol. 2, no. 4, pp. 1229–1247, 2021.

[16] J. Cong, X. Yang, Y. Hao, L. Kloo, and L. Sun, "A highly efficient colourless sulfur/iodide-based hybrid electrolyte for dye-sensitized solar cells," *RSC advances*, vol. 2, no. 9, pp. 3625–3629, 2012.

[17] B. Valeur, "Molecular fluorescence principles and applications," *Book*, 2001.

[18] J. R. Lakowicz, "Principles of fluorescence spectroscopy," *Book, Third Edition*, 2006.

[19] R. Katoh and A. Furube, "Electron injection efficiency in dye-sensitized solar cells," *Journal of Photochemistry and Photobiology C: Photochemistry Reviews*, vol. 20, pp. 1–16, 2014.

[20] P. Persson, R. Bergström, L. Ojamäe, and S. Lunell, "Quantum-chemical studies of metal oxides for photoelectrochemical applications," 2002.

[21] J. Zhao *et al.*, "Electronic potential of a chemisorption interface," *Physical Review B*, vol. 78, no. 8, p. 085 419, 2008.

[22] J.-E. Moser, "Dynamics of interfacial and surface electron transfer processes," *Dye-sensitized solar cells*, pp. 403–456, 2010.

[23] C. S. Ponseca Jr, P. Chabera, J. Uhlig, P. Persson, and V. Sundstrom, "Ultrafast electron dynamics in solar energy conversion," *Chemical reviews*, vol. 117, no. 16, pp. 10 940–11 024, 2017.

[24] A. Hagfeldt, G. Boschloo, L. Sun, L. Kloo, and H. Pettersson, "Dye-sensitized solar cells," *Chemical reviews*, vol. 110, no. 11, pp. 6595–6663, 2010.

[25] M. J. Griffith *et al.*, "Porphyrins for dye-sensitised solar cells: New insights into efficiency-determining electron transfer steps," *Chemical Communications*, vol. 48, no. 35, pp. 4145–4162, 2012.

[26] A. Listorti, B. O'regan, and J. R. Durrant, "Electron transfer dynamics in dye-sensitized solar cells," *Chemistry of Materials*, vol. 23, no. 15, pp. 3381–3399, 2011.

[27] J. Van de Lagemaat and A. Frank, "Nonthermalized electron transport in dye-sensitized nanocrystalline tio2 films: Transient photocurrent and random-walk modeling studies," *The Journal of Physical Chemistry B*, vol. 105, no. 45, pp. 11 194–11 205, 2001.

[28] B. O'regan, J. Moser, M. Anderson, and M. Graetzel, "Vectorial electron injection into transparent semiconductor membranes and electric field effects on the dynamics of light-induced charge separation," *Journal of Physical Chemistry*, vol. 94, no. 24, pp. 8720–8726, 1990.

[29] S. Soedergren, A. Hagfeldt, J. Olsson, and S.-E. Lindquist, "Theoretical models for the action spectrum and the current-voltage characteristics of microporous semiconductor films in photoelectrochemical cells," *The Journal of Physical Chemistry*, vol. 98, no. 21, pp. 5552–5556, 1994.

[30] A. Solbrand, H. Lindström, H. Rensmo, A. Hagfeldt, S.-E. Lindquist, and S. Södergren, "Electron transport in the nanostructured tio2- electrolyte system studied with time-resolved photocurrents," *The Journal of Physical Chemistry B*, vol. 101, no. 14, pp. 2514–2518, 1997.

[31] K. Zhu, S.-R. Jang, and A. J. Frank, "Impact of high charge-collection efficiencies and dark energy-loss processes on transport, recombination, and photovoltaic properties of dye-sensitized solar cells," *The Journal of Physical Chemistry Letters*, vol. 2, no. 9, pp. 1070–1076, 2011.

[32] G. Schlichthörl, S. Huang, J. Sprague, and A. J. Frank, "Band edge movement and recombination kinetics in dye-sensitized nanocrystalline tio2 solar cells: A study by intensity modulated photovoltage spectroscopy," *The Journal of Physical Chemistry B*, vol. 101, no. 41, pp. 8141–8155, 1997.

[33] R. Chandler, A. Houtepen, J. Nelson, and D. Vanmaekelbergh, "Electron transport in quantum dot solids: Monte carlo simulations of the effects of shell filling, coulomb repulsions, and site disorder," *Physical Review B*, vol. 75, no. 8, p. 085 325, 2007.

[34] A. Barzykin and M. Tachiya, "Mechanism of charge recombination in dye-sensitized nanocrystalline semiconductors: Random flight model," *The Journal of Physical Chemistry B*, vol. 106, no. 17, pp. 4356–4363, 2002.

[35] R. A. Marcus and N. Sutin, "Electron transfers in chemistry and biology," *Biochimica et Biophysica Acta (BBA)-Reviews on Bioenergetics*, vol. 811, no. 3, pp. 265–322, 1985.

[36] R. A. Marcus, "On the theory of oxidation-reduction reactions involving electron transfer. i," *The Journal of chemical physics*, vol. 24, no. 5, pp. 966–978, 1956.

[37] ——, "Chemical and electrochemical electron-transfer theory," *Annual review of physical chemistry*, vol. 15, no. 1, pp. 155–196, 1964.

[38] H. Lu, J. N. Prieskorn, and J. T. Hupp, "Fast interfacial electron transfer: Evidence for inverted region kinetic behavior," *Journal of the American Chemical Society*, vol. 115, no. 11, pp. 4927–4928, 1993.

[39] J. N. Clifford *et al.*, "Molecular control of recombination dynamics in dye-sensitized nanocrystalline tio2 films: Free energy vs distance dependence," *Journal of the American Chemical Society*, vol. 126, no. 16, pp. 5225–5233, 2004.

[40] H. GERISCHER, "Charge transfer processes at semiconductor-electrolyte interfaces in connection with problems of catalysis," *SURFACE SCIENCE*, vol. 18, pp. 97–122, 1967.

[41] ——, "Electrochemical techniques for the study of photosensitization," *Photochemistry and Photobiology*, vol. 16, pp. 243–260, 1972.

[42] J. Wu *et al.*, "Electrolytes in dye-sensitized solar cells," *Chemical reviews*, vol. 115, no. 5, pp. 2136–2173, 2015.

[43] G. Boschloo and A. Hagfeldt, "Characteristics of the iodide/triiodide redox mediator in dye-sensitized solar cells," *Accounts of chemical research*, vol. 42, no. 11, pp. 1819–1826, 2009.

[44] F. Schiffmann, J. VandeVondele, J. Hutter, A. Urakawa, R. Wirz, and A. Baiker, "An atomistic picture of the regeneration process in dye sensitized solar cells," *Proceedings of the National Academy of Sciences*, vol. 107, no. 11, pp. 4830–4833, 2010.

[45] T. Privalov, G. Boschloo, A. Hagfeldt, P. H. Svensson, and L. Kloo, "A study of the interactions between i-/i3- redox mediators and organometallic sensitizing dyes in solar cells," *The Journal of Physical Chemistry C*, vol. 113, no. 2, pp. 783–790, 2009.

[46] J. G. Rowley, B. H. Farnum, S. Ardo, and G. J. Meyer, "Iodide chemistry in dye-sensitized solar cells: Making and breaking i- i bonds for solar energy conversion," *The Journal of Physical Chemistry Letters*, vol. 1, no. 20, pp. 3132–3140, 2010.

[47] R. R. Lunt, "Theoretical limits for visibly transparent photovoltaics," *Applied Physics Letters*, vol. 101, no. 4, p. 043 902, 2012.

[48] W. Shockley and H. J. Queisser, "Detailed balance limit of efficiency of p-n junction solar cells," *Journal of applied physics*, vol. 32, no. 3, pp. 510–519, 1961.

[49] C. J. Traverse, R. Pandey, M. C. Barr, and R. R. Lunt, "Emergence of highly transparent photovoltaics for distributed applications," *Nature Energy*, vol. 2, no. 11, pp. 849–860, 2017.

[50] F. Grifoni *et al.*, "Toward sustainable, colorless, and transparent photovoltaics: State of the art and perspectives for the development of selective near-infrared dye-sensitized solar cells," *Advanced Energy Materials*, p. 2 101 598, 2021.

[51] M. R. P. R. W. Hunt, "Measuring colour," *Advanced Energy Materials, Fourth Edition*, 2011.

[52] J. Mescher *et al.*, "Design rules for semi-transparent organic tandem solar cells for window integration," *Organic Electronics*, vol. 15, no. 7, pp. 1476–1480, 2014.

[53] A. Roy, A. Ghosh, S. Bhandari, P. Selvaraj, S. Sundaram, and T. K. Mallick, "Color comfort evaluation of dye-sensitized solar cell (dssc) based building-integrated photovoltaic (bipv) glazing after 2 years of ambient exposure," *The Journal of Physical Chemistry C*, vol. 123, no. 39, pp. 23 834–23 837, 2019.

[54] I. C. on Illumination, "Cie 15: Technical report: Colorimetry, 3rd edition," pp. 1476–1480, 2004.

[55] ——, "Proc. of the 8th session of cie, cambridge, 19-29," pp. 1476–1480, 1931.

[56] K. McLaren, "Xiii—the development of the cie 1976 (l* a* b*) uniform colour space and colour-difference formula," *Journal of the Society of Dyers and Colourists*, vol. 92, no. 9, pp. 338–341, 1976.

[57] A. R. Noboru Ohta, "Colorimetry: Fundamentals and applications," *Book*, 2005.

[58] J. Yoon *et al.*, "Ultrathin silicon solar microcells for semitransparent, mechanically flexible and microconcentrator module designs," in *Materials for Sustainable Energy: A Collection of Peer-Reviewed Research and Review Articles from Nature Publishing Group*, World Scientific, 2011, pp. 38–46.

[59] W. Shockley and H. J. Queisser, "Detailed balance limit of efficiency of p-n junction solar cells," *Journal of applied physics*, vol. 32, no. 3, pp. 510–519, 1961.

[60] G. E. Eperon *et al.*, "Efficient, semitransparent neutral-colored solar cells based on microstructured formamidinium lead trihalide perovskite," *The journal of physical chemistry letters*, vol. 6, no. 1, pp. 129–138, 2015.

[61] G. E. Eperon, V. M. Burlakov, A. Goriely, and H. J. Snaith, "Neutral color semitransparent microstructured perovskite solar cells," *ACS nano*, vol. 8, no. 1, pp. 591–598, 2014.

[62] C. Xia, F. Chen, and M. Liu, "Reduced-temperature solid oxide fuel cells fabricated by screen printing," *Electrochemical and Solid State Letters*, vol. 4, no. 5, A52, 2001.

[63] H. D. Goldberg, R. B. Brown, D. P. Liu, and M. E. Meyerhoff, "Screen printing: A technology for the batch fabrication of integrated chemical-sensor arrays," *Sensors and Actuators B: Chemical*, vol. 21, no. 3, pp. 171–183, 1994.

[64] J. Zhang, S. Li, P. Yang, W. Que, and W. Liu, "Deposition of transparent tio2 nanotubes-films via electrophoretic technique for photovoltaic applications," *Science China Materials*, vol. 58, no. 10, pp. 785–790, 2015.

[65] C. A. Grimes and G. K. Mor, *TiO2 nanotube arrays: synthesis, properties, and applications*. Springer Science & Business Media, 2009.

[66] A. Bahramian and D. Vashaee, "In-situ fabricated transparent conducting nanofiber-shape polyaniline/coral-like tio2 thin film: Application in bifacial dye-sensitized solar cells," *Solar Energy Materials and Solar Cells*, vol. 143, pp. 284–295, 2015.

[67] Y. Zhang and N.-G. Park, "A thin film ($<$ 200 nm) perovskite solar cell with 18% efficiency," *Journal of Materials Chemistry A*, vol. 8, no. 34, pp. 17 420–17 428, 2020.

[68] X. Zhang, C. Hägglund, M. B. Johansson, K. Sveinbjörnsson, and E. M. Johansson, "Fine tuned nanolayered metal/metal oxide electrode for semitransparent colloidal quantum dot solar cells," *Advanced Functional Materials*, vol. 26, no. 12, pp. 1921–1929, 2016.

[69] J.-Y. Lee, S. T. Connor, Y. Cui, and P. Peumans, "Semitransparent organic photovoltaic cells with laminated top electrode," *Nano letters*, vol. 10, no. 4, pp. 1276–1279, 2010.

[70] R. Betancur, P. Romero-Gomez, A. Martinez-Otero, X. Elias, M. Maymó, and J. Martorell, "Transparent polymer solar cells employing a layered light-trapping architecture," *Nature Photonics*, vol. 7, no. 12, pp. 995–1000, 2013.

[71] K. Zhang *et al.*, "High-performance, transparent, dye-sensitized solar cells for see-through photovoltaic windows," *Advanced Energy Materials*, vol. 4, no. 11, p. 1 301 966, 2014.

[72] J. Batchelder, A. Zewai, and T. Cole, "Luminescent solar concentrators. 1: Theory of operation and techniques for performance evaluation," *Applied Optics*, vol. 18, no. 18, pp. 3090–3110, 1979.

[73] L. H. Slooff *et al.*, "A luminescent solar concentrator with 7.1% power conversion efficiency," *physica status solidi (RRL)–Rapid Research Letters*, vol. 2, no. 6, pp. 257–259, 2008.

[74] R.-T. Chen, J. L. H. Chau, and G.-L. Hwang, "Design and fabrication of diffusive solar cell window," *Renewable energy*, vol. 40, no. 1, pp. 24–28, 2012.

[75] F. Meinardi *et al.*, "Highly efficient large-area colourless luminescent solar concentrators using heavy-metal-free colloidal quantum dots," *Nature nanotechnology*, vol. 10, no. 10, pp. 878–885, 2015.

[76] F. Mateen, S. Y. Lee, and S.-K. Hong, "Luminescent solar concentrators based on thermally activated delayed fluorescence dyes," *Journal of Materials Chemistry A*, vol. 8, no. 7, pp. 3708–3716, 2020.

[77] C. J. Traverse, R. Pandey, M. C. Barr, and R. R. Lunt, "Emergence of highly transparent photovoltaics for distributed applications," *Nature Energy*, vol. 2, no. 11, pp. 849–860, 2017.

[78] Y. Zhao and R. R. Lunt, "Transparent luminescent solar concentrators for large-area solar windows enabled by massive stokes-shift nanocluster phosphors," *Advanced Energy Materials*, vol. 3, no. 9, pp. 1143–1148, 2013.

[79] Y. Zhao, G. A. Meek, B. G. Levine, and R. R. Lunt, "Near-infrared harvesting transparent luminescent solar concentrators," *Advanced Optical Materials*, vol. 2, no. 7, pp. 606–611, 2014.

[80] R. R. Lunt and V. Bulovic, "Transparent, near-infrared organic photovoltaic solar cells for window and energy-scavenging applications," *Applied Physics Letters*, vol. 98, no. 11, p. 61, 2011.

[81] C.-C. Chen *et al.*, "Visibly transparent polymer solar cells produced by solution processing," *ACS nano*, vol. 6, no. 8, pp. 7185–7190, 2012.

[82] F. Liu *et al.*, "Efficient semitransparent solar cells with high nir responsiveness enabled by a small-bandgap electron acceptor," *Advanced Materials*, vol. 29, no. 21, p. 1 606 574, 2017.

[83] W. Wang *et al.*, "Fused hexacyclic nonfullerene acceptor with strong near-infrared absorption for semitransparent organic solar cells with 9.77% efficiency," *Advanced materials*, vol. 29, no. 31, p. 1 701 308, 2017.

[84] K. Zhang *et al.*, "High-performance, transparent, dye-sensitized solar cells for see-through photovoltaic windows," *Advanced Energy Materials*, vol. 4, no. 11, p. 1 301 966, 2014.

[85] Q. Huaulmé *et al.*, "Photochromic dye-sensitized solar cells with light-driven adjustable optical transmission and power conversion efficiency," *Nature Energy*, vol. 5, no. 6, pp. 468–477, 2020.

[86] W. Naim *et al.*, "Transparent and colorless dye-sensitized solar cells exceeding 75% average visible transmittance," *Jacs Au*, vol. 1, no. 4, pp. 409–426, 2021.

[87] M.-Q. Yang, M. Gao, M. Hong, and G. W. Ho, "Visible-to-nir photon harvesting: Progressive engineering of catalysts for solar-powered environmental purification and fuel production," *Advanced Materials*, vol. 30, no. 47, p. 1 802 894, 2018.

[88] J. Park, G. Viscardi, C. Barolo, and N. Barbero, "Near-infrared sensitization in dye-sensitized solar cells," *CHIMIA International Journal for Chemistry*, vol. 67, no. 3, pp. 129–135, 2013.

[89] A. De Vos, *Thermodynamics of solar energy conversion*. John Wiley & Sons, 2008.

[90] S. Paek *et al.*, "Efficient and stable panchromatic squaraine dyes for dye-sensitized solar cells," *Chemical Communications*, vol. 47, no. 10, pp. 2874–2876, 2011.

[91] C. Martın, M. Ziółek, and A. Douhal, "Ultrafast and fast charge separation processes in real dye-sensitized solar cells," *Journal of Photochemistry and Photobiology C: Photochemistry Reviews*, vol. 26, pp. 1–30, 2016.

[92] K. Pydzińska and M. Ziółek, "Solar cells sensitized with near-infrared absorbing dye: Problems with sunlight conversion efficiency revealed in ultrafast laser spectroscopy studies," *Dyes and Pigments*, vol. 122, pp. 272–279, 2015.

[93] M. Ziółek, J. Karolczak, M. Zalas, Y. Hao, H. Tian, and A. Douhal, "Aggregation and electrolyte composition effects on the efficiency of dye-sensitized solar cells. a case of a near-infrared absorbing dye for tandem cells," *The Journal of Physical Chemistry C*, vol. 118, no. 1, pp. 194–205, 2014.

[94] W. Ghann *et al.*, "Photophysical properties of near-ir cyanine dyes and their application as photosensitizers in dye sensitized solar cells," *Inorganica Chimica Acta*, vol. 467, pp. 123–131, 2017.

[95] K. Takechi, P. V. Kamat, R. R. Avirah, K. Jyothish, and D. Ramaiah, "Harvesting infrared photons with croconate dyes," *Chemistry of Materials*, vol. 20, no. 1, pp. 265–272, 2008.

[96] G. M. Fischer, A. P. Ehlers, A. Zumbusch, and E. Daltrozzo, "Near-infrared dyes and fluorophores based on diketopyrrolopyrroles," *Angewandte Chemie International Edition*, vol. 46, no. 20, pp. 3750–3753, 2007.

[97] T. Higashino, Y. Kurumisawa, S. Nimura, H. Iiyama, and H. Imahori, "Enhanced donor–π–acceptor character of a porphyrin dye incorporating naphthobisthiadiazole for efficient near-infrared light absorption," *European Journal of Organic Chemistry*, vol. 2018, no. 20-21, pp. 2537–2547, 2018.

[98] W. M. Campbell *et al.*, "Highly efficient porphyrin sensitizers for dye-sensitized solar cells," *The Journal of Physical Chemistry C*, vol. 111, no. 32, pp. 11 760–11 762, 2007.

[99] Ö. Birel, S. Nadeem, and H. Duman, "Porphyrin-based dye-sensitized solar cells (dsscs): A review," 2017.

[100] M. Urbani, M. Grätzel, M. K. Nazeeruddin, and T. Torres, "Meso-substituted porphyrins for dye-sensitized solar cells," *Chemical reviews*, vol. 114, no. 24, pp. 12 330–12 396, 2014.

[101] A. B. P. Lever and C. C. Leznoff, *Phthalocyanines: properties and applications*. New York: VCH, 1989-c1996., 1996.

[102] M. K. Nazeeruddin *et al.*, "Efficient near-ir sensitization of nanocrystalline tio 2 films by zinc and aluminum phthalocyanines," *Journal of Porphyrins and Phthalocyanines*, vol. 3, no. 03, pp. 230–237, 1999.

[103] T. Ikeuchi, H. Nomoto, N. Masaki, M. J. Griffith, S. Mori, and M. Kimura, "Molecular engineering of zinc phthalocyanine sensitizers for efficient dye-sensitized solar cells," *Chemical communications*, vol. 50, no. 16, pp. 1941–1943, 2014.

[104] J. Van Houten, "A century of chemical dynamics traced through the nobel prizes. 1998: Walter kohn and john pople," *Journal of Chemical Education*, vol. 79, no. 11, p. 1297, 2002.

[105] D. L. Andrews and A. A. Demidov, *An introduction to laser spectroscopy*. Springer Science & Business Media, 2012.

[106] G. Lanzani, *The photophysics behind photovoltaics and photonics*. John Wiley & Sons, 2012.

[107] S. Woutersen and P. Hamm, "Time-resolved two-dimensional vibrational spectroscopy of a short α-helix in water," *The Journal of Chemical Physics*, vol. 115, no. 16, pp. 7737–7743, 2001.

[108] R. A. Palmer, C. J. Manning, J. L. Chao, I. Noda, A. E. Dowrey, and C. Marcott, "Application of step-scan interferometry to two-dimensional fourier transform infrared (2d ft-ir) correlation spectroscopy," *Applied spectroscopy*, vol. 45, no. 1, pp. 12–17, 1991.

[109] P. Mal, J. Lüttig, S. Mueller, M. H. Schreck, C. Lambert, and T. Brixner, "Coherently and fluorescence-detected two-dimensional electronic spectroscopy: Direct comparison on squaraine dimers," *Physical Chemistry Chemical Physics*, vol. 22, no. 37, pp. 21 222–21 237, 2020.

[110] M. Maiuri, M. Garavelli, and G. Cerullo, "Ultrafast spectroscopy: State of the art and open challenges," *Journal of the American Chemical Society*, vol. 142, no. 1, pp. 3–15, 2019.

[111] J. Réhault, M. Maiuri, C. Manzoni, D. Brida, J. Helbing, and G. Cerullo, "2d ir spectroscopy with phase-locked pulse pairs from a birefringent delay line," *Optics express*, vol. 22, no. 8, pp. 9063–9072, 2014.

[112] J. Sobuś, J. Karolczak, D. Komar, J. A. Anta, and M. Ziółek, "Transient states and the role of excited state self-quenching of indoline dyes in complete dye-sensitized solar cells," *Dyes and Pigments*, vol. 113, pp. 692–701, 2015.

[113] H.-W. Bahng, A. Hagfeldt, and J.-E. Moser, "Lateral intermolecular electronic interactions of diketopyrrolopyrrole d- π–a solar dye sensitizers adsorbed on mesoporous alumina," *The Journal of Physical Chemistry C*, vol. 122, no. 34, pp. 19 348–19 358, 2018.

[114] ——, "Donor effect on the photoinduced interfacial charge transfer dynamics of d- π–a diketopyrrolopyrrole dye sensitizers adsorbed on titanium dioxide," *The Journal of Physical Chemistry C*, vol. 122, no. 34, pp. 19 359–19 369, 2018.

[115] C. A. Schmuttenmaer, "Exploring dynamics in the far-infrared with terahertz spectroscopy," *Chemical reviews*, vol. 104, no. 4, pp. 1759–1780, 2004.

[116] J. C. Brauer, A. Marchioro, A. A. Paraecattil, A. A. Oskouei, and J.-E. Moser, "Dynamics of interfacial charge transfer states and carriers separation in dye-sensitized solar cells: A time-resolved terahertz spectroscopy study," *The Journal of Physical Chemistry C*, vol. 119, no. 47, pp. 26 266–26 274, 2015.

[117] H. Němec *et al.*, "Influence of the electron-cation interaction on electron mobility in dye-sensitized zno and tio 2 nanocrystals: A study using ultrafast terahertz spectroscopy," *Physical review letters*, vol. 104, no. 19, p. 197 401, 2010.

[118] H. Němec, P. Kužel, and V. Sundström, "Charge transport in nanostructured materials for solar energy conversion studied by time-resolved terahertz spectroscopy," *Journal of Photochemistry and Photobiology A: Chemistry*, vol. 215, no. 2-3, pp. 123–139, 2010.

[119] K. Haldrup *et al.*, "Observing solvation dynamics with simultaneous femtosecond x-ray emission spectroscopy and x-ray scattering," *The journal of physical chemistry B*, vol. 120, no. 6, pp. 1158–1168, 2016.

[120] O. Gessner and M. Gühr, "Monitoring ultrafast chemical dynamics by time-domain x-ray photo-and auger-electron spectroscopy," *Accounts of chemical research*, vol. 49, no. 1, pp. 138–145, 2016.

[121] U. Bergmann and P. Glatzel, "X-ray emission spectroscopy," *Photosynthesis research*, vol. 102, no. 2, pp. 255–266, 2009.

[122] H. W. Kim *et al.*, "Soft x-ray absorption and photoemission spectroscopy study of semiconductor oxide nanoparticles for dye-sensitized solar cell: Znsno3 and zn2sno4," *Solid State Communications*, vol. 236, pp. 32–36, 2016.

[123] J. Penner-Hahn, *In comprehensive coordination chemistry ii, ; mccleverty ja, meyer tj, eds*, 2003.

[124] C. Bressler and M. Chergui, "Ultrafast x-ray absorption spectroscopy," *Chemical reviews*, vol. 104, no. 4, pp. 1781–1812, 2004.

[125] M. H. Rittmann-Frank, C. J. Milne, J. Rittmann, M. Reinhard, T. J. Penfold, and M. Chergui, "Mapping of the photoinduced electron traps in tio2 by picosecond x-ray absorption spectroscopy," *Angewandte Chemie*, vol. 126, no. 23, pp. 5968–5972, 2014.

[126] L. X. Chen and X. Zhang, "Photochemical processes revealed by x-ray transient absorption spectroscopy," *The Journal of Physical Chemistry Letters*, vol. 4, no. 22, pp. 4000–4013, 2013.

[127] X. Zhang *et al.*, "Visualizing interfacial charge transfer in ru-dye-sensitized tio2 nanoparticles using x-ray transient absorption spectroscopy," *The Journal of Physical Chemistry Letters*, vol. 2, no. 6, pp. 628–632, 2011.

[128] Y. Obara *et al.*, "Femtosecond time-resolved x-ray absorption spectroscopy of anatase tio2 nanoparticles using xfel," *Structural Dynamics*, vol. 4, no. 4, p. 044 033, 2017.

[129] B. E. Van Kuiken *et al.*, "Probing the electronic structure of a photoexcited solar cell dye with transient x-ray absorption spectroscopy," *The journal of physical chemistry letters*, vol. 3, no. 12, pp. 1695–1700, 2012.

[130] M. Honda, M. Yanagida, L. Han, and K. Miyano, "X-ray characterization of dye adsorption in coadsorbed dye-sensitized solar cells," *The Journal of Physical Chemistry C*, vol. 117, no. 33, pp. 17 033–17 038, 2013.

[131] M. D. Fayer, *Ultrafast infrared vibrational spectroscopy*. CRC Press, 2013.

[132] B. Dereka, A. Rosspeintner, Z. Li, R. Liska, and E. Vauthey, "Direct visualization of excited-state symmetry breaking using ultrafast time-resolved infrared spectroscopy," *Journal of the American Chemical Society*, vol. 138, no. 13, pp. 4643–4649, 2016.

[133] A. I. Ivanov, B. Dereka, and E. Vauthey, "A simple model of solvent-induced symmetry-breaking charge transfer in excited quadrupolar molecules," *The Journal of chemical physics*, vol. 146, no. 16, p. 164 306, 2017.

[134] J. S. Beckwith *et al.*, "Specific monitoring of excited-state symmetry breaking by femtosecond broadband fluorescence upconversion spectroscopy," *The journal of physical chemistry letters*, vol. 8, no. 23, pp. 5878–5883, 2017.

[135] A. Furube, "Time resolved infrared spectroscopy of metal oxides and interfaces," in *Solar Energy Conversion*, Royal Society of Chemistry Cambridge, 2013, pp. 281–300.

[136] N. A. Anderson and T. Lian, "Ultrafast electron transfer at the molecule-semiconductor nanoparticle interface," *Annu. Rev. Phys. Chem.*, vol. 56, pp. 491–519, 2005.

[137] R. R. Frontiera and R. A. Mathies, "Femtosecond stimulated raman spectroscopy," *Laser & Photonics Reviews*, vol. 5, no. 1, pp. 102–113, 2011.

[138] A. Glinka, J. Kubicki, and M. Ziółek, "Complexity of electron injection dynamics and light soaking effects in efficient dyes for modern dssc," *Energies*, vol. 14, no. 2, p. 407, 2021.

Chapter 3

Photophysics

In this PhD Thesis, the study has been focused on the examination of the ultrafast mechanisms of the dyes incorporated in real DSSCs. All the measured photophysical properties of the dye-sensitizers in solution start with the photoexcitation/absorption and ends with the luminescence. In DSSCs upon attachment to the SC different species such as molecular aggregates, between the dye-monomers can be formed and intra/intermolecular processes of energy transfer and electron transfer can take place. The fundamental photophysics of both monomers and aggregates are well known since many decades, but a quick reminder of the most important mechanisms is important, as well as the up-to-date bibliography highlights on aggregates.

3.1 Basic Photophysical Processes

The Perrin-Jablonski diagram (Figure 3.1) demonstrates, in the simpler form, the molecular electronic states with their respective vibronic levels and the basic relaxation pathways upon absorption/excitation. It is a stochastic overall representation of the system containing important information relative to the unimolecular processes and is often used for oversimplified descriptions of a photophysical model. However it misses information such as the coordinate-dependent state crossing, thus it doesn't contain information about the nonadiabatic transitions at conical intersections, which can be important for systems that undergo, for example, isomerization. In additional, it ignores the rotational modes of the molecule and the interaction with the environment's bath, which participates in the energy reorganization upon the transitions. A typical and generally experimentally observed, relationship between the time scales of the basic photophysical mechanisms is $\sim 10-20\ fs$ for absorption, $10^{-12}-10^{-10}\,s$ for vibronic relaxation (VR), $10^{-11}-10^{-9}\,s$

for internal conversion (IC), $10^{-10} - 10^{-8}\,s$ for intersystem crossing (ISC), $10^{-10} - 10^{-7} s$ for fluorescence and finally $10^{-6}\,s - min$ for phosphorescence. For the systems of our study ISC and therefore phosphorescence don't occur.

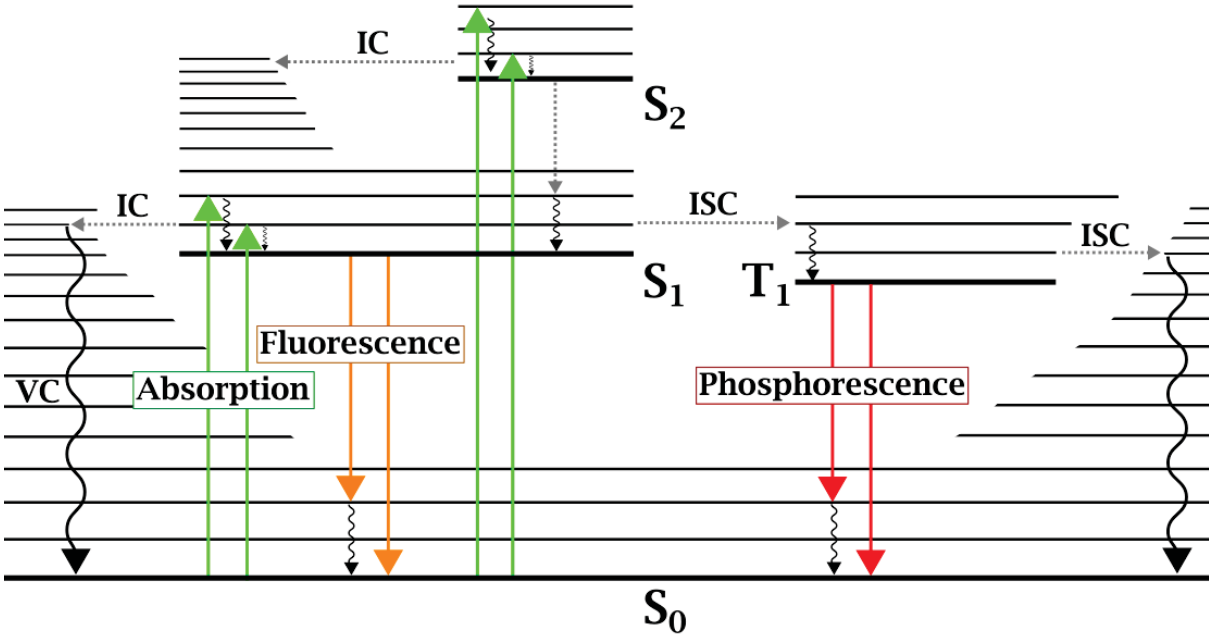

Figure 3.1: Perrin-Jablonski diagram for unimolecular processes in the optically excited dye-molecule. (i) Absorption, (ii) vibronic relaxation or cooling (VR or VC), internal conversion (IC), intersystem crossing (ISC), fluorescence and phosphorescence.

Absorption expresses the probability for an electronic transition to occur from the ground state to states of higher energy or equivalent from a lower occupied molecular orbital to higher unoccupied orbitals. Experimentally in the standard cases absorption can be calculated using Beer-Lambert law [1–4] as:

$$A(\lambda) = -logT(\lambda) = -log(\frac{I_\lambda^0}{I_\lambda}) = \varepsilon(\lambda)CD \tag{3.1}$$

where, T is the transmission and I_λ^0 and I_λ the light intensities when enter and exit the absorptive sample, respectively. In Beer-Lambert's part, $\varepsilon(\lambda)$ is the molar absorption coefficient ($Lmol^{-1}\ cm^{-1}$), C the concentration of molecules ($mol\ L^{-1}$) and D the sample's thickness (cm). The VR process is slower compare to absorption in agreement with the adiabatic or Born-Oppenheimer approximation assuming that electronic and nuclear motions can be separated. The relation of nuclear and electronic energy levels is, approximately, $E_e = 100E^N$, derived by the adiabatic approximation [3]. Upon excitation to a higher vibronic level of an excited state the system, via vibrational cooling

or thermalization, relaxes to the zero vibronic level of the electronic state. The excited system will eventually be driven to the lowest level of the first singlet excited state (S_1) and from there it will either relax to the ground state (S_0) (Kasha's rule) radiatively via fluorescence, or non-radiatively via IC [5]. Alternatively, S_1 can be driven through the non-radiative process of ISC [6] to the first triplet excited state (T_1) and then deactivate to the S_0 radiatively through phosphorescence [1, 2] or non-radiatively through IC. IC is a S-S transition and therefore dipole-allowed, when ISC is S-T transition that requires a change of spin, consisting a forbidden-transition, meaning a transition of low probability. Therefore phosphorescence is a rare mechanism, usually occurring in dyes containing heavy atoms (e.g. metal complexes) and in the scope of this Thesis only fluorescence is observed. In general terms, the total deactivation rate of the system is described as the sum of the radiative rates (k_R) and non-radiative rates (k_{NR}) and the photoluminescence's quantum yield (PL)

$$\eta_{PL} = \frac{k_R}{k_R + k_{NR}} \tag{3.2}$$

directly showing that the overall emitting character of the molecule depends on this exact competition between radiative and non-radiative processes.

Experimentally, the fluorescence intensity I_F at a specific wavelength λ_F is proportional to the emission spectrum $F_\lambda(\lambda_F)$ which wavelength integration in the range $[0, \infty]$ gives the fluorescence yield φ, the intensity of the incident light $I_0(\lambda_E)$ and the number of absorbed photons (or the absorption intensity $I_A(\lambda_E)$). Then, from substitution of $I_A(\lambda_E)$ from the Beer-Lambert law, the fluorescence intensity for a fixed excitation wavelength λ_E and relative low concentration C, can be written as

$$I_F(\lambda_E, \lambda_F) \propto 2.3kF_\lambda(\lambda_F)I_0(\lambda_E)\varepsilon(\lambda_E)CD \tag{3.3}$$

and indicates that the fluorescence intensity is proportional to the concentration, only for low absorption. In the above equation $\varepsilon(\lambda_E)$ is the molar extinction coefficient at λ_E and k a proportionality constant that depends on the instrument's detection solid angle and the bandwidth of the monochromator.

3.2 Theories of Energy and Electron Transfer

Excitation energy transfer and photoinduced electron transfer mechanisms are the central pillars for systems used in solar energy-harvesting applications. The subject of this Thesis highlights the DSSCs' technology, in which the charge separation in the dye/SC interface is critical for the total performance. Energy transfer (ET) by itself doesn't lead to charge separation, but in densed packed systems such as DSSCs, intra and intermolecular processes can occur and finally affect the photocycle of the device.

3.2.1 Excitation Energy Transfer

ET or energy migration can occur between molecules of the same or different species and it requires donor (D) and acceptor (A) species (Figure 3.2). It can be radiative or non-radiative. Radiative it is displayed in the sense of re-absorption that reduces the quantum yield of donor's emission. On account of this, it can be the main loss parameter for particular technologies, such as LSCs as it was described in chapter 2. The probability (α) of self-absorption depends greatly on the overlap of the donor's emission and acceptor's absorption spectra and expressed for relatively low concentrations as [1]:

$$\alpha = \frac{2.303CD}{\eta_F} \int_{v_{max}}^{v_{min}} F(\nu)\varepsilon(\nu)d\nu \tag{3.4}$$

where $F(\nu)$ the fluorescence spectrum over all frequencies and the integral represents the spectral overlap and (η_F) the fluorescence quantum yield of the donor in absence of the acceptor.

Non-radiative ET is expressed either by Coulombic interactions and is often called Förster Resonance Energy Transfer (FRET), or by exchange mechanisms and then is called Dexter Electron Exchange (DEE).

It is important to highlight that for both FRET and DEE the intermolecular coupling between the D and A is very weak. The vibrational relaxation is much faster than the energy transfer process and in this adiabatic case, similar to Kasha's rule the system relaxes to the lower vibrational level and the transfer occurs in later times. In this case the energy transfer rate, which is a parameter that contains a lot of information and is an important process for energy harvesting applications, depends on the spectral overlap J between the donor's fluorescence spectrum F(λ) and the acceptor's absorption extinction

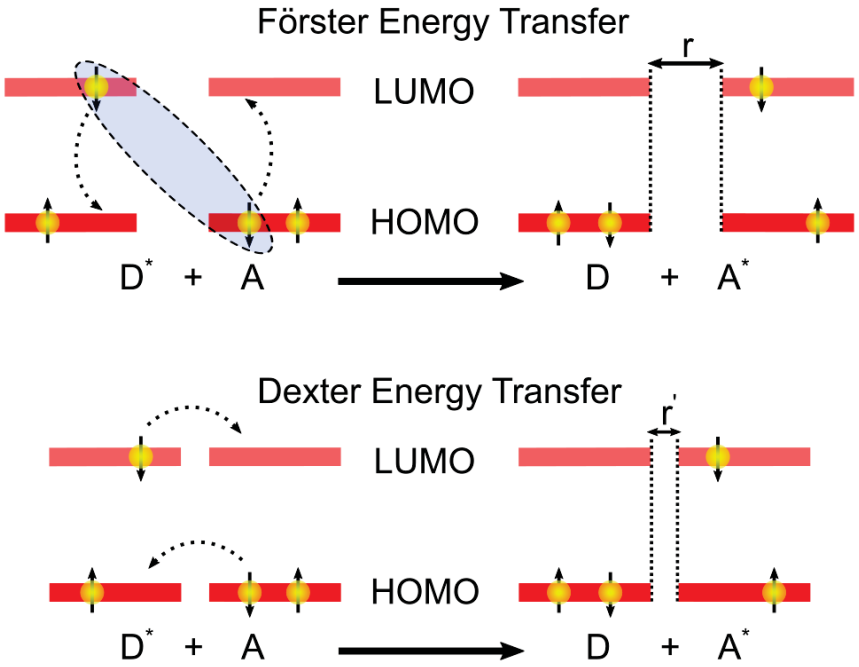

Figure 3.2: Schematic representation of the photophysical aspects of long range FRET (top) and short range DEE (bellow) processes with intermolecular distances r>10Å>r'.

coefficient ε(λ):

$$J = \int F(\lambda)\varepsilon(\lambda)\lambda^4 d\lambda \tag{3.5}$$

In the above mentioned conditions the rate of ET for the system D-A can be described by Fermi's Golden rule, which by its turn is proportional to the square of the interaction energy of the system ($k \propto U^2$). U by its turn contains both the Coulombic term (U_C) and the exchange term (U_E). As it was mentioned the difference between FRET and DEE lies in the distance between the D and A that defines the interaction energy of the system. Starting from the final wavefunctions of the two species system (Ψ_{D^*A}, Ψ_{DA^*}) and considering that only two electrons (1 and 2) are involved in a transition, the interaction energies (Coulombic and exchange) from the perturbation theory are defined as:

$$U_C = \langle \Phi_D^*(1)\Phi_A(2)|V|\Phi_D(1)\Phi_A^*(2)\rangle \tag{3.6}$$

and

$$U_E = \langle \Phi_D^*(1)\Phi_A(2)|V|\Phi_D(2)\Phi_A^*(1)\rangle \tag{3.7}$$

where the perturbation V is the Coulombic interaction that causes the transition and is expressed as a multipole expansion. For the case of FRET only the first dipole-dipole

term is weighted and the equation 3.6 can be re-written as:

$$U_C = \frac{(\overrightarrow{\mu_D} \cdot \overrightarrow{\mu_A}|r|^2) - 3(\overrightarrow{\mu_D} \cdot \overrightarrow{r})(\overrightarrow{\mu_A} \cdot \overrightarrow{r})}{|r|^5} \tag{3.8}$$

where μ_D, μ_A the excitation transition dipole moments of D and A respectively and r the intermolecular distance. Finally, the FRET rate is expressed as:

$$k_{ET} = \frac{1}{\tau_D}(\frac{R_0}{r})^6 \tag{3.9}$$

where τ_D the excited state lifetime of the D in absence of the A and $R_0 \propto J$ the Förster distance, which is defined as the distance in which the ET efficiency η_{ET} is 50 %. η_{ET} can straightforwardly, be defined as:

$$\eta_{ET} = \frac{k_{ET}}{k_{ET} + \frac{1}{\tau_D}} = \frac{1}{1 + (\frac{r}{R_0})^{1/6}} \tag{3.10}$$

The significant information derived from the equation 3.9 is the dependence of the k_{ET} with the 6^{th} power of the distance D-A. For solid-state, densed packed and inhomogeneous samples, such as the DSSCs, the dye-to-dye distances come as a distribution. Therefore, k_{ET} cannot be resolved by a single exponential kinetic rate equation and comes out as a distribution too. The degree of the inhomogeneity can be evaluated by fluorescence time-resolved studies including it in the fitting function as a power to the exponential population decay [7–12].

For DEE, the exchange term U_E of the total interaction energy represents the electrostatic interaction between the electron densities. It has quantum-mechanical origin and for electron transfer to occur the wavefunction overlap is essential. It dominates when the D and A transitions are spin forbidden and r $<$ 10 Å, which essentially is assumed a "contact" case. Consequently, we can write:

$$U_E = \langle \Phi_D^*(1)\Phi_A(2)|\frac{e^2}{r}|\Phi_D(2)\Phi_A^*(1)\rangle \tag{3.11}$$

and again based on Fermi's golden rule,

$$k_{ET} = \frac{2\pi}{h} K \exp\frac{-2r}{L} J \tag{3.12}$$

where K a constant not related to optical properties, h the Planck's constant and L the Bohr radius. Noteworthy, Dexter's exchange k_{ET} doesn't depend like in FRET case, at

the 6^{th} power of r, but owns an exponential dependence.

3.2.2 Electron transfer

Different from energy migration, electron transfer is a mechanism in which an electron is permanently relocated from the D to the A and constitutes an important photochemical process. The rate of the electron injection was first described according to the well-known Marcus Theory [13, 14]. In the classical approximation the total free energy G is plotted with respect to one-dimensional global reaction coordinate x by simply using the linear approximation [3]. Figure 3.3.(A-E) presents in detail different possible configurations of various A's displacements with respect to the D's energy height. To allow, energetically, electron transfer to occur the energy curve of A must be lower than the one of D (figure 3.3.C) and the reaction is then called exergonic. If D and A are identical (figure 3.3.B), both parabolas are symmetric and located at the same energy level then the situation describes a self-exchange mechanism with no clear-charge separation between the moieties (similar to Dexter exchange). Evolution in x leads the system to the Intersection Point (IP) of the D's and A's curves or at the Transition State (TS) according to Marcus Theory. At the point a quasi-equilibrium between the D and A takes place and electron transfer has a probability to follow via thermal activated hopping (Figure 3.3.C-E). The energetic barrier ΔG^* for electron transfer to occur is defined with straight forward mathematics from figure 3.3.C as:

$$\Delta G^* = \frac{\lambda}{4}[1 + \frac{\Delta G^0}{\lambda}]^2 \tag{3.13}$$

The reorganization energy is denoted as λ and is defined, in a general way, as the energy required to alter the configuration of the D into the configuration of A after electron transfer. An important parameter for the DSSC applications is the driving force, ΔG^0 that is consequently defined as the difference of the electronic potentials between the D and the A or between the Dye and the SC for DSSCs. Interestingly, when the driving force increases (Figure 3.3.c to 3.3.d) the electron transfer rate accordingly increases (Figure 3.3.G), but there is a critical point after maximization of the rate that additional growth of the driving force results in decrease of electron transfer rates. This inverted region has been predicted by Marcus theory (Figure 3.3.E) and demonstrated experimentally.

In the classical picture, as it was mentioned above the two energy curves are distinguished and the transfer occurs at the intersection point. If the interaction energy is large compared to the reorganization energy and according to a quantum approach the

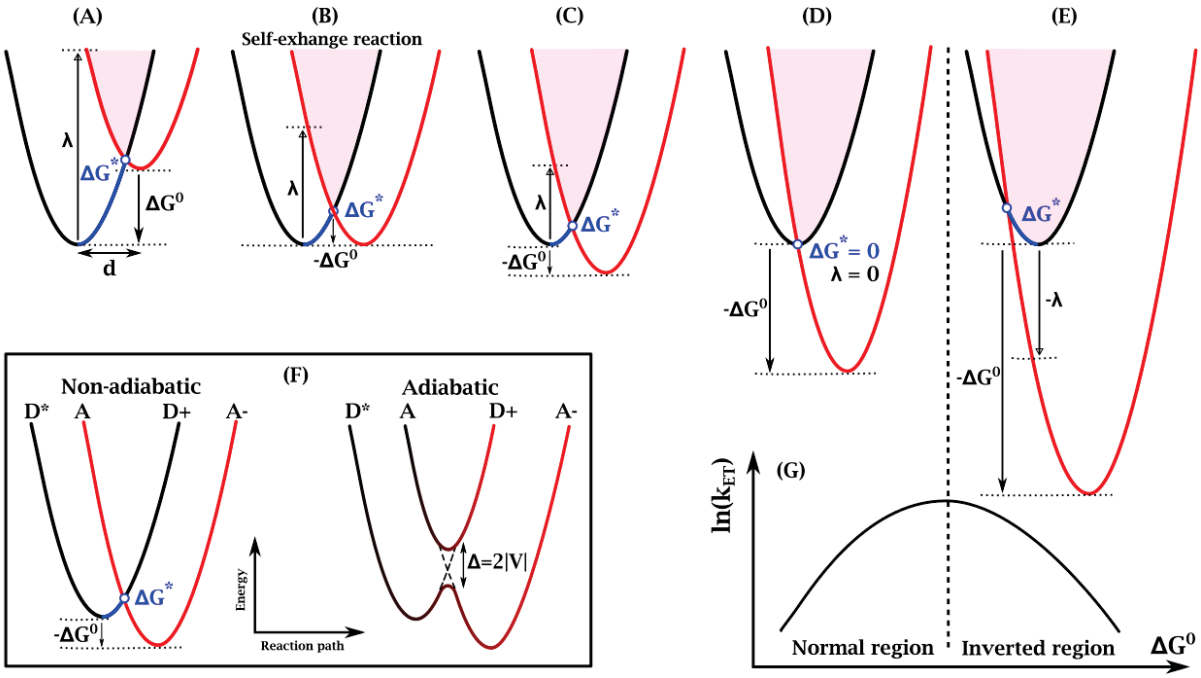

Figure 3.3: Schematic representation of the free energy parabolas of a D and A at distant d and varying the energy level height of the A from high to low (A)-(E) with respect to the D's height. (F) demonstrates the difference between the non-adiabatic (left) and adiabatic (right) regime and (G) illustrates the dependence of the electron transfer rate to the driving force for injection and revealing the predicted Marcus inverted region.

intersection point is energetically degenerate and the degeneracy is removed by an energetic splitting Δ, which equals to twice the interaction energy or the electronic coupling of dye-SC. This case is commonly described as an adiabatic regime (Figure 3.3.F.left). In the adiabatic case, which constitutes the classic Marcus regime, there is no direct distinction between D and A and the reaction takes place in one adiabatic state, according to the Born-Oppenheimer approximation, through the evolution of x-reaction path. The non-adiabatic regime dominates when the coupling between D and A is weak and refers to direct transitions from vibronic level of D to a vibronic level of A. This regime is studied for low temperatures and therefore for the high temperature limit ($\hbar\omega_{vib} << kT$) both vibrational systems can be treated classically and the expression for electron transfer becomes the conventional electron transfer rate equation via Marcus [3, 13–22]:

$$K_{ET} = \frac{2\pi}{\hbar} V^2 (\frac{1}{2\pi\lambda kT})^{1/2} \exp[-\frac{(\lambda + \Delta G_0)^2}{4\lambda kT}] \tag{3.14}$$

where V is the electronic coupling of the D and A that depends on the overlap of the electronic wavefunctions and also exponentially scales with the distance D-A.

For the interconnected system Dye-SC, it is important to highlight that Marcus theory refers to a transition from one electronic state of the dye to the density of states (DOS) of the SC. Therefore in the classical view (Figure 3.3.F.left) the A state is replaced by a manifold of parabolas representing the CB levels of the SC. Thus, for the transition from the LUMO to a i-th conduction band of the SC, in the equation 3.14, the rate $K_{ET(i)}$ and the coupling $V_{(i)}$ would be replaced. In the same manner, if due to the heterogeneity of the sample there is a distribution of D states, then the corresponding distribution of A states ρ within the distribution of D states is also taken into consideration. Finally, in a strong approximation it can be assumed that the excited state of the dye is in an optimal position with a range of conduction bands of the manifold and therefore (for the high temperature limit) there is no need for energy matching mechanism through molecular vibrations and only the K_{ET} depends only to the electronic coupling [19, 23, 24]. The final K_{ET} relationship in this case described in equation 2.3 essentially corresponds to Fermi's Golden rule. Interestingly, electron transfer can be one of the fastest mechanisms in nature with fast electron injection times to have been found in DSSCs to be even 6 fs [19]. For strong coupling cases electron injection occurs much faster than vibrational relaxation, from a higher vibronic mode of the excited dye.

3.3 Exciton Theory of molecular aggregates

In closed packed systems such as the DSSCs two dye-monomers can be brought in very close distances and electrostatically interact. The product of this interaction could be the formation of aggregates or as it was described by M.Pope [25] physical dimers. Physical dimers are a product of a specific spatial arrangement of the two monomers that are just bound by dipole-dipole (van der Waals) forces without forming a chemical bond [3]. Therefore, the spectroscopic properties of these broader systems result from a superposition of there constructing units (monomers). In many cases there is an energetic interaction that indicates a common response in the total molecular behavior. This general response is integrated in one entity named exciton [25]. Therefore, excitons form after excitation in the fs time scale. More analytically, they are neutral quasi-particles, consisting of an electron (e^-) and a hole (h^+), electrostatically attracted with each other as introduced in the first place by Frenkel (1931) [26] and generalized afterwards by Peierls (1932) and Wannier (1937). An alternative definition given by Feynman defined an exciton as a neutral quasi-particle that can move inside a molecular structure without

affecting the structure itself [27].

In Figure 3.4, an organized package of lattice sites in a SC is demonstrated. There are two extreme cases of excitons. If the distance of e-h or the exciton's radius's is larger than the lattice constant inside the inorganic crystal then the systems is described by the Wannier-Mott excitons. At room temperature, the binding energy is very low ($\leqslant 40meV$) and the Wannier-Mott excitons can dissociate into free carriers. The alternative extreme case is defined by the Frenkel excitons and can be found in solids consisting of weakly interacting units, such as aggregates. In this scenario the radius is smaller or of similar size as the molecular moiety (< 5 Å). At room temperature, Frenkel excitons are stable compare to a previous case and delocalized. Finally, the intermediate case of a charge-transfer exciton is defined as polaron. The diameter of the exciton covers the sites of the neighbor molecules and the systems can be formed usually in organic solids. The polaron is weakly Coulombic bound compared to Frenkel excitons, but it doesn't completely dissociate into free charges.

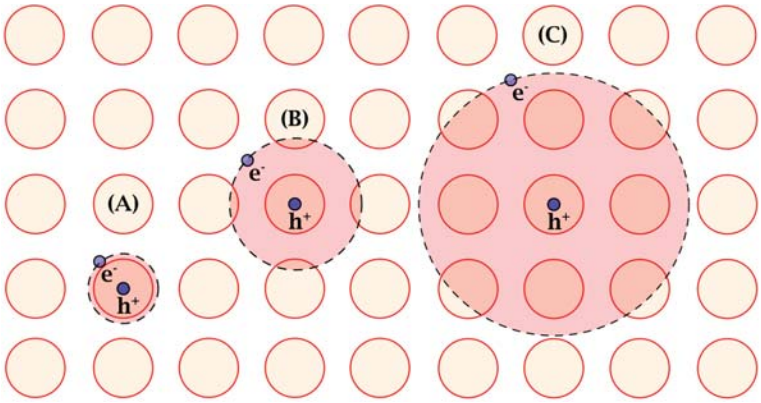

Figure 3.4: Different exciton types of various exciton radius over the lattice sites.(A) Frenkel exciton, (B) Charge-transfer exciton or Polaron and (C) Wannier-Mott exciton.

3.3.1 Kasha's classic theory

As it was mentioned above weak Coulombic interaction between two monomers induces the formation of physical dimers. Kasha described the energy band splitting (Figure 3.5) of the final dimer or aggregate, based on the point dipole approximation model that he developed [28]. In terms of the first interaction, the excited state S_1 of the dimer is energetically lower than the monomer's one, by a ΔE factor that denotes the weak attractive Coulombic energy of the interaction of the excited state S_1 of the first with

the S_1 of the second. Therefore, the new S_{1agg} is initially degenerate by containing both absorption intensities. The degeneracy breaks resulting into two possible excited states of higher and lower energy. The reasoning lies in the interaction of the transition of dipole moments two interacting monomers. If they oscillate in phase the dipole-dipole interaction is repulsive and the formed state is pushed energetically higher and the opposite attractive interaction takes place for the out-of-phase dipoles. The resonance interaction energy V has already been expressed, according to the point dipole approximation between the two transition dipole moment, in equation 8 and herein is re-written for the two monomers as follows:

$$V_{Coul} = \frac{(\overrightarrow{\mu_1} \cdot \overrightarrow{\mu_2}|R|^2) - 3(\overrightarrow{\mu_1} \cdot \overrightarrow{R})(\overrightarrow{\mu_2} \cdot \overrightarrow{R})}{|R|^5} \tag{3.15}$$

where μ_1 and μ_2 the transition dipole moments of the monomer 1 and 2, respectively and R the intermolecular distance. For the same molecules $\overline{\mu_1} = \overline{\mu_2}$ and for parallel dipoles or H-aggregates, $\overline{\mu_1} \cdot R = 0$ and for head-to-tail dipoles or J-aggregates, $\overline{\mu_1} \cdot R = \mu_1 R$. Consequently, for the first case, of H-aggregates the interaction energy is $V = \frac{\overline{\mu_1}^2}{\overline{R}^3} > 0$ and for the second of J-aggregates $V = -2\frac{\overline{\mu_1}^2}{\overline{R}^3} < 0$. All the in-between displacements in this co-planar geometry are described by $V = \frac{\overline{\mu_1}^2}{\overline{R}^3}(1-3cos^2\theta)$ where always one transition is allowed and θ varies (Figure 3.5) from 0^o for J-aggregates to 90^o for H. Interestingly, both transitions can be populated and be active by owning a sufficient dipole moment, for an oblique geometry, where:

$$V = \frac{\overline{\mu_1}^2}{\overline{R}^3}(cos\alpha + 3cos^2\theta) \tag{3.16}$$

according to Figure 3.5, where $a = 0$ *or* π. If α varies in between, then the total dipole configuration falls in a 3D conformation and the predictions becomes more complicated.

In basic spectroscopic systems such as dyes in solution phase or plain DSSC interfaces where no wider molecular configurations are formed the prediction based on 2D H and J aggregates is commonly used and reproducing the experimental results. In general, the interaction energy V will define the energy band splitting of the aggregates compared to monomers (Davidov splitting = 2V). In principle, H-aggregates spectroscopically are energetically blue-shifted with suppressed radiative decay yield with respect to the monomers, while J-aggregates are red-shifted with enhanced radiative decay yield. Experimental shows vibronic structure. For the classic case of aggregates, the vibronic progression is altered compared to the monomers. The ratio of the absorption vibronic

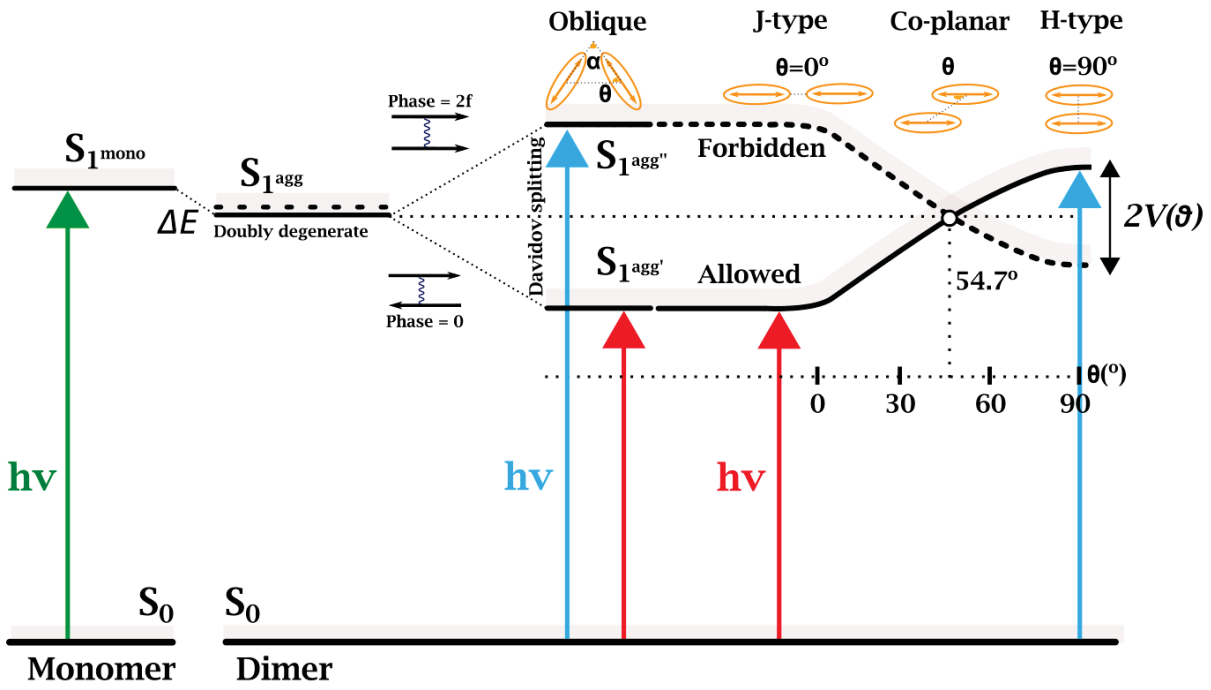

Figure 3.5: Schematic representation of the allowed molecular transition depending on the type of aggregates and comparing to the monomer's energy level.

peaks 0-0/1-0 of the H-aggregate and therefore the oscillation strength is suppressed for the H-aggregate, while it is enhanced for the J-aggregate compare to the single monomer's [29]. Consequently, the 0-0/0-1 ratio of the aggregate's vibronic peaks is enhanced for J-aggregates and minimized near 0 for the H-type [29].

3.3.2 Beyond Kasha's approach

Kasha's model has successfully been used to account for the basic photophysical properties of many molecular systems that undergo aggregation and is sufficient to interpret the experimental results. It predicts the possible arrangement of the aggregates and which excited state is active and therefore contributes to the emission. Despite the great success of the model, it doesn't take into account the local vibrational coupling, the close range interaction (<4 Å) and it is limited only to the Coulombic coupling between molecules.

At short distances, the wavefunctions of the two monomers overlap (HOMO-HOMO, LUMO-LUMO) and this facilitates the diffusion of the exciton with the electron to be in the neighbor molecule. Therefore, for short-range interactions Charge-Transfer (CT)

excitons start to dominate and the CT-exciton coupling (or interaction energy) V_{CT} is defined by Spano e.al. [30–32] as:

$$V_{CT} = -2\frac{t_e t_h}{E_{CT} - E_{S1}} \tag{3.17}$$

where E_{CT} the energy of the CT exciton, E_{S1} the monomer transition energy and t_e and t_h the dissociation or electron and hole transfer integrals, respectively and $V_{coul} << |E_{CT} - E_{S1}|$ with V_{coul} defined in equation 3.15. It is important to highlight that in this description the vibrational coupling is excluded, as well as the Coulombic or Frenkel integral. This type of new interaction changes the aggregate properties. Experimentally, this model it has been demonstrated for a series of systems that undergo π-π stacking and form H and J aggregates, such as pyrelene or pyrelene-based dyes [30]. From straightforward investigation of the equation 3.17, when $t_e t_h < 0$ and $V_{CT} > 0$ the scenario refers to H-aggregates and when the opposite is valid it refers to J-aggregates. The linear dependence of V_{CT} on the product $t_e t_h$ reveals the high sensitivity of the CT coupling to even small displacements of the monomer components. Figure 3.6 illustrates the coupling sign for the two regimes, Coulombic and CT, respectively, over displacements along the long and the short axis of a reference perylene dye. When for the classical Kasha's case there is only one change of the sign moving from the H to the J aggregate arrangement, for the short-distance CT case there are four sign changes related to the sign of $t_e t_h$. The sign of the $t_e t_h$ as a fact of the long axis distance depends on the precise spatial form of the homo and LUMO wavefunctions, here exemplified for perylene [30]. At this point and according to chapter 3.2.1, it is of interest to underline that in the short distance regime Dexter direct energy transfer takes place. However, the CT mediated coupling refers to an exciton (e-h pair) transfer to a quasi-CT intermediate state and it has been found for the case of π-stacked perylenes by Scholes et al. [33] that Dexter interaction is negligible compared to V_{CT}.

Concluding the above, it has been proven and demonstrated that indeed in special cases, such as the π-π stacking arrangements it is possible to allow manifold H and J-type of aggregate configurations between molecular monomers that they don't interact electrostatically, but they undergo partial wavefunction overlap for distances less than 4 Å. The co-existence of both Frenkel and CT excitonic interactions is possible and in this principle Spano et.al. [30, 31] based a new, expanded formalism to define the type of aggregates in the system. A two-letter notation was introduced, where the first letter reflects the nature of the aggregate according to Kasha's classic model and the second letter reflects the nature of aggregate affected by the CT-mediated coupling only. Thus, the

final photophysical properties of the aggregate are defined by the interference of these two coupling contributions and can act constructively or destructively in the extreme cases. When the Frenkel (or Kasha) coupling is stronger the first letter is a capital letter and

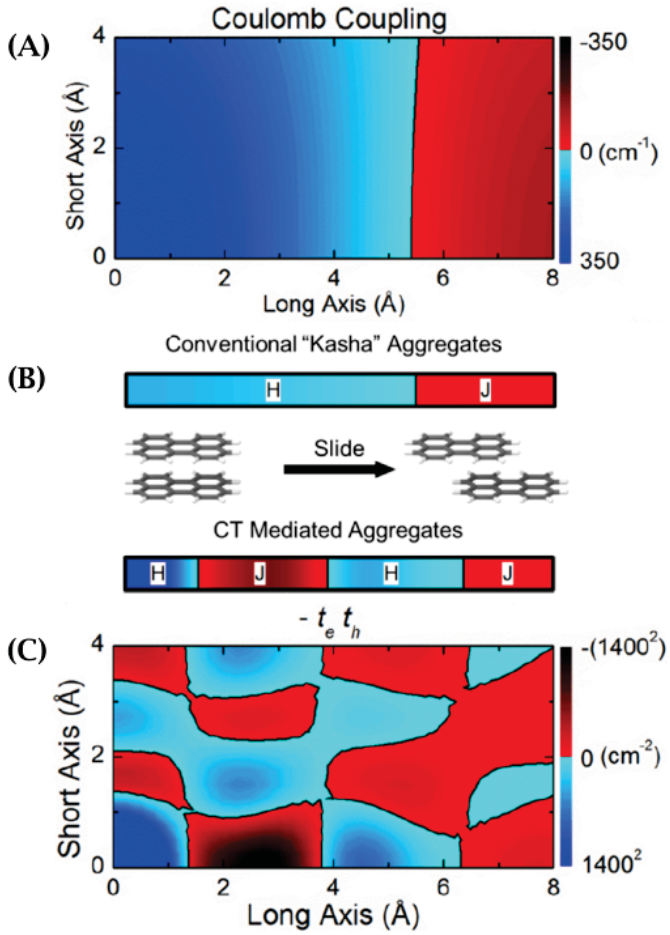

Figure 3.6: 2D maps presenting the (A) Coulomb ($radius_{exciton}$>3.5 Å) and (C) Charge Transfer ($radius_{exciton} < 3.5$ Å) coupling against the transverse displacement, evaluated by DFT calculations, for π-stacked perylene aggregates. (B) A schematic illustration of the coupling sign for the conventional aggregates (Coulombic) and for CT aggregates, as two perylene monomers are geometrically displaced from parallel to head-to-tail conformations (H-to-J aggregates). The image has been taken and modified from reference [30]

the final aggregate photophysics are described by the conventional model giving the possible combinations Hj, Hh, Jj and Jh. On the contrary, when the CT coupling dominates the possible combinations are hH, jH, jJ and hJ. An interesting case is the "null" HJ-aggregate, which demonstrates total destructive interference an the absorption spectrum, as well as the vibronic levels resembles the corresponding ones of the monomer. This type of analysis introduced by Spano could be of great interest for material design and

synthesis for real applications e.g. a HH-aggregate absorber for DSSCs that essentially owns enhanced exciton bandwidth and therefore greater charge mobility [32]. Finally, in Frenkel theory there is the consideration that the total number of excitations is a well-defined number and for simplicity one excitation is usually introduced. However, for a more general description two or more excitons can be considered and in this case the incorporation of local vibronic couplings in the total Hamiltonian that describes the system is necessary. The effect of this coupling in exciton-exciton interactions could possibly impact the photophysical properties of such aggregated systems. Finally, cases beyond the Kasha's model have been observed for a series of molecules e.g. very polar cyanine dyes, squaraine and quadrupolar organic dyes that form non-emissive J-aggregates. Therefore, several groups (e.g. Panailli et.al. [34, 35]) have developed extended theories to account for the effect of the polarizability of the molecules, as well as the environment effect (e.g. solvent's polarity) in the final photophysical properties of the aggregates and predicted non-conventional behavior that triggers interest for future studies.

In the scope of this PhD Thesis the interpretation of the experimental data is made in the idea of the conventional-Kasha's model for aggregates, considering only the Coulombic interactions and localized excitons in the Frenkel regime. Nonetheless, possible deviations and particularities of the experimental data could be interpreted based on the short intermolecular distances between the monomers and the aggregates at the closed-packed DSSC interface that introduce additional coupling factors.

References

[1] B. Valeur and M. N. Berberan-Santos, *Molecular fluorescence: principles and applications*. John Wiley & Sons, 2012.

[2] J. R. Lakowicz, *Principles of fluorescence spectroscopy*. Springer science & business media, 2013.

[3] G. Lanzani, *The photophysics behind photovoltaics and photonics*. John Wiley & Sons, 2012.

[4] J. R. Albani, *Principles and applications of fluorescence spectroscopy*. John Wiley & Sons, 2008.

[5] J. Hamilton, *Internal conversion processes*. Elsevier, 2012.

[6] G. G. Guilbault, *Practical fluorescence*. CRC Press, 2020.

[7] M. Berberan-Santos, E. Bodunov, and B. Valeur, "Mathematical functions for the analysis of luminescence decays with underlying distributions 1. kohlrausch decay function (stretched exponential)," *Chemical Physics*, vol. 315, no. 1-2, pp. 171–182, 2005.

[8] S. E. Koops, B. C. O'Regan, P. R. Barnes, and J. R. Durrant, "Parameters influencing the efficiency of electron injection in dye-sensitized solar cells," *Journal of the American Chemical Society*, vol. 131, no. 13, pp. 4808–4818, 2009.

[9] K. B. Lee *et al.*, "Application of the stretched exponential function to fluorescence lifetime imaging," *Biophysical journal*, vol. 81, no. 3, pp. 1265–1274, 2001.

[10] V. Novelli, N. Barbero, C. Barolo, G. Viscardi, M. Sliwa, and F. Sauvage, "Electrolyte containing lithium cation in squaraine-sensitized solar cells: Interactions and consequences for performance and charge transfer dynamics," *Physical Chemistry Chemical Physics*, vol. 19, no. 40, pp. 27 670–27 681, 2017.

[11] A. Listorti *et al.*, "The mechanism behind the beneficial effect of light soaking on injection efficiency and photocurrent in dye sensitized solar cells," *Energy & Environmental Science*, vol. 4, no. 9, pp. 3494–3501, 2011.

[12] J. Navas, R. Alcántara, C. Fernández-Lorenzo, and J. Martın-Calleja, "Evaluation of decay photocurrent measurements in dye-sensitized solar cells: Application to laser beam-induced current technique," *International journal of energy research*, vol. 36, no. 2, pp. 193–203, 2012.

[13] R. A. Marcus and N. Sutin, "Electron transfers in chemistry and biology," *Biochimica et Biophysica Acta (BBA)-Reviews on Bioenergetics*, vol. 811, no. 3, pp. 265–322, 1985.

[14] R. A. Marcus, "Electron transfer reactions in chemistry. theory and experiment," *Reviews of Modern Physics*, vol. 65, no. 3, p. 599, 1993.

[15] V. May and O. Kühn, *Charge and energy transfer dynamics in molecular systems*. John Wiley & Sons, 2008.

[16] B. N. DiMarco, L. Troian-Gautier, R. N. Sampaio, and G. J. Meyer, "Dye-sensitized electron transfer from tio2 to oxidized triphenylamines that follows first-order kinetics," *Chemical science*, vol. 9, no. 4, pp. 940–949, 2018.

[17] D. F. Watson and G. J. Meyer, "Electron injection at dye-sensitized semiconductor electrodes," *Annu. Rev. Phys. Chem.*, vol. 56, pp. 119–156, 2005.

[18] A. Listorti, B. O'regan, and J. R. Durrant, "Electron transfer dynamics in dye-sensitized solar cells," *Chemistry of Materials*, vol. 23, no. 15, pp. 3381–3399, 2011.

[19] V. K. Thorsmølle, B. Wenger, J. Teuscher, C. Bauer, and J.-E. Moser, "Dynamics of photoinduced interfacial electron transfer and charge transport in dye-sensitized mesoscopic semiconductors," *CHIMIA International Journal for Chemistry*, vol. 61, no. 10, pp. 631–634, 2007.

[20] S. Ramakrishna, F. Willig, and V. May, "Theory of ultrafast photoinduced heterogeneous electron transfer: Decay of vibrational coherence into a finite electronic–vibrational quasicontinuum," *The Journal of Chemical Physics*, vol. 115, no. 6, pp. 2743–2756, 2001.

[21] V. Vaissier, P. Barnes, J. Kirkpatrick, and J. Nelson, "Influence of polar medium on the reorganization energy of charge transfer between dyes in a dye sensitized film," *Physical Chemistry Chemical Physics*, vol. 15, no. 13, pp. 4804–4814, 2013.

[22] H. Wei, J.-W. Luo, S.-S. Li, and L.-W. Wang, "Revealing the origin of fast electron transfer in tio2-based dye-sensitized solar cells," *Journal of the American Chemical Society*, vol. 138, no. 26, pp. 8165–8174, 2016.

[23] C. Martın, M. Ziółek, and A. Douhal, "Ultrafast and fast charge separation processes in real dye-sensitized solar cells," *Journal of Photochemistry and Photobiology C: Photochemistry Reviews*, vol. 26, pp. 1–30, 2016.

[24] C. S. Ponseca Jr, P. Chabera, J. Uhlig, P. Persson, and V. Sundstrom, "Ultrafast electron dynamics in solar energy conversion," *Chemical reviews*, vol. 117, no. 16, pp. 10 940–11 024, 2017.

[25] M. Pope, C. E. Swenberg, *et al.*, *Electronic processes in organic crystals and polymers*. Oxford University Press on Demand, 1999, vol. 39.

[26] J. Frenkel, "On the transformation of light into heat in solids. i," *Physical Review*, vol. 37, no. 1, p. 17, 1931.

[27] R. Feynman, R. Leighton, and M. Sands, *The feynman lectures on physics, vol. iii*, 1965.

[28] B. Dellinger and M. Kasha, "Phenomenology of solvent matrix spectroscopic effects," *Chemical Physics Letters*, vol. 38, no. 1, pp. 9–14, 1976.

[29] F. C. Spano and C. Silva, "H-and j-aggregate behavior in polymeric semiconductors," *Annual review of physical chemistry*, vol. 65, pp. 477–500, 2014.

[30] N. J. Hestand and F. C. Spano, "Molecular aggregate photophysics beyond the kasha model: Novel design principles for organic materials," *Accounts of chemical research*, vol. 50, no. 2, pp. 341–350, 2017.

[31] ——, "Expanded theory of h-and j-molecular aggregates: The effects of vibronic coupling and intermolecular charge transfer," *Chemical reviews*, vol. 118, no. 15, pp. 7069–7163, 2018.

[32] ——, "Interference between coulombic and ct-mediated couplings in molecular aggregates: H-to j-aggregate transformation in perylene-based π-stacks," *The Journal of chemical physics*, vol. 143, no. 24, p. 244 707, 2015.

[33] R. D. Harcourt, K. P. Ghiggino, G. D. Scholes, and S. Speiser, "On the origin of matrix elements for electronic excitation (energy) transfer," *The Journal of chemical physics*, vol. 105, no. 5, pp. 1897–1901, 1996.

[34] M. Anzola and A. Painelli, "Aggregates of polar dyes: Beyond the exciton model," *Physical Chemistry Chemical Physics*, vol. 23, no. 14, pp. 8282–8291, 2021.

[35] S. Sanyal, A. Painelli, S. K. Pati, F. Terenziani, and C. Sissa, "Aggregates of quadrupolar dyes for two-photon absorption: The role of intermolecular interactions," *Physical Chemistry Chemical Physics*, vol. 18, no. 40, pp. 28 198–28 208, 2016.

Chapter 4

Experimental Methods

The study of DSSCs lies in a multidisciplinary field and numerous experimental techniques are called forth for an in-detail analysis. In the framework of the current PhD Thesis, absorption and fluorescence spectroscopy are used, both in the steady-state and time-resolved regime, from tens of fs up to several ns. Therefore, in the following section, the main experimental techniques and set-ups will be presented and described.

4.1 Steady-State spectroscopy

The absorption spectrometer that was used is the model LAMBDA 950 UV/Vis by PerkinElmer. It offers the capability of probing over the near-UV up to the near-IR region. There are two sample positions, one for the sample under study and the second for the reference, the absorption of which is usually subtracted (e.g. solvent for solution samples). For the DSSCs, we perform two measurements of both the complete DSSC device and the "half-DSSC" with no sensitizers, in order to monitor and subtract, if needed, the background absorption of the electrolyte, the glass substrates and SC.

For obtaining the fluorescence steady-state spectra a HORIBA model fluorimeter (Fluoromax 4) was used. Similarly, it offers the capability for lamp-excitation from the near-UV to the near-IR part of the spectrum and the detection is reliable up to IR (900 nm). The samples under investigation are the dyes either in solution, in specific solvents with cuvettes of 0.1 cm thickness, or in complete DSSC devices. The absorption and emission wavelength maxima, vibronic levels and intensity contain, in a first approach, very important information relative to the dyes' basic photophysical properties and it allows us to organize insightfully the experimental strategy. In addition, it is meaningful to monitor the degradation over time, as well as the sample-to-sample reproducibility and sample's active area homogeneity.

4.2 Non-linear Optics

The essence of non-linear spectroscopy lies in the light-matter interaction. When an external electric field $\vec{E}$ (e.g. laser beam) propagates in a dielectric material it induces a macroscopic polarization $\vec{P}$, as a result of the photophysical properties $\chi(\omega)$, or $\varepsilon(\omega)$ of the material. For low electric field intensities the induced polarization depends linearly on the electric field as: $\vec{P}(\omega) = \chi(\omega) \cdot \vec{E}(\omega)$, where ω is the angular frequency and (ω) the optical susceptibility of the material, which by its turn depends on the complex refractive index $\tilde{n}(\omega)$. The linear regime breaks when the intensity of the incident light becomes very high (E gets closer to the Coulombic field) and therefore the induced electric dipoles in the medium don't oscillate as the initial electric field (non-harmonically). In the same manner, the non-linear response occurs when multiple beams of different or of the same frequencies interact at the same point in the material. On that occasion it is possible the different electric fields on the sample, under specific conditions to add up constructively, generating new frequencies and oscillations of higher intensity. In this case the total polarization is defined as $P = P^L + P^{NL}$ and more in detail as:

$$P = \varepsilon_0[\chi^{(1)} \cdot \vec{E} + \chi^{(2)} \cdot \vec{E}^2 + \chi^{(3)} \cdot \vec{E}^3 + ... + \chi^{(n)} \cdot E^n] \tag{4.1}$$

where $\chi^{(1)}$ is the linear optical susceptibility, $\chi^{(2)}$ and $\chi^{(3)}$ the (non-linear) second and third order optical susceptibilities, respectively.

4.2.1 Non-linear optical processes (SFG, SHG, DFM, WLG)

Some important non-linear processes are Second Harmonic Generation (SHG), Third Harmonic Generation (THG), Sum Frequency Generation (SFG), Difference Frequency Mixing (DFM) and White Light Generation (WLG). The origins of the above quoted phenomena are revealed by Equation 4.1. As it was mentioned above and relative to our spectroscopic means, only the processes resulting from the second and third order polarizations are relevant to the scope of the present PhD Thesis. Sorting into categories only SHG, SFG and DFM are produced by the second order of the polarization while THG, Self-focusing (SF), Self-Phase Modulation (SPM), WLG and Cross-Phase Modulation (XPM) originate from the third order of polarization. In principle, second order processes can be generated in non-centrosymmetric crystals (e.g. β-BB0), because, for the centrosymmetric ones, the condition $\chi^{(2)} = 0$ is valid, due to the reversibility of the polarization $P^{(2)} = -P^{(2)}$ for opposite directions of the electric field through the

crystal [1]. In the same manner, third order processes take place in isotropic media or centrosymmetric crystals (e.g. solution samples or a-BBO).

Regarding the second order polarization, the above processes can be derived as follows. Considering the interaction of two beams with electric fields E_1, E_2 and frequencies ω_1, ω_2, the analytical form of the 2^{nd} order polarization can be written as:

$$P^{(2)} = 2\varepsilon_0\chi^{(2)}(E_1E_1^*+E_2E_2^*) + \varepsilon_0\chi^{(2)}\{E_1^2exp(-i2\omega_1t) + E_2^2exp(-i2\omega_2t)+ 2E_1E_2exp[-i(\omega_1+\omega_2)]t + 2E_1E_2^*exp[-i(\omega_1-\omega_2)]t\} \tag{4.2}$$

From the analytical expression of the second order polarization, for the two-wave interaction, the contributions of new frequencies appear. In detail, $2\omega_1$ and $2\omega_2$ refer to the SHG processes, respectively, $\omega_1+\omega_2$ to the SFG, $\omega_1-\omega_2$ to DFM and finally the zero frequency ω=0 is also predicted.

In a non-centrosymmetric medium, all processes occur, but with different efficiencies, because the phase-matching conditions are different. As a general principle for bulk media, for a non-linear process to appear, two conditions must be fulfilled [1–4], the conservation of energy ($\Delta E = 0$, where $E = \hbar\omega$) and the phase matching conditions that derive from the conservation of momentum ($\Delta\vec{k} = 0$, where $\vec{k}$ the wavector), between the interacting beam(s) and the produced beam(s). The main processes, on which our spectroscopic techniques are based, are described below.

For **Fluorescence Up-Conversion (FLUPS)** [5, 6] (see section 4.4), SFG is the major process that allows us to monitor the fluorescence decay with $\sim$ 200 fs time resolution. The focused fluorescence and the time-delayed (gate) laser beam, of $\sim$ 50 fs duration, are focused in the center of a non-centrosymmetric BBO crystal and both overlay spatially and temporally. Therefore, for the Sum Frequency Generated third beam, energy conservation requires $\omega_3 = \omega_1 + \omega_2$ and from momentum conservation the phase-matching condition can be defined as $\vec{k}_3 = \vec{k}_1 + \vec{k}_2$. For collinear alignment, or similar to our system that the configuration follows the paraxial approximation, the phase matching condition can be expressed as [2]:

$$\frac{n_{UP}}{\lambda_{UP}} = \frac{n_F}{\lambda_F} + \frac{n_G}{\lambda_G} \tag{4.3}$$

where n and λ refer to the refractive index and wavelength, respectively and the indexes UP, F and G refer to the Up-Converted, the Fluorescence and the Gate beams. Consequently, for two beams of the same frequency ω the SFG signal is of frequency $\omega' = 2\omega$ and simply represents the SHG process.

In figure 4.1 the SFG is schematically illustrated for two beams propagating through a non-linear medium in a non-collinear geometry. Non-collinear geometry is used to eliminate unwanted contributions due to Group Velocity Dispersion that together with Group Velocity Mismatch (GVM), can limit greatly the time-resolution, as described in detail in [3]. A more detailed analysis regarding the phase matching conditions and the crystal's properties applied to the Fluorescence Up-Conversion technique will be made in section 4.5.

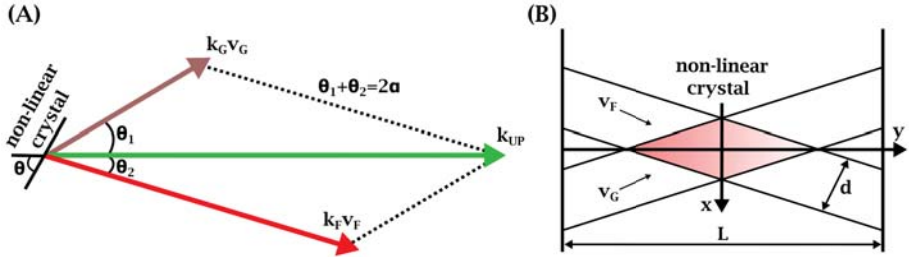

Figure 4.1: (A) Sum Frequency Generation in a non-collinear configuration, between the Fluorescence and the Gate beams in a non-linear crystal. (B) Schematic representation of the pulse overlap in a non-collinear configuration. Where k are the wavevectors and v the group velocities. The image has been taken and modified from [3].

Relative to the **Transient Absorption (TA)** technique [7] (see section 4.5) one important process is White Light Generation (WLG) [8, 9]. WLG is a third order polarization phenomenon and thus can occur in a centrosymmetric crystal of specific material, such as YAG, sapphire et al. [10]. For the WLG in our system a sapphire crystal is used, with excitation at 800 nm, due to its excellent thermal resistance and broad spectrum in the near-IR region of interest. The generation of the super-continuum is based on the optical Kerr effect. When the intensity of the electric field (pump laser beam), which is incident on the centrosymmetric crystal, becomes high and induces higher order even-number polarization, the refractive index obtains linear dependence on the electric field's intensity as: $n \approx n_0 + \frac{3\chi^{(3)}}{4\varepsilon_0 c n_0^2} I$. Laser beams own a Gaussian spatial profile with the wings having lower intensity than the central region. Therefore, when they propagate through the material and due to the optical Kerr's effect, the beam converges (self-focusing) similar to the case of a positive lens. The continuum generation is triggered by self-focusing. This process depends on the power of the incident beam [9] that should reach or exceed the critical value defined as: $P_{crit} = \frac{3.77\lambda_p^2}{8\pi n_0 n_c}$, where λ_p is the wavelength of the pump beam, n_0 and n_c the refractive index of the air and the crystal, respectively. The most critical parameter of the WLG is Self-Phase Modulation (SPM), which results from the Optical Kerr effect and is commonly accepted to be triggered by self-focusing [8, 11].

In detail, when the pump pulse propagates through the crystal of specific thickness d, a change of phase is induced, which depends on the intensity dependent refractive index n_c. Consequently, frequency modulation is induced, creating new frequencies and broadening the pump's pulse spectrum.

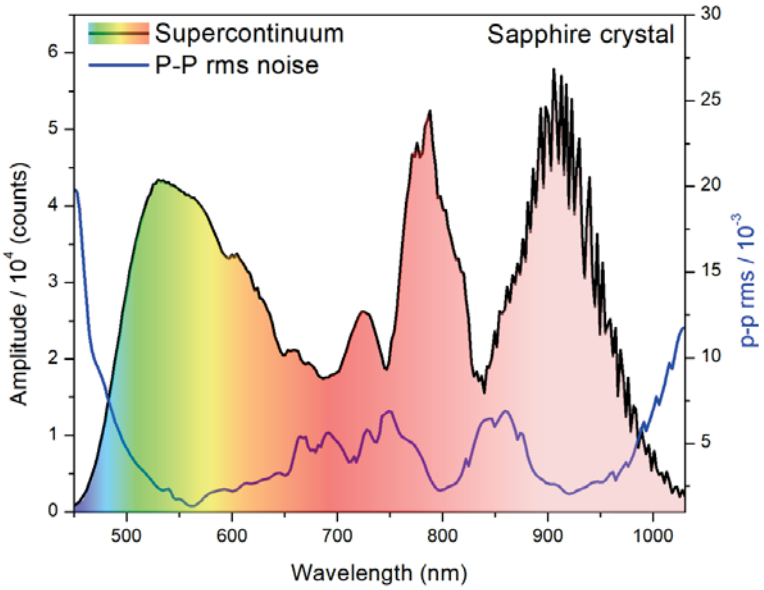

Figure 4.2: Supercontinuum spectrum (black line) generated in a 2 mm Sapphire crystal with excitation at 800 nm and the relative peak-to-peak RMS noise (blue line). The main 800 nm pump beam contribution is spatially blocked and the residual is filtered out using a dye filter (OD $\sim$ 1.6/mm), based on the Indocyanine Green dye (**IR125**) in $CHCl_3 : DMSO$ (9:1). At $\geq$850 nm wavelengths the WL shows a pattern with fringes, due to "the etaloning effect" in the back illuminated CCD chirp (interferences in the cavity).

In the figure above, a white light spectrum, typical for our measurements, is presented. It is produced in a 2 mm sapphire crystal and extended from 450 nm to 1030 nm. The excitation wavelength is at 800 nm and the pulse incidents on the crystal in a orthogonal geometry. The spectrum is an average of 5000 collected laser shots. For low-noise results, the relative peak-to-peak rms (root-mean-square) level should be kept bellow 1 %. Prior to the interaction on the crystal, the pump beam diameter, as well as the power are carefully controlled with an iris and an optical density filter, respectively. Noteworthy, the 800 nm pump beam was spatially blocked after the WLG and additional contributions that could saturate the detection, were reduced using dye-filters based on the near-IR absorbing indocyanine **IR125** dye in solution of $DMSO : CHCl_3$ ($\sim$ 9:1) of OD $\sim$ 1.6/mm. The final spectrum is obtained by combining two different measurements, one for each of the two spectral regions (440-750 nm and 750-1030 nm) covered by our

spectrometer.

4.2.2 (Non-Collinear) Optical Parametric Amplification

For our experiments we need excitation wavelengths that match the electronic or vibronic transitions of the condensed phase systems under study. For the fs-fluorescence and transmission time-resolved experiments the excitation wavelength should be tuned over a wide spectral range from the visible up to the near-IR, maintaining at the same time the best time resolution possible for the narrow and selective final excitation spectrum. To fulfil the above mentioned criteria we utilize an Optical Parametric Amplification (OPA) system in collinear geometry. The OPA principle can be explained in terms of photon energy [12–14], as it was demonstrated for SFG in section 4.1.1. In the OPA a high energy photon propagates in a non-linear crystal and exits the material in a virtual excited state. In parallel with the pump beam, a seed (or signal) pulse of lower energy stimulates a decay into an intermediate state, giving rise to a new signal photon in the same phase as the stimulating initial seed one. This mechanism demonstrates the amplification process and for energy conservation to be satisfied, an additional idler photon is generated. Fundamentally, OPA is also a DFM process, but with an amplification effect on the signal beam with the relative phase matching condition to be fulfilled as: $k_p + k_s + k_i = 0$, for collinear geometry. In Figure 4.3.A,B the wavevectors and group

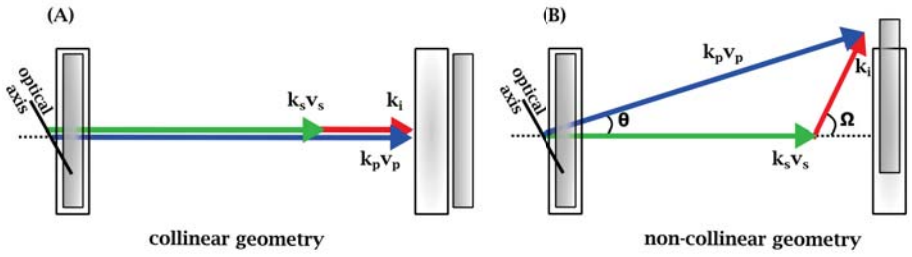

Figure 4.3: Schematic representation of (A) collinear and (B) non-collinear interaction geometry with the characteristic wavevectors k and group velocities v for the pump, signal and idler beams. The open rectangulars represent the signal pulses and the filled rectangulars the idler pulses, before and after the transition through the non-linear crystal. The image has been taken and modified from [14].

velocities are presented as arrows for the pump, signal and idler beams, for a collinear and non-collinear geometry, respectively. For the latter, the pump and the signal/seed incident and pass the crystal with an angle θ between them and therefore the direction of the idler results from the relative vector equation. In addition, phase matching must

be fulfilled in both x-y axis or parallel and normal to the signal wave-vector as:

$$\begin{aligned} \Delta k_{par} &= k_p cos\theta - k_s - k_i cos\Omega = 0, \\ \Delta k_{norm} &= k_p sin\theta - k_i sin\Omega = 0 \end{aligned} \tag{4.4}$$

where Ω is the angle between the signal and the idler. For a fixed θ, it depends on the signal wavelength, but phase matching does not ensure the matching of group velocities. In Figure 4.3.A for collinear geometry, due to GVD, the red wavelengths travel through the material with higher group velocities and GVM occurs, resulting in the separation of the signal and idler beams. On the contrary, in the case of non-collinear geometry (Figure 4.3.B) velocity matching can be achieved during the propagation in the non-linear crystal. On the other side, non-collinear geometry is advantageous when we aim at short (sub - 10 fs) pulses with broad spectral profile. It has been found that the broadband phase-matching occurs when the projection of the signal's group velocity equals to the group velocity of the idler's pulse as: $v_s = v_i cos\Omega$.

For our experimental instrumentation, the TAS and FLUPS set-ups share the same excitation pathway, which is a commercial TOPAS-Prime excitation box (Lightconversion). Originally, it contains a double-stage OPA system with software-controlled options for varying the BBO angles, as well as the delay times to finely tune the desired wavelength. Additional SFG, SHG and THG modules allow for the generation of $\sim$ 50 - 80 fs pulses with $>$ 50 nJ energy in the range of 270 - 1550 nm. Our fundamental 800 nm beam is generated by a 5 kHz Ti:Sapphire amplifier and is injected in the TOPAS box. In a brief outline, in the first stage, a portion of the 800 nm beam is used to generate the seed supercontinuum in a Sapphire crystal and it steers in a BBO crystal, where it interacts with a second portion of the 800 nm to generate and amplify the desired wavelength (signal). The interaction scheme is non-collinear, but in the paraxial approximation ($sin\theta \approx \theta$), just to spatially filter out the pump and idler. For further amplification at the second stage, the resulting signal is driven to a second BBO crystal and interacts in a collinear scheme with a third portion of the 800 nm. The signal, idler and if needed, the 800 nm pump beams are driven to the exit of the TOPAS. Moreover, there is a possibility for further tuning of the desire wavelengths by adding two additional mixers afterwards and with the use of appropriate dichroic mirrors the beams of the desired wavelengths can be isolated. For example, for near-IR excitation at 740 nm, we generate at the exit of TOPAS a signal of 1480 nm and by using the SHG mixer we converted and select the SH-Signal at 740 nm.

For the Streak camera measurements, the fundamental beam is produced by a Tan-

gerine system with central wavelength at 1030 nm. The homemade OPA system is similar to TOPAS, but it is a single stage OPA. The WL is generated with the 1030 nm beam and the amplification is made with its SH (515 nm) [15]. The output wavelengths range in the 560-900 nm spectral region. Last, in sections 4.3-4.5 the experimental set-ups and principles will be presented.

4.3 Streak Camera set-up

In the field of time-resolved molecular spectroscopy, time-resolved fluorescence spectroscopy is a broadly used technique to monitor the excited state dynamics of systems under study. Monitoring exclusively the fluorescence in various time-scales can be advantageous compared to other non-background-free techniques, such as TA. In particular, for DSSC systems important information relative to the charge separation can be extracted. As it was mentioned previously, in our experiments two time-resolved fluorescence set-ups are used. First the streak camera, which is utilized when fs-resolution is not required and when time-windows longer than 1 ns are required for detection. Second, the broadband-Fluorescence-Up-conversion set-up, which offers time resolution of 200 fs.

The streak camera model that is used in our experiments is the HAMAMATSU C10627 with a well known operational principle [16]. The sample is excited and the produced fluorescence is collected, collimated and focused on the detector combining a spectrograph and a streak camera tube. For our experiments additional polarizers were used in the detection, in order to secure magic angle ($MA \sim 54.7^o$) conditions between the detected fluorescence and the excitation polarization. In Figure 4.4 the streak camera apparatus, as well as its multi-step operation are pictorially illustrated. Initially, the beam focuses on the entrance slit. The slit width is adjusted, in order to avoid saturation or double pulse detection in photon counting mode (best signal/noise ratio). The wire-like photo-cathode is in the exit focal plane of the spectrograph. It converts the photons into electrons, accelerated and released into the vacuum tube by the accelerated mesh. The number of generated electrons is proportional to the intensity of the incident photons. In the main streak tube there are two metallic plates as electrodes, connected to a "sweep circuit" which generates an electric field in the vertical axis. The frequency and the time of the sweep circuit is synchronized with the incoming pulse. At time zero an electronic trigger signal is applied to the electrodes and when the incoming fluorescence pulse arrives, a high speed sweep potential is applied. Subsequently, the incoming

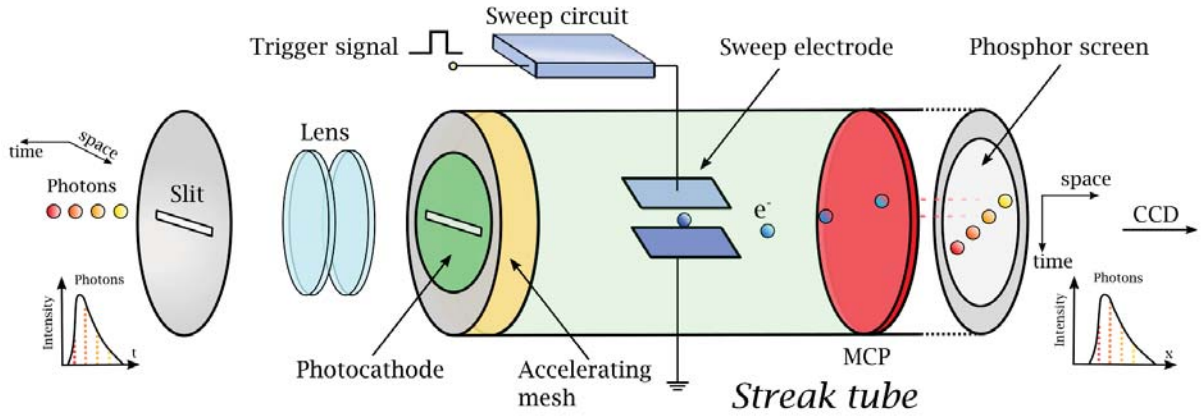

Figure 4.4: Schematic representation of the Streak camera apparatus. *The figure has been modified based on reference [16].

electrons, depending on their arrival time, get deflected at different angles. Then, they are driven to a Micro-Channel Plate (MCP), where they are multiplied several thousands of times and finally bombarded on a Phosphor screen to re-emit photons detected by a CCD camera. The imprinting in the horizontal axis refers to the spectral profile of the fluorescence and in the normal axis to the temporal profile, when the intensity is also defined in the graphical contour, because higher photon flux generates more electrons.

The time resolution is a critical parameter and in the streak camera it is restricted by several factors [17] depending on the various electric signals and mostly the sweep voltage response. Therefore, the best time resolution offered by the streak camera is constrained to $\sim 10\ ps$. For achieving shorter time resolution of $\sim 200\ fs$ a state-of-the-art up-conversion technique is used, which essentially utilizes a second laser beam as gate and finally in this case the time-resolution depends on the pulse duration of the beam.

4.4 Broadband Fluorescence Up-Conversion

Fluorescence Up-Conversion is an advantageous technique, in order to monitor the relaxation dynamics from an excited electronic molecular state with a sub-ps time resolution. In Figure 4.5 the experimental set-up is presented in a concise schematic way, as well as an "1-1" imaging system (right-below) of the center of the BBO crystal. Our laser system is a Ti:Sapphire (FemtoLasers Synergy 20) source with center wavelength at 800 nm, producing pulses of 20 fs temporal resolution and repetition rate of 80 MHz. The fundamental beam goes through a Chirped Pulsed Amplification system (CPA-Amplitude

Technology Pulsar) to finally produce pulses of 0.5 mJ energy, 40 fs time resolution and tuned to 5 kHz. The excitation wavelength is finely tuned through multiple non-linear

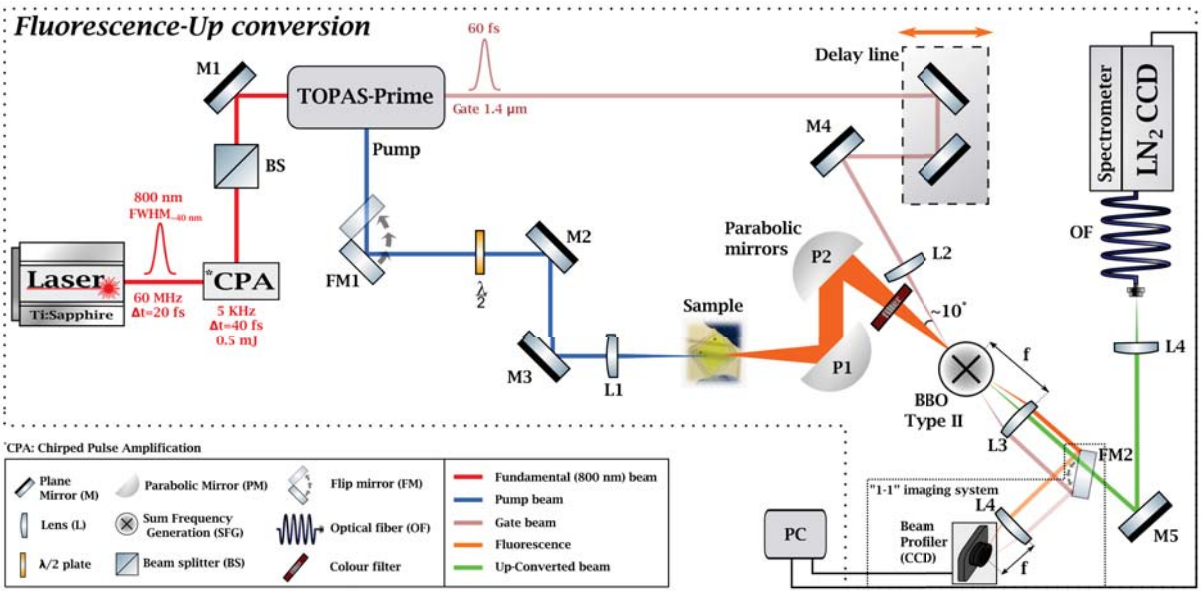

Figure 4.5: Simplified schematic representation of the broadband Fluorescence-Up-Conversion (FLUPS) set-up. Right-bellow (dashed-frame) it demonstrates the "1-1" imaging system of the center of the BBO crystal.

processes in the TOPAS-Prime box, the operation of which was described in section 4.2.2. The pump finally excites the sample and the produced fluorescence is collected, collimated and focused in a 1 mm thick β-BBO. In parallel, the amplified signal resulting from the OPA process inside TOPAS, is used as the gate beam. The gate beam goes through a delay stage, offering minimum time steps of 6.7 fs and is focused on the β-BBO crystal achieving temporal (time zero) with spatial overlap with the fluorescence spot. When the crystal is rotated to the PM angle, energy and momentum conservation (type II phase-matching) are fulfilled and SFG can occur, as it was described in section 4.2.1 producing the final Up-Converted signal. After time zero the gate pulses arrive with a time delay τ and the initial decay curves for the fluorescence wavelengths are reconstructed from the up-converted intensity (I_{UP}) as a function of τ (Figure 4.6) as:

$$I_{UP}(\tau) = \int_{-\infty}^{\infty} I_{FL}(t) I_G(t-\tau) dt \tag{4.5}$$

where I_{FL} and I_G the intensity of the fluorescence and gate beam, respectively. It is important to mention that for MA conditions the pump beam polarization has been rotated by 57.4^o relative to the one of the gate beam.

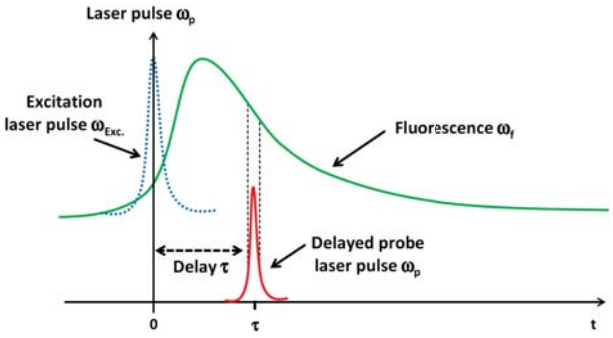

Figure 4.6: Schematic diagram showing the basic principles of the fluorescence up-conversion technique. The picture was taken from [6].

The β-BBO crystal in an uniaxial birefringent crystal, with an ordinary axis (o) and an extraordinary axis (e) orthogonal to each other. In our experimental configuration we make use of type II phase matching (O+E→E), with the fluorescence to be in the ordinary and the gate in the extraordinary. The type II configuration can be advantageous for broadband detection sacrificing the up-conversion efficiency [5]. Interestingly, for small signal conditions, when there is no depletion of the fluorescence and gate pulse powers [6], the up-conversion quantum efficiency can be defined as [5, 18]:

$$n_q(\Delta k) = \frac{N_{up}^{z=L}}{N_f^{z=0}} \propto \frac{d_{eff}^2 L^2}{\lambda_f \lambda_{up} n_{(0)}(\lambda_f) n_{(e)}(\lambda_g) n_{(e)}(\lambda_{up}, \theta_{up})} I_g^{z=0} (\frac{sin(L\Delta k/2)}{L\Delta k/2})^2 L^2 \quad (4.6)$$

where, N_{up} and N_f are the photon flux for the up-converted and fluorescence signals, respectively and d_{eff} the effective non-linear optical coefficient [12] that depends on the propagation direction and polarization of the three waves, λ the wavelength, n the refractive index, I_g the power of the gate and Δk the phase mismatch in the crystal of thickness L. Two strategies, in order to increase the quantum efficiency is either to use thicker BBO crystals increasing in this manner the GVM and thus sacrificing time resolution, or to increase the gate intensity. However, amplifying the gate beam also enhances various artifacts, such as the SHG that can spectrally overlay with the up-converted signal.

Finally the up converted signal is driven and focused on an optical fiber, which delivers the signal to the entrance slit of the spectrometer. A CCD camera, with a LN_2 cooling system detects the signal over a total spectral range of 200 nm with highest sensitivity. The experimental challenge of up-conversion is especially pronounced for systems with very low radiative rates, (e.g. triplet states), since the number of fluorescence photons per time is low. Indeed, since the efficiency of the up-conversion process $n_q(\Delta k = 0)$ is $< 10^-3$ [2], all experimental parameters must be optimized. First, the spatial overlap

between fluorescence and gate spots on the crystal to ensure that there is no "mismatch" due to bad alignment. Second, both spots must ideally show Gaussian intensity distributions, which requires especially for the fluorescence spot a careful alignment of the lens L1 (Figure 4.5). For this reason we implemented an "1-1" imaging system of the critical overlap of the two beams in the center of the BBO crystal (Figure 4.7-dashed frame right-below) to a CCD camera ("beam profiler") to monitor the focused beam spots. The spatial profiles, of the focused fluorescence (580 nm) of a reference Rhodamine B sample and gate (1438 nm) beam spots are shown in Figure 4.7. The conditions aren't optimised and the fluorescence spot can be decreased even more. For maximum gain the fluorescence spot must be homogeneous and the Gate beam optimally focused on the BBO, however there is a limitation for the gate diameter, because higher energy density give rise to additional non-linear effects, such as THG, as well as WL on the lens L3. It is important to highlight that the CCD's quantum efficiency is very low in the near-IR, thus the observed profile of the gate beam reflects the two-photon-absorption in the silicon detector and not directly the IR beam. For our experiments the usual gate wavelength is at 1270 nm with the typical average power of 200 mW and the pump is ordinarily tuned to excite the near-IR dyes from 700-800 nm.

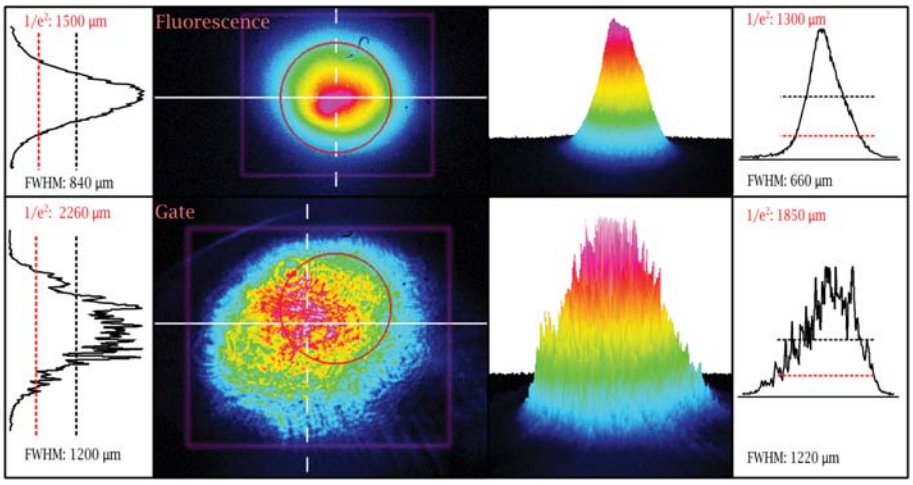

Figure 4.7: Individual 2D and 3D spatial profiles of the fluorescence (up) and the gate (down) beam-spots in the center of the BBO crystal where they spatially overlap. The test sample is Rhodamine B with emission maximum at 580 nm and the gate beam is tuned at 1438 nm. Left and right panels present the corresponding spatial profiles through an x-axis or y-axis "cut" of the beams. The fluorescence spot is 300 μm.

4.5 fs-Transient Absorption

In the section of pump-probe techniques and referring to the electronic third order non-linear spectroscopies [19, 20] the most common is Transient absorption spectroscopy (TAS). The detailed theoretical formalism is not essential to describe the experiment and it is out of the scope of the present PhD Thesis.

The experimental set-up used for the current PhD has been described in detail elsewhere [21] and is schematically demonstrated in Figure B.2. Both FLUPS and TA share the same laser source producing pulses at 800 nm and 5 kHz repetition rate. One portion of the fundamental 800 nm beam is driven to the OPA system. In this manner, the pump beam is generated in the TOPAS-Prime through the OPA sequence, similarly to FLUPS. The pump beam passes a chopper (111.5 Hz) that is tuned to half the frequency

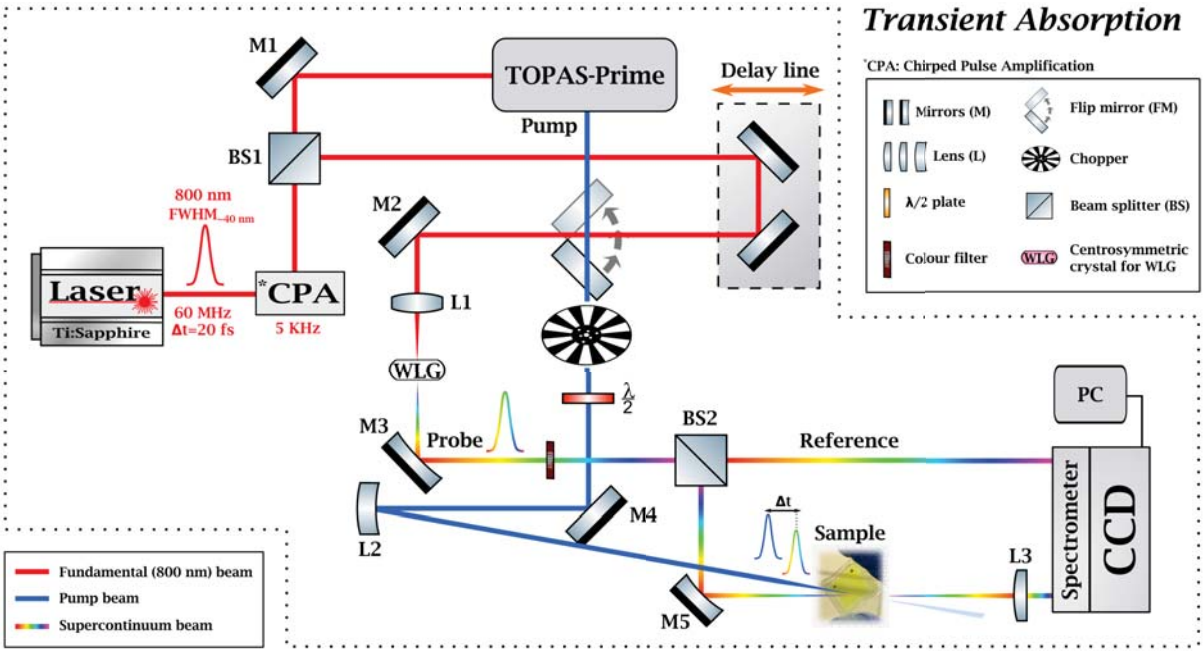

Figure 4.8: Simplified schematic representation of the fs-Transient Absorption set-up.

of spectral acquisition (223 Hz) and focused to excite the sample. Another portion of the fundamental goes through a delay stage and is focused on a 2 mm Sapphire crystal to generate the White-Light (WL) (e.g. Figure 4.2). The WL is driven and focused on the sample, orthogonal with respect to the sample surface. It goes through the sample, collimates and focuses by a pair of parabolic mirrors and it is steered to the spectrometer to finally be analyzed in a CCD camera system. We use parabolic mirrors instead of lenses, in order to reduce the GVD and in this way, the GVD is defined only by the Sap-

phire crystal. The changes that have been induced in the sample after photoexcitation are imprinted in the changes of the broadband WL after the sample and therefore by monitoring the absorption with and without pump (controlled by the chopper), the final difference absorption (ΔA) spectra are obtained for various delays between the pump and the probe. Thus, experimentally and by recalling the Beer-Lambert's law (equation 3.1), the measured $\Delta A(\lambda, t)$ can be expressed as:

$$\Delta A(\lambda, t) = A(\lambda, t)_{pump,on} - A(\lambda, t)_{pump,off} = -\log \frac{I(\lambda, t)_{pump,on}}{I(\lambda, t)_{pump,off}} \tag{4.7}$$

where $A(\lambda, t)_{pump,off}$ is the absorbance of the WL and $I(\lambda, t)_{pump,off}$ the intensity of the transmitted WL at time delay t with no presence of the pump. Similarly, $A(\lambda, t)_{pump,on}$ and $I(\lambda, t)_{pump,on}$ refer to the absorbance and intensity of the transmitted probe when the pump is present and excites the sample.

To account for and minimize the noise induced by the WL, a second portion of the supercontinuum, after its generation, is steered into another part of the CCD camera as reference. Then the real measured quantity can be derived from the extended equation 4.7 by adding the ratio of the intensities of the reference probe beam without and with the pump as: $\Delta A(\lambda, t) \times (\frac{I(\lambda,t)_{pump,off,ref}}{A(\lambda,t)_{pump,on,ref}})$. Relative to the experimental conditions, it is important to mention that for MA conditions the pump polarization is adjusted via a half-wave plate to be in 57.4^o compare to the probe (WL) polarization. Furthermore, the WL power has been greatly reduced via OD and dye filters, before the sample, especially in the near-IR region, so as to eliminate possible excitation effects on the sample by the probe beam and finally we confirm that the power of the probe is at least 90 % less than pump's power.

In more detail and complementary to equation 4.7, the change of the sample's absorption can be expressed as:

$$\Delta A(\lambda, t) = \sum_{n=1}^{n_{comp}} \varepsilon(\lambda)_n \Delta C(t)_n D \tag{4.8}$$

where, ΔC_n is the concentration change in the state S_n at time t after excitation, $\varepsilon(\lambda)$ the extinction coefficient relative to the S_n state at a given wavelength and D the sample's thickness.

TAS is advantageous because it offers the capability to locate and monitor various spectral features in a broad regional map. Figure 4.9.A.B illustrates in a scheme, the basic features obtained by TAS and their corresponding energy levels and transitions.

These basic contributions that will be discussed are the Ground-State Bleach (GSB), the Stimulated Emission (SE), the Excited-State Absorption (ESA) and the Photoproduct Absorption (PA) [7]. First and relative to the GSB, after photoexcitation a fraction of molecules is promoted to the excited state, therefore by monitoring the Ground-State and according to Equation 4.8 the difference of the concentration of dyes in the Ground State after photoexcitation minus the concentration of dyes in the Ground State with no presence of pump gives a negative values. Consequently, the GSB signal is always negative and it should be located in the spectral region of the stationary absorption. When the sample is excited and a probe photon arrives, it can either promote the system to a higher excited state, whose absorption corresponds to the ESA signal, or it can stimulate a transition back to the Ground State via the process of SE, which spectrally should be located in the region of stationary emission corresponding to the optically allowed transition. In the same manner and opposite to the GSB, ESA is always a positive signal, when SE is always negative. The latter can be attributed to the fact that more photons arrive in the detector resulting in negative ΔA. In many systems, such as the

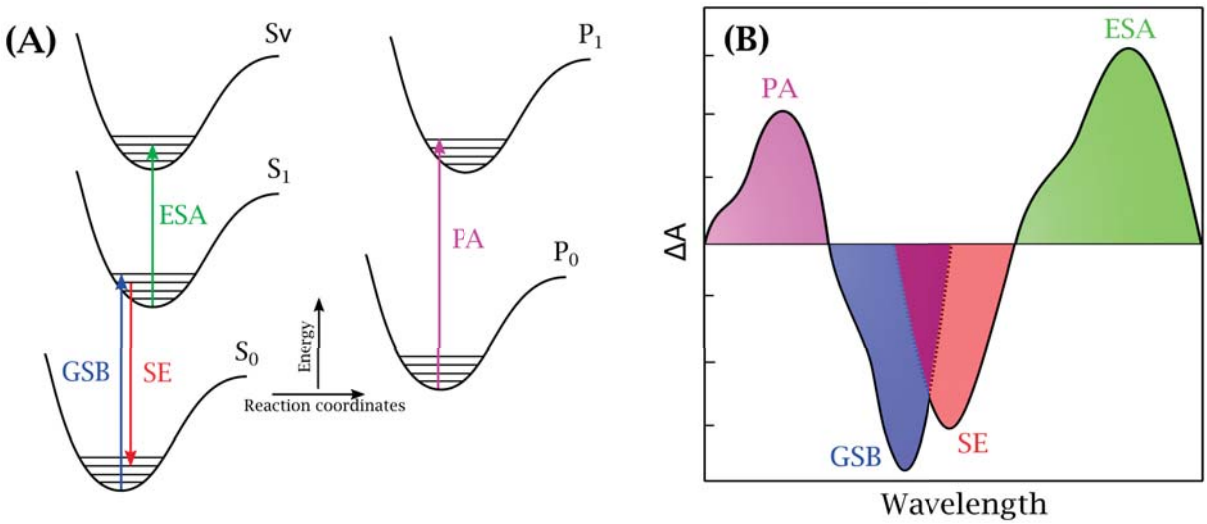

Figure 4.9: (A) Schematic illustration of the major electronic processes probed with TAS. (B) A stochastic representation of the different absorption (ΔA) spectra reflecting the different photophysical processes of Ground State Bleach (GSB), Stimulate Emission (SE), Excited-State Absorption (ESA) and Photo-product Absorption (PA).

pyrrolocyanines dyes that we study for the DSSC applications, the SE spectrally overlaps partially with the GSB and therefore for analytical studies of the kinetic components of the fluorescence, additional measurements were performed with FLUPS. Final spectral component is the PA that generally refers to the formation of new species, usually long lived, such as isomerized dyes or the formation of dye radicals, for instance due to oxi-

dation or protonation and is expressed as a positive signal. It is of great importance to highlight that in operational DSSCs after efficient photo-injection the sensitizer is left in the cationic form and the formation of the new species follows the evolution of the PA in the TAS spectra.

4.6 Data analysis

The experimental results obtained either by the Streak Camera, or by the TAS and FLUPS techniques, are usually treated and analyzed in both qualitative and quantitative ways. In the following sections the fitting functions that describe best our measurements are presented, as well as the data background subtraction and correction methods.

4.6.1 Background and artifact corrections

Non-linear spectroscopic techniques, such as Transient Absorption and Fluorescence Up-conversion, involve two laser beams, therefore there is interaction of two electric fields at different (or the same) frequencies in the material and their operation principle is based on $\chi^{(2)}$, $\chi^{(3)}$, respectively. Therefore and based on the fact that many phenomena can occur due to the higher order polarizations, various additional signals called "artifacts" can appear in the experimental data. However, these processes require temporal overlap and thus they usually appear near the "time zero" of the experimental data. At longer delay times usually only the dynamic mechanisms preserve and the characterization and corrections for these artifact signals will be described later in this chapter.

Artifacts don't carry any physical meaning or useful information. For this manner it is essential to correct for these processes, in order to clarify the "useful" data. The artifacts correction is of significant importance mainly for the TAS results. The main artifacts reported are the Cross-Phase Modulation (XPM), Two-Photon Absorption (TPA) and Stimulated-Raman amplification (SRA) [22].

The high power pump beam excites the sample and induces a temporal change in the refractive index of the cuvette walls or the solvent itself for liquid samples, or the glass part for a DSSC, across the excitation length. Subsequently, the probe light goes through the same path and its phase is modulated by the induced change of the refractive index based on optical Kerr effect. The modification of the signal occurs around time zero, when there is temporal overlap between the two pulses and it is defined as XPM. By its

turn TA can occur when high pump energies are used and depending on the cross section for TPA both pump and probe photons, it can be simultaneously absorbed resulting in a signal higher than the $S_0 - S_1$ absorption energy (UV-VIS). Finally, SRA can occur when the pump wavelength is close to the probe resulting in a sudden increase of ΔOD at solvent-specific wavelengths.

Another standard and important step of data analysis, necessary for both FLUPS and TAS is the background subtraction. In the current section both the "raw" data graphs and the main data-"filtering" algorithmic steps are presented.

- **Background subtraction**

The first step for data analysis for both set-ups is the background subtraction. The increased background level could refer to dark noise and by adjusting the electronic gain it can be amplified or reduced. By averaging the ΔA in negative times for each wavelength and consequently subtracting the mean value for all time-points in the data set (for each wavelength), the background level is corrected to match the offset level 0. For the case of TAS, there is also the solvent's response that must be subtracted, referring to the XPM signal in times $< 100\ fs$ around time-zero. Therefore, in addition to the main data-set we measure just the solvent maintaining the same experimental conditions (cuvette's thickness e.t.c). The subtraction is based on the formula: $\Delta A(\lambda,t)_{final} = \Delta A(\lambda,t)_{measured} - a\Delta A(\lambda,t)_{solvent}$ that includes the dark-noise background subtracted data-sets and the parameter α that is adjusted from 0 to 1 for the best match of the XPM signals to subtract. For the DSSC samples, due to the shift in position between the two samples (the complete and the "empty" DSSCs in absence of sensitizer), the correction for the glass response is difficult to be made. Therefore, α is set to zero and to fit the experimental data, when XPM is present, we introduce in the fitting function (section 4.6.2) a correction for Gaussian signals (IRF).

- **Chirp correction**

Another undesirable effect present in the TAS data is the Group-Velocity-Dispersion (GVD) that temporally shifts the measured ΔA signal at early times (<0.6 ps) with "red" wavelengths arriving faster than the "blue" (chirp). GVD is especially pronounced when fs-pulses propagate through materials (lens, cuvette, glass substrate e.t.c) and originates from the dependence of the group velocity (v_g) $(\frac{\partial k}{\partial \omega})^{-1}$ of light on the wavelength as: $GVD = \frac{\partial}{\partial \omega}(\frac{1}{\partial v_g}) = \frac{\partial^2 k}{\partial \omega^2}$. The background and solvent response corrections, as well as the correction for the chirp is made with a Python code and the latter are made by

fitting the chirp with a polynomial function around time zero. In Figure 4.10, the 2D maps of ΔA for the initial (A) and chirp-corrected (C) data are demonstrated, as well as the time profiles of XPM for three different wavelengths for the corresponding cases (B) and (C), respectively. The pronounced chirp of 300 fs in just 50 nm (from 530-580 nm in Figure 4.10.B) is mostly due to the thick (3 mm) glass substrate of the sample that is used for the DSSC assembly. For the solution studies in this Thesis, a flow cell was used with ultra-thin walls of 0.5 mm. Finally, in Figure 4.10 only the spectral region

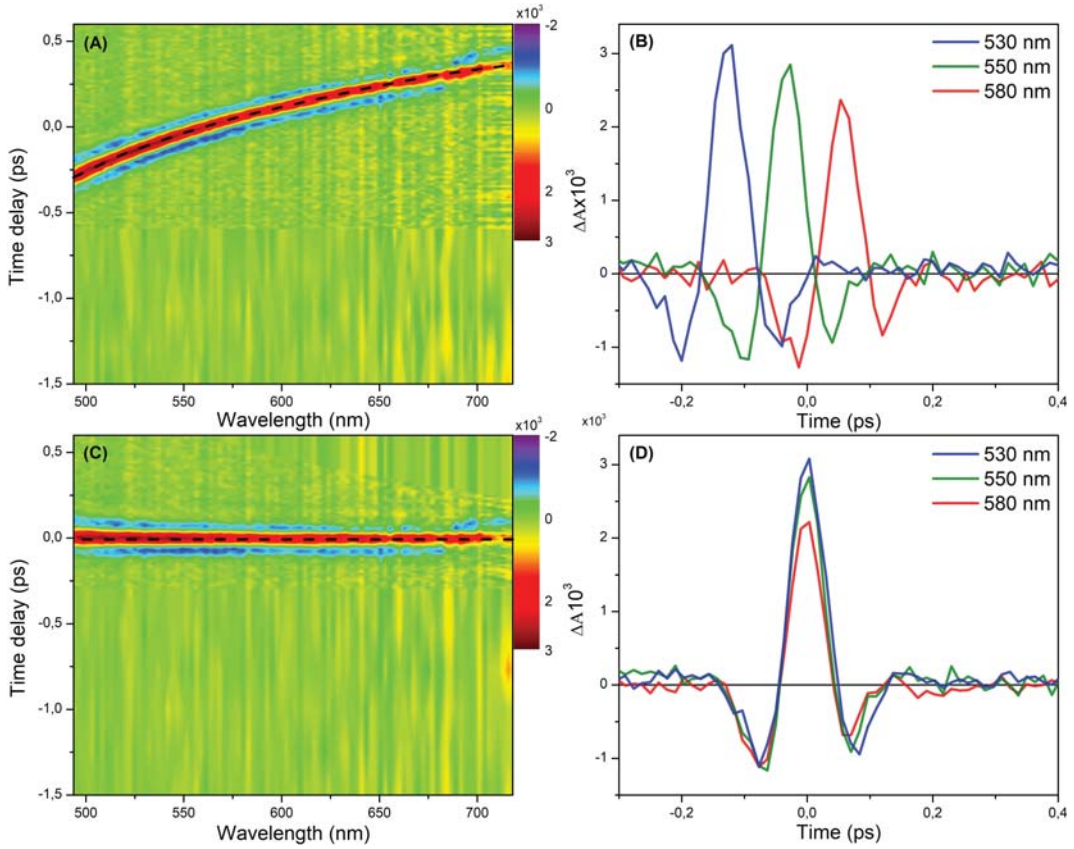

Figure 4.10: Transient absorption data, with excitation at 800 nm, of a 3 mm glass coated with a 3-4 μm TiO_2 nanoparticles layer used as anode for DSSC devices. (A) The 2D map (time-wavelength) of ΔA with no chirp correction. (B) The temporal profile of the XPM signal in the non-chirp corrected data at three different wavelengths (530 nm, 550 nm and 580 nm). Due to GVD the short wavelength components arrive later than the long ones. (C) The 2D map (time-wavelength) of ΔA after chirp correction (D) The temporal profiles of the XPM signal in the chirp corrected data at three different wavelengths (530 nm, 550 nm and 580 nm).

450-750 nm is shown, restricted by the spectrometer's bandwidth and for the present studies additional measurements, in the near IR region (700-1030 nm), have been made. The above mentioned corrections have been made for both data-sets (visible and near-IR

spectral regions) and finally they have been spectrally combined resulting in the final data.

4.6.2 Fitting functions

In this section the basic fitting functions that are applied on the experimental results, in the framework of the current project, are presented. The fitting functions are assigned to single wavelength analysis and the global approach is presented in section 4.6.3, as well as the closely connected spectro-temporal profile analysis.

For the fluorescence decay fittings, obtained by the streak-camera or FLUPS techniques, in the simpler case in solution, the decay reflects only the deactivation from the first excited singlet state (S_1) to the ground state (S_0). Therefore, the time evolution of the concentration (C) of the excited state population can be derived from the first order rate equation as:

$$\frac{dC(t)}{dt} = -k \times C(t) \tag{4.9}$$

where k the decay rate. The solution of this equation is:

$$C(t) = C_{S1} e^{(-kt)} \tag{4.10}$$

where C_{S1} is the concentration of the molecules that have been excited to the S_1 state. It was shown in Equation 3.3 that the intensity of the fluorescence is proportional to the concentration of the excited dyes. Therefore, from equation 4.10 the intensity of the fluorescence decay follows an exponential decrease. In more complicated systems, in which multiple processes occur, or when there are many species with different dynamics, the average fluorescence decay can be expressed as a multi-exponential decay function:

$$I(t) = \sum_{i=1} A_i e^{\frac{-t}{\tau_i}} \tag{4.11}$$

where i is the number of mechanisms or species involved in the measured fluorescence, Ai the corresponding contribution of this mechanism or species to the overall average fluorescence decay and τ_i the corresponding lifetime.

For all experiments the temporal resolution is limited by the Instrument's Response Function (IRF), which in a good approximation is supposed to be a Gaussian function of standard deviation σ and zero offset (for the Gaussian centroid). Therefore the fitting function for single wavelength kinetic analysis is expressed as a convolution of the

Equation 4.11 with the IRF (Gaussian) function as:

$$I(t) = \sum_{i=1} A_i e^{\frac{-t}{\tau_i}} \circledast \frac{1}{\sigma\sqrt{2\pi}} e^{-\frac{t^2}{2\sigma^2}} \tag{4.12}$$

The solution of equation 4.12 for a decay starting from an initial time t_0 gives the analytical form of the function, which is used for the single wavelength kinetic fittings as:

$$I(t) = A_0 + \sum_{i=1} \frac{A_i}{2} exp(\frac{\sigma^2}{2\tau_i^2}) exp(-\frac{t-t_0}{\tau_i})[1 + erf(\frac{t-t_0-\sigma^2/\tau_i}{\sigma\sqrt{2}})] \tag{4.13}$$

where A_0 is a possible offset and erf the error function.

The above defined fitting function has been implemented in the OriginPro2021 software and it is used for Streak camera, FLUPS and TAS data analysis, when only a single wavelength kinetic fitting was needed. The fitting algorithm proceeds with target criterion to reduce the parameter χ^2 that determines the quality of the fit and it is defined as:

$$\chi^2 = \int |I_{exp}(t_i) - I_{fit}(t_i)|\, dt \tag{4.14}$$

where, $I_{exp}(t_i)$ the experimental data and $I_{fit}(t_i)$ the fitting data. The kinetic difference defines the fitting residuals.

For the study of DSSCs, in various works another mathematical approach, as fitting model, has been proposed using the Stretched exponential or Kohlrausch function [23–26]. When the different decay times τ_i have very similar values, or they follow a distribution function, equation 4.11 is approximated by:

$$I(t) = Ae^{(\frac{-t}{\tau})^\beta} \tag{4.15}$$

where β is the inhomogeneity or stretch parameter taking values $0 \leq \beta \leq 1$, with $\beta = 1$ the standard multi-exponential case.

In the solid-state samples, such as the DSSCs the reasoning behind the introduction of the β parameter lies the inhomogeneity of the samples' active area. Specifically, on a microscopical level the dyes are chemically adsorbed onto the SC's surface in high concentrations and this can stretch the overall measured fluorescence decay due to two reasons. Firstly, electron injection from the dyes to the SC is strongly affected by the dye-to-SC distance and secondly, when molecular aggregates are formed on the SC surface in a distribution of intermolecular distances. Analytically, distribution of distances (nm) between neighbour dyes, or the existence of weakly attached dyes on the surface

with lower injection yield, results in a distribution of driving forces for injection due to different configurations. This can lead to temporal stretch of the injection and FRET times, resulting in an overall stretched fluorescence decay. The above mentioned kind of approach simplifies the analysis by reducing the total number of lifetimes, obtained from the fitting and facilitates the interpretation having at the same time physical meaning.

4.6.3 Global and spectro-temporal analysis

A different approach for obtaining the lifetimes of the various mechanisms is the Global analysis. In broadband experiments such as TA it is convenient and straightforward to apply on the experimental data. Global analysis assumes that the system is described by a limited set of rates or decay times so that all spectral features and kinetics traces can be described by the same lifetimes τ_i. Then equation 4.11 can be re-written as:

$$\Delta A(\lambda, t) = \sum_{i=1}^{N} A_i(\lambda) e^{\frac{-t}{\tau_i}} \tag{4.16}$$

where the intensity is replaced by the ΔA. Essentially, Global fit results in N time constants that fit optimal (reduced χ^2) the kinetic curves for each wavelength in the ΔA spectral map. It is important to highlight that for the aforementioned analysis the number of the fits would be equal to the number of the channels e.g. 134 in our case. The global fitting would then take more than 1 h on a modern pc. To facilitate the fits procedure only the major kinetic contributions are chosen and in this way the noisy data are filtered out. To achieve the noise filtering, by weighting the "important" kinetic contributions, a mathematical operation is used named Singular Value Decomposition (SVD), which is essentially a matrix factorization technique [27–29]. The experimental data-set is represented as a 2D matrix $M_{m,n}$ as a set of wavelength and time. The SVD analysis decomposes the data matrix in three separate matrices as:

$$M_{m,n}(\lambda, t) = U_{mm}(\lambda) S_{m,n} V^T_{n,n}(t) \tag{4.17}$$

where $U_{mm}(\lambda)$ is a (mxm) matrix containing the wavelength singular vectors (left singular vectors) as columns and $V^T_{n,n}$ is the transposed V matrix containing the temporal singular vectors (right singular vectors) as rows. Moreover, the kinetic traces in V matrices form orthogonal bases and $S_{m,n}$ is a diagonal matrix $(m \times n)$ with values of decreasing order, named Singular values (SVs). The SVs constitute the weighty factors of the high signal

data and the remaining ones represent the noise contaminated data. By plotting the left and right singular vectors for specific SVs and by evaluating the quality of the plotted profiles, the necessary number of SVs can be chosen. Then, by selections of relevant SVs, the number of fits minimizes, since it is equal to the number of equal SVs. Only these restricted number of kinetic traces in $V_{n,n}(t)$ is then fitted globally according to eq. 4.16.

In various cases, it is advantageous to plot the spectral response of the system for the given time constants obtained by Global Analysis. This spectral response is correlated with the Decay Associated Difference Spectra (DADS) and it can be calculated as:

$$DADS_i(\lambda) = \sum_{s=1}^{K} \sum_{i=1}^{N} A_{s,i} U_s(\lambda) \tag{4.18}$$

where, $A_{s,i}$ is the pre-exponential factor related to the time constant τ_i in the kinetic trace U_S for the SVs, with k the number of significant SVs. In a different writing, equation 4.16 can be expressed as:

$$\Delta A(\lambda, t) = \sum_{i=1} DADS_i(\lambda) e^{\frac{-t}{\tau_i}} \tag{4.19}$$

where the pre-exponential factor refers to the DADS(λ). It is of interest to mention that the pre-exponential factor, which was initially expressed in equation 4.11 and adapted for Global analysis in equation 4.16, originates from the solution of the first order concentration equation (eq. 4.9, 4.10). The DADS refer to parallel decay of all excited species, since every lifetime is a distinct decay process, monitoring spectrally only the increasing and decreasing of the populations probed at a given wavelength. Thus, the DADS analysis constitutes a first approach and without necessarily a priori knowledge of the photophysical reaction scheme.

Interestingly, a different approach can be applied, in which a sequential decay model [30] is assumed, where the decay from the first state gives rise to the population of a second state (Figure 4.11.B). For the sequential model the concentration evolution can be described by the following equations, in which we assume a total population C_{total}, from which a portion C_1 is in the S_1 state and C_0 is the population in the ground state. After excitation, $C1$ decays into the state S_1' with rate $k_{11'}$. The population of $S_1^{'}$, C_2,

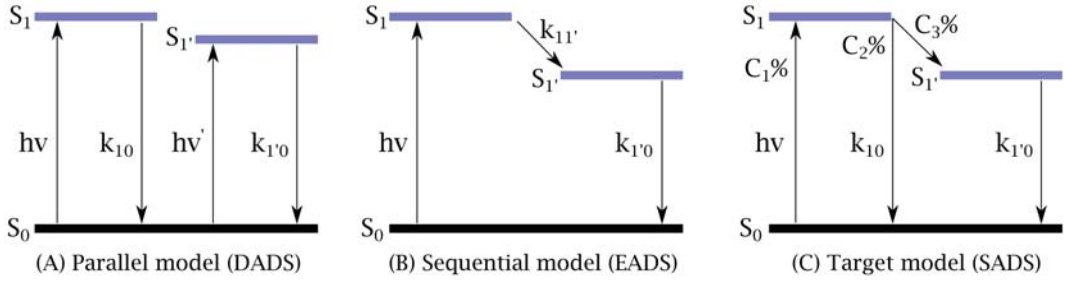

Figure 4.11: Energy levels and corresponding excitation and reaction pathways described by a: (A) Parallel (B) Sequential and (C) Target model.

decays back to S_O with the rate $k_{1'_0}$. Analytically, from solving the equations,

$$\begin{aligned} &\frac{dC_1(t)}{dt} = -k_{11'} \cdot C_1(t), \ \frac{dC_2(t)}{dt} = -k_{1'0} \cdot C_2(t) + k_{11'} \cdot C_1(t) \\ &\sum_{i=0}^{2} C_i(t) = C_{total} \Longrightarrow C_0(t) = C_{total} - C_1(t) - C_2(t) \end{aligned} \tag{4.20}$$

the time-dependent concentrations are:

$$\begin{aligned} C_1(t) &= C_1(0) \cdot e^{-k_{11'}}, \\ C_2(t) &= \frac{C_1(0) \cdot k_{11'}}{k_{11'} - k_{1'0}} \cdot (e^{-k_{1'0}} - e^{-k_{11'}}) \\ C_0(t) &= \frac{C_1(0)}{k'_{11} - k_{1'0}} \cdot (k_{1'0} \cdot e^{-k_{11'}} - k'_{11} e^{-k_{1'0}}) + C_{total} \end{aligned} \tag{4.21}$$

From Beer-Lambert law and considering 1 cm sample thickness, the $\Delta A(\lambda, t) = A(\lambda, t) - A_0(\lambda)$ signal can been easily obtained as:

$$\begin{aligned} \Delta A(\lambda, t) = \Big(C_1() \cdot \varepsilon_1(\lambda) - \frac{C_1(0) \cdot k_{11'}}{k_{11'} - k_{1'0}} \cdot \varepsilon_2(\lambda) + \frac{C_1(0) \cdot k_{1'0}}{k_{11'} - k_{1'0}} \cdot \varepsilon_0(\lambda)\Big) \cdot e^{-k_{11'} \cdot t} + \\ \Big(\frac{C_1(0) \cdot k_{11'}}{k_{11'} - k_{1'0}} \cdot \varepsilon_2(\lambda) - \frac{C_1(0) \cdot k_{11'}}{k_{11'} - k_{1'0}} \cdot \varepsilon_0(\lambda)\Big) \cdot e^{-k_{1'0} \cdot t} \end{aligned} \tag{4.22}$$

An important observation can been made that ΔA is again expressed as a sum of exponential decays resulting in the same time constants obtained by Global fit, but with different pre-exponential amplitudes (EADS).

$$\Delta A(\lambda, t) = \sum_{i=1} EADS_i(\lambda) e^{\frac{-t}{\tau_i}} \tag{4.23}$$

Finally, one may compute the Species Associated Difference Spectra (SADS) that reflect the spectral behavior of the various species or states (monomers, aggregates or oxidized molecules) evolving with different time constants [31]. They are found based on a target analysis model (Figure 4.11), which can be considered as a generalization of the sequential model. A disadvantage of the method is that a priori knowledge about the photophysical reaction scheme is necessary. When the transition pathways, as well as the percentage of the excited populations are guessed, the kinetic model can be computed (in a similar manner as in equation 4.22) resulting in new pre-exponential factors that are primarily a linear combination of DADS or EADS.

$$\Delta A(\lambda, t) = \sum_{i=1} SADS_i(\lambda) e^{\frac{-t}{\tau_i}} \tag{4.24}$$

The decision of the model applied to the experimental data is not always straightforward and must be made carefully, taking into consideration the fitting residuals, as well as the physical explanation of the calculated Associated Difference Spectra. The software used for the Global analysis, calculation and plot of the DADS, EADS or SADS is Glotaran [27].

4.6.4 Sample preparation

In the current PhD Thesis, the samples under study were either in solution phase, or in the form of complete DSSC prototype devices. For the liquid-phase studies, solutions of low concentration were prepared ($3 - 5 \times 10^{-5}$ M) to avoid re-absorption phenomena, as well as transmission saturation for the TAS measurements. Thus, the OD/mm was kept between 0.15-0.55/mm.

The major components of the DSSC are the anode, the cathode that both undergo characteristic treatment before use, the electrolyte and the dye. Starting with the photoanode, it consists of a TEC11 type conductive glass coated with a fluorine doped tin oxide (FTO) layer. The glass is cleaned via baths of detergent solution, ethanol and at last by gradual heating in a specific program (up to 450^o C). Then, the anode undergoes $TiCl_4$ treatment (40 $mmol/L TiCl_4$ solution) in 70 ^oC for 30 min, which is a classic pre- and post-treatment for nanocrystalline TiO_2 films, which drastically enhances the SC adhesion and reduces the interfacial recombination with the I_3^- in the electrolyte. The next step is the screen printing using a commercial TiO_2 paste (e.g. Solaronix). For the samples that were studied in this Thesis, the DSSCs' anodes contained only one coated

layer of transparent nano-sized nanoparticles (20 nm diameter) of 3-4 mm thickness. The thickness were examined with a profilometer, which has similar operation as the AFM (Atomic Force Microscopy). Finally, after screen printing a second $TiCl_4$ treatment is made and the anode undergoes a final gradual heating process to be purified by evaporating the water and the paste additives.

Concerning the cathode glass treatment, we use a TEC7 type of conductive glass, similarly coated with a fluorine doped tin oxide (FTO) layer. We use pieces of 1.7-2 cm x 1.2-1.8 cm glasses, depending on the active area of the anode that we prepare. The electrolyte is injected from the cathode after the assembly of the DSSC, thus we drill one or two 1 mm holes in the cathode either via conventional mechanical drilling or via the sand-blasting technique. The glasses then undergo ethanol/acetonitrile cleaning via sonication and before the assembly, another platinum (Pt) treatment (H_2PtCl_6) and heating at 410 ^oC for 15 min has been made. The Pt nanoparticles act as electro-catalysts and in this manner they increase the cathode roughness, resulting in the decrease of the charge transfer resistance. In our studies, we focus on the ultrafast photophysical studies of the DSSCs, concerning mechanisms occurring faster than a ns, such as electron injection and therefore the platinum treatment wasn't necessary to be made.

The electrolytes used were nitrile based (acetonitrile or 85/15 acetonitrile/valenonitrile) containing 1 M LiI (lithium iodide), 1 M $DMII$ (1,3-dimethylimidazole iodide) and 0.3 M I_2 (iodine) additives. These parameters refer to the standard DSSC conditions that were found after thorough optimization to give the best photovoltaic performances (W.Naim-LRCS laboratory). It is important to highlight that in the following chapter an electrolyte study is demonstrated, examining the effect of LiI on the electron injection dynamics and efficiency. For this purpose, different electrolytes of increasing LiI concentration are used. The anode and cathode glass plates and electrolyte solutions are made by our partners in Amiens (W. Naim, T. Alnasser, F. Sauvage). In Strasbourg, we made the final dyeing of the anode and the full assembly of the DSSCs, including the electrolyte incorporation.

The DSSC device assembly procedure is described in the following (Figure 4.12). The anode glass is heated at $350 - 500$ ^oC (depending on the SC material) and dipped overnight (15-17 h) in a solution dye bath of very high concentration (10^{-4} M), near the concentration saturation limit. After the dye-loading period, the anode is removed from the bath-solution and cleaned with ethanol, in order to wash away possible non-attached dyes on the surface. A transparent Surlyn polymer (25 μm thickness), cut as an open square to cover the peripheral sites of the anode's active area, is placed between the an-

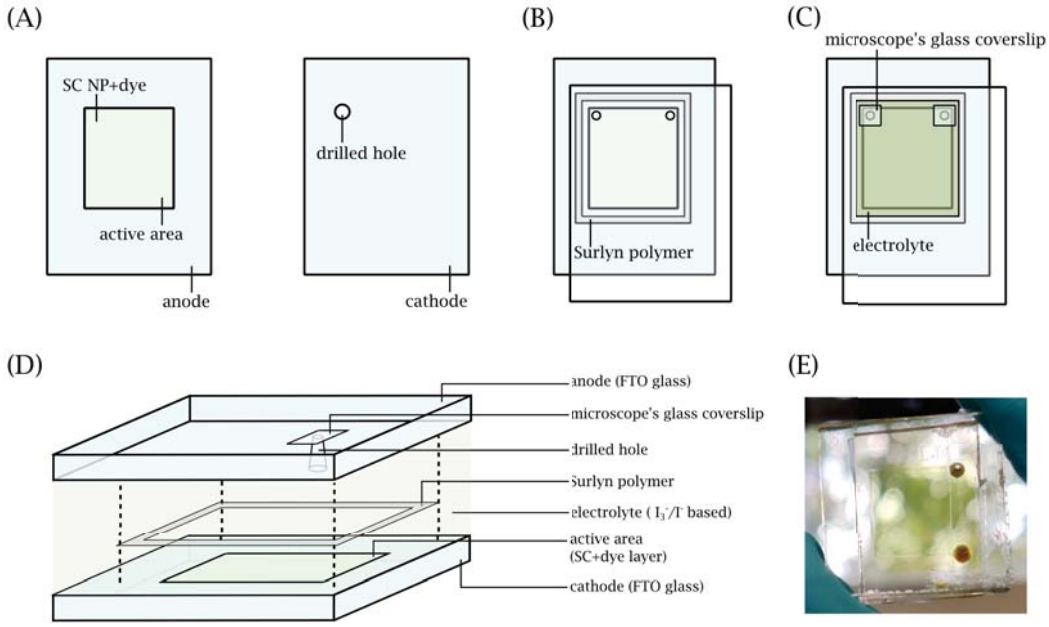

Figure 4.12: A schematic illustration (A) of the anode and cathode DSSC counterparts, (B) of an assembled DSSC without electrolyte and (C) sealed with the electrolyte. (D) The corresponding exploded axonometric and (E) a picture of a real semi-transparent DSSC.

ode and the cathode. When heated above 130 ^oC the Surlyn film melts. Hence, the film fulfills the double purpose of both gluing the two glasses and containing the electrolyte. It is critical that the Surlyn films melt well and hermetically close the interstitial space between the electrodes. Otherwise the electrolyte, to be added in the next step, might spill out, or evaporate overnight. The electrolyte is injected through the capillary holes using the vacuum back-filling technique. After the electrolyte injection the holes are sealed with additional Surlyn polymer, which is melted and covered by thin slip glasses used for microscopy. To ensure better long-run stability, the DSSC edges were additionally sealed with a dispersed two component glue, containing the epoxy resin Amosil 4 (Solaronix).

References

[1] E. Vauthey, "Introduction to nonlinear optical spectroscopic techniques for investigating ultrafast processes," *Lectures of Virtual European University on Lasers*, 2006.

[2] J. Shah, "Ultrafast luminescence spectroscopy using sum frequency generation," *IEEE Journal of Quantum Electronics*, vol. 24, no. 2, pp. 276–288, 1988.

[3] H. Rhee and T. Joo, "Noncollinear phase matching in fluorescence upconversion," *Optics letters*, vol. 30, no. 1, pp. 96–98, 2005.

[4] L. Zhao, J. L. P. Lustres, V. Farztdinov, and N. P. Ernsting, "Femtosecond fluorescence spectroscopy by upconversion with tilted gate pulses," *Physical Chemistry Chemical Physics*, vol. 7, no. 8, pp. 1716–1725, 2005.

[5] M. Gerecke, G. Bierhance, M. Gutmann, N. P. Ernsting, and A. Rosspeintner, "Femtosecond broadband fluorescence upconversion spectroscopy: Spectral coverage versus efficiency," *Review of Scientific Instruments*, vol. 87, no. 5, p. 053 115, 2016.

[6] H. Chosrowjan, S. Taniguchi, and F. Tanaka, "Ultrafast fluorescence upconversion technique and its applications to proteins," *The FEBS journal*, vol. 282, no. 16, pp. 3003–3015, 2015.

[7] R. Berera, R. van Grondelle, and J. T. Kennis, "Ultrafast transient absorption spectroscopy: Principles and application to photosynthetic systems," *Photosynthesis research*, vol. 101, no. 2, pp. 105–118, 2009.

[8] S. Uhlig, *Self-organized surface structures with ultrafast white-light: First investigation of LIPSS with supercontinuum*. Springer, 2015.

[9] R. R. Alfano, *The supercontinuum laser source: the ultimate white light*. Springer, 2016.

[10] M. Bradler, P. Baum, and E. Riedle, "Femtosecond continuum generation in bulk laser host materials with sub-μj pump pulses," *Applied Physics B*, vol. 97, no. 3, pp. 561–574, 2009.

[11] A. Brodeur and S. Chin, "Ultrafast white-light continuum generation and self-focusing in transparent condensed media," *JOSA B*, vol. 16, no. 4, pp. 637–650, 1999.

[12] G. Cerullo and S. De Silvestri, "Ultrafast optical parametric amplifiers," *Review of scientific instruments*, vol. 74, no. 1, pp. 1–18, 2003.

[13] C. Manzoni and G. Cerullo, "Design criteria for ultrafast optical parametric amplifiers," *Journal of Optics*, vol. 18, no. 10, p. 103 501, 2016.

[14] E. Riedle *et al.*, "Generation of 10 to 50 fs pulses tunable through all of the visible and the nir," *Applied Physics B*, vol. 71, no. 3, pp. 457–465, 2000.

[15] J. Nillon, O. Crégut, C. Bressler, and S. Haacke, "Two mhz tunable non collinear optical parametric amplifiers with pulse durations down to 6 fs," *Optics express*, vol. 22, no. 12, pp. 14 964–14 974, 2014.

[16] Hamamatsu. "Guide to streak cameras." (2008), [Online]. Available: `https://www.hamamatsu.com/resources/pdf/sys/SHSS0006E_STREAK.pdf` (visited on 11/04/2021).

[17] V. Wlotzko, W. Uhring, and P. Summ, "Impact of laser phase and amplitude noises on streak camera temporal resolution," *Review of Scientific Instruments*, vol. 86, no. 9, p. 094 703, 2015.

[18] G. Zgrablic, "Solvent effects on the ultrafast dynamics of the retinal chromophore of bacteriorhodopsin," Ph.D. dissertation, École Polytechnique Fédérale de Lausanne, 2006.

[19] W. T. Pollard, S.-Y. Lee, and R. A. Mathies, "Wave packet theory of dynamic absorption spectra in femtosecond pump–probe experiments," *The Journal of chemical physics*, vol. 92, no. 7, pp. 4012–4029, 1990.

[20] A. Tokmakoff, *Lecture notes in non-linear spectroscopy*, Apr. 2008.

[21] W. Naim *et al.*, "Transparent and colorless dye-sensitized solar cells exceeding 75% average visible transmittance," *Jacs Au*, vol. 1, no. 4, pp. 409–426, 2021.

[22] M. Lorenc, M. Ziolek, R. Naskrecki, J. Karolczak, J. Kubicki, and A. Maciejewski, "Artifacts in femtosecond transient absorption spectroscopy," *Applied Physics B*, vol. 74, no. 1, pp. 19–27, 2002.

[23] S. E. Koops, B. C. O'Regan, P. R. Barnes, and J. R. Durrant, "Parameters influencing the efficiency of electron injection in dye-sensitized solar cells," *Journal of the American Chemical Society*, vol. 131, no. 13, pp. 4808–4818, 2009.

[24] A. Listorti *et al.*, "The mechanism behind the beneficial effect of light soaking on injection efficiency and photocurrent in dye sensitized solar cells," *Energy & Environmental Science*, vol. 4, no. 9, pp. 3494–3501, 2011.

[25] J. Navas, R. Alcántara, C. Fernández-Lorenzo, and J. Martın-Calleja, "Evaluation of decay photocurrent measurements in dye-sensitized solar cells: Application to laser beam-induced current technique," *International journal of energy research*, vol. 36, no. 2, pp. 193–203, 2012.

[26] K. B. Lee *et al.*, "Application of the stretched exponential function to fluorescence lifetime imaging," *Biophysical journal*, vol. 81, no. 3, pp. 1265–1274, 2001.

[27] J. J. Snellenburg, S. P. Laptenok, R. Seger, K. M. Mullen, and I. H. van Stokkum, "Glotaran: A java-based graphical user interface for the r package timp," 2012.

[28] W.-G. Chen and M. S. Braiman, "Kinetic analysis of time-resolved infrared difference spectra of the l and m intermediates of bacteriorhodopsin," *Photochemistry and photobiology*, vol. 54, no. 6, pp. 905–910, 1991.

[29] I. H. van Stokkum, D. S. Larsen, and R. Van Grondelle, "Global and target analysis of time-resolved spectra," *Biochimica et Biophysica Acta (BBA)-Bioenergetics*, vol. 1657, no. 2-3, pp. 82–104, 2004.

[30] J. E. Loefroth, "Time-resolved emission spectra, decay-associated spectra, and species-associated spectra," *The Journal of Physical Chemistry*, vol. 90, no. 6, pp. 1160–1168, 1986.

[31] A. Ghosh, S. Ghosh, G. Ghosh, B. Jana, and A. Patra, "Global and target analysis of relaxation processes of the collapsed state of p3ht polymer nanoparticles," *Physical Chemistry Chemical Physics*, vol. 22, no. 4, pp. 2229–2237, 2020.

Chapter 5

Experimental results

In the present chapter the experimental results and findings of the PhD research are demonstrated within the collaborative ANR project VISION-NIR (coordinator F. Sauvage). The general aim is the construction of real-world and efficient DSSC devices, transparent or semi-transparent, suitable for low-intensity indoor applications. Three appealing candidates, as dye-sensitizers, are presented and a detailed study has been made, not only in basic solution phase, but when they are incorporated in complete devices too. Considering the fact that the most crucial parameter for achieving high Power-Conversion-Efficiencies (PCE), is the electron injection from the dye to the semiconductor, ultrafast spectroscopy has been performed, resulting not only in identifying the injection times and efficiency, but the additional loss channels too. The construction of the photophysical model, defined in the dye-sensitized system, is of great significance, in order to understand the PCE-AVT limitations and therefore improve the dye synthesis performed by the project partners. One of the advantages of DSSCs, compared with other photovoltaic devices, is the option for easy modifications of the dye and therefore the tuning of its optical properties.

5.1 Dye molecules under investigation

There are numerous near-IR dyes suitable for transparent DSSC applications. The major categories were briefly mentioned in the 2.2.3 section. For the studies regarding this Thesis we have investigated three dyes with the code names **VG20-C16** (or just **VG20**), **TB207** and **TB423**. When **VG20** stands out by itself in this study, **TB207** and **TB423** are closely related, by belonging to the same dye category. Thus, they are

analyzed in the second part of the experimental studies of this Chapter. **TB423** owns identical structure with **TB207**, except the side group that is bulkier and a single carboxylic group.

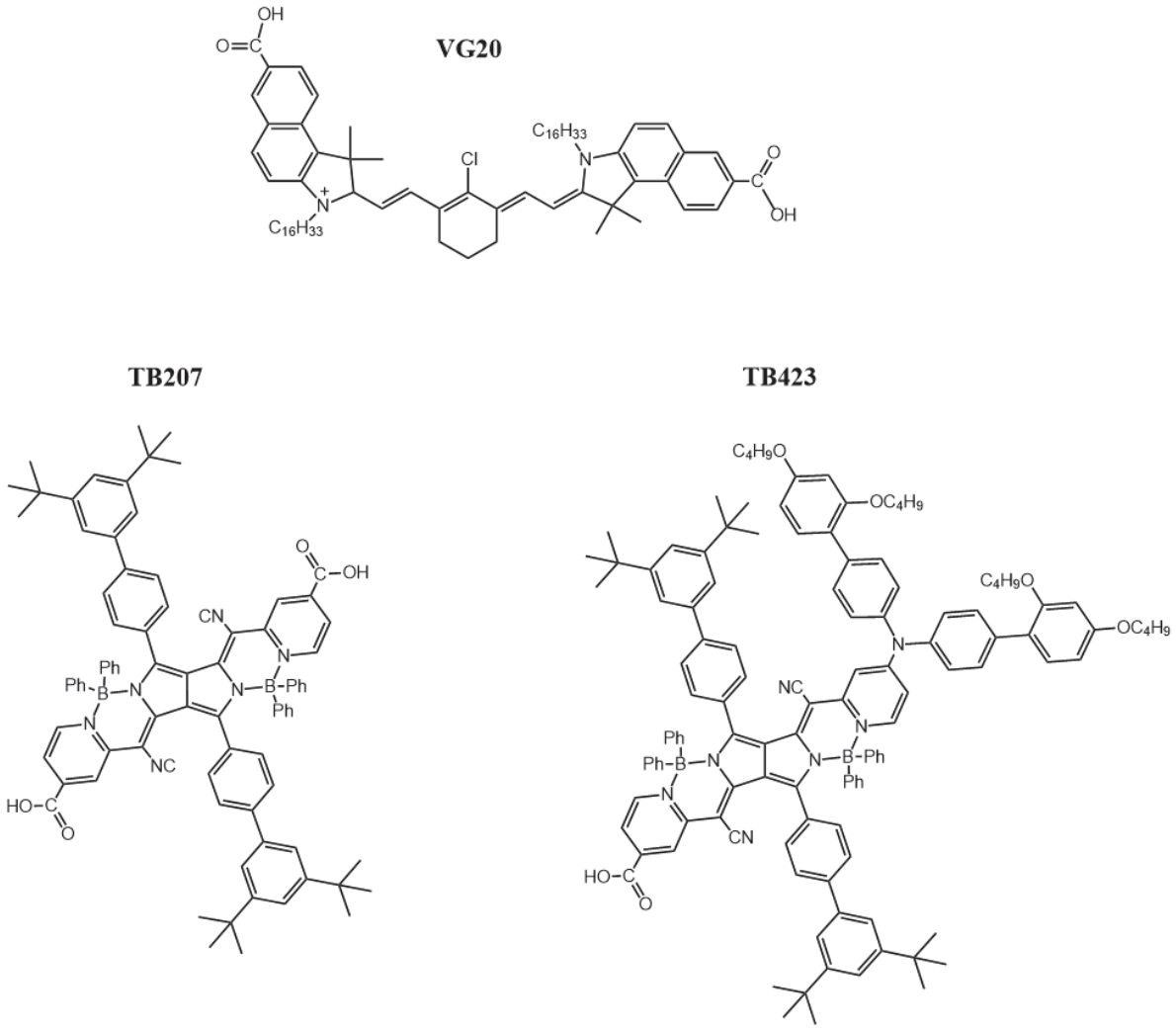

Figure 5.1: Chemical structures of the molecules under study with the code names **VG20**, **TB207** and **TB423**.

The chemical structure of **VG20**, is presented in Figure 5.1 (top). **VG20** was synthesized by the group of Claudia Barolo at the University of Torino and the analytical syntheses procedure has been described elsewhere [1]. It is an updated version of the **VG** series of dyes that had a central squaric group, with **VG1** to demonstrate PCE of 4.7 %, but with the absorption peaking at 644 nm [2, 3]. For further absorption shift towards the near-IR and inspired by the seminal work of Arakawa et al. [4] the symmetric **VG20** cyanine dye was synthesized. The novelty of the dye is the position of the anchoring groups and the length of the side hydrocarbon side chains. In more detail, **VG20** belongs to

the category of long polymethine chain dyes and specifically the heptamethines. The extended length of the chain with the addition of a chlorocyclohexenyl in the center, greatly shifts the absorption in the near-IR. The chlorocyclohexenyl, with the cloride atom to be in the meso-position of the ring, enhances the electron withdrawing efficiency through the chain, whose absorption is essentially associated with the length of the π-conjugation. In addition, this alicyclic ring further enhances the thermal and photochemical stability in cyanine dyes [3]. In addition, it has been shown that the benzoindolenine contributes to further absorption red-shift. The introduction of two carboxylic (-COOH) anchoring groups at the sides, along the long axis of the dye, ensures efficient dye loading on the semiconductor (SC) surface, as well as, better overlap of the dye's LUMO with the conduction band (CB) of the SC. The final components of interest are the alkyl chains that have a decisive role in the photophysics of the dye and the total performance of the DSSC device [3]. **VG20** possesses a long alkyl chain, of C16 carbons that affects the planarity of the dye, in order to reduce the head-to-tail aggregate formation and increase the distance between neighboring dyes, weakening in general the electrostatic interaction that promotes the aggregate formation. It has been shown that aggregates are harmful not only for the photovoltaic performances, but for the AVT and the aesthetic assignment of the DSSCs, too. However, the chain's length effect is of great interest, as it has been demonstrated for an extension from C2 to C16. The absorption spectrum shifts by 6 nm by increasing the chain's length, without affecting greatly the position of the HOMO and LUMO and the excited state lifetime elongates by one order of magnitude, from C2 to C6 [1]. By increasing the alkyl chain's length the molar extinction coefficient of the dye also becomes higher and for the C16 configuration has been calculated to be $\varepsilon = 154'000 M^{-1} cm^{-1}$ in ethanol. Finally, the long excited state lifetime, the near-IR absorption with weak contributions from the visible part of the spectral region and the high molar extinction coefficient, makes **VG20-C16** a promising candidate for (semi)-transparent DSSC applications.

The second part, of the experimental section of the current PhD Thesis, is focused on the last two dyes with code names **TB207** and **TB423**, with their chemical structures illustrated in Figure B.1. Both **TB** dyes were synthesized by the group of F. Odobel at the CEISAM lab at the University of Nantes. They both belong to the sub-category of pyrrolopyrrole-cyanine dyes (PPCys) that was first reported by Daltrozzo et al. [5–7] and similarly to classic cyanines and pyrrolopyrrole dyes, their absorption maximum is shifted in the near-IR part of the spectrum ($>$ 700 nm). Starting with the symmetric **TB207** dye, the synthesis was based on a typical diketopyrrolopyrrole (DPP) core, offering sol-

ubility. Initially, during the synthesis, the uncomplexed pyridine core unit conjugates with the cyanine moiety and in another step is complexed with Boron (B) using BPh_2, leading to a red-shifted and narrow absorption band. In more detail, the introduction of the Phenyls (Ph_2), resulting in additional red-shift of the absorption, because Ph induces the reduction of the electron density of Boron (B). An analogous to **TB207**, initially prepared, TB dye with Fluorine (F) instead of Ph exhibited more blue-shifted and therefore visible absorption, as well as lower PCE efficiency and therefore, it is not reported here, but only to highlight the effect of Ph_2. It possible that the bulkier geometry of Ph_2, prevents in a degree the parallel aggregate formation and in general the non-linear dye structure, efficiently reduces the aggregates on the SC surface, in comparison to **VG20**. Interestingly, the carboxylic (-COOH) anchoring groups are added to the edges of the conjugated backbone of the dye and compared to its counterpart dye, without anchoring groups, the absorption is further bathochromically shifted by 27 nm. It is possible that the further electron withdrawing ability of the -COOH groups stabilizes the LUMO and offers better overlap with the CB of the SC, as well. TDFT calculations (Appendix A.1) showed that the HOMO is located at the central core of the dye and the LUMO extends further with contributions to the -COOH groups. As expected the initial soluble DPP part is "dull" to the electron density change, but the relative angle, in both HOMO and LUMO, of the middle benzene ring of the DPP body, creates a bulkier geometry preventing in addition the formation of H-aggregates. In general, the TB dye-series of the novel PPCys category, were inspired to prevent aggregate formation (as it is considered a drawback [1]), allowing efficient charge separation, upon excitation, for injection and at the same time, maintaining the advantageous characteristics of strong absorption in the near-IR and long excited state lifetimes.

As it is shown in the following section, aggregates are still present for **TB207**. Therefore, another dye is proposed based on **TB207** with the code name **TB423**. **TB423** is the non-symmetric version of **TB207**, with only one -COOH group and in the position of the other (in **TB207**), a bulkier substituent is added, increasing in this manner the steric hindrance and reduce even further the aggregate formation. Moreover, the electron rich properties of the substitute facilities the oxidation of the dye. As it is shown in the section below, the absorption of **TB423** is 10 nm blue-shifted compared with **TB207**, but the lower oxidative potential reveals great potential for the dye-sensitizer's performance in real DSSC applications.

All three dyes showed considerable advantages for DSSC development in the field of transparent technologies. They all present high molar extinction coefficients in the

near-IR and low in the visible and near-UV, improving drastically the level of AVT and at the same time, they exhibit the highest up-to-date PCE values for near-IR dyes. Their steady-state and time resolved spectroscopic differences are presented in this Thesis, probing various effects with most interest on the aggregates effect for the charge-separation at the dye-SC interface.

5.2 Steady-state absorption/fluorescence

Steady-state spectroscopy offers great insight on the basic photophysical properties of the systems under investigation. The time-integrated data obtained by these techniques provide a first insight and a deeper level of understanding of the photophysical mechanisms given by the complementary time-resolved studies. In this section the steady-state absorption and fluorescence spectra of all three, **VG20**, **TB207** and **TB423** dyes are presented, both in solution and when incorporated in real DSSCs. Also, the photovoltaic performances that were used as base for the organization of the experiments that took place in the current PhD project, are shown.

5.2.1 Dyes in solution

Figure 2.1.A depicts the steady-state absorption (SSA) spectra of **VG20** in EtOH/DMSO (9/1), TB207 and TB423 in EtOH/$CHCl_3$ (9/1). Supplementary, Figure 2.1.B demonstrates the corresponding steady-state-fluorescence spectra with excitation near the absorption maximum of each dye.

The absorption spectrum of all three dyes is shifted above 700 nm, exhibiting narrow bands and almost no absorption in the visible spectral region. Therefore the yield for $S_0 - S_n$ transitions, where n>1 excited states, is very low and the absorption main band in the near-IR corresponds to the $S_0 - S_1$ transition. **TB207** and **TB423** absorption spectra are identical with a lower band feature at $\sim 700\ nm$ that corresponds to a vibronic level. Increasing the molecular concentration doesn't have any impact on this higher energy band and therefore it is considered that in solution there is no formation of aggregates and the dye population refers to pure monomers. **TB423** absorption and emission maxima are 20 nm blue-shifted compared with **TB207**, when **VG20**'s maximum is located further into the near-IR at 840 nm with a similar vibronic feature at 720 nm. The fluorescence spectra are mirror image of the absorption, however the accuracy

of the SSE spectra greatly reduces above 900 nm, due to the low quantum efficiency of the detector, which is not properly corrected for in our instrument.

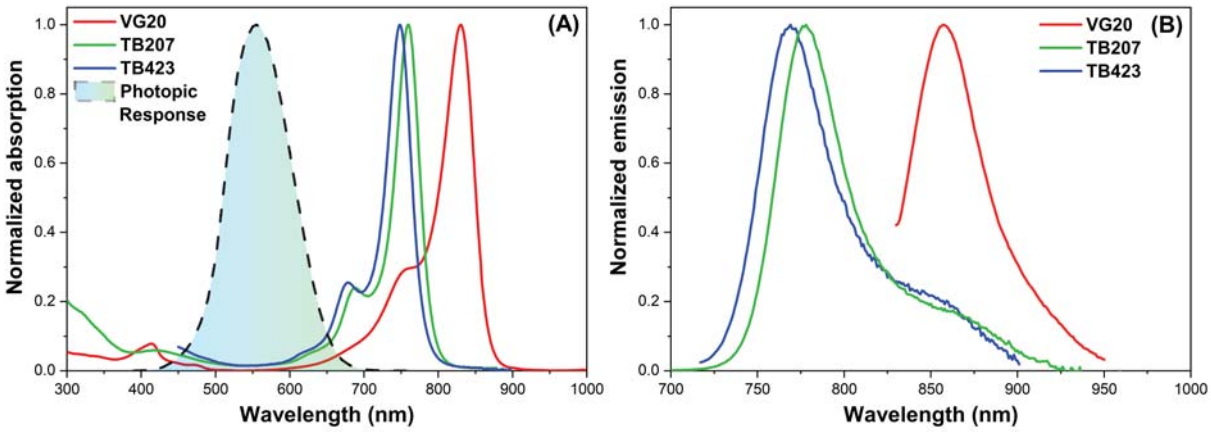

Figure 5.2: (A) The steady-state absorption spectra of **VG20**, **TB207** and **TB423**. The human eye phototopic response is shown, as reference. (B) The corresponding steady-state emission spectra for excitation at 820 nm (**VG20**), 700 nm (**TB207**) and 690 nm (**TB423**).

In Table 5.1 the spectroscopic properties of the dyes are presented. As illustrated in Figure 5.2, the Stokes shift of the dyes is relatively small, below 19-29 nm. Noteworthy, the cyanine and PPCys dyes under study exhibit some of the highest molar extinction coefficients, which makes them perfect near-IR harvesting antennas and suitable for DSSCs operating in the near-IR. The fluorescence quantum yield (Φ_F) and oscillation strength (f), for the $S_0 - S_1$ transition, of **VG20** in solution is also presented in Table 5.1 and the latter were calculated, for all dyes, according to the equation:

$$f = 4.32 \times 10^{-9} \int_{S_1,band} \varepsilon(\nu) d\nu \tag{5.1}$$

Among the three dyes, **VG20** has the highest f, when both **TB** dyes have similar values.

Table 5.1: Spectroscopic properties of **VG20**, **TB207** and **TB423** in solution. The ε has been calculated for **VG20** in EtOH, when for the **TB** dyes in DMC and corresponds to λ_{abs}^{max}.

Dyes	$\boldsymbol{\lambda_{abs}^{max}}$ $\boldsymbol{(nm)}$	$\boldsymbol{\lambda_{pl}^{max}}$ $\boldsymbol{(nm)}$	$\boldsymbol{\Delta\lambda}$ $\boldsymbol{(nm)}$	$\boldsymbol{\varepsilon}$ $\boldsymbol{(M^{-1}cm^{-1})}$	$\boldsymbol{f}$	$\boldsymbol{\Phi_F}$
VG20	830	857	27	1.54E+05	0.80	0.47
TB207	759	778	19	1.38E+05	0.68	-
TB423	748	769	21	1.34E+05	0.69	-

Moreover, f values are in the usual range of values that have been reported for similar dyes [6, 8].

5.2.2 Dyes in complete DSSCs

The study of the dyes in solution is essential to determine the basic photophysical properties of the dye, with higher freedom of movement at ambient temperature and in a first approach works as reference. The target of the present PhD Thesis is connected to a broader multidisciplinary framework that demands the study of real DSSC devices. Therefore, the dyes under investigation are incorporated as sensitizers in various DSSCs, in order to examine specific properties relative to their electron injection. The main division of the DSSC samples lies in two categories depending on the SC material used in the anode part and a discussion is made for injecting and non-injecting DSSCs. To understand, in a secondary step, the photophysics of the dye and the role of aggregates upon attachment on the SC, we utilize materials of high energy CB, such as ZrO_2 for **VG20** and Al_2O_3 for the **TB** dyes. As it will be explained in detail in the following sections, by choosing a SC of high CB level, relative to the dyes' LUMO, the LUMO-CB transition isn't energetically allowed, therefore the injection channel is closed and a simplified study, focusing only on the additional mechanisms, can be made.

The steady-state absorption (SSA) spectra of the three dyes incorporated in real DSSCs are presented in Figure 5.3. To obtain the SSA of the DSSCs, we subtracted the device background using a reference sample of an "empty" DSSC, containing only the anode-cathode and the electrolyte. For the Al_2O_3 samples the background was subtracted by a straight line fit for better quality results. The solid-line spectra correspond to the non-injecting DSSCs of ZrO_2 SC for **VG20** and Al_2O_3 for **TB207** and **TB423** and the dashed spectra to the injecting TiO_2 DSSCs. The filled-dashed spectra represent the corresponding solution spectra for all three dyes, red-shifted where necessary to overlap with the injecting DSSC spectra. The solution spectra reflects systems containing exclusively dye monomers,since increasing the solution concentration or adding de-aggregating agent didn't affect the spectral features. Therefore, as it was mentioned above, the higher energy spectral shoulder can be indeed attributed to a vibronic level.

Interestingly, for all **VG20**, **TB207** and **TB423** ((A), (B) and (C)) dyes, when they are incorporated in solid samples (DSSCs) the absorption spectra show pronounced differences. Starting with the **VG20** (Figure 5.3.A) ZrO_2 DSSC (solid line) the absorption spectrum is distinctively broader than for solution. An additional spectral peak rises for

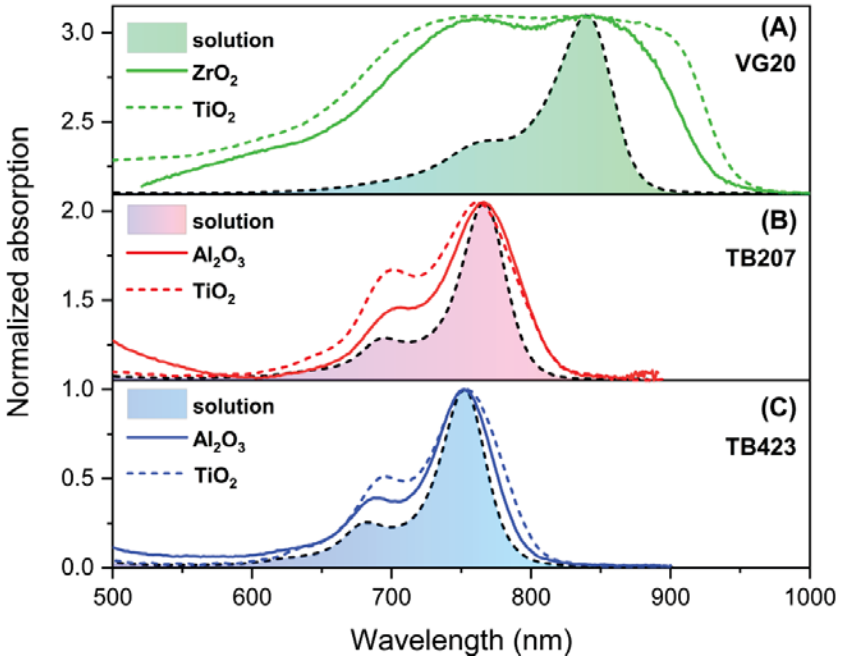

Figure 5.3: Steady-state absorption spectra of (A) **VG20**, (B) **TB207** and (C) **TB423** in real DSSC devices, with no addition of de-aggregating agent. The solid lines correspond to the non-injecting (ZrO_2 and Al_2O_3) DSSC absorption spectra and the dashed to the injecting TiO_2 DSSCs, while the filled-dashed spectra represent the absorption in solution, red-shifted by 10 nm (A), 6 nm (B) and 4 nm (C) as reference.

the DSSC at 750-800 nm, where the vibronic level of solution is located, but for the solid sample is attributed to the formation of molecular aggregates on the SC surface. The amplitude of the shoulder can vary from DSSC to DSSC, depending on the dye loading time and the de-aggregating agent concentration, as it is shown in the following section. The appearance of the high energy band is strictly correlated with H-type aggregates, as it was recalled and illustrated in section 3.3.1 (Figure 3.5). However, the broadening of the spectrum hints to a the second energy band of lower energy, which is also optically active, directly indicating either the co-existence of both H and J aggregates on the SC surface, or more likely for densely packed systems such as the DSSCs, aggregates of relative oblique geometry. Similar to ZrO_2, TiO_2 DSSCs (dashed-line) show a very broad absorption spectrum and features of aggregate bands. The observation is valid for the **TB** dyes too, in which the TiO_2 DSSC absorption spectra are broader, than the Al_2O_3 and slightly ref-shifted (4-5 nm) compared with the solution, due to the different dielectric environment. Moreover, the total OD is higher ($\sim 0.1-0.2$) for the injecting DSSCs, because of the different properties of the injecting and non-injecting SCs. Another interesting observation is the degree of aggregates that form on the SC surface for all three

dyes. The cyanine **VG20** tends to form aggregates significantly easier than the PPCy dyes **TB207** and **TB423**, as it can be seen from the SSA (Figure 5.3). Furthermore and comparing between the two **TB** dyes, the bulkier **TB423** dye, tends to form slightly less aggregates compared to their counterpart **TB207**. Both **TB** dyes have similar molar extinction coefficient (Table 5.1) and in the normalized solution SSA spectra, the amplitude of the vibronic level is almost identical. Therefore the degree of aggregation can be briefly calculated from $a = A_{max/}A_{H-shoulder}$ resulting in the values presented in Table 5.2. The lower values of the ratio indicate the higher degree of aggregates in the system.

Table 5.2: The ratio of the main monomer absorption band against the high energy aggregate band as it was extracted from the SSA.

Dyes	$a_{Al_2O_3}$	a_{TiO_2}
TB207	1.4	1.2
TB423	2.6	2.0

Aggregates in DSSCs have been reported to have negative effect on the total photovoltaic performances by reducing the injection efficiency from the dye to the SC [2, 9–13] and also they reduce the AVT, due to their contribution in absorption towards the visible [3]. On account of this, various tactics have been used to reduce aggregates with the most common, the utilization of Chenodeoxycholic acid (CDCA, Sigma Aldrich), which is essentially a bile acid, as a de-aggregating agent. The method is based on co-sensitization

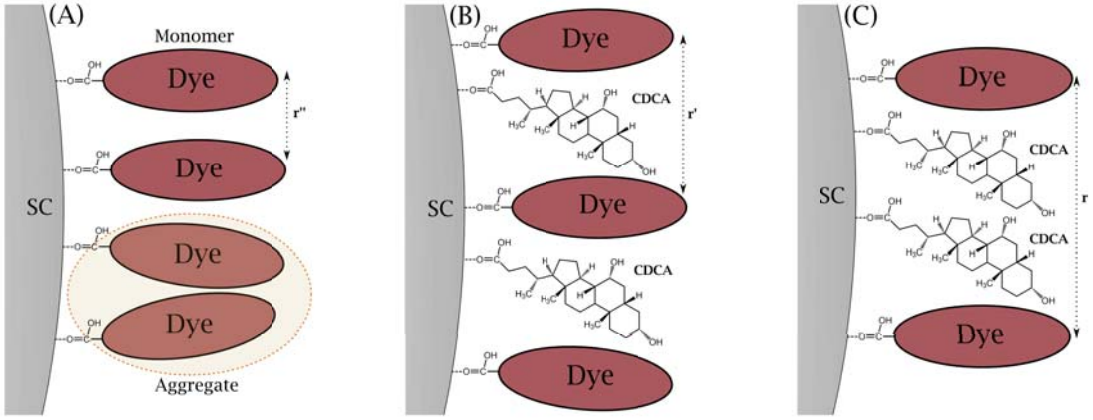

Figure 5.4: A schematic illustration of the dye-SC interface for three different cases, increasing the CDCA concentration from (A) to (C). By adding CDCA the intermolecular distance, from A-C increases ($r'' < r' < r$).

of both the dye and CDCA on the SC surface and therefore many dye-bath solutions have

been prepared, increasing the CDCA concentration with respect to the dye concentration. In Figure 5.4, a schematic illustration of the effect of CDCA is presented. In case (A), when there is no CDCA in the system, the intermolecular distances are short, constituting more feasible a face-to-face molecular conformation. As it was mentioned above, an interpretation based on the two-band observation, includes aggregates of oblique geometry, but lateral side-by-side assemblies are also possible to form. From (B) to (C), by adding CDCA, the intermolecular distances increase and the aggregate percentage decreases. In our studies, after a thorough optimization, with reference point the PCE measurements, the best compromise between high dye loading and reduced aggregate percentage has been found for each of the three dyes and these conditions are referred to the "standard conditions".

In Figure 5.5 the normalized SSA spectra for all three dyes are shown for non-injecting (A, C and E) and injecting (B, D and F) DSSCs, increasing the CDCA concentration. In addition, the inset graphs show the corresponding non-normalized SSA. The values of the SSA and SSE maxima, as well as the corresponding Stokes shift, increasing the CDCA concentration, are shown in table 5.4, for the non-injecting DSSCs and in table 5.5 for the injecting TiO_2 ones. It is straightforward to observe that decreasing the CDCA concentration, the absorption intensity increases due to the higher OD (Inset graphs). For the non-injecting (ZrO_2, Al_2O_3) CDCA-free devices, the total OD is around $\sim$ 0.4 for all dyes, while for the injecting (TiO_2) devices is almost two times higher, varying from 0.6 (**VG20**) to 1.0 (**TB423**) and 1.2 (**TB207**). This variation, most probably, is due to the different SC material properties, as well as the SC layer, for the **TB** injecting and non-injecting SC cases. For all cases, the general trend of reducing aggregates by increasing the CDCA concentration is pronounced. The reducion of aggregates can be seen as a decrease of the intense high energy absorption shoulder in 750 nm for **VG20**, 700 nm for **TB207** and 680 nm for **TB423**, as well as steepening of the spectra at longer wavelengths. Indeed, in all cases, in the highest [CDCA] case the absorption is very close in shape to the solution spectrum that has been already explained to correspond to a 100 % monomers case. The decrease of the shoulder intensity with CDCA, is another proof of the additional high energy aggregate band presence, in these wavelengths, compared to just the vibronic nature in solution. Eye-caching is the case of the most aggregated **VG20** samples (A-B) that compared to the **TB** series, in order to efficient de-aggregate the systems, very high CDCA concentrations are needed (approximately 10 times more). Interestingly, even at very high [CDCA], the SSA spectra never correlates completely with the solution spectra, indicating that aggregates always form in the DSSC samples.

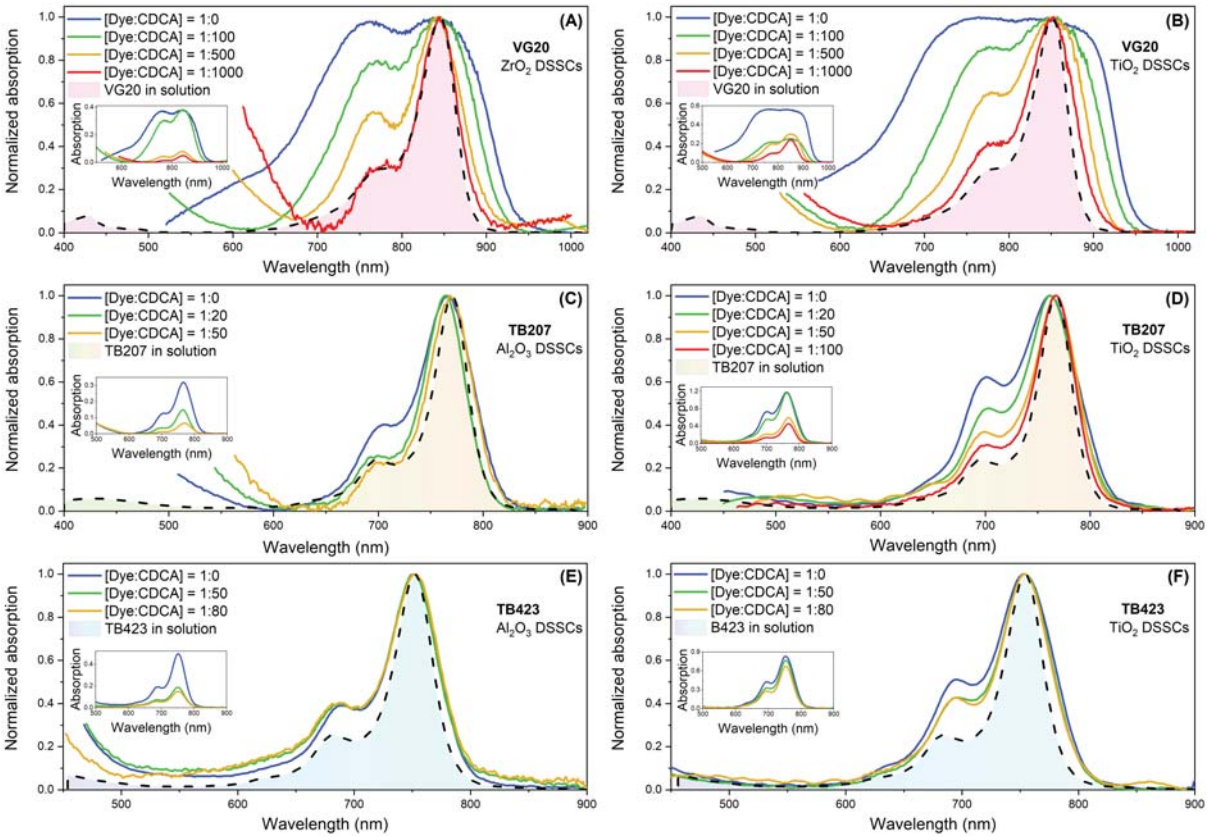

Figure 5.5: SSA spectra of **VG20** (A, B), **TB207** (C, D) and **TB423** (E, F) incorporated in real DSSC devices, increasing CDCA concentration. In the left (A, B and C) are presented the SSA spectra for the non-injecting DSSCs while in the right (B ,D and F) the SSA spectra for the injecting DSSCs. The corresponding, normalized SSA spectra in solution are presented as filled spectra, red-shifted ($< 10\ nm$) to overlap with the highest [CDCA] DSSC. Inset: Non-normalized corresponding spectra.

Two exceptions can be seen for **VG20** in ZrO_2 for 1:1000 [Dye:CDCA] and for **TB207** in Al_2O_3 for 1:50 [Dye:CDCA], however the background subtraction might be misleading and add a small error ($< 10\%$) in the exact shape of the SSA. Moreover, even in these cases the absorption spectra width is slightly broader than in solution, still indicating the existence of aggregates. The above described observations are illustrated in Figure 5.6, which shows the ratio of the high energy peak due to aggregates against the CDCA:Dye ratio. The ratio for various DSSCs, increasing CDCA, gives in a good approximation, the aggregate formation trend, however the FWHM of the spectra is an additional parameter that hides relative information. **VG20** is clearly shown to be the dye that tend to aggregate easier and very high CDCA concentrations are needed to de-aggregate, without reaching an environment with exclusively monomers. By its turn, **TB207** needs a small

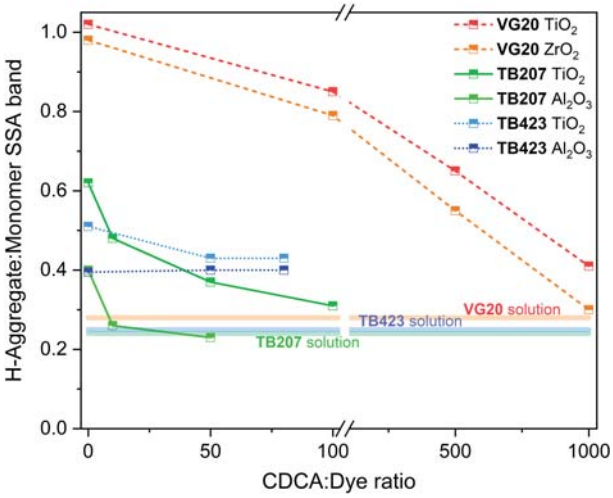

Figure 5.6: Peak ratio of H-aggregate band/Monomer band for different DSSCs, increasing CDCA for **VG20**, **TB207** and **TB423** on both injecting and non-injecting DSSCs. The monomer threshold lines are the ratios of the vibronic levels to the monomer peaks, for all three dyes and refer to the pure monomer environment.

amount of CDCA to efficiently reduce aggregates. Interestingly and in accordance with the spectra, **TB423** appears to depend, among all dyes, the least on CDCA.

In the content of this Thesis, for communication reasons, the devices are labeled with the ratio of the concentrations [Dye:CDCA] related to the concentrations of their corresponding bath solutions. However, this doesn't necessarily reflect the real concentration ratio on the SC surface, as it has been shown for similar dyes, such as phthalocyanines on TiO_2 [13], for which the CDCA was proposed to adsorb on the surface in smaller percentages than the dye. Finally, in the experimental section, the effect of CDCA on the injection rates, efficiency and therefore photovoltaic performances has been explored in detail. Therefore, it can be of interest to isolate the absorption spectra of the aggregates and monomers in the various DSSCs. By subtracting the monomers' absorption spectra, which is equivalent to the absorption of pure monomers, from the absorption spectra of the complete DSSCs, such as presented in Figure 5.5, the normalized absorption spectra of the aggregates for the TiO_2 DSSCs of different CDCA concentration have been derived and plotted in Figure 5.7.A,B and C for **VG20**, **TB207** and **TB427**, respectively. The relation of the degree of aggregates to the injection efficiencies can be significant, in order to understand better the effect of aggregates to the overall photovoltaic performances. It is evident that the aggregates that have two active absorption bands, of higher and lower energy, as it is predicted by the classic exciton theory for aggregates (chapter 3.3.1) can either be represented by an oblique geometry of angle ϑ, between the dipole moments of

the two monomers that make the aggregate, or by a co-planar tilt of the monomers by and angle α. However, taking into consideration that in all cases the lower energy band is higher in amplitude than the higher one, the most probable configuration is related to oblique plane geometry [14–18]. Therefore, in all DSSC systems under study, no pure H or

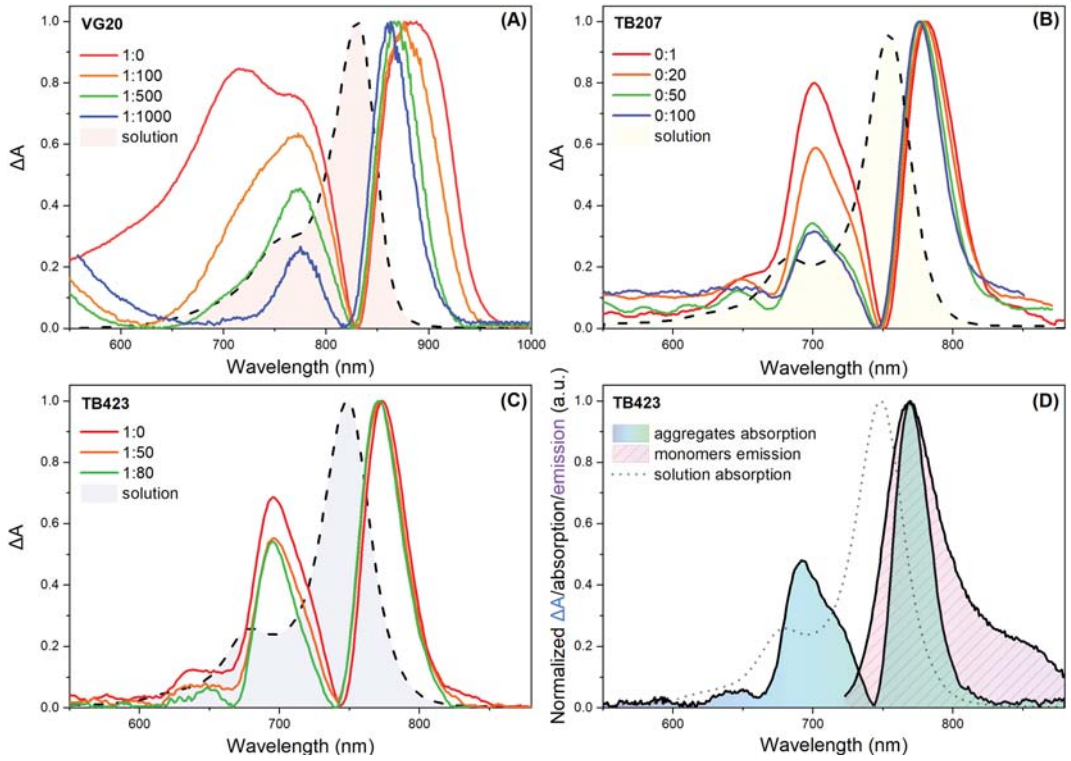

Figure 5.7: Aggregates absorption spectra ($\Delta A = A_{DSSC} - A_{solution}$) extracted from the total TiO_2 DSSCs, increasing CDCA concentration for (A) **VG20**, (B) **TB207** and (C) **TB423** by subtracting the corresponding spectra in solution. (D) Spectral overlap of the lower energy **TB423** aggregates absorption band, extracted from the Al_2O_3 DSSC absorption for 1:0 [Dye:CDCA], with the emission spectrum of the **TB423** monomers. As dashed/dotted lines are defined the corresponding steady-state absorption spectra of the solutions.

J aggregates are formed, but rather aggregates of intermediate geometries and both states are energetically allowed to be populated. However, due to the approximate derivation of the aggregates absorption spectra, as well as the fact that increasing CDCA the features slightly change, the exact determination of the aggregates molar extinction coefficient and therefore the concentration of aggregates for each sample, is difficult to determine precisely. For all dyes, increasing the CDCA concentration and therefore increasing the intermolecular distances to de-aggregate the system, the aggregate type appears to vary, accordingly. Specifically, by adding CDCA the higher energy band gradually decreases

with respect to the lower energy band (I_H/I_J) (Table 5.3) and therefore, the geometry is modified to a more J-oblique configuration. This is reasonable by taking into consideration that the anchoring groups of all dyes are located in the molecular edges, implying a grafting configuration in which the dyes are exposed to interaction with the parallel plane of the neighboring ones. The CDCA molecules in the system, can act as dye stabilizers and the angle (θ) between the two monomers, forming the dimer, will be smaller, as the dyes tend to tilt more to form the dimer. Relative to the geometry and therefore the nature of aggregates, more information can be extracted from Figure 5.7.A,B and C. For oblique dimers equation 3.16 described the interaction energy (V), which would be half the Davidov Splitting (DS). DS is determined as the energetic difference between the excitonic bands of the aggregates, which are presented in Figure 5.7 and the corresponding values are shown in Table 5.3. The values of DS are close to 0.2 eV, in the same range as it has been found for similar dyes, such as pentamethine cyanines [19, 20]. The transition dipole moments of the high $\overline{M}^{+} = 2\overline{\mu}^2 cos^2(\theta)$ and low $\overline{M}^{-} = 2\overline{\mu}^2 sin^2(\theta)$ aggregate energy bands are proportional to the corresponding oscillator strengths f_H and f_J, respectively. Moreover, from Figure 3.5, $\alpha = \pi - 2\theta$ and therefore the angle α that the two monomers form, is calculated by the relation [14–16, 18]:

$$f_J/f_H = tan^2(\alpha/2) = A_1/A_2 \tag{5.2}$$

where A, the areas of the aggregates band in Figure 5.7. Consequently, from the interaction energy of oblique dimers that is described in equation 3.16, the monomer's dipole moment can be expressed as [14]:

$$\overline{\mu_1} = \frac{3hce^2}{8\pi^2 mc^2} \cdot \frac{f}{\overline{\nu}} = 1.07 \times 10^{-14} \frac{hcf}{\overline{\nu}} (in\ erg\ cm^3) \tag{5.3}$$

where $f = 4.32 \times 10^{-9} \int \varepsilon(\nu) d\nu$ the monomer oscillator strength, $\overline{\nu}$ the monomer energy in cm^{-1} (maximum wavenumber in the absorption spectrum) and $\int \varepsilon(\nu) d\nu$, the area of the monomer absorption band. Therefore, by simple substitution and solving for the intermolecular distance R(Å) from equation 3.16 the following equation can be derived [14–16, 18]:

$$R = \left(\frac{(1.85)10^2 \int \varepsilon(\overline{\nu}) d\overline{\nu} [cos(\alpha) + 3sin(\alpha/2)]}{V\overline{\nu}} \right)^{1/3} \tag{5.4}$$

All the values are presented in table 5.3. The angles (α) between the monomers of the aggregate increases, as [CDCA] increases, towards 180°, which is the ideal J-type

conformation. This observation is in agreement with the increase of lower energy band, compared to the higher one, as the [CDCA] increases. CDCA attached on the SC prevents the parallel aggregation, however even with high CDCA concentrations, neighboring dyes are attracted, in close distances and form aggregates in oblique geometry, but with more obtuse angles. The higher the intermolecular distance, the larger the α angle e.g. for **VG20** TiO_2 DSSC with [1:10] dye:CDCA ration $\alpha = 88.8°$ and for [1:1000] the angle becomes becomes 124°(table.5.3). The centre-to-centre distances of the monomers in the aggregate don't change significantly, but with a weak tendency, as the intermolecular distances increases. The mean (R) values are 19-20 Å, which is two to three times longer than the ones reported for Rhodamine dyes [16, 18] or pentamethine cyanine dyes [21], possibly due to the longer long-axis length and larger oscillator strength of **VG20**.

Table 5.3: Aggregate properties of **VG20**, **TB207** and **TB423** in TiO_2 DSSCs.

Dyes	**[Dye:CDCA]**	I_H/I_J	$\Delta\nu$ (eV)	f_J/f_H	α (deg)	R $(Å)$
VG20	1:0	-	-	-	-	-
	1:100	0.63	0.19	0.96	88.8°	20.0
	1:500	0.45	0.18	1.42	99.9°	20.4
	1:1000	0.25	0.16	3.55	124.0°	20.9
TB207	1:0	0.80	0.18	0.91	87.1°	18.4
	1:20	0.59	0.18	1.28	97.0°	18.7
	1:50	0.34	0.18	1.95	108.9°	18.6
	1:100	0.32	0.17	1.95	108.9°	19.0
TB423	1:0	0.69	0.18	1.06	91.6°	18.6
	1:50	0.55	0.18	1.48	100.4°	18.8
	1:80	0.54	0.18	1.77	106.1°	18.8

The interaction of monomers and aggregates is examined via time resolved techniques in the following sections. Already, in Figure 5.7.D, it is shown that the low energy aggregate band of a **TB423** Al_2O_3 DSSC, with no addition of CDCA, fully overlaps with the emission spectrum of the solution sample, which represents the pure monomer population. Therefore, for monomers as donors and aggregates as acceptors, processes such as Energy Transfer are energetically favored to occur. Förster Energy transfer (ET) for monomers to aggregates have already been reported to be the main loss channel limiting efficient injection to the SC [12] and the evidences will be described analytically in the following sections.

Relative to the radiative character of the aggregates little information can be ex-

tracted from the Steady-State Emission spectra (SSE). The corresponding spectra for **VG20**, **TB208** and **TB423** are presented in Figure 5.8.A.B and C, respectively, for both injecting and non-injecting DSSCs. The relative spectral maxima values, as well as the Stokes shift are shown in tables 5.4-5.5, for both non-injecting and infecting DSSCs, for various [CDCA], respectively. In Figure 5.8.D the SSE spectra of an **TB423** Al_2O_3 DSSC with no CDCA, are presented, at various excitation wavelengths, in order to excite a greater or lesser percentage of aggregates in the system. The SSE spectra are normalized, as their measured intensity depends, each time, on various experimental factors and thus, they are expressed in arbitrary units. However, a straightforward observation

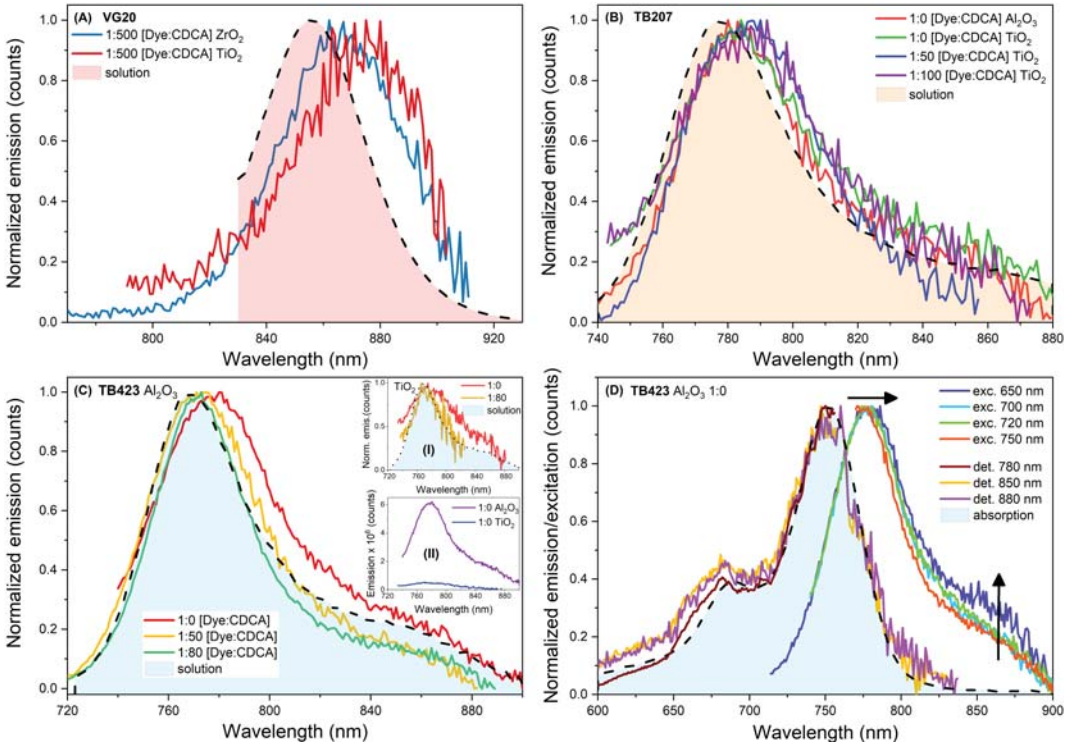

Figure 5.8: Normalized steady-state emission spectra of (A) **VG20** in ZrO_2 and TiO_2 DSSCs of 1:500 [Dye:CDCA], (B) **TB207** in Al_2O3 and TiO_2 DSSCs, increasing CDCA concentration and (C) **TB423** in Al_2O_3 and TiO_2 (inset I) DSSCs. Inset II, highlights the comparison of OD_{max} for the 1:0 Al_2O_3 DSSCs. (D) Normalized emission spectra of **TB423** Al_2O_3 DSSC of 1:0 [Dye:CDCA] at different excitation wavelengths and normalized excitation spectra at different detection wavelengths. As dashed lines are defined the corresponding steady-state absorption spectra of the solutions.

is that the total intensity of the TiO_2 DSSCs is strongly quenched ($\sim$ 10 times), compared to the corresponding no-injecting DSSCs (e.g. inset II of Figure 5.8.C), due to injection in the SC, which is essentially a non-radiative process. Another observation is that by increasing the CDCA concentration and therefore, de-aggregate the system, the

SSE spectra are generally slightly blue-shifted. This observation is more pronounced for **TB423** Al_2O_3 DSSCs (Figure 5.8), in which the signal/noise ratio is higher compared to TiO_2. As it is predicted, by the classic exciton theory only J-aggregates have radiative character, while H are completely "dark". Moreover, intermediate cases have been predicted (Figure 3.5), such as for oblique aggregates, for which the angle between the transition dipole moments of the monomers defines the radiative nature of the aggregates with radiative rate k_r according to the equation [16]:

$$k_{r,agg} = 2k_{r,mono}cos^2\theta \tag{5.5}$$

If aggregates have fluorescent character, the emission should be located in longer wavelengths than the monomer emission. Therefore, the above mentioned red-shift (7 nm) of the emission (Figure 5.8.C) from the more aggregated case of 1:0 [dye:CDCA] to the least aggregates 1:80, could be attributed to an additional contribution from aggregates emission. Moreover the spectral shift and the FWHM of the more aggregated DSSCs decreases upon de-aggregation to finally reach the solution's one. Investigating more in detail, the normalized emission spectra at different excitation wavelengths, of more aggregated **TB423** Al_2O_3 DSSC, with no CDCA, are presented in Figure 5.8. To identify the spectral region of the emissive states, the excitation spectra detected at different wavelengths, are portrayed too, as well as the absorption spectrum of the DSSC (dotted-line). It should be mentioned that in DSSCs both monomers and aggregates exist and therefore the emission and excitation spectra are a superposition of both contributions. The 650 nm excitation is energetically closer to the aggregates higher energy level than the monomers first excited state and the corresponding emission is slightly red-shifted (5 nm) compared to solution. The shift is followed by the appearance of an additional weak intensity band at 850-890 nm, indicating possible contribution in the emission from aggregates. When the excitation is tuned near the maximum of the solution and therefore the monomers population, the additional band and the FWHM decreases. Probing near the maximum of the emission (780 nm), as well as in longer wavelengths where the J-band of the aggregates is located (850 nm and 880 nm),only a small increase in shorter wavelengths can be observed in the excitation spectra and they both overlay with the absorption spectrum. Therefore, the main radiative state is the monomer S_1. In conclusion, they are indications for fluorescence from aggregates, but with no clear contribution, in terms of a separate band in the complete DSSC samples, even in the more aggregated cases, with no addition of CDCA, due to the presence of monomers and possibly the lower radiative yield of the aggregates.

Table 5.4: Spectroscopic properties of **VG20**, **TB207** and **TB423** in non-injecting DSSCs, increasing the CDCA concentration. $\Delta\lambda$ = Stokes shift.

Dyes	**[Dye:CDCA]**	$\boldsymbol{\lambda_{abs}^{max}}$ $\boldsymbol{(nm)}$	$\boldsymbol{\lambda_{pl}^{max}}$ $\boldsymbol{(nm)}$	$\boldsymbol{\Delta\lambda}$ $\boldsymbol{(nm)}$
VG20	1:0	840	-	-
	1:100	842	-	-
	1:500	842	866	24
	1:1000	843	-	-
TB207	1:0	766	781	15
	1:20	764	-	-
	1:50	769	-	-
TB423	1:0	752	777	25
	1:50	751	772	21
	1:80	752	771	19

Table 5.5: Spectroscopic properties of **VG20**, **TB207** and **TB423** in TiO_2 DSSCs, increasing the CDCA concentration.

Dyes	**[Dye:CDCA]**	$\boldsymbol{\lambda_{abs}^{max}}$ $\boldsymbol{(nm)}$	$\boldsymbol{\lambda_{pl}^{max}}$ $\boldsymbol{(nm)}$	$\boldsymbol{\Delta\lambda}$ $\boldsymbol{(nm)}$
VG20	1:0	-	-	-
	1:100	850	-	-
	1:500	852	874	22
	1:1000	851	-	-
TB207	1:0	761	782	21
	1:20	762	-	-
	1:50	767	787	20
	1:100	767	789	22
TB423	1:0	753	775	22
	1:50	754	-	-
	1:80	754	770	16

5.3 PV performances and dye regeneration

In this section, before the ultrafast-time resolved study and for the complete analysis, the total photovoltaic performances and regeneration times are identified and presented, as well as the spectral position of the oxidized, after injection dyes. The measurements were performed by W. Naim and I. Dzeba in F. Sauvage's group (LRCS, University of Picardie Jules Verne). The photovoltaic parameters were determined under A.M.1.5G conditions ($P_{ill} = 100\ mW/cm^2$) using a 3A class Newport SOL3A sun simulator [22]. The regeneration dynamics were monitored via a ns-transient absorption technique (flash photolysis), offering an available time window in the ms-μs time-scale.

Starting with the ms-μs TAS, the experimental strategy is the study on two DSSCs, one operational with redox couple in the electrolyte and one only with inert electrolyte (ACN) without redox couple. In the second case, the dynamic range of the recombination mechanisms is identified and by simple substitution of these rates in the average rate of the operational DSSC, the regeneration times can be identified, as well as the recombination efficiency, according to the relation:

$$\Phi_{reg} = \frac{< k_{reg} >}{< k_{reg} > + < k_{rec} >} \tag{5.6}$$

where, $< k_{reg} >$ and $< k_{rec} >$ the regeneration and recombination rates, respectively. In Figure 5.9.A,C and D the spectral features of **VG20**, **TB207** and **TB423**, in the cationic form, are presented. In (A) the spectra were extracted by gradually adding the oxidizing agent Ce^{4+} and by each time subtracting the initial Ce^{4+}-free absorption spectrum from the absorption spectrum with the oxidized dye. In a different approach for the **TB** dyes instead of absorption, spectroelectrochemical spectra where measured, by gradually oxidizing the dyes and the difference in absorption is calculated by subtracting, each time, the spectrum where zero voltage was applied. The spectroelectrochemical measurements were performed by T. Baron in F. Odobel's group (CEISAM, University of Nantes). For all dyes the corresponding cations absorb in higher energies, than the neutral dye, in the range of 400-600 nm, which range has also been reported for similar pentamethine cyanine dyes [23]. Interestingly, the μs-ms TAS (Figure 5.9.B) reveals the absorption of **VG20** cation for an injecting TiO_2 DSSC. In the 2 μs time window all the ultrafast photophysical processes have been completed and the spectrum corresponds to the dye-cation absorption, after the ultrafast injection, which is 50 - 100 nm red-shifted compared to solution, possible due to the different dielectric environment in the

solid-state sample. From Figure 5.9, the molar absorption coefficient of the dye radical cation in solution is about 25 times weaker compared to the neutral form in the same solution ($\varepsilon \approx 6200\ L/mol \cdot cm$). Relative to the regeneration times, the 2D TAS profiles,

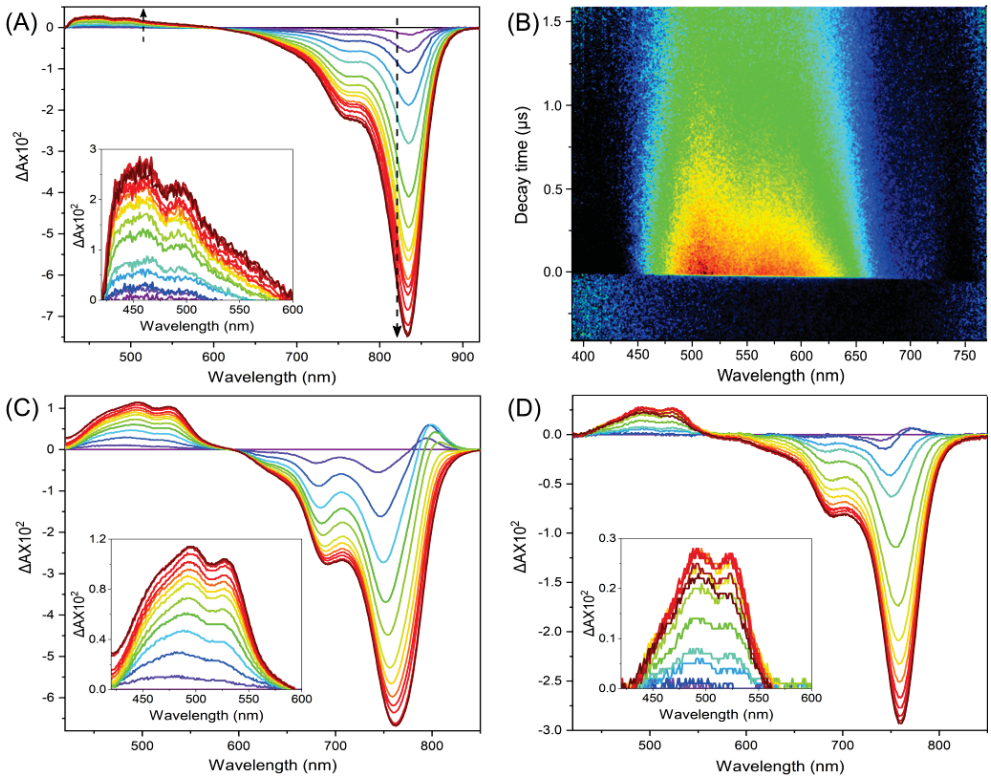

Figure 5.9: (A) Titration of a **VG20** EtOH/DMSO solution with the oxidant Ce^{4+}. ΔA denotes for changes of steady-state UV-visible absorption spectra $A([Ce^{4+}]) - A([Ce^{4+} = 0])$. The arrow indicates increasing Ce^{4+} concentration : bleaching of the neutral absorbance at 835 nm and rise of the cation absorption band, below 600 nm. (B) Time-resolved transient absorption spectral streak image of the **VG20** based DSSC for the I_3^-/I^- redox couple. (C) and (D) Titration of **TB207** and TB423 **solutions**, respectively, obtained by spectroelectrochemical measurements. ΔA denotes for changes of electrochemical spectra $A([V]) - A([0] = 0)$. The spectral region of the dye cation onsets is shown in the insets.

obtained via streak camera, for **TB207** in a regenerative and non-regenerative DSSCs, are presented in a 2 µs time-window, in Figure A.2.(A), (B), respectively and for **VG20** in Figure 5.9. In table 5.6, the corresponding times, for TiO_2 DSSCs with I_3^-/I^- redox couple in the electrolyte, derived from two-exponential decay fittings, are presented for both dyes. The times in the regenerating DSSCs, are faster for **TB207** compared to **VG20** and the recombination times found via TAS are much longer, in the range of ms for both dyes. It can be seen in Figure A.2.(B), that in the time window of 2 µs, the **TB207** cation signal hasn't recovered yet. Therefore, regeneration from the electrolyte

Table 5.6: Regeneration times and efficiency for **VG20** and **TB207** TiO_2 DSSCs with I_3^-/I^- redox couple in the electrolyte.

Dyes	τ_1 (μs)	τ_2 (μs)	Φ_{reg} %
VG20	1.5	19.4	> 98.0
TB207	0.4	2.5	99.7

occurs faster than geminate recombination and the losses are minimized resulting in regeneration efficiencies that reach almost unity. The range of values in table 5.6 are in the same order of magnitude as those reported for D-π-A dyes [2, 24, 25].

The PCE efficiency and the photovoltaic performances constitute the guideline for the current experimental work. In table 5.7, the photovoltaic performances are presented for all three dyes in operational $TiO2$ DSSCs with I_3^-/I^- redox couple in the electrolyte and 1 M Li^+, increasing the CDCA concentration. An important observation is that by

Table 5.7: Photovoltaic performances of **VG20**, **TB207** and **TB423** increasing CDCA concentration for 3 layer TiO_2 DSSCs with the electrolyte of standard conditions (1 M Li^+).

Dyes	**[Dye:CDCA]**	$\boldsymbol{J_{SC}}$ $\boldsymbol{(mA/cm^2)}$	$\boldsymbol{V_{OC}}$ $\boldsymbol{(mV)}$	$\boldsymbol{FF}$	$\boldsymbol{\eta}$ (%)
VG20	1:100	9.3	312	0.62	1.8
	1:500 (RT)	12.1	347	0.58	2.5
	1:500 (-20 C^o)	11.2	422	0.65	3.1
TB207	1:0	15.65	348	0.57	3.2
	1:10	14.90	367	0.59	3.4
	1:20	14.29	372	0.60	3.3
	1:50	16.49	394	0.58	3.9
	1:60	15.88	374	0.56	3.4
TB423	1:0	14.34	342	0.52	2.7
	1:5	14.31	388	0.52	3.0
	1:20	15.21	382	0.47	2.8

increasing [CDCA] the J_{SC} and therefore the total PCE (or n %) increases. Therefore, aggregates either don't inject at all, or the injection yield is much lower than for monomers and finally, they act as the main limiting factor for injection. After thorough optimization, the best compromise between high dye loading and aggregates reduction was found to be [1:500] Dye:CDCA for **VG20**, resulting in PCE_{max} of 3.1 %, when the sensitization

took place over a week in $-20\ ^oC$ [1] and [1:50] for **TB207** with the impressive PCE_{max} of 3.9 %. Interestingly, for **TB423**, the effect of aggregates is almost negligible with PCE_{max} to be 3.0 %, but further studies have to be made. The final observation is in agreement with the results in Figure 5.5, which show that for **TB423**, CDCA has a minor effect in de-aggregation, but the SSA spectra show that aggregates do form in **TB423** (Figure 5.5-5.7). The weak dependence of J_SC on [CDCA] then suggest that either FRET to aggregates is not operative, or that carrier injection from aggregates is possible. This will be addressed in section 5.5.2. The possibility for **TB423** aggregates to inject with higher yields than **TB207** ones, due to their relative higher HOMO levels, cannot be excluded.

The most pronounced effect of CDCA on PCE is observed for the **VG20**. This is expected, because this family of dyes is notorious in forming aggregates and one order of magnitude higher concentrations of CDCA is needed, in order to reach the optimum results. In addition, it should be mentioned that the best efficiencies were found for DSSCs containing 3 SC layers of different NP sizes, two scattering (5 μm thickness each) and one for transmission (8 μm thickness). If one transmission layer is used, the PCE drops for **VG20** to 2.1 % instead of 3.1 %. For the fs-ps time-resolved measurements in this Thesis, DSSCs of only one layer for transmission were examined.

Another interesting effect that has been examined (only for **VG20**), is the effect of the Li^+ additive in the ACN-(I_3^-/I^-) based electrolyte. The LUMO level has been determined via cyclic voltametry to be -0.43 V (vs NHE), when the $E_{CB,TiO_2} \approx -0.45$. Therefore, when the regeneration has been proven favorable, the weak driving force for

Table 5.8: Photovoltaic performances of **VG20** and **TB207**, increasing Li^+ concentration for TiO_2 DSSCs for 3 layer TiO_2 DSSCs with [Dye:CDCA] of the standard condition [1:500].

Dyes	**[Li$^+$] (M)**	$\boldsymbol{J_{SC}\ (mA/cm^2)}$	$\boldsymbol{V_{OC}\ (mV)}$	$\boldsymbol{FF}$	$\boldsymbol{\eta}$ (%)
VG20	0.10	5.5	395	66	1.6
	0.25	8.4	375	58	1.9
	0.50	9.6	368	56	2.2
	1.00	12.1	347	58	2.5
TB207	0.10	0.70	407	0.63	0.17
	0.25	13.22	381	0.59	3.01
	0.50	13.90	415	0.58	3.35
	1.00	16.48	394	0.58	3.85

injection postulates difficulties for the step of electron injection. For this reason, additives where added in the electrolyte. In detail, Li^+ atoms are adsorbed on the SC, shifting towards negative energies the CB, bellow the LUMO level. In table 5.8, the photovoltaic performances for both **VG20** and **TB207** are shown, for the TiO_2 DSSCs of optimal $[Dye : CDCA]$ ratio, respectively, increasing the $[Li^+]$ in the electrolyte. For both dyes the optimal conditions correspond to 1 M of lithium in the electrolyte, resulting in higher PCE values. With no addition of lithium, the PCE is close to zero, but for even small amounts (e.g. 0.25 M) the PCE drastically rises. In higher concentrations than 1 M the PCE drops, indicating the critical energetic LUMO/CB equilibrium, for the optimization of the driving force, before the entrance to the Marcus inverted region. It is important to underline that lithium presents additional side effects, such as possible contribution to aggregate formation and to the carrier transport toward the collection. For all the fs-measurements all the DSSCs were made with the optimal $[Li^+] = 1\ M$.

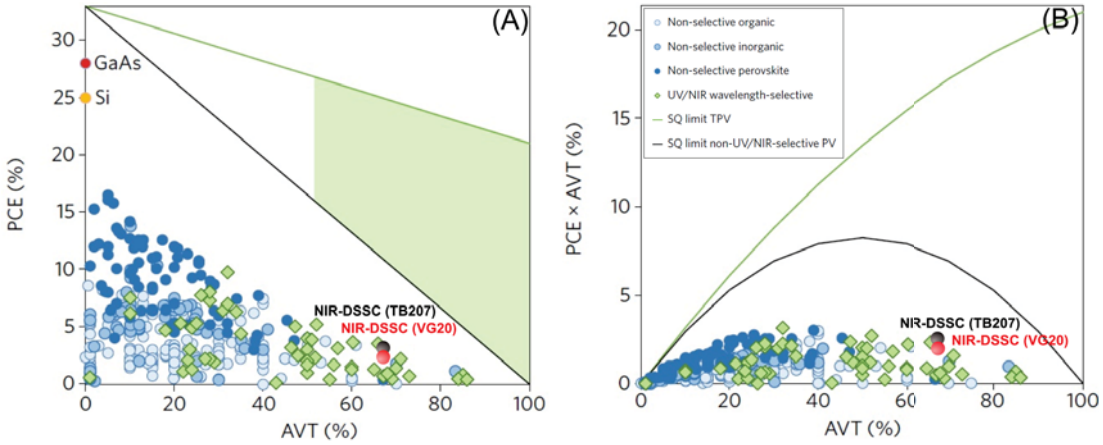

Figure 5.10: Survey of TPV. (A) PCE versus AVT for wavelength-selective and non-wavelength selective organic, inorganic and perovskite TPV technologies. Wavelength - selective TPVs have peak absorption in the UV and NIR portions of the spectrum. (B) Plot of the light utilization efficiency (LUE, defined as the product of PCE and AVT (Equation 2.15) versus AVT. The green shaded region in (A) denotes the target PCE and AVT only achievable with UV and NIR TPV solar technologies. The images were taken and modified, based on [26]. For **VG20** and **TB207** the evaluation was made with optimized conditions utilizing Iodine/iodide electrolyte; values for PCE recorded for 6 μm-thick TiO_2 without scattering layer.

In conclusion and taking into consideration the general framework of TPV devices, Figure 5.10 [26] presents the correlation between PCE and AVT and the updated values for various state-of-the-art devices. **VG20** and **TB207** were found to show PCE_{max} of 3.1 and 3.9 with $AVTs$ of 76 % and 75 %, respectively. As it has already been mentioned in chapter 2.2, by increasing AVT the PCE decreases proportionally. In the up-to-date

TPV survey, correlating AVT and PCE, both **VG20** and **TB207** are in remarkable positions, in the category of wavelength-selective TPVs. These are values for DSSCs, but for the same AVT values, the theoretical limit allows further optimization of PCE that can reach up to 12 %, which is the current record for opaque DSSCs.

5.4 Time resolved spectroscopy on VG20

The operational success of a DSSC, depends on various parameters, essentially based on the SC, dye and electrolyte energy tuning and therefore the relative dynamics of various mechanisms. Consequently, the time resolved measurements offer the capability to explore these dynamics and in the ultrafast time domain, electron injection rates from the dye to the SC can be determined, as well as the relative efficiencies and the competitive mechanisms that limit the total performance.

5.4.1 Ultrafast spectroscopy of VG20 in solution

First fs-time resolved experiments were performed in solution, in order to monitor and report the basic photophysical properties of the isolated dyes in an environment with more degrees of freedom. At this point it is important to highlight that for all ultrafast time-resolved studies performed, detailed investigation was made relative to the effect of the excitation energy fluence/pulse on the samples. The solid-state DSSC samples were found to be very sensitive to the excitation power, due to the possible competition between the electron injection and energy transfer between D-A with the Singlet-Singlet annihilation process that for high powers and densely packed systems, can occur on a similar time scale. In Figure A.3 of the Appendix, the relative power tests in both solution and DSSCs are presented and in order to simplify the study and minimize these effects that could give rise to additional processes, very low excitation powers were chose (30-50 mW for solution and 15-35 mW for DSSCs). In this manner, it is confirmed that the samples are excited within the linear-regime of excitation.

In Figure 5.11.A and B. the streak camera luminescence decays of **VG20** in solution and the corresponding transient spectra at various delays are shown, respectively. Both the fluorescence kinetics and the single wavelength kinetics of the transient spectra, were fitted with a two exponential function convoluted with the IRF and the corresponding values are shown in table 5.9. The two sub-ns components identified via streak camera

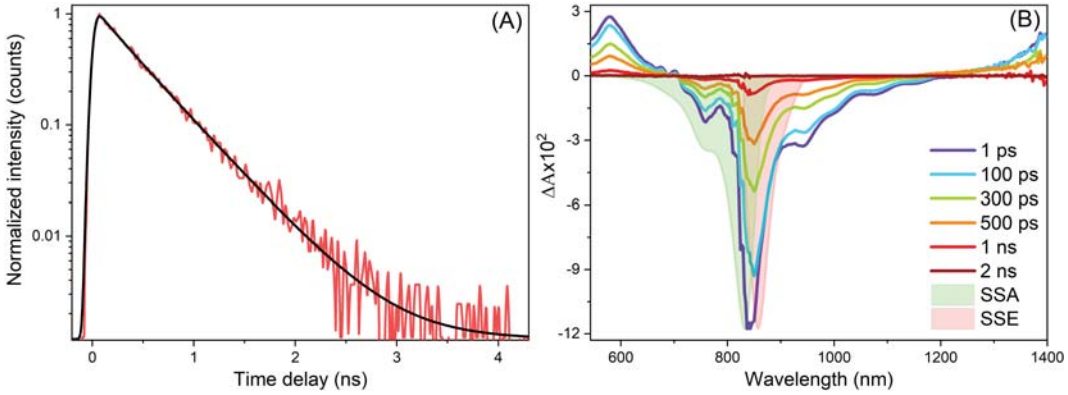

Figure 5.11: Time-resolved study of **VG20** dye (100 μmol/L) in 9:1 EtOH:DMSO solvent mixture including 50 mmol/L of CDCA by (A) Time-Correlated Single Photon Counting (TCSPC) kinetic as an average over the whole fluorescence spectrum. (B) Femtosecond pump-probe transient absorption spectra at different delays. The excitation was at 810 nm with a 90 $\mu J/cm^2$ pulse energy.

Table 5.9: TA kinetic parameters for **VG20** in EtOH:DMSO (9:1) solvent mixture obtained by femtosecond transient absorption spectroscopy.

λ (nm)	A_1 %	τ_1 (ps)	A_2 %	τ_2 (ps)
585	-15	4.2	100	410
760	-3	2.6	100	358
840	-10	1.1	100	323
950	-15	0.9	100	353
GA	-	8.2	-	365
Streak	93	390	7	925

measurements, 390 ps (93 %) and 925 ps (7 %) are attributed to the coexistence of cis and trans forms in solution. These values for **VG20**, are significantly faster than the ones found for other organic dyes or the benchmark ruthenium, used in DSSCs, which lie between 2 and 100 ns [2, 27–29], but we will see that the excited state quenching processes in DSSCs is $\sim$ 10 times faster for **VG20**.

The transient TAS spectra of **VG20** in solution are presented in Figure 5.11.B. Two positive signals are located in the spectral region of 500-640 nm and 1200-1400 nm, corresponding to the high and low energy ESA signals of **VG20** monomers. The broad negative signal (640-1200 nm) is a superposition of both the GSB and SE, as they spectrally match the inverted SSA (filled-green) and SSE (filled-red) spectra, respectively. In a first visual inspection, all spectral features appear to decay in parallel, with no additional rise of photoproduct species or due to interaction of different species, meaning that we are observing only the excited state decay.

In Figure 5.12, the kinetic decay curves, detected at 585, 769, 840 and 950 nm in (A) the first 10 ps and (B) in a full decay of 2 ns, are compared. The values obtained by fs-TAS (table 5.9) for single wavelength fittings are in agreement with the streak camera

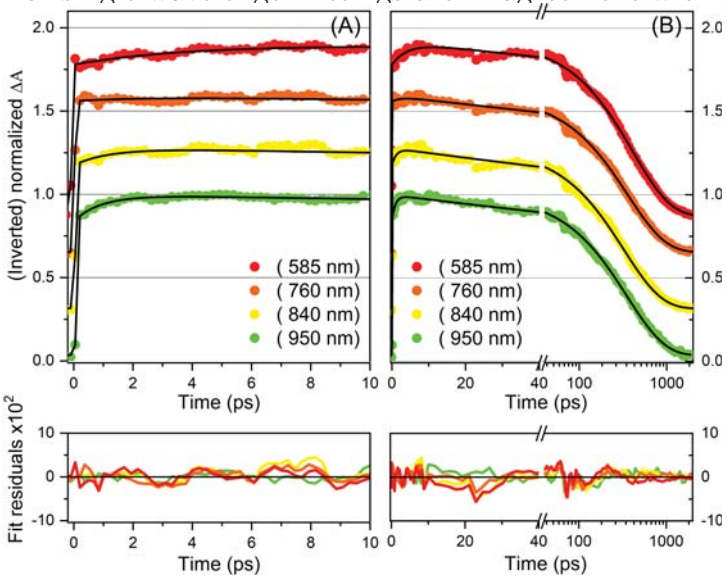

Figure 5.12: TA kinetic profiles of **VG20** in EtOH/DMSO (9/1) solution at various characteristic wavelengths: 585 nm, 760 nm, 840 nm and 950 nm, and at two different time scales. Fit residuals are provided in the bottom right. The sample was pumped at 810 nm with 90 $\mu J/cm^2$ energy pulse. Fit residuals (bottom left and right) are for 2-component exponential fits, convoluted with the 50 - fs instrument response function.

data, but no longer component is identified, possibly due to the limited dynamic range in TAS. In addition, the rise times in the range of 1-4 ps, for single kinetic fittings, are attributed to vibronic cooling processes due to thermalization in solution.

In addition, to single kinetic analysis, Global Analysis was performed and the DADS are shown in Figure 5.13, assuming a parallel excitation model. Two times were extracted, with the main contribution at 365 ps showing a negative signal peaking at 850 nm and a positive at 550 nm, indicating that the $S_1 - S_0$ relaxation time is in agreement with the ones obtained by single kinetic fittings and the streak camera analysis. The first time at 8.2 ps shows a negative feature and the maximum of the ESA, at 840 nm and a positive at 880 nm. The latter alternately positive and negative features indicate a gradual red-shift of the SE at early times, which is a typical sign of vibrational cooling due to thermalization processes in solution.

5.4.2 Ultrafast spectroscopy of VG20 in complete ZrO_2 and TiO_2 DSSCs

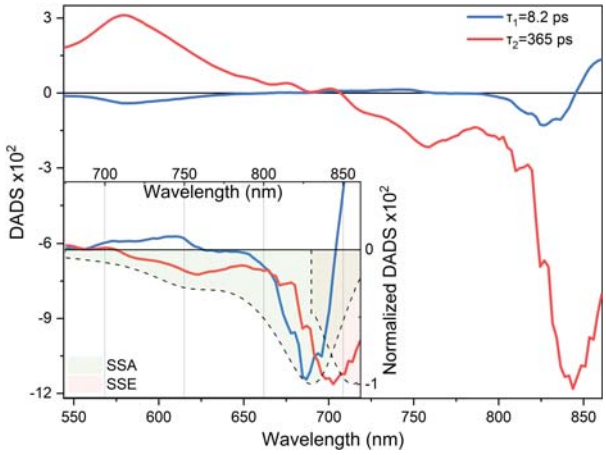

Figure 5.13: Wavelength-dependent amplitudes of **VG20** in EtOH/DMSO (9/1). The excitation was at 810 nm with a 90 $\mu J/cm^2$ pulse energy. Inset: The negative signals overlayed with the SSA and SSE.

In this section, after the solution investigation, the time-resolved analysis in real DSSCs is presented, for the cyanine **VG20** dye. The experimental strategy lies in the comparative study of non-injecting (ZrO_2) and injecting (TiO_2) systems. Figure 5.14.A., presents the differential absorption spectra, obtained in an average-representing data set, characteristic for ZrO_2 DSSCs. The transient absorption kinetics are presented in the Appendix (Figure A.4) for selected wavelengths. They clearly show wavelength dependent delay times and rise components, indicating various species or states, unlike solution. The transient spectra are characterized by a prominent ESA peaking at 580 nm, which in comparison to the data in solution, decays much faster in 40 ps (1/e). The negative signal extends in the range 700-1030 nm, matches the position of SSA and SSE and therefore, similar to solution, corresponds to GSB and SE from monomers. Furthermore, the GSB band for DSSCs, shows a double structure akin to the SSA spectrum corresponding to the aggregates GSB, peaking at 750 nm and the GSB of the monomers peaking at 850 nm. Interestingly, the aggregates GSB exhibits a small rise in the first 3 ps, while the monomer SE and ESA decay. The proposed photophysical mechanism taking place, is Förster Energy Transfer from the monomers excited state to the aggregates absorption at lower energy. Energy transfer (ET) occurs towards the low-energy aggregate excited state, as it is indicated by the long wavelength absorption band of the aggregate spectrum, but since both states share the same ground state, this process also increases the GSB of the high-energy transition. During the rise time of the GSB at 750 nm, the ESA at 480-640 nm demonstrates an inhomogeneous decay, with the higher energy part (520 nm) to decay slower than the initial maximum at 580 nm. In the 10 ps spectrum a weak

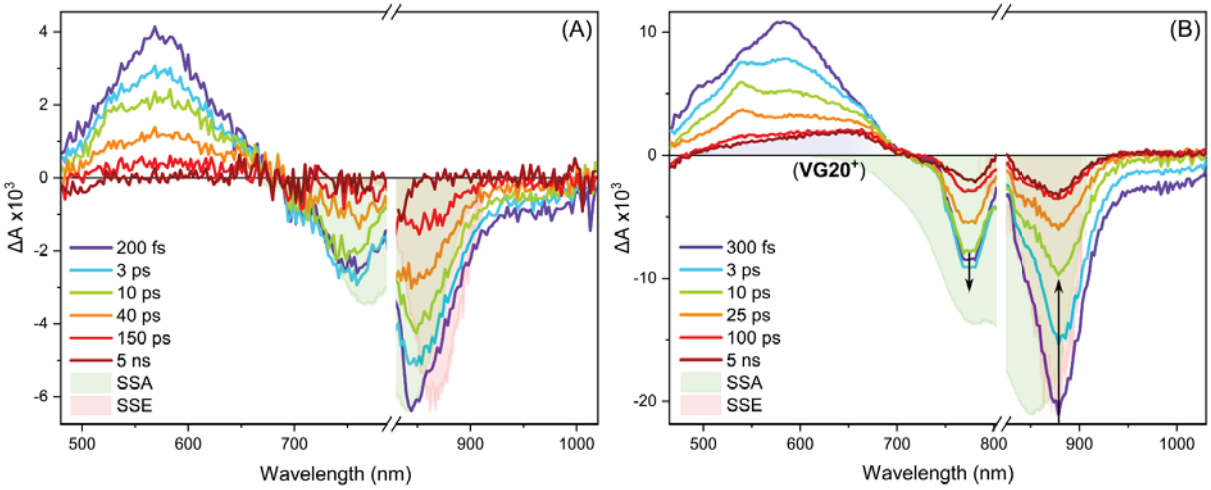

Figure 5.14: Transient spectra of **VG20** dye anchored on (A) non-injecting ZrO_2 nanocrystals and (B) injecting TiO_2 nanocrystals, for optimal [CDCA]. The devices were excited at 800 nm with an energy of 90 $\mu J/cm^2$. The electrolyte is composed of 1 mol/L $DMII$, 30 $mmol/L$ I_2, and 1 mol/L LiI in acetonitrile. SSA and SSE are steady-state absorption and emission spectra arbitrarily scaled for comparison and allow identification of the regions where ground state bleach (GSB) and stimulated emission (SE) dominate the signal. The SSE spectrum is available only for $\lambda < 920$ nm, due to the limited sensitivity of the fluorometer used.

and narrow band emerges at 530 nm. This observation reveals that in contrast to the solution, in which the high energy ESA refers to monomers only, in the DSSC this broad signal (480-640 nm) contains features of both the ESA of monomers and aggregates. A similarity with the solution is that for the ZrO_2 DSSC, there is a full decay of all species at long times (5 ns), revealing that no long-lived photoproduct is formed at earlier times and therefore no electron injection occurs, as expected for DSSCs with SC with a CB higher than the LUMO (e.g. ZrO_2). However, the much faster decay times are due to efficient quenching by the aggregates, due to ET. Finally, in the region 900-1030 nm, it can be considered that only the SE from monomers is involved and the analysis of the pure SE dynamics should contain all the components related to the quenching mechanisms. Therefore, no need for additional and complementary fs-fluorescence measurements were needed to be done for **VG20**.

The excited state dynamics of the injecting and operating TiO_2 DSSCs were also examined. Figure 5.14.B illustrates the transient spectra at various delays in optimal CDCA concentration. Kinetics for selected wavelengths are shown in the Appendix (Figure A.5) and appear wavelength-dependent, such as for ZrO_2 DSSCs with similar main spectral features (Figure 5.14) as for the non-injecting DSSC. A broad ESA signal extends from 480-700 nm with an even more pronounced bi-modal decay due to aggregates.

Indeed, within the ESA decay the higher energy part decays slower, forming eventually a distinguished peak at 540 nm, referring to the ESA part of the aggregates with a different relaxation than the monomers ESA. In general, the decay evolution is even faster than in ZrO_2 and in only 25 ps all spectral features have decayed, leaving an extended residual positive band, spanning the visible part of the spectrum and peaking at 660 nm (cf. 100 ps delay), which doesn't decay further within the 5 ns time window of the set-up. Such a residual long-lived signature is assigned to the absorption of the **VG20** radical cation $\boldsymbol{VG20^+}$, in good agreement with the transient spectra measured using the ns-TAS experiment (Figure 5.9.B). In the near-IR part, SE is observed in the 850-1030 nm range, which decays into the noise within 25 ps. The GSB signal, similar to the case of ZrO_2, exhibits a double peak structure, identical to the SSA structure, due to monomers and aggregates. The high energy band, peaking at 780 nm, corresponds to the GSB of the aggregates, while the lower energy band at 880 nm, up to 1030 nm to represent both the GSB and the SE from monomers. The 880 nm band has decayed by half its amplitude within 10 ps and reaches the stable level of 20 % of the initial value by 100 ps. While the fast decay is due to SE decay and partial ground state recovery, the long-time asymptote is due to formation of the radical dye cation and mirrors the percentage of monomers that never return to the ground state, in the available time-window. In the same manner as it was described for the ZrO_2 DSSC, in 3 ps a small rise of the 780 nm band demonstrates a clear evidence of the aggregate excitation via FRET from monomers (Figure 5.14.A). In the same time, the sharp absorption feature at 540 nm develops, indicating the monomers-aggregates energy transfer in the visible spectral region. From the transient spectra it is possible to calculate approximately the injection efficiency as follows. If all molecules (monomers and aggregates) were to inject and convert to photoproducts and since the cation absorption is negligible in the region of dominant GSB (800-900 nm)[1], the negative ΔA signal should not decay with time, contrary to what is observed herein, meaning that the carrier injection yield (Φ_{inj}) is well below 100 %. Therefore the Φ_{inj} can be expressed as the ratio of the concentration of the dyes that didn't return to the ground state (or equivalently the ones that injected and converted to cations) to the total excited ones. Therefore, from Beer-Lambert law, for the same wavelength the molar extinction coefficients and sample thicknesses can be removed and finally:

$$\Phi_{inj} = \frac{-\Delta C_{t_0}}{-\Delta C_{t\to\inf}} = \frac{C_{VG20^+}}{C_{VG20^*}} = \frac{\Delta A_{GSB_{max},t\to\infty}}{\Delta A_{GSB_{max},t=0}} \tag{5.7}$$

[1]Remember the weak extinction coefficient of $\boldsymbol{VG20^+}$ (Figure 5.9)

Consequently, for the real data, the ratio GSB(t = 0.2 ps)/GSB(t = 5 ns) provides an estimate of Φ_{inj}. Nevertheless, part of ΔA intensity contains SE contribution, thus the determination of the pure GSB component can be challenging. Nevertheless, analyzing the ΔA(t = 0.2 ps)/ΔA(t = 5 ns) ratio at different wavelengths (770-850 nm) provides an upper limit of $\Phi_{inj} \approx$ 30-35 %. These values are lower than the IPCE one for the corresponding wavelength ($\approx$ 40-45 %), but relatively consistent. The deviation is explained by the TAS experimental conditions that are different than the corresponding IPCE ones, in terms of excitation power (i.e. nonlinear response of DSSCs between cell photocurrent and incident light power) and the absence of a scattering layer in the device made for TAS measurements.

In order to highlight the carrier injection processes and their kinetics, the kinetic traces obtained by averaging seven TiO_2-based and three ZrO_2-based devices, are shown in Figure 5.15. The filled area around the decay kinetics results from the calculated standard error over the averaged number of samples and the dotted kinetics correspond to outlier samples. This statistical characterization approximately visualizes a very high sample-to-sample reproducibility. Selected wavelengths represent (A) the monomer ESA, (B) the dye radical cation absorption, (C) the low-energy GSB band and (D) the SE. The prominent long-lived signal for TiO_2 is due to the **VG20** radical cation absorption (580 and 650 nm) and incomplete GSB recovery (880 nm). Note a small positive absorption in the SE trace (975 nm) of TiO_2 ($\lambda \approx$ 975 nm), which is most likely due to absorption by free carriers in TiO_2 or to a near-IR tail of the radical cation absorption. Finally, the SE part of ZrO_2, as it has already been mentioned, decays slower than for TiO_2, because in the latter two quenching mechanisms take place (ET and injection).

The photophysical model, suggested by the data, is pictorially illustrated in a modified Perrin-Jablonski diagram in Figure 5.16.C and the two corresponding reaction schemes, for both ZrO_2 and TiO_2 DSSCs are shown in Figure 5.17 for both monomers and aggregates, starting from photoexcitation and reaching the complete relaxation towards the ground state. Four exponentials describe the data best, as it can be seen in detail in Figure A.6 of the Appendix. As summarized in table A.2, of the Appendix, the characteristic lifetimes for TiO_2 are in the 0.5-1 ps, 4-8 ps and 20-40 ps range, in addition to a fixed 100 ns time accounting for the non-decaying signals at long times. In order to determine the most characteristic lifetimes and mechanisms, a global fit approach was carried out, i.e. the wavelength-dependent decay times are approximated by four wavelength-independent values and the relevant Decay Associated Different Spectra (DADS) were constructed for both the injecting and non-injecting DSSCs. For TiO_2 (Figure 5.16.B), the constants

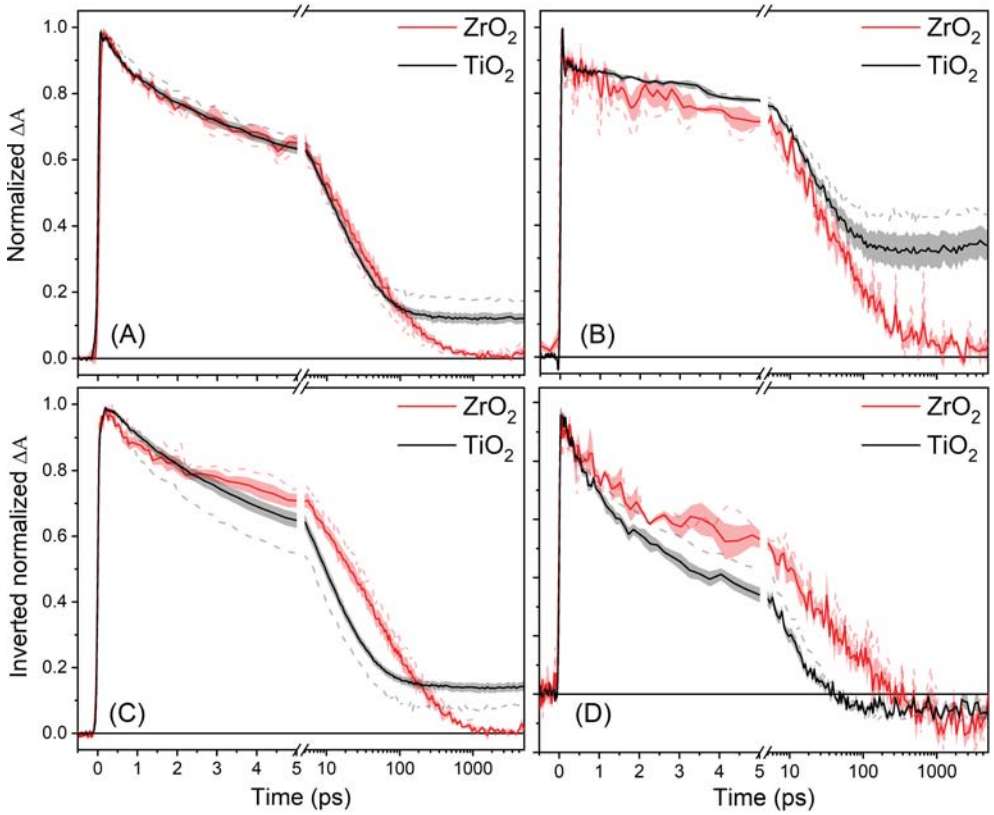

Figure 5.15: Comparison of normalized transient absorption kinetic profiles (solid line) for the **VG20**-based DSSC using either ZrO_2, or TiO_2 nanocrystals at (a) 570 nm (ZrO_2) and 585 nm (TiO_2), (b) 640 nm (ZrO_2) and 650 nm (TiO_2), (c) 860 nm (ZrO_2) and 880 nm (TiO_2), and (d) 960 nm (ZrO_2) and 975 nm (TiO_2). The kinetic sign is inverted for (C) and (D). All DSSC devices were excited at 800 nm with 90 $\mu J/cm^2$. The kinetics are averaged over seven samples for TiO_2 and three samples for ZrO_2. The devices were pumped at 800 nm with an energy of 90 $\mu J/cm^2$. The filled graphs indicate the statistical standard error and the dotted-line kinetics corresponding to the more deviated from the averaged value kinetic.

obtained via global analysis are 0.4 ps, 4.3 ps, 25 ps and 100 ns (Table 5.10), with the latter value being fixed for the fit. The special features of the DADS, allow identifying the main excited state processes, i.e. the monomer-to-aggregate energy transfer, the carrier injection/radical cation formation and their respective lifetimes.

In order to facilitate the interpretation of the photophysically rich analysis and based on the rather complicated DADS features, a graphical illustration of the various species and mechanisms is shown in Figure 5.16, for TiO_2 DSSCs. As it was already suggested from the TAS spectra, the high energy ESA band (480-700 nm) contains all monomer, aggregate and radical-monomer features, while the negative signals (700-1030 nm), involve

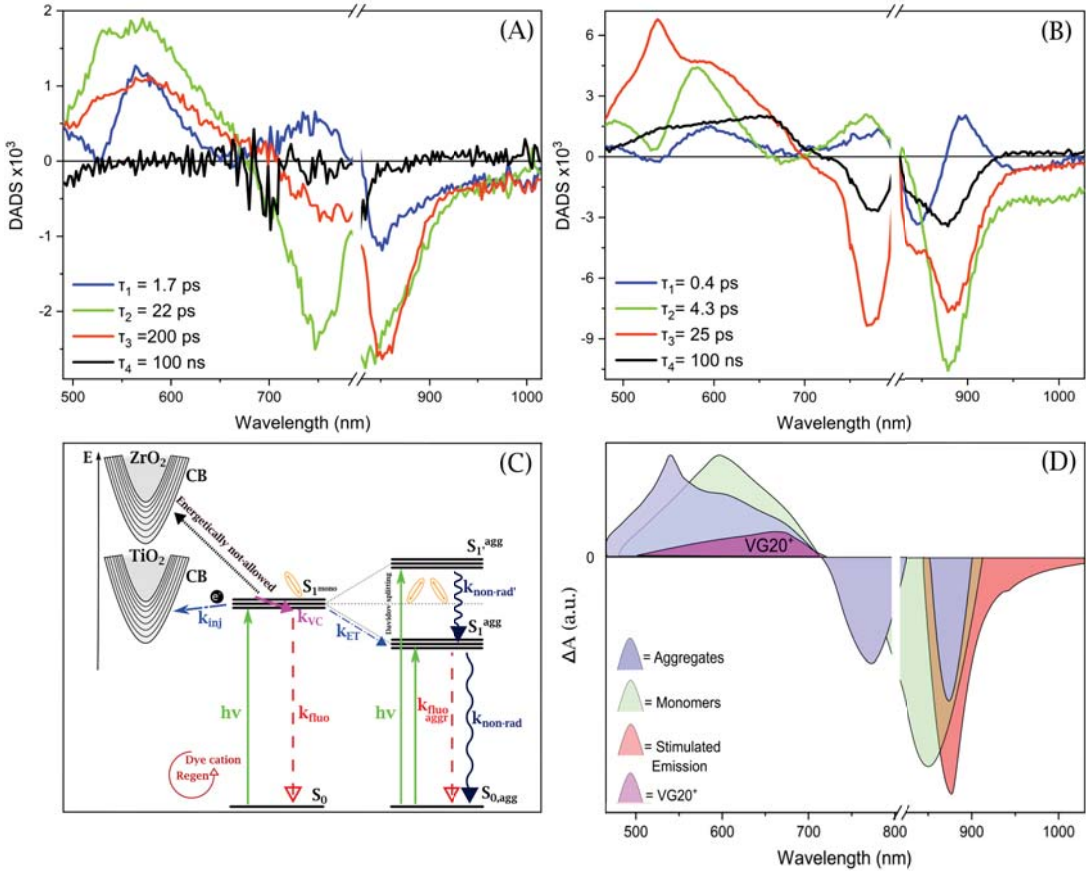

Figure 5.16: Wavelength-dependent amplitudes of **VG20** in (A) non-injecting ZrO_2 and (B) injecting TiO_2 DSSCS. (C) Simplified photophysical excited state diagram for both monomers and aggregates in the dye-SC interface and (D) a pictorial representation of ΔA spectra corresponding to the various species (monomers, aggregates and dye-cations) and SE, for TiO_2 DSSCs. The devices were pumped at 800 nm with an energy of 90 $\mu J/cm^2$.

both the monomer and two-band aggregates GSB, as well as, the SE from the monomers. The rise of the 770 nm GSB band and the 530 nm aggregateESA peak are the fingerprint of ET, reflected in the DADS with dominating positive and negative signals, respectively. Hence, the energy transfer with rate k_{ET} is operative during the sub-ps (0.4 ps) and the $\approx$ 4 ps phases (Figure 5.16.B). Charge injection/radical cation formation is best identified as a rise of the absorption at the radical cation peak wavelength (660-670 nm) and monomer excited state decay, i.e. the decay of SE (>950 nm). The DADS of Figure 5.16.B, demonstrates that charge injection, with rate k_{inj}, occurs concomitantly with the energy transfer, dominantly during the $\approx$ 4 ps time scale and to a minor extent at shorter times (0.4 ps DADS). In the same manner, at shorter times (0.4 ps), in addition to ET, solvation takes place, as it can be observed by the gradual red-shift of the SE. In the

DADS it can be seen, for 0.4 ps, as a negative GSB/SE feature peaking at 850 nm and a SE positive feature at 880 nm. This features indicate that the initially excited species, undergo solvation in 0.4 ps and eventually relax through thermalization processes, to a more stabilized S_1 state, of lower energy. This spectral response is similar to the one quoted for **VG20** DADS in solution (Figure 5.11). The 25 ps (DADS) is characterized by both the SE and ESA decays, for both monomers and aggregates (peak at 530 nm), but these decay amplitudes hide, possibly, weaker signatures of radical cation formation, since the 25 ps DADS at 660 nm is purely positive (i.e. ESA decay). Again the small cation extinction coefficient may be the reason.

Table 5.10: Average lifetimes, characterizing the main photophysical processes for **VG20** on ZrO_2 and TiO_2 DSSCs obtained from fs-Transient Absorption Studies*.

VG20 DSSCs	$\boldsymbol{\tau_1}$ **(*ps*)**	$\boldsymbol{\tau_2}$ **(*ps*)**	$\boldsymbol{\tau_3}$ **(*ps*)**	$\boldsymbol{\tau_4}$ **(*ns*)**
TiO_2 [1:500]	0.4	4.3	25	100
ZrO_2 [1:500]	1.7	22	200	100

*τ_1 is dominated by monomer-to-aggregate energy transfer. For TiO_2 devices, electron injection occurs on both the τ_1 and τ_2 time scales.

The same global analysis on ZrO_2 is reported in Figure 5.16.A. It reveals four time constants: 1.7 ps, 22 ps and 200 ps (Table 5.10), in addition to a long-lived, but almost vanishing 100 ns, used for consistency with the fittings of the TiO_2 data, but with an amplitude in the noise level. The fastest 1.7 ps component (blue line) displays DADS very similar to that of TiO_2, with all the features consistent with the features of monomer-to-aggregate energy transfer (k_{ET}). The ca. 22 ps component (green curve) displays signatures of both monomer and aggregate excited state decay. In detail, when the monomer SE ($>$ 850 nm) decays in parallel with the aggregate GSB recovery (750 nm) and the monomer ESA decay (450-680 nm), including the weak sharp feature of the aggregate ESA at 530 nm. The most plausible explanation is that aggregates decay in parallel with the remaining monomers. This is indicated by the SE component of the 22 ps DADS, due to monomers only. Note that the fast $\simeq$ 4 ps component, observed for electron injection (DADS negative at 660-680 nm) is absent as expected. Remarkably, the longer $\approx$ 200 ps component (red curve) is due to a second, slower, monomer excited state decay (k_{nr}), since it displays SE, ESA, and GSB recovery very similarly, although with a shorter lifetime, to **VG20** in solution (Figure 5.11). This population of monomers could correspond to weakly attached monomers or non-attached dyes diffused in the electrolyte

or in general to monomers that don't interact with aggregates, in order to undergo ET and therefore they decay independently.

In summary, the comparison of **VG20** on TiO_2 and ZrO_2, allows to identify the kinetic signatures of electron injection from monomers (k_{inj}) clearly within 4 ps. Also, the reduction of τ_1 from 1.7 to 0.4 ps indicates that injection occurs in TiO_2 and sub-ps time scale, too. However, injection is competing with monomer-to-aggregate energy transfer (k_{ET}) identified already on a 0.4 ps time scale, but also on the slower 4 ps lifetime (Table 5.10). The wide range of injection times has already been mentioned originate from sample inhomogeneity. The inhomogeneity could originate from dyes attached to the SC NP, in a distribution of distances, resulting in a distribution of injection rates or even from loosely or non- attached dyes in the electrolyte that also inject. In Figure 5.17 the excited state reaction schemes for both ZrO_2 and TiO_2 DSSCs are presented. For a given excitation both monomers and aggregates can be excited, however aggregates can be excited by ET from monomers too, relaxing in $\sim$ 25 ps.

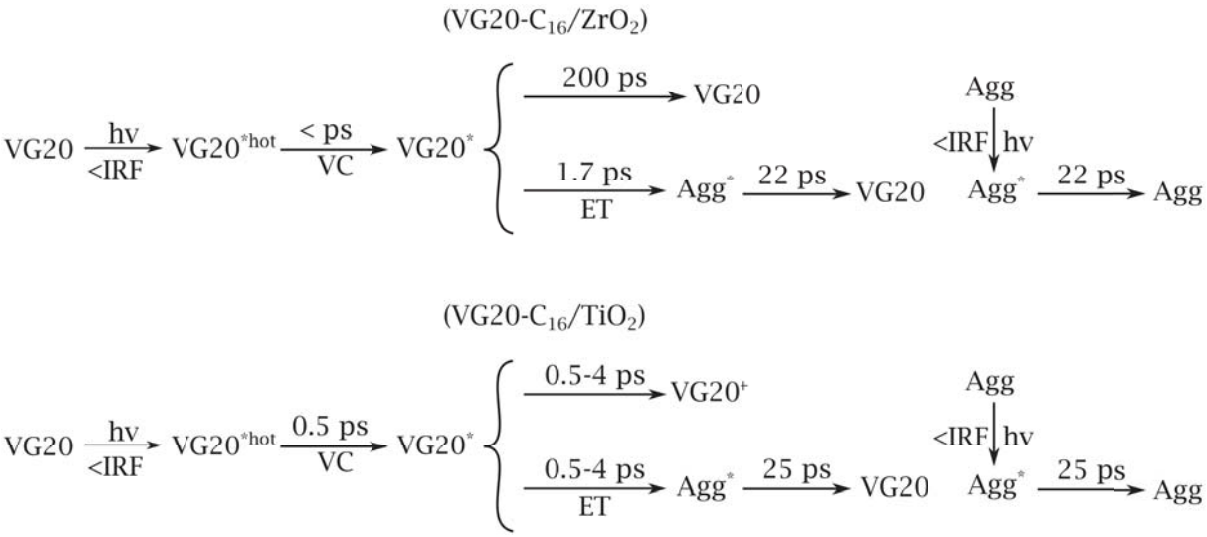

Figure 5.17: Excited state reaction schemes: On TiO_2, **VG20*** can form the $\boldsymbol{VG20^+}$ cation due to electron injection, or decay into excited state aggregates (Agg*) due to energy transfer. Photo-excited aggregates return to the ground state (**VG20**) due to self-quenching. On ZrO_2, **VG20*** undergoes ET, but also dominantly non-radiative recombination to **VG20**. Lifetimes as discussed in the text.

5.4.3 The effect of CDCA on VG20 ZrO_2 and TiO_2 DSSCs

In the previous section a photophysical model, describing best the experimental data, was constructed for the **VG20** DSSCs. The DSSC samples were always prepared under optimal conditions and the main limiting factor for injection and therefore higher PCE was found to be the presence of aggregates. Therefore, in this section the aggregates effect is examined, by studying a series of both non-injecting and injecting DSSCs, prepared at different [Dye:CDCA] concentrations, starting from DSSCs with no addition of CDCA, up to very high concentrations [1:1000]. The effect of the increase of the intermolecular distances (upon adding CDCA) on the ET and injection rates are examined via TAS and the determination of the injection efficiencies of various systems of different aggregate percentages can be made.

The TAS spectra at chosen time delays are presented in Figure 5.18.A-D, for ZrO_2 DSSCs, while increasing the CDCA concentration, respectively. The corresponding SSA were presented in Figure 5.5.A. The sample in Figure 5.18.C, is the same as in Figure 5.14.A and is kept just for comparison with the more and less aggregated DSSCs. These systems have been made to be essentially non-injecting and therefore only the ET process is present. By first inspection, all spectral features are similar and they were analytically characterized in section 5.4.2. The signal-to-noise ratio is higher for the [1:0] and [1:100] DSSCs, as the total OD of the samples is ∼4 times higher than for the [1:500] and [1:100] DSSCs (Figure 5.5.A.Inset). Adding CDCA, significantly reduces aggregates by sacrificing OD and the total signal drops by a factor of 6-7, from the [1:100] to the [1:500] Dye:CDCA ratio and another factor of ≈ 2 for [1:1000] CDCA. Furthermore, the attribution of the aggregate features is confirmed and validated by the spectral trend, as the CDCA concentration increases. More in detail, for all cases, a positive ESA band is observed at ∼450-680 nm, containing, essentially, both the aggregate (at higher energies) and monomer (at lower energies) ESA, as it has already been suggested (see sharp aggregate feature at 530-540 nm for low [CDCA]). In the same manner, the broad negative signal (∼680-1030 nm), consists of the GSB of aggregates (700-780 nm) and the GSB/SE of monomers (780-1030 nm), in agreement with the SSA and SSE spectral positions. Note that the region around ∼900-1030 nm can be analyzed as a pure SE region, with a small contribution of possible free-electron in the SC absorption that can be noticed as a negligible long time positive signal (>1 ns). The main GSB signal, is generally blue-shifted at early times (∼ 100 fs) with reference to the maximum ΔA:SE, due to the initial population of the hot S_1 state, as it has already been suggested. In the zero CDCA case (A), after 100 fs a pronounced $\mathrm{ESA}_a gg$ peak at 540 nm starts to form, completely resolved from the initial and faster decaying max of the ESA at 580 nm. Moreover, for

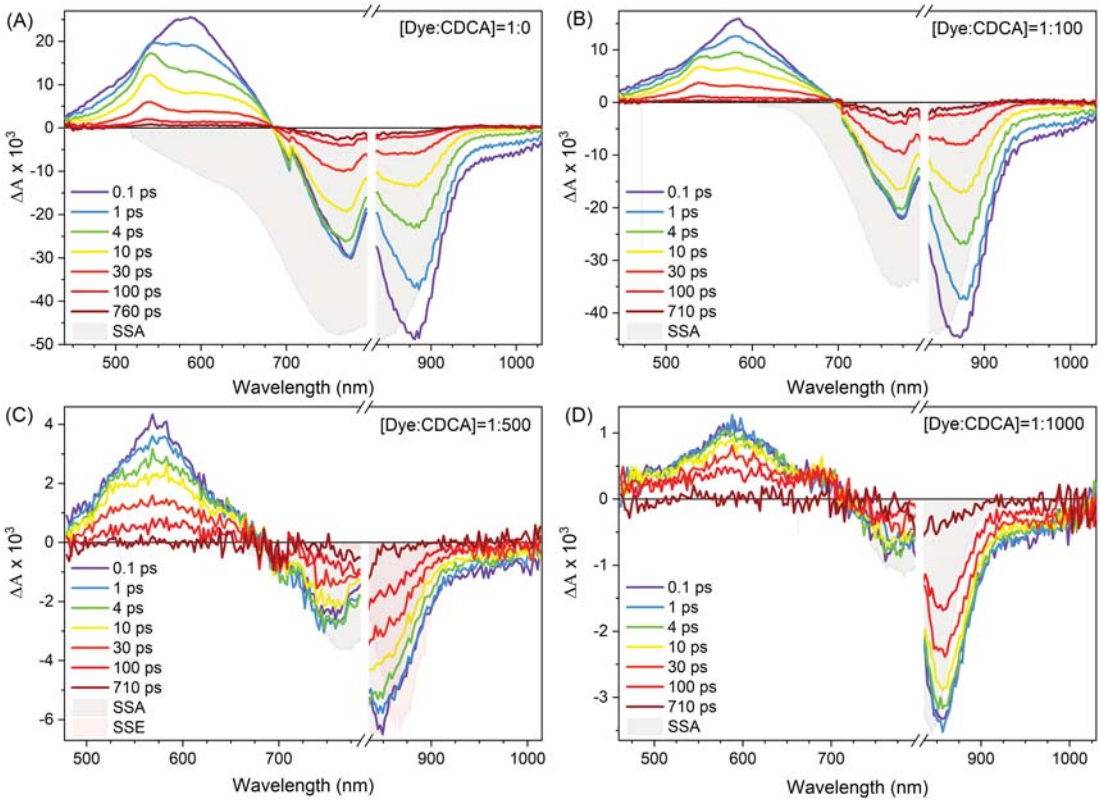

Figure 5.18: Transient spectra at different time-delays of **VG20** ZrO_2 DSSCs of (A) [1:0], (B) [1:100], (C) [1:500] and (D) [1:1000] Dye:CDCA concentration ratios. The devices were excited at 800 nm with an energy of 90 $\mu J/cm^2$. The electrolyte is composed of 1 mol/L $DMII$, 30 $mmol/L$ I_2, and 1 mol/L LiI in acetonitrile. The inverted SSA and SSE are the steady-state absorption and emission spectra arbitrarily scaled for comparison, for selected DSSCs and allow identification of the regions where ground state bleach (GSB) and stimulated emission (SE) dominate the signal.

the extreme case of zero CDCA, the aggregate ESA (540 nm), shows a small rise. In the NIR region, this dynamic progression is accompanied by a rise of the aggregates GSB (758-780 nm) that has been attributed to ET from monomers in aggregates in the first ps. In the less aggregated samples (B) and (C), the amplitude of the ESA shoulder (540 nm) is decreased, compared to the amplitude of the monomers ESA (580 nm). In the least aggregated case (D), the shoulder cannot be observed, similarly to the monomer TAS spectra, consistent with it originating from aggregate ESA. Eye catching is the difference in the GSB recovery times for all four systems. For the [1:0] DSSC, the GSB (880 nm) depletes by half ΔA, compared to the initial intensity at 4 ps, while for increasing [CDCA] the recovery becomes slower and finally for the [1:1000] DSSC, the intensity depletes in half in $\sim$ 100 ps. The 770 nm GSB, after the ET rise, appears to decay slower revealing the slower deactivation times of the aggregates.

Since, the ZrO_2 DSSC are called non-injecting systems, there should be no photo-product formation at 650 nm, as it has been mentioned in section 5.4.3 for the [1:500] DSSC. However, in [1:0] and [1:100] DSSCs (Figure 5.18.A,B.), in which the signal/noise ratio is higher, the long time transient spectra show a small positive signal in the 450-690 nm region and a negative bleach residual (<10 %), indicating a minor formation of **VG20** cations. This particularity has been observed for similar systems and can be attributed to two scenarios, either to injection to deep trap states of ZrO_2 or to an aggregates' effect. The second has been proposed for solid state DSSCs [13], referring to intra-aggregate electron transfer from one monomer to another, explaining also the competition of this process with the injection to the SC from the aggregates.

To illustrate the differences of the complicated spectral evolution, the kinetics are displayed, for selected wavelengths in Figures 5.19 and 5.20. Table 5.11, contains the life-

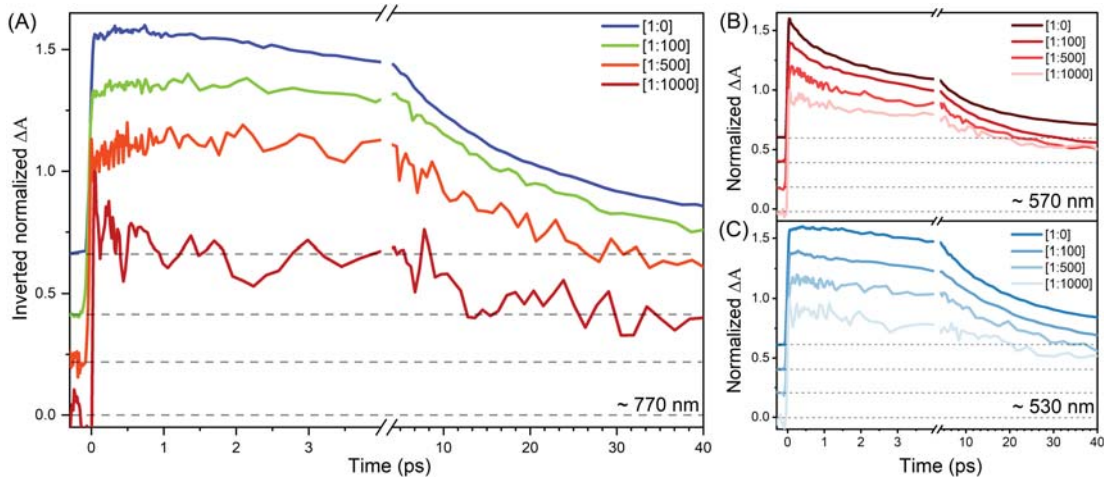

Figure 5.19: Normalized and shifted in the y-axis, kinetic traces of **VG20** ZrO_2 DSSCs of different CDCA concentrations in the visible spectral region, obtained by TAS. Detection at (A) 770 nm, (B) 570 nm and (C) 530, probing the aggregate GSB (inverted sign), the monomer ESA and the aggregate ESA, respectively.

times, as they were calculated from global analysis for simplicity, using four exponential functions convoluted with the IRF and for only the selected SE kinetic, for all CDCA concentrations under study. The complete tables with the fitting times for numerous wavelengths, expanded in the whole spectral region for both the ZrO_2 and TiO_2 DSSCs are shown in the Appendix tables A.1, A.2. Probing the ET process, Figure 5.19.A, shows the kinetics, detected at the aggregate GSB (770 nm). It is evident that from [1:0] to [1:1000], there is a clear trend in early times, relative to a rise, which reveals the ET from monomers to aggregates. It is in agreement with the corresponding rapid decays of the monomers SE (920-980 nm) (Figure 5.20. 880 nm). By visual inspection,

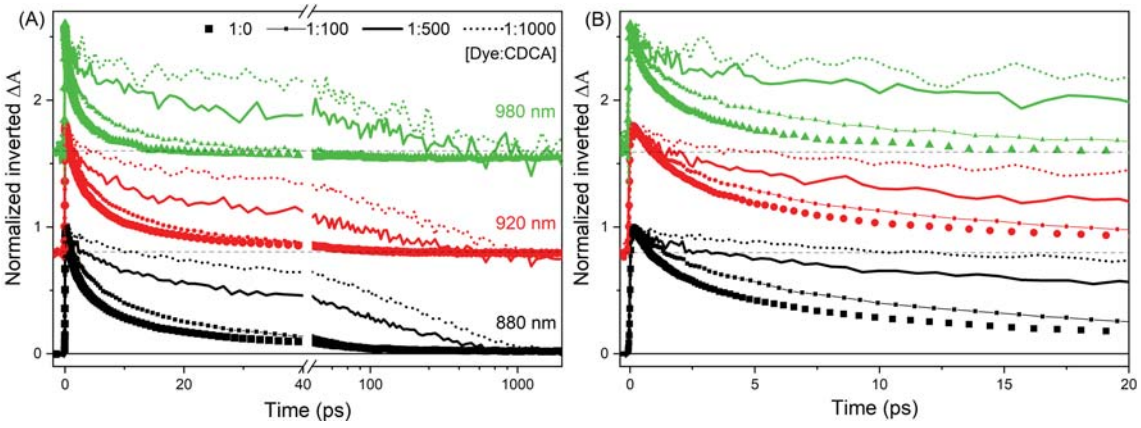

Figure 5.20: Normalized kinetic traces of **VG20** ZrO_2 DSSCs of different CDCA concentrations in the near-IR spectral region (920 and 980 nm), probing the GSB (880 nm) of the monomers and the SE parts. (A) The kinetics in the full time window with a brake at 40 ps and (B) The kinetics in the first 20 ps. The colour code refers to detection wavelength and the traces shifted vertically.

the rise is faster in the more aggregated samples and for the least aggregated [1:1000] there is a slow decay, indicating the co-existence of both monomers and aggregates GSB signals and therefore the exact determination of the ET times is complicated. Indeed, the single wavelength fits (table A.1) reveal rise times in the range of 0.7-1.4 ps with an unexpected small dependence on the CDCA concentration. The same uncertainty, in the CDCA effect on the ET times, is found when one examines the ESA of the monomers (530 nm) and aggregates (570 nm) (Figure 5.19.B and C, respectively).

The effect of [CDCA] is more obvious in the near-IR (Figure 5.20), it is evident that for smaller CDCA concentrations the total dynamics of the SE part (980 nm) and the GSB/SE of the monomers become drastically faster, as it is expected for the more aggregated DSSCs, with the most pronounced ET contributions, The ET times should appear as a faster SE decay as a function of [CDCA]. Indeed, the faster times range from 0.3 ps for [1:0] to 1.4 for [1:1000], with the contribution to decrease from 31 % to 21 %, respectively, as the ET contribution decreases (table 5.11). Therefore, it can be concluded, as it was expected that by increasing the intermolecular distances between donor and acceptor the ET times increase.

The other time constants are rather difficult to precisely identify and therefore the DADS have been plotted and presented in the Appendix (Figure A.7) to visualize the spectral responses and attribute, in a wider approximation the ET and the aggregate/monomer relaxation times. The time constants obtained by global analysis are in the same range as the ones determined for the SE. For all DADS, the last time was fixed

to 100 ns to fit the long time residual signal. For the [1:0] and [1:100] samples, the DADS

Table 5.11: Fit values for the SE decay of **VG20** ZrO_2 DSSCs of different CDCA concentrations and the corresponding time constants obtained by GA.

[Dye:CDCA]	**λ(nm)**	$A_1\%$	$\tau_1 ps$	$A_2\%$	$\tau_2 ps$	$A_3\%$	$\tau_3 ps$	$A_4\%$	$\tau_4 ps$
[1:0]	980	31	0.3	50.6	2.2	18.3	14	-4.5	inf
	GA	-	0.5	-	3.6	-	25.0	-	100
[1:100]	980	28.7	0.5	50	4.1	22.3	32	-4.9	inf
	GA	-	0.3	-	4.1	-	31.0	-	100
[1:500]	960	36.4	1.2	41.5	20.0	32.1	383	-7.6	inf
	GA	-	1.7	-	21.4	-	193	-	100
[1:1000]	970	21	1.4	36.2	70.7	40	217	3.0	inf
	GA	-	0.9	-	21.3	-	300	-	100

for the first two times ($\sim$ 300 fs, $\sim$ 4 ps) show clear evidence of ET, rise of the aggregate ESA (540 nm), a decay of signal of monomer ESA (580 nm), rise of the aggregate GSB region (770 nm) and a SE decay (980 nm). Furthermore, both components show strong SE decays. The DADS of τ_3, shows only monomer features and therefore is attributed to the relaxation of monomers that don't undergo ET at all. For the least aggregated sample [1:1000], there are no strong ET features and the τ_3 value approximates the lifetime found in solution (100 % monomers).

The investigation of the non-injecting DSSCs of various CDCA concentrations, revealed the dependence of the ET times on CDCA and hence on the average donor-acceptor intermolecular distances. In the same experimental approach, on the injecting TiO_2 DSSCs, the effect of CDCA on the injection times and yields can be identified. In Figure 5.21.A-D, the transient spectra of **VG20** TiO_2 DSSCs are presented for [1:0], [1:100], [1:500] and [1:1000] dye:CDCA concentration ratios, respectively. As it was mentioned in section 5.4.3 for the [1:500] case, the main spectral features are almost identical to ZrO_2, with the exception of photoproduct absorption at long times (460-680 nm). The inverted SSA are also included as "filled spectra and appear to be slightly blue-shifted compared to the main GSB. The TiO_2 DSSCs have higher optical density (OD) than the ZrO_2 devices and already from the SSA spectra it has been shown that they are more aggregated (Figure 5.5). The SSA of the extreme case of zero CDCA (Figure 5.21.A), exhibits higher absorption of the aggregate feature (770 nm), compared to the monomer one (850 nm). In addition, the corresponding main GSB in the TAS spectra is absorption

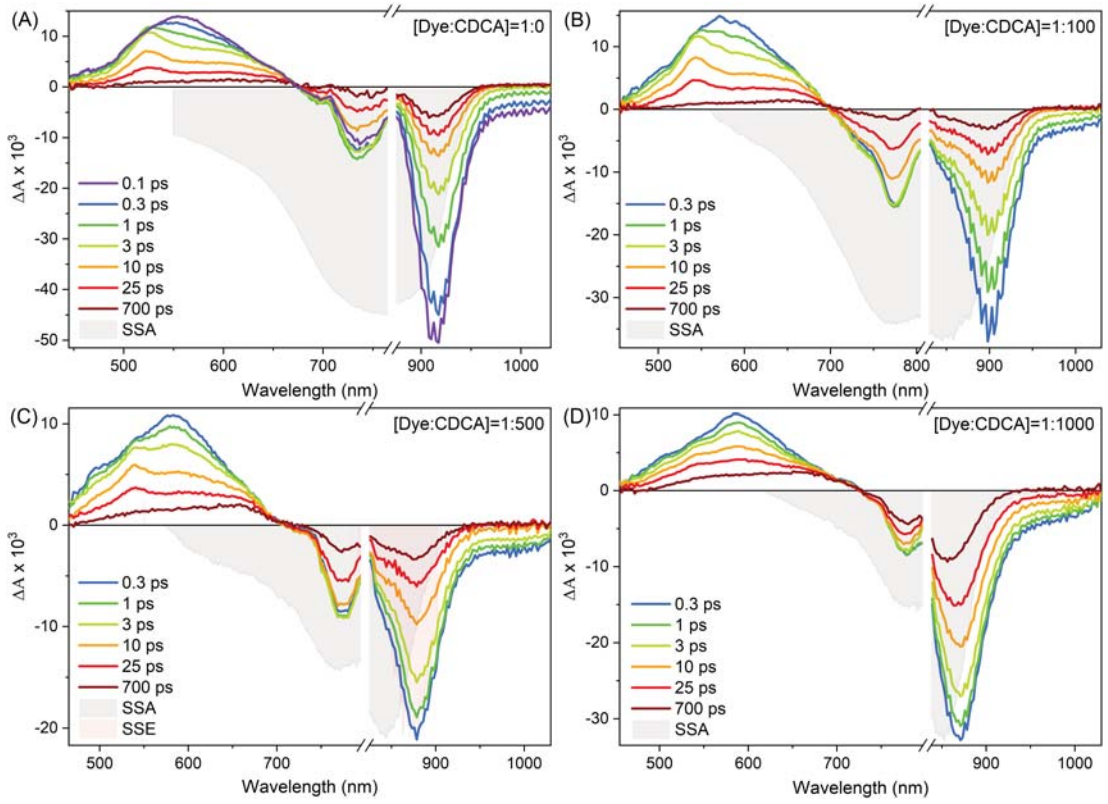

Figure 5.21: Transient spectra at different time-delays of **VG20** TiO_2 DSSCs of (A) [1:0], (B) [1:100], (C) [1:500] and (D) [1:1000] Dye:CDCA concentration ratios. The devices were excited at 800 nm with an energy of 90 $\mu J/cm^2$. The electrolyte is composed of 1 mol/L $DMII$, 30 $mmol/L$ I_2, *and* 1 mol/L LiI in acetonitrile. SSA and SSE are steady-state absorption and emission spectra arbitrarily scaled for comparison, for selected DSSCs and allow identification of the regions where ground state bleach (GSB) and stimulated emission (SE) dominate the signal.

saturated and the GSB is masked. The ET features are identical to ZrO_2, as expected. In the more aggregated DSSCs of lower [CDCA], the aggregate ESA feature at 540 nm is sharper and rises from sub-ps to 3 ps times and then decays slower than the monomers ESA at 580 nm. In the same times the aggregate GSB (770 nm) shows similar trend.

The GSB/SE part of the spectrum (880-900 nm) reaches its half intensity (ΔA) for [1:0] $\sim$ 1 ps, much faster than in ZrO_2, due to the presence of electron injection in TiO_2. Upon de-aggregation, the decay becomes slower and for [1:1000] the half GSB value is reached in around 10 ps. This trend, as well as the rise at 770 nm, due to ET, are well illustrated, by comparing selected kinetics in Figure 5.22.A, in the full time-window with a break at 20 ps and in Figure 5.22.B, in a 2 ps range. Impressively, the SE part ($\sim$ 1000 nm) for [1:0] has almost fully decayed in only 2-3 ps. The fitting values resulting from a four exponential convoluted with the IRF of the SE and the corresponding GA values are

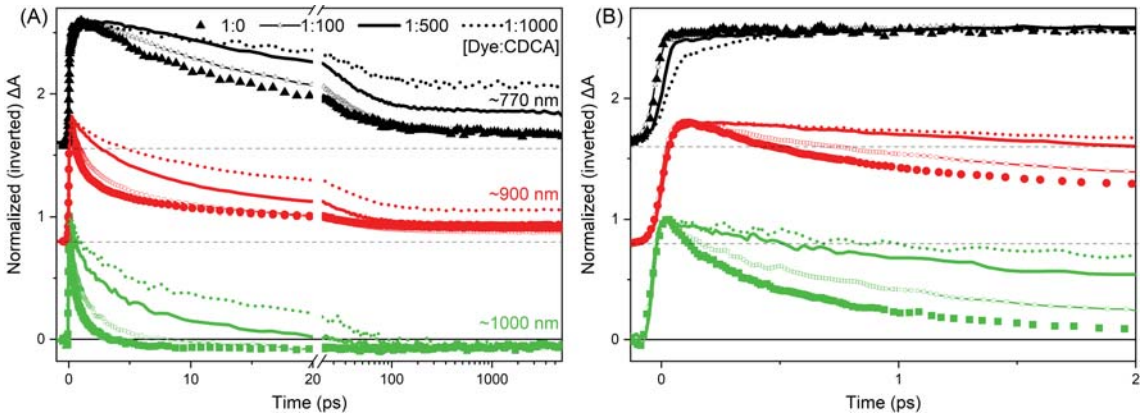

Figure 5.22: Normalized and shifted in the y-axis, kinetic traces of **VG20** TiO_2 DSSCs of different CDCA concentrations in the near-IR spectral region, obtained by TAS with detection at 770, 900 and 1000 nm, probing the GSB of the aggregates and the GSB/SE of the monomers. (A) The kinetics are presented in the full time window, with a linear scale up to the brake at 20 ps and in logarithmic scale afterwards (B) The kinetics in the first 2 ps in a linear scale.

presented in table 5.12. The complete table for numerous wavelengths is shown in the Appendix (table A.2). Interestingly and compared to ZrO_2, the third 100-300 ps component, for the high [CDCA] samples is absent for TiO_2, due to the efficient "double" quenching (ET and injection).

Table 5.12: Fitting values of **VG20** TiO_2 DSSCs of different CDCA concentrations.

[Dye:CDCA]	**λ(nm)**	A_1%	$\tau_1 ps$	A_2%	$\tau_2 ps$	A_3%	$\tau_3 ps$	A_4%	$\tau_4 ps$
[1:0]	1000	29.5	0.1	47	0.6	23.3	2.6	-5.4	inf
	GA	-	0.4	-	1.9	-	18.0	-	inf
[1:100]	995	23	0.2	53	1.2	24	5.6	-5.2	inf
	GA	-	0.3	-	2.0	-	20	-	inf
[1:500]	985	25	0.7	44	4	31	15	-4.7	inf
	GA	-	0.4	-	4.2	-	24	-	inf
[1:1000]	990	22	1.2	42	7.9	36	39	-55	inf
	GA	-	0.5	-	5	-	36	-	inf

The injection efficiency can be evaluated with the method described in eq. (5.7) and the results are presented in table 5.13 for all four samples. The general trend is that the injection efficiency increases, by increasing the CDCA concentration. Even with zero CDCA there is a 10 % injection and increases further from [1:500] to [1:1000]. This

major observation validates that the injection originates dominantly from monomers, i.e. aggregates inject with much lower efficiency. Therefore aggregates work as the main loss channel limiting the PCE, in accordance with the PCE table on the CDCA dependence (5.7). The total PCE depends on many factors, one is the short-circuit current density (J_{sc}), which by its turn depends on the absorption of the dye, as well as the injection efficiency. Thus, there is always a competition between these two and the best compromise has been found for the [1:500] dye:CDCA.

Table 5.13: The ratio of the main monomer absorption band against the aggregate band, as it was extracted from the SSA.

[Dye:CDCA]	$\mathbf{\Phi_{inj}}$ %
1:0	11.8
1:100	8.0
1:500	17.0
1:1000	30.1

Relative to the injection rates the determination is not straightforward. Probing the single wavelength kinetics, at 650-680 nm (Figure 5.23), for all four CDCA concentrations, a small rise of around $\sim$ 0.5-1.3 ps (Table A.2) is observed. Note that the sub-200 fs time-window is an artifact signal.

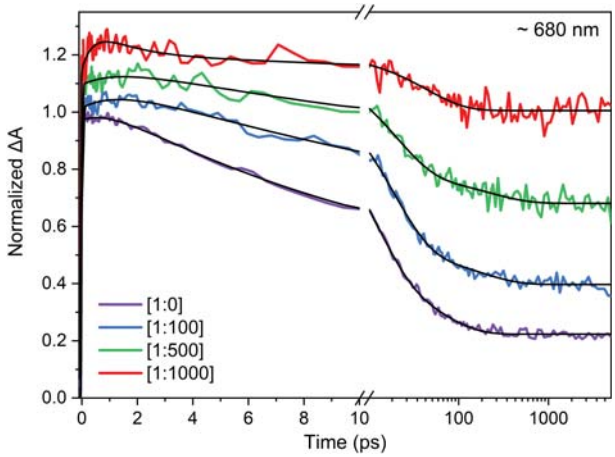

Figure 5.23: TAS spectra of **VG20** TiO_2 DSSCs for [1:0], [1:100], [1:500] and [1:1000] CDCA concentrations, detected at 680 nm (Photo cation rise).

In order to detect the effect of [CDCA] on either ET or injection times, the DADS were constructed as presented in the Appendix (Figure A.8), in a similar manner as for ZrO_2. For all cases there is a sub-ps component and a second that ranges from 2-5 ps, as

[CDCA] increases. Both components show, clearly, ET character, with the same DADS shapes as for ZrO_2. The increase of the second component has been attributed to the increase of the intermolecular distances and therefore the elongation of ET times and both processes appear in a distribution of times (the features for injection appear as a rise at 680 nm). The third component ($\sim 18-36\ ps$) refers to the aggregates/monomers relaxation, as discussed for ZrO_2 and the last was fixed in >ns times to fit the residual non-decaying signal, due to the photoproduct. The times obtained by global analysis are in the same range as the ones determined from the single wavelength kinetics and it can be concluded that both ET and injection occur in the same range of times that come out as overlaying time distribution and compete each other. However, from [1:0] to [1:1000], ET becomes slower with less contribution, resulting in higher injection efficiencies and finally PCE. To summarize, the inhomogeneity of the system temporally stretches the ET and possible the injection times and therefore there is little value of quoting a specific injection time, but rather a range of times.

5.4.4 The effect of Li^+ concentration in the electrolyte on VG20 TiO_2 DSSCs

A different approach to improve the injection, is the study of the electrolyte additives on the injection dynamics of the TiO_2 DSSCs. For this reason, additional studies were performed on various TiO_2 DSSCs of [1:500] dye:CDCA ratio, increasing the Li^+ concentration in the electrolyte. The effect of Li^+ has already been reported and it has been proven crucial for the total photovoltaic performances (section 5.3). Adding Li^+ shifted the CB to lower energies than the LUMO energies, enhancing significantly in this way the driving force for injection [30]. It has been found that the optimal conditions were 1 M (PCE $\sim$ 2.5 %) (table 5.8). Further increase reduces the PCE, possibly due to an increasingly inverted Marcus regime.

For the investigation of the Li^+ effect, four TiO_2 DSSCs of [1:500] dye:CDCA were assembled with 0, 0.05, 0.5 and 1 M of Li^+ in the I_3^-/I^- based electrolyte, respectively. In Figure 5.24 the corresponding transient spectra, at different delays are presented from zero (A) to higher Li^+ concentrated (B$\rightarrow$ D) samples. It is important to highlight that the SSA spectra (A.9) show variations of 10 % of the A_{agg}/A_{mono} among the samples, however there is no clear evidence that Li^+ presence, drastically enhances the aggregate formation. Consequently, the main process under investigation is the electron injection. The filled negative spectra at 2 ns, reveal the GSB residual and the corresponding pos-

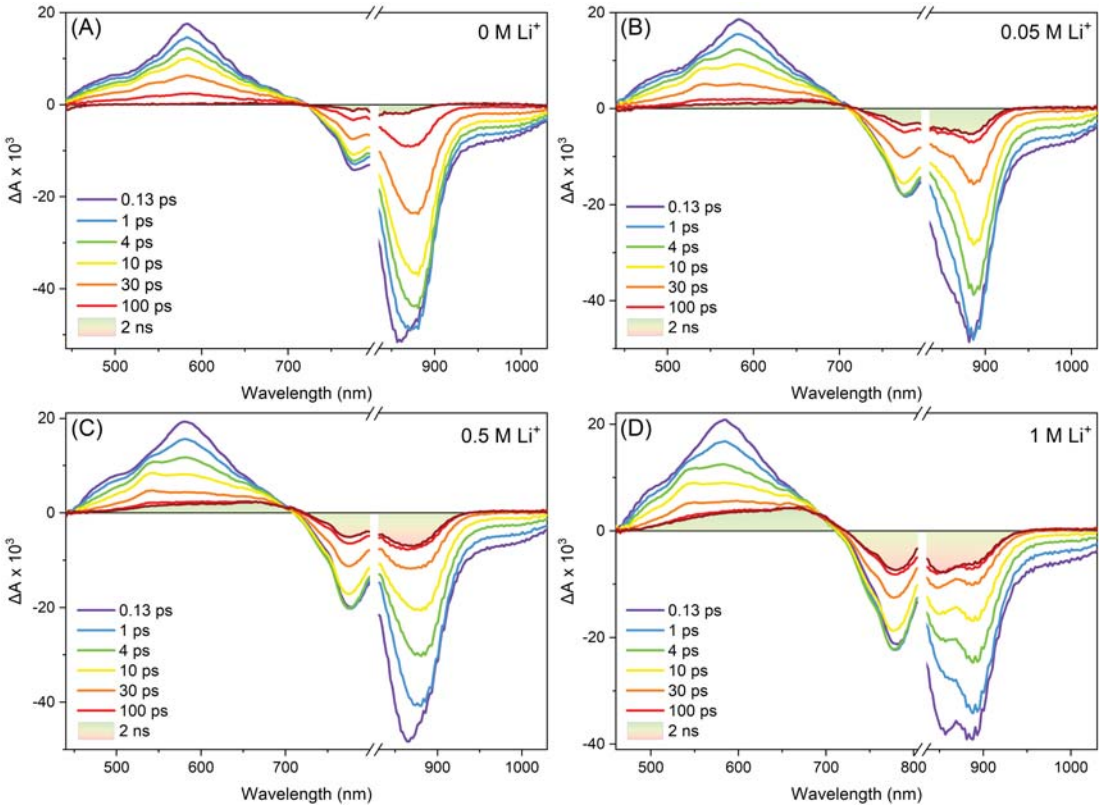

Figure 5.24: Transient spectra at different time-delays of **VG20** TiO_2 DSSCs of (A) 0 M, (B) 0.05 M, (C) 0.5 M and (D) 1 M Li^+ in the electrolyte. The devices were excited at 800 nm with an energy of 90 $\mu J/cm^2$. The DSSCs were made under optimal conditions of [1:500] dye:CDCA. The filled spectra at 2 ns indicate the $VG20^+$ versus GS difference spectra.

itive the **VG20** cation absorption. Noteworthy, even for the 0 M Li^+ system (Figure 5.24.A), there is indication that injection occurs, as revealed by the non-decaying residual GSB signal at $\sim$ 850-880 nm. A straightforward observation is that by increasing the Li^+ concentration the residual ΔA_{max} increases. The injection efficiencies, calculated by amplitudes in the GSB region are presented in table 5.14, revealing the pronounced Li^+ effect on injection. For no addition of Li^+, the injection efficiency is almost near zero and with only 0.05 M of Li^+ addition, it drastically increases to 8 %, when for the optimal values of 1 M, the PCE is reported to be 30 %, in agreement with the observations in section 5.3 and the table (table 5.8) (photovoltaic performances).

Relative to the TAS spectral features, they are generally similar, with no additional PA, due to Li^+. Interestingly, the least efficient DSSCs undergo slower relaxation e.g. the GSB (860 nm) for the 0 M Li^+, reached the half-maximum intensity in $\sim$ 30 ps, when for 1 M in about $\sim$4 ps, due to the enhanced quenching, as a result of the larger driving

Table 5.14: Injection efficiency as obtained by TAS as a function of the Li^+ concentration.

$[Li^+]$	Φ_{inj} %
0 M	0.1
0.05 M	8.0
0.5 M	20.0
1 M	30.1

force for injection.

To demonstrate the trend of the dynamic evolution for all four samples, in Figure 5.25, the corresponding SE kinetics ($\sim$ 1000 nm) are presented. By visual inspection, the above mentioned spectral observation is confirmed, with the decays to be faster in the first 4 ps for the samples of higher $[Li^+]$. In table 5.15, the four time constants obtained

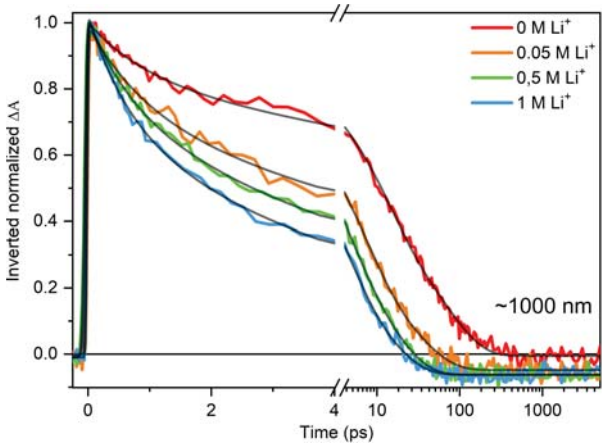

Figure 5.25: SE kinetics of **VG20** TiO_2 [1:500] dye:CDCA DSSC, increasing the $[Li^+]$ in the electrolyte.

by single wavelength fittings, as well as the ones found by GA, are presented and appear to be in a good agreement between them. The major observation of the SE analysis, is that the contribution of the sub-ns components are enhanced in amplitude, for higher $[Li^+]$ systems. In parallel the SE times become significantly shorter from 1 ps (0 M) to 0.6 (A M) and 11 ps (0 M) to 3.7 ps (1 M), resulting in the straightforward conclusion that the injection dynamics are captured in the first two time components and they indeed, greatly depend on the CB energy level (and therefore the Li^+ concentration). Note that the τ_3 SE component becomes faster too, but its amplitude decreases. For the DSSC of standard conditions (1 M Li^+), injection occurs in a distribution of times from 0.6-3.7 ps, validating the initial conclusion of section 5.4.2. The ET contribution, shouldn't alter

significantly from sample-to-sample, as indicated by the SSA spectra and occurs in similar times as the injection. Finally, the last component was fixed in very long times, above the time-window given by the experimental set-up, in order to fit the positive residual signal, which is present in all four kinetics. Eye-catching is that the more injecting the system (e.g. 1 M Li^+), the higher the amplitude of the positive residual signal. This observation supports the suggestion that this positive signal is part of the PA absorption signal, peaking at 680 nm at long times, with a possible tail spanning up to the near-IR ($\sim$ 1000 nm).

Table 5.15: GA and SE (1000 nm) fitting values of **VG20** TiO_2 DSSCs of different Li^+ concentrations.

$[Li^+]$	λ(nm)	A_1%	$\tau_1(ps)$	A_2%	$\tau_2(ps)$	A_3%	$\tau_3(ps)$	A_4%	$\tau_4(ps)$
0 M	1000	17	1	44	11	40	71	-0.05	inf
	GA	-	0.6	-	9	-	63	-	inf
0.05 M	1000	23	0.9	49	6.6	28	32	-3.7	inf
	GA	-	0.4	-	5	-	32	-	inf
0.5 M	1000	24	0.7	49	4	28	16	-3.8	inf
	GA	-	0.5	-	4.9	-	27	-	inf
1 M	1000	28	0.6	46	3.7	26	14	-5.5	inf
	GA	-	0.5	-	4.3	-	25	-	inf

The complete table with the kinetic fitting parameters in various wavelengths is showed in the Appendix (table A.3).

The DADS have been plotted and presented in the Appendix (Figure A.11) for all four samples. The injection is confirmed to occur in the shortest times, as it is shown by the negative DADS signal at the PA absorption (680 nm). Very interestingly, the long time DADS (>5 ns), for the 1 M Li^+, is relatively structured with three peaks (aggregate and monomer), indicating possible injection from aggregates too. The ET trends are presented in the first two components (sub-ps and 4-9 ps), with slightly weaker contribution in the 0 M Li^+ case, as it is the least aggregated (Figure A.11).

5.4.5 The excitation wavelength effects

To investigate a possible contribution in injection from aggregates, the following series of experiments were conducted. For the injecting TiO_2 DSSCs, wavelength-selective

experiments were performed, exciting more or less the aggregate population, compared to the one of the monomers. Three excitation wavelengths are selected: 810 nm that corresponds to the standard excitation for all **VG20** measurements and matches the monomers S_1 band maximum, 740 nm and 880 nm that energetically match the aggregate higher and lower excited states, respectively (see Figure 5.26.D). The same experiments were conducted for the non-injecting ZrO_2 DSSCs that essentially only monitors differences in the ET contribution. It is important to highlight that for each DSSC the experiments were performed in the same day, in order to avoid the effects related to sample aging.

In Figure 5.26.A-C, the TAS spectra of a TiO_2 **VG20** DSSC are presented, with excitation at 740, 810 and 880 nm, respectively. The DSSC is of high CDCA concentration [1:1000] and therefore the aggregate percentage is low. Figure 5.26.D, shows the SSA spectrum of the DSSC, the extracted aggregate absorption spectrum for the given device and the spectral profiles of the excitation pulses. It is evident that the highest ratio monomers:aggregates is excited at 810 nm and the lowest at 880 nm. While for 880 nm the lowest energy level of the aggregates is excited, at 740 nm mostly the monomers and the high energy aggregate state are excited. From the latter state, either fast monomer-to-aggregate ET can occur, either monomer-SC injection, or internal conversion to the lower aggregates state and finally relaxation to the ground state.

Figure 5.26 shows that the TAS spectral features are identical, but with minor differences. However, interesting information has been recorded, relative to the injection efficiency from the different excited energy levels. In table 5.16 the ratio $\Delta A^{5ns}_{670\ nm}/\Delta A^{0.1ps}_{580\ nm}$ (cation absorption/monomers ESA) is evaluated for the different excitation wavelengths, as measure of the injection efficiency, because the previously reported method based on the GSB ratio has too much error, due to laser scattering at 880 nm. Exciting at higher energies (740 nm) the injecting efficiency is $\sim$ 5 % higher, than for the standard 810 nm excitation. This observation is in agreement with the Incident-Photon-to-Current Efficiency (IPCE) spectrum for **VG20** DSSCs [1] (p.A27), which has higher spectral intensities at shorter wavelengths ($<$ 780 nm), than at the monomer SSA maximum (840 nm). It reveals more efficient injection from the higher energy states and is confirmed by the values in table 5.16. The origin of the high energy injecting states are yet to be identified. The spectral region that is populated after 740 nm excitation, contains both the higher aggregate energy level and the monomer S_1 vibronic transition. Most favorable to contribute to the injection are the monomers and the higher efficiency can be simple explained by the more favorable energetic overlap, between the hot vibronic levels of monomers with the CB of TiO_2. In this case, the driving force is higher and ultrafast

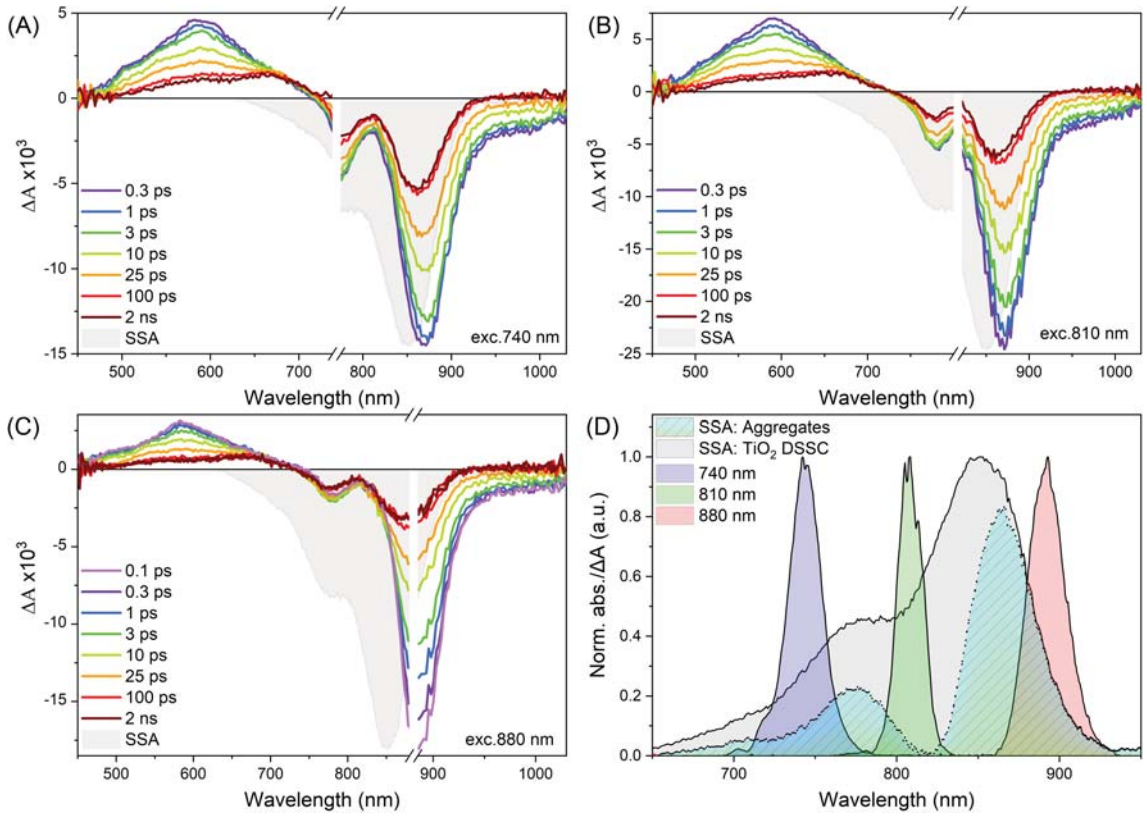

Figure 5.26: Transient spectra at different time-delays of **VG20** TiO_2 [1:1000] dye:CDCA DSSCs with (A) 740 nm, (B) 810 nm and (C) 880 nm excitation. (D) The SSA absorption of the DSSC, the extracted absorption (ΔA) of the aggregates in the device and the three excitation spectral profiles. The devices were excited with an energy of 90 $\mu J/cm^2$.

Table 5.16: Peak ratio of the monomers, early time ESA, against the long time PA and peak ratio (A/B), between the SSA monomer absorption main band and the aggregate absorption. The A/B ratio refers to Figure 5.27.

Excitation wavelength	$\boldsymbol{\Delta A^{5ns}_{670\ nm}/\Delta A^{0.1ps}_{580\ nm}}$	**A/B**
740 nm	33 %	2.3
810 nm	27 %	2.9
880 nm	27 %	2.5

injection can occur in competition with vibronic relaxation [31]. The second possible interpretation is related to the question whether there is injection from the aggregates. When injection from the lower aggregate state at 880 nm energetically appears to be unlikely, injection from the higher exited aggregate state, triggered by exciting at 740 nm, could occur. A small indication of possible aggregate injection is presented in Figure 5.27, where the transient spectra at 2 ns, for all three excitations, are compared. At 2 ns,

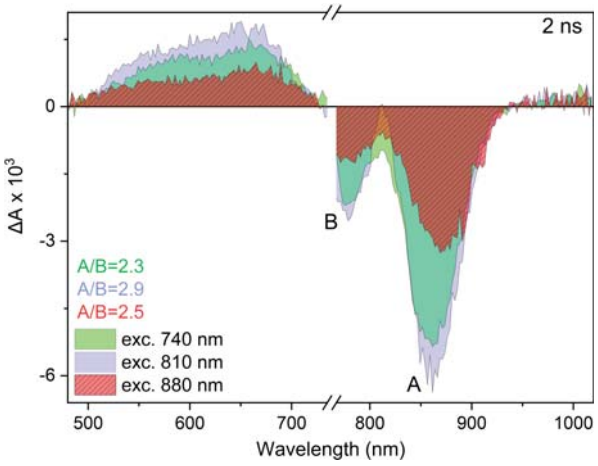

Figure 5.27: TAS at 2 ns, of a **VG20** TiO_2 DSSC, excited at 740 nm, 810 nm and 880 nm. The ratio A/B of the GSB features, indicates the degree of aggregation, in the system that doesn't recover to the ground state.

only the residual positive signal remains (PA) and the negative (GSB) that should reflect the species that were oxidized. The ratio A/B (GSB_{mono}/GSB_{agg}) is smaller (table 5.16) for 740 nm excitation, indicating that a small portion of aggregates contribute to the injection. However, due to the very low contribution the exact distinction of monomer versus aggregate injection rates are not easy to quantify.

The SE kinetics (985 nm) are plotted in Figure 5.28.A and the corresponding fit parameters are presented in table 5.17, together with the GA time constants. The plotted DADS are presented in the Appendix (Figure A.12), for both TiO_2 and ZrO_2 DSSCs. The kinetics appear to overlay and all the early time differences, are in the noise level.

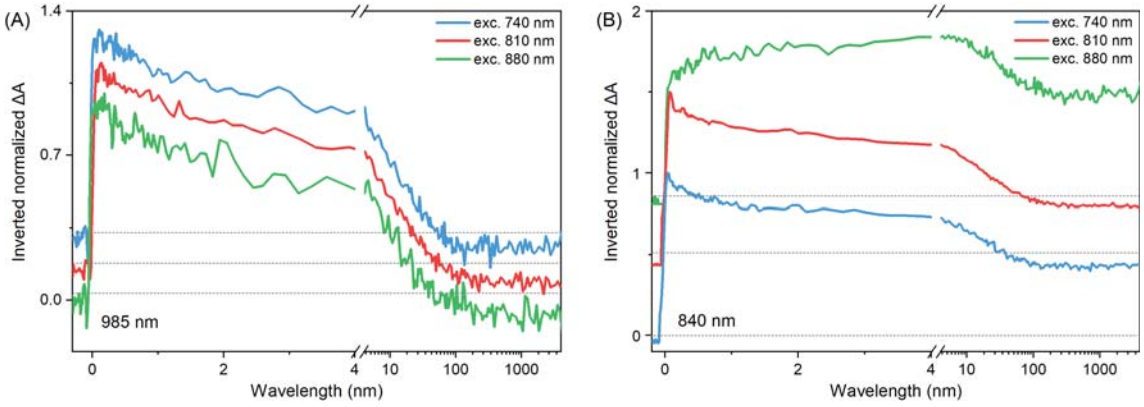

Figure 5.28: (A) SE (985 nm) and (B) GSB (840 nm) kinetics of **VG20** TiO_2 [1:1000] dye:CDCA DSSC, excited at 740, 810 and 880 nm.

The values are in a good agreement for all excitation wavelengths, as well as with the GA

values. They are in the same range as they have already been found for the [1:1000] TiO_2 DSSCs. Therefore, the injection times, as well as the ET times are included in the first two time constants and they have been found to be in the range of 1-12 ps. Moreover, the deviated 150 ps value for the 880 nm excitation case, is probably overestimated due to the noise of the data. The complete fitting tables for all cases are presented in the Appendix (A.4, A.5).

Table 5.17: Fitting values of a **VG20** TiO_2 1:1000 DSSC at different excitation wavelengths.

λ_{pump}	$\lambda_{det}(nm)$	$A_1\%$	$\tau_1(ps)$	$A_2\%$	$\tau_2(ps)$	$A_3\%$	$\tau_3(ps)$	$A_4\%$	$\tau_4(ps)$
740 nm	985	10	0.8	40	5	50	27	-5	inf
	GA	-	0.3	-	7.2	-	34	-	inf
810 nm	985	13	0.9	52	6.4	40	39	-6	inf
	GA	-	0.3	-	5.9	-	37	-	inf
880 nm	985	22	1	68	12	13	150	-7	inf
	GA	-	0.5	-	5.8	-	36	-	inf

The complete table with the kinetic fitting parameters in various wavelengths is showed in the Appendix (table A.5).

Another interesting observation can be made relative to the GSB for 880 nm excitation. Detecting at 840 nm (monomer GSB) the kinetic shows a pronounced rise (Figure 5.28.B), compared to the case of higher energy excitation, where the kinetics rapidly decay. Figure 5.29, shows that for the 880 excitation case, at 0.1 ps the GSB is relatively narrow and in 10 ps it becomes significantly broader, where for the 810 nm excitation case (Figure 5.29.Inset) there is not change in the GSB width, upon increasing the time delay. This is a minor effect, but could indicate that aggregates convert into monomers by a thermally activated reverse energy transfer. This would be consistent with the observation that monomers and aggregates seem to be in thermal equilibrium after $\sim$ 2 ps, since the above discussed DADS of τ_3 (25-40 ps) shows that both excited states decay in parallel. Another possible scenario could be that spectrohole burning occurs, which indeed has been observed to exhibit the same spectral trend in $\sim$ 100 fs times [32], for a highly heterogeneous collection of dyes in a broadband DSSC.

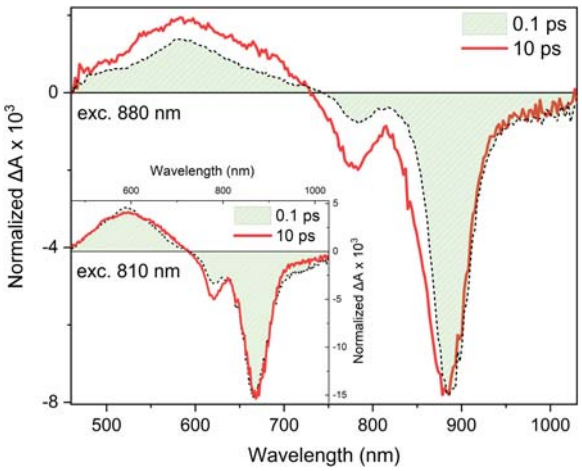

Figure 5.29: TAS spectra at 0.1 and 10 ps of **VG20** TiO_2 DSSC, exciting at 880 nm. Inset: TAS spectra at 0.1 and 10 ps of **VG20** TiO_2 DSSC, exciting at 810 nm. The devices were excited with an energy of 90 $\mu J/cm^2$.

5.5 Time resolved spectroscopy on TB-dyes

The second series of dyes have code names **TB207** and **TB423** and belong to the new family of pyrrolopyrrole-cyanine dyes (PPCys). Similarly to **VG20** they are near-IR absorbing dyes with excellent absorbing properties. When for **VG20**, the degree of aggregates is the main drawback for efficient charge injection, the **TB** dyes were synthesized aiming to minimize the self-molecular assembles on the SC surface. Indeed, by already recalling the SSA spectra of the **TB**-based DSSCs (Figure 5.5) and the plot of the ratio of the aggregates high energy absorption maximum intensity to the monomers one, upon increasing the CDCA concentration (Figure 5.6), it is evident that even without co-adsorbent the **TB** DSSCs are less aggregated (at least two times) than the **VG20** ones. When for **TB207**, CDCA is still needed to reach the optimal condition of [1:50] dye:CDCA, **TB423** showed smaller [CDCA] dependence on de-aggregation. Certainly, **TB423** has been synthesized as an improved version of its symmetric counterpart **TB207**, having a one side, distinguishable bulkier, triphenylamine-based component that greatly prevents side-to-side aggregate formation on the SC surface, without changing the absorption energy. Consequently, it has already been showed that after optimization, **TB207** PCE can reach values up to 3.9 % (table 5.7), exceeding **VG20** performance, when **TB423** still needs to be optimized, but has already showed negligible dependence of the PCE on [CDCA]. In addition, both dyes exhibit excellent AVT, reaching the impressive value of 70 %. In the current section the time-resolved study of the **TB** dyes

is demonstrated, in the fs-ps and ns time domain, revealing the relative time constants for the ultrafast processes and investigating possible competitive pathways to efficient electron injection. Therefore, in similar manner as for **VG20**, the **TB** dyes were studied in solution phase, as well as when they were incorporated in real non-injecting Al_2O3 and injecting TiO_2 DSSCs. To close the circuit of the devices and ensure efficient regeneration, I_3^-/I^- based electrolyte was used for all samples, with the addition of $1MLi^+$, to shift the CB lower than the dyes' LUMO and secure the optimal conditions for injection. In the end of the studied, the photophysical models, govern **TB207** and **TB423** DSSCs, have been constructed, illustrating in the form of reaction schemes, the various processes with their relative time constants.

5.5.1 Excited state reaction scheme of TB207 and TB423

The first step of the studies, is the investigation of the dyes in solution mixture ($EtOH : CHCl_3$) (9:1) and the identification of the excited state lifetimes. It is important to highlight that by increasing the dye concentration in solution, no difference in the SSA spectral features were observed, indicating that the solution samples can be treated as a 100 % monomers case. In Figure 5.30.A,B the 2D maps of the time-resolved fluorescence decays are displayed for **TB207** and **TB423**, respectively, as they were obtained by streak camera measurements. The upper panels, show the spectra as they were time

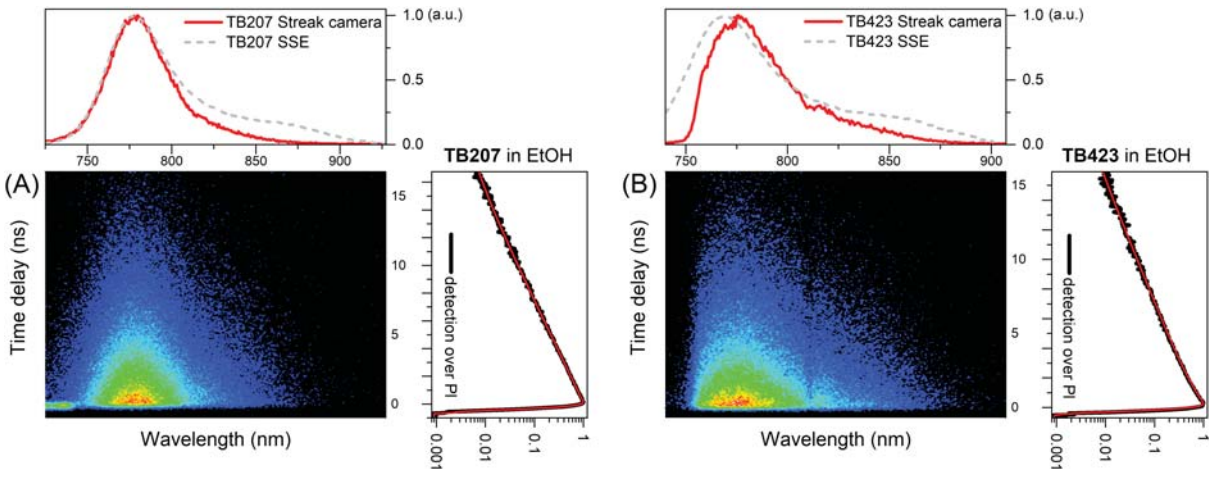

Figure 5.30: Streak camera 2D spectro-temporal profiles of (A) **TB207** and (B) **TB423** in EtOH solutions, in a 20 ns time window. The **TB207** devices were excited at 830 nm and the **TB423** one at 820 nm with an energy of 26 $\mu J/cm^2$.

integrated in the full time window and they perfectly overlap with the respective SSE

spectra. The right panels, show the kinetics profiles with fits, over detection in the whole spectral window. Starting with **TB207**, the decay appears single exponential and the major decay time is found to be 3.2 ns (table 5.18), which is already many times longer than the 360 ps for **VG20**. The long excited state lifetimes are necessary for DSSC applications, ensuring that the $S_1 - S_0$ relaxation, doesn't compete with the electron injection in the SC. A small rise of 20 ps, is also identified and can be attributed, in solution, to dynamic relaxation due to solvation. The rise manifests as a small red-shift upon the first tens of ps and it is mostly visible in the corresponding FLUPS data (Figure A.13.A), in which the IRF is much shorter ($\sim$ 200 fs). An additional 300 ps component has been found, but of very low amplitude and it could be attributed to a longer solvation process, which has essentially been demonstrated in the bibliography to occur in a range of times, from sub-ps to hundreds of ps [33]. Similarly, for **TB423** a rise of 40 ps is observed (Figure A.13.A), due to solvation, which is slightly longer than for **TB207**, due to the increased size of **TB423**. Important is that the decay is bi-exponential, with a longer main component at 3.5 ns and a smaller at 1 ns. The first, is in the same time range as for **TB207** and corresponds to the excited state lifetime of the monomer dyes and the 1 ns one, could refer to shorter-lived isomerized **TB423** dyes, formed most probable from rotation around the Ph-N bonds of the bulkier side component, in the low viscosity solvent. Nonetheless, in real DSSCs, typical times for ET or electron transfer are in the range of ps-tens of ps and the **TB**-dyes demonstrate long enough lifetimes, which aren't in competition with the essentially ultrafast processes.

Table 5.18: Luminescence's decay fitting values of **TB207** and **TB423** in EtOH. The luminescence's decay is analyzed by both FLUPS and streak camera.

Dyes	$\boldsymbol{A_1}$ %	$\boldsymbol{\tau_1^{flups}}$ (ps)	$\boldsymbol{A_2}$ %	$\boldsymbol{\tau_2^{streak}}$ (ns)	$\boldsymbol{A_3}$ %	$\boldsymbol{\tau_3^{streak}}$ (ns)
TB207	-13	20	4	300	96	3.2
TB423	-16	45	34	1	66	3.5

Continuing the investigation in solution, in Figure 5.31.A.B, the transient absorption spectra of various time-delays are presented, over a 5 ns time window, of **TB207** and **TB423**, respectively. Both cases have similar spectral features with the **TB207** to be 10 nm red-shifted compared to **TB423**, following the inverted SSA and SSE spectra (filled black and red spectra, respectively). The positive ESA signals (450-700 nm and 900-1030 nm) are 10 times weaker in intensity than the negative ones (700-900 nm) for **TB207** and 20 times for **TB423** with the latter to contain both GSB and SE of the

monomers. Therefore, the spectra are presented with a break at the negative y-axis, in order to demonstrate in the same scale the weaker positive signals. The GSB spectrum is relatively steep at shorten wavelengths, because it is compensate by the broad positive ESA signals. Relative to the dynamics, for **TB207**, all signals appear to decay in parallel with no additional photoproduct absorption rise, when for **TB423** the general trend is the same, but with a weaker inhomogeneous decay of the positive 450-650 nm ESA. This spectral region could contain the absorption features of the isomerized **TB423** dyes, however the signal/noise ratio is too low to precisely identify this trend. The decays can

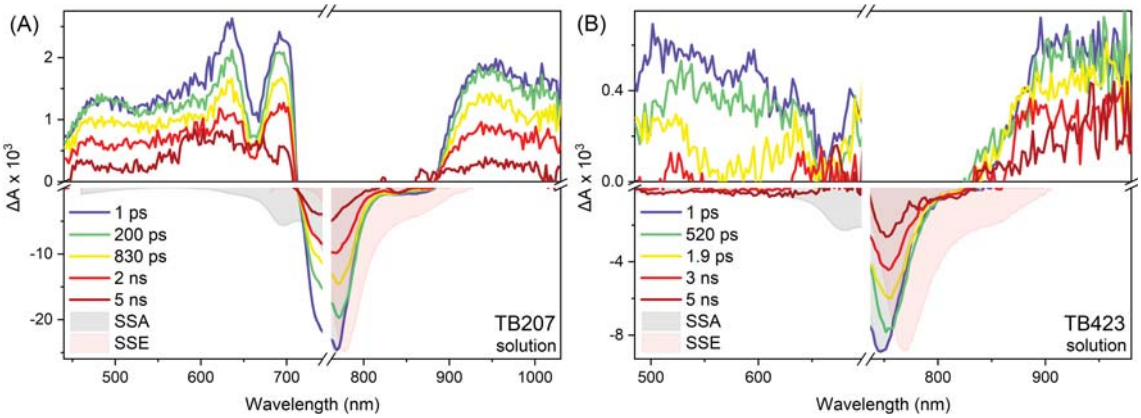

Figure 5.31: Transient spectra at different time delays of (A) **TB207** and (B) **TB423** in $EtOH : CHCl_3$ solutions, in a 5 ns time window. The **TB207** devices were excited at 730 nm and the **TB423** one at 720 nm with an energy of 26 $\mu J/cm^2$.

be better described by 3 exponentials and the precise fitting details are shown in the Appendix (Figure A.14), as well as the times obtained for both single wavelength and global fits (table A.6). The values are in agreement with the ones obtained with FLUPS, revealing a $>$ ns main component, referring to the excited state lifetime. In addition, two rise components, one in the ps or sub-ps and the second in 30 ps for **TB207** and 40 ps for **TB423** range, due to solvation. The DADS and EADS for **TB207** are similarly presented in the Appendix (Figure A.15). Indeed, the first two components of lower contribution, exhibit a gradual negative and positive trend in the DADS, in the GSB/SE region, leading finally to the GSB/SE main decay in longer times, which is spectrally slightly red-shifted, compared to the the early time ($\sim$ 100 fs) signal after excitation. This shift that was also initially observed in the FLUPS data, is easily observed in the EADS too, revealing a three energy level model ($S_0 \rightarrow S_{1,hot} \rightarrow S_1$).

From the solution studies it was identified that the main process is the $S_1 - S_0$ transition that occurs in long enough times (3.3-3.5 ns), in order not to compete with the ultrafast processes, such as injection. The next step is the spectroscopic study of **TB-**

dyes when they are incorporated in solid-state samples. Starting from the simpler case, the non-injecting systems are studied, using Al_2O_3 SCs. In Figure 5.32.A-C, the transient spectra of **TB207** Al_2O_3 DSSCs are presented, for selected time delays, for 1:0, 1:20 and 1:50 dye:CDCA concentration ratios, respectively, when in 5.32.D are the corresponding spectra for **TB423** Al_2O3 DSSC with zero CDCA. By a first visual inspection, all TAS exhibit similar spectral features as in solution, which are the two positive high and low energy ESA signals and a negative GSB/SE combination, as it is validated by the overlap with the inverted SSA and SSE spectra (filled black and red spectra). Starting from the **TB207** Al_2O_3 DSSC (Figure 5.32.A), the high energy ESA broadly extends from 450-700 nm and the low one from 830-1030 nm, while the negative GSB/SE signal is located in the spectral range 700-830 nm. However, in comparison to solution, the ESA doesn't

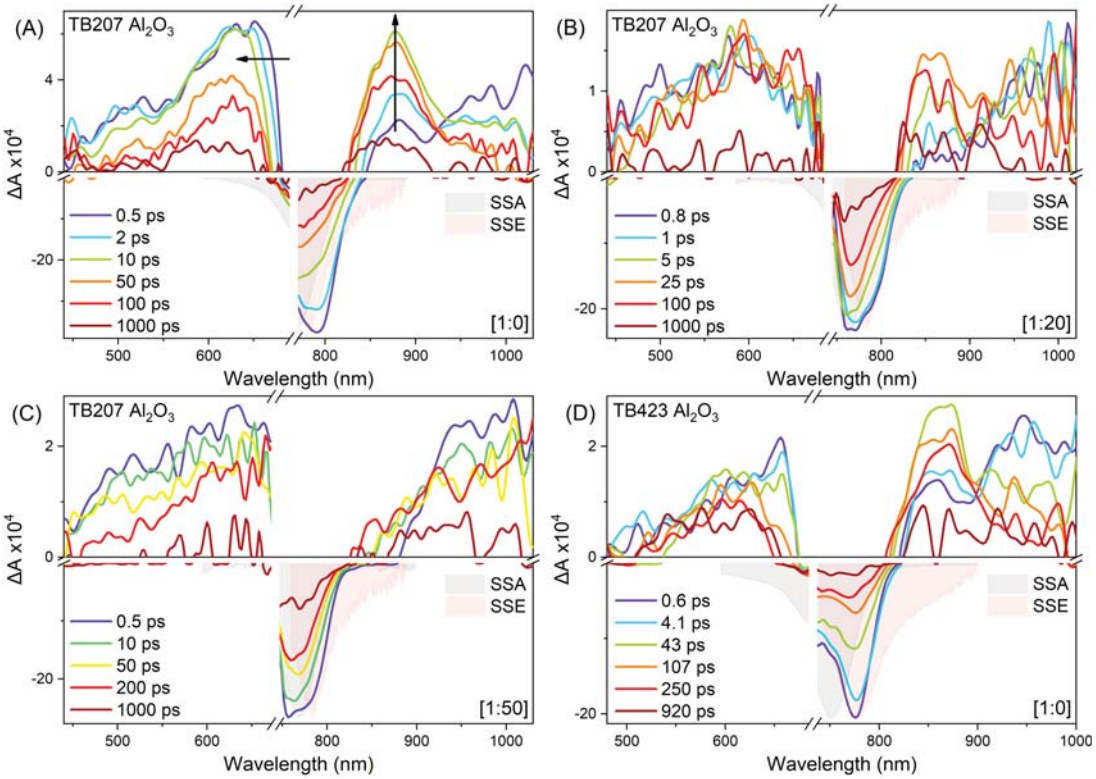

Figure 5.32: TAS at different time delays of **TB207** Al_2O_3 DSSCs of (A) [1:0] (B) [1:20] and (C) [1:50] dye:CDCA ratio and (D) TAS of **TB423** Al_2O_3 [1:0] DSSC, in a 5 ns time window. The **TB207** devices were excited at 730 nm and the **TB423** one at 720 nm with an energy of 26 $\mu J/cm^2$. As filled black and red spectra are the inverted SSA and SSE, respectively.

decay homogeneously in the whole spectral range. For zero CDCA concentration (Figure 5.32.A) at 810-910 nm a distinguishable signal rises, maximizes in 10 ps and slowly decays

afterwards, when in parallel the longer wavelength part of the ESA (930-1030 nm) decays. In the visible spectral region, the higher energy ESA (450-700 nm) slightly blue-shifts, stabilizes in 10 ps, forming a clear isobestic point with the GSB and afterwards slowly decays. Already, from the SSA of **TB207** in DSSCs (Figure 5.5), it is evident that aggregates have been formed and therefore these features and dynamic progression, are due to aggregates and their interaction with the monomers, as it was discussed in detail in the previous section for **VG20**. Even though, the GSB part that energetically matches the SSA's high energy shoulder (690-750 nm) that is attributed to the aggregates, is masked due to the laser pump, a small rise in 10 ps is present. Therefore, similarly to **VG20** ET from the monomers to aggregates occurs, which is energetically allowed for oblique aggregates, as it was described for **VG20**. Upon adding CDCA, from [1:20] (panel B) to [1:50] (panel C) the maximum amplitude of the 810-910 nm ESA is lower and the rise time is longer ($>$ 25 ps), in agreement with FRET theory and the dependence of ET time upon increasing the D-A distances. Taking the above into consideration, the two positive signals contain both the ESA of aggregates (450-670 nm and 810-910 nm) and the ESA of monomers (450-690 nm and 900-1030 nm). Panel D, includes the TAS of **TB423** for 0 mM CDCA, which are identical to **TB207**. Noteworthy is that the peak signal of the ESA of aggregates (810-910 nm) maximizes in 40 ps instead of 10 ps, as for **TB207** and the slower ET times are due to the increased size of **TB423** and therefore longer intermolecular distances between monomers and aggregates.

The TAS spectral features of the **TB** dyes are rather complicated and the SE signal cannot be purely detected, without contribution from the GSB or the near-IR ESA and the identification of the fluorescence dynamics is crucial, because it should contain the components of ET and electron injection, for the injecting samples. Therefore, FLUPS experiments were performed on the DSSCs, in order to purely monitor the fluorescence decay with an IRF of ∼200 fs. The FLUPS 2D spectro-temporal map for the **TB207** Al_2O_3 DSSC is presented in Figure 5.33, where in the upper panel, the spectra at selected time delays are shown and in the left panel the normalized kinetic profiles at different wavelengths. The bright signal (750-850 nm) around time zero is due to Raman scattering and its contribution (up to $\sim$ 200 fs) in the plotted kinetics have been manually deleted. Probing at different wavelengths, at the maximum of the emission (800 nm) and at longer wavelengths (850 nm), there is no change of the kinetics and therefore, no evidence for fluorescence contribution from other species e.g. aggregates. The decay is very fast compared to solution and already in 10 ps the signal is at half maximum, due to quenching by ET. Moreover, from the 2D profile, there is evidence of a slight red-shift of

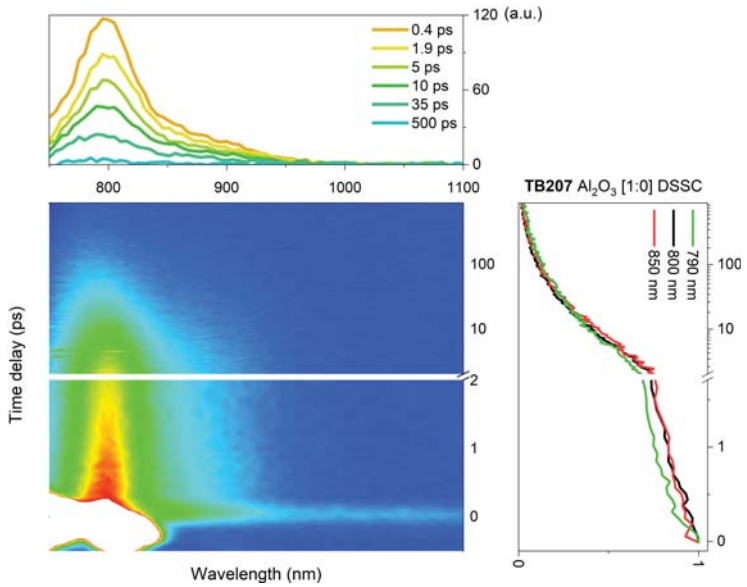

Figure 5.33: FLUPS 2D spectro-temporal profile of **TB207** Al_2O_3 DSSC of zero CDCA, in a 1 ns time window. The device as excited at 730 nm with an energy of 26 $\mu J/cm^2$.

the fluorescence signal, in the first picoseconds, due to the faster contribution of solvation.

In this manner, the emission originates mainly from monomer species, as it was initially suggested from the SSE inspection and ET from monomer to aggregates occurs, as it was shown in the TAS spectra, quenching the total lifetime. The dynamic effect of ET can be examined by both the TAS and FLUPS dynamics. In Figure 5.34, the

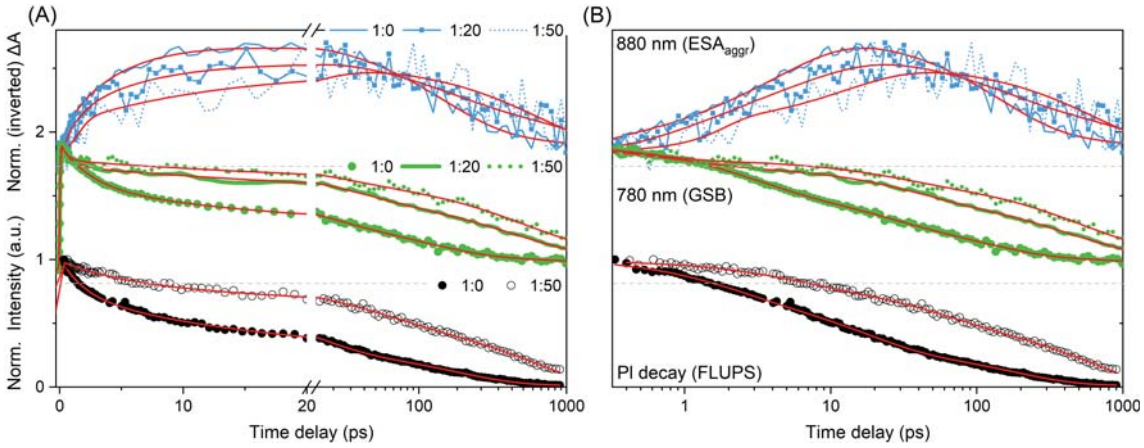

Figure 5.34: Kinetics of **TB207** Al_2O_3 1:0 DSSC obtained by TAS and FLUPS. The device was excited at 830 nm with an energy of 26 $\mu J/cm^2$ for both TAS and FLUPS experiments.

kinetics of selected wavelengths are presented, probing the ESA of the aggregates at 880 nm and the GSB of the monomers at 780 nm, for Al_2O_3 DSSCs of different CDCA con-

centration. In addition, in black, are illustrated the kinetics measured with FLUPS and therefore are related with the fluorescence decay exclusively. The (A) panel demonstrates the kinetics over the full time window with a break at 20 ps and the panel (B) presents the same kinetics over a logarithmic time axis .It is noteworthy to highlight that both TAS and FLUPS measurements obtained for the same DSSC samples, in order to prevent carrying additional error, due to sample-to-sample reproducibility limitations. Moreover, the time between the measurements with the different techniques, were maximum one day, in order to prevent sample aging over time. Probing at 880 nm, the kinetics rise is evident from the TAS spectra, in the first ps and maximized in 20 ps. Noteworthy, the signal tends to maximize in longer times as the CDCA increases, due to the increase of the intermolecular distances of the monomers and aggregates, resulting in slower FRET times. In table 5.19, the fitting parameters of the various kinetics are presented for all **TB207** Al_2O_3 DSSCs, increasing the CDCA concentration. Four time constants describe

Table 5.19: Fitting values of **TB207** Al_2O_3 DSSCs of different CDCA concentrations obtained by TAS and FLUPS.

[Dye:CDCA]	**λ(nm)**	A_1%	$\tau_1(ps)$	A_2%	$\tau_2(ps)$	A_3%	$\tau_3(ps)$	A_4%	$\tau_4(ps)$
[1:0]	880	-10	0.8	-71	4.9	76	140	23	3400
	GA	-	0.2	-	5	-	85	-	2000
	FLUPS	35	2	39	17	26	180	-	
[1:20]	880	-27	1.3	-57	7.2	45	140	55	1800
	GA	-	0.2	-	5	-	120	-	2000
[1:50]	880	-80	0.14	-63	13	90	620	10	inf
	GA	-	<IRF	-	3	-	100	-	1100
	FLUPS	24	1.8	19	34	57	840	-	-

the systems better, with the rise times to appear in two time-ranges. As it has already been suggested, due to the inhomogeneity of the system, the FRET times comes out as a distribution of rates and the process already starts from the sub-ps time domain. For zero CDCA, the longer FRET time is found to be 4.9 ps and by increasing [CDCA], it slows down, reaching 13 ps for the [1:50] DSSC, with reduced amplitude. From the monomers aspect, probing the GSB at 780 nm, the signal decreases with slower rates as the CDCA increases, due to lower ET quenching with similar trend to be observed for the fluorescence decays (FLUPS), as well (Figure 5.34.(black)). The GA values, are also found to be in a good agreement with the single wavelength fits, with the DADS to be presented

in the Appendix (Figure A.16), revealing the ET spectral trends to be indeed in the first to time components. The FLUPS kinetics are well described by three time constants with the times to be relatively longer. The ET components are similarly contained in the first two components τ_1 and τ_2, as their contribution decreases by increasing [CDCA], from 13 to 34 ps, for [1:0] and [1:50], respectively. The difference is due to the absence of the sub-ps component in the FLUPS data, as well as, because of the, longer than TAS IRF, considering the laser scattering around time zero. What is more, the absence of the slower component (>2000 ps) in the FLUPS kinetics, which essentially has non-radiative character and is related to aggregates (see aggregate ESA at 1 ns in the TAS spectrum in Figure 5.32.A).

The **TB423** fluorescence dynamics for **TB423** Al_2O_3 DSSCs of [1:0] and [1:80] dye:CDCA concentration ratio, are presented in Figure 5.35 and the fitting parameters in table 5.20. Very interesting is that for zero CDCA, the kinetics are much faster and the

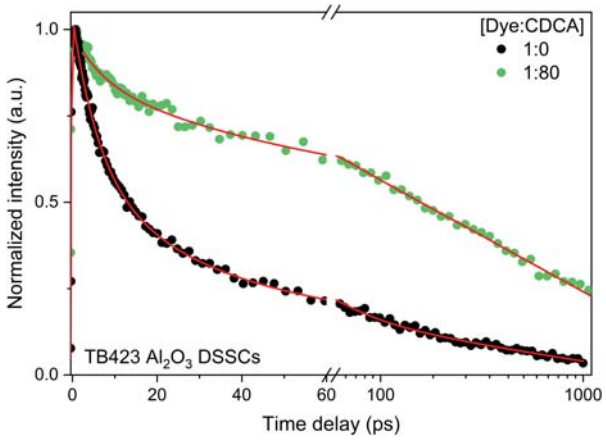

Figure 5.35: FLUPS kinetics of **TB423** Al_2O_3 DSSCs of [1:0] and [1:80] dye:CDCA concentration, in a 1 ns time window. The devices were excited at 720 nm with an energy of 26 $\mu J/cm^2$.

intensity is half of the maximum in less than 20 ps, while for the [1:80] samples the fluorescence still decays in longer times than the experimentally available time window. The SSA spectra, indicate that the effect of CDCA is negligible in the **TB423** Al_2O_3 DSSC absorption (Figure 5.6) and therefore it can be assumed that the percentage of aggregates in not greatly reduced upon adding CDCA. However, aggregates still exist and the pronounced difference of the kinetics, are due to the increased intermolecular distances and therefore the increase of the ET times. Similarly to **TB207**, the contribution of the first two components is reduced upon de-aggregation and therefore, it can be concluded that this is the range of ET times for **TB423**. Furthermore, while the first component ∼

6-7 ps doesn't appear to change when adding CDCA, the second becomes more than two times slower, from 10 to 24 ps. When comparing both **TB** dyes for zero CDCA, it should be highlighted that the ET times are almost two times longer for **TB423**, with the second component to be 29 ps, while for **TB207** it is 17 ps with the ET in the fluorescence to be for both dyes is larger than 90 %. The time elongation can be attributed to the longer dye size and therefore the increased intermolecular dye-distances on the nanoparticles that can greatly affect the FRET rates. The FRET time range is of considerable importance, as it has already been found for **VG20**, where electron injection and ET time ranges generally overlap, constitute them competitive channels and resulting in reduced total PCE.

Table 5.20: Fitting values **TB423** Al_2O_3 DSSC FLUPS kinetics of different CDCA concentrations.

[Dye:CDCA]	$\boldsymbol{A_1}\%$	$\boldsymbol{\tau_1(ps)}$	$\boldsymbol{A_2}\%$	$\boldsymbol{\tau_2(ps)}$	$\boldsymbol{A_3}\%$	$\boldsymbol{\tau_3(ps)}$	$\boldsymbol{A_4}\%$	$\boldsymbol{\tau_4(ps)}$
[1:0]	45	6.2	35	29	10	100	10	740
[1:80]	10	6.9	23	48	24	225	43	1800

The individual studies of the dyes in solution and in non-injecting DSSCs has been proved a standard and efficient method to investigate the various processes taking place in a real DSSC device. The ultimate target is to determine the injection rates and yields in the injecting DSSCs and to identify the possible limitations for injection that reduce the PCE. In Figure 5.36.A-C the transient spectra at different delays are presented, for selected **TB207** TiO_2 DSSCs, increasing the CDCA concentration and in Figure 5.36.D the respective **TB423** DSSC, with zero CDCA for comparison. All TAS for **TB207** and **TB423** TiO_2 DSSCs under study, are presented in the Appendix (Figure A.18), for additional CDCA concentrations.

Starting with the **TB207** DSSC of 1:0 dye:CDCA ratio (Figure 5.36.A), all the spectral features are similar to $Al2O_3$ ones. Two prominent positive signals, previously attributed to the ESA of monomers and aggregates spans the visible from 450-690 nm and the near-IR from 840-1030 nm. Noteworthy, the near-IR ESA exhibits a biphasic behaviour with the 950-1030 nm part to decay and the 840-950 nm part to rise, in the first 10 ps and therefore the signals can be attributed to the ESA of monomers and aggregates, respectively, as for Al_2O_3. The negative signal at $\sim$ 740-820 nm, refers to the monomers GSB/SE and at 690-740 nm to the aggregates GSB, as they overlap with the inverted SSA and SSE spectra. Already in 10 ps the GSB reduces to half of the initial intensity

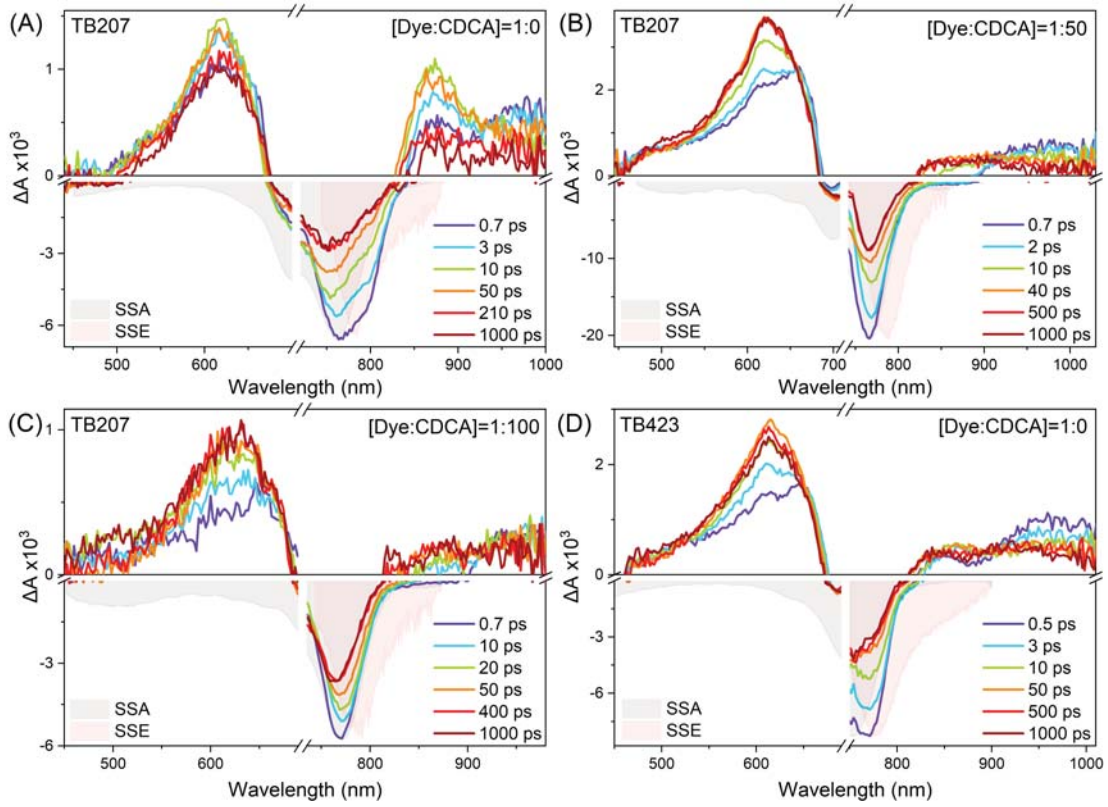

Figure 5.36: TAS of **TB207** TiO_2 DSSCs of (A) [1:0], [1:50] and [1:100] dye:CDCA concentration ratio and (D) **TB423** TiO_2 DSSCs of [1:0] ratio. The **TB207** DSSCs were excited at 730 nm and the **TB423** at 720 nm, with an energy of 26 $\mu J/cm^2$.

and after tens of ps the GSB signal stabilizes to a permanent ΔA level without decaying. This observation was made for **VG20** too and it is expected for the injecting DSSCs, in which a specific percentage of dyes, after injecting to the SC, are converted to cations and never recover to the ground state, until their regeneration from the electrolyte, on longer time scales. Turning our focus to the visible ESA, a gradual 10 nm shift is also present. The shift is due to the decay of the ESA part ($\sim$ 640-670 nm) near the GSB with a parallel increase of the higher energy ESA ($\sim$ 500-630), forming a clear isobestic point at 665 nm (Figure 5.36.A). Interestingly, after 10 ps the ESA slightly decays and when is about about 15 % of the maximum value it remains there, during the whole time window of 5 ns. Therefore, this asymptotic signal reflects the photoproduct absorption or the **TB207** cations, whose formation time starts rising in the sub-ps time domain. On longer times, a very weak and non-decaying, positive signal, spanning in the near-IR region (820-1030 nm), is also present, referring to either a long low energy tail of the cation signal, or to the absorption of free electrons in the SC, similarly to **VG20**. The spectral position of the **TB207** cations, was also found to be at similar energies, as for

VG20, in agreement with the spectral position of the reduced dyes, obtained via spectro-electrochemical measurements (Figure 5.9). The appearance of the non-decaying signals (PA in ESA), the GSB residual (700-820 nm), as well as the faster dynamics compared to Al_2O3, due to the additional quenching process, confirms the injecting nature of the **TB** based DSSCs.

Upon increasing the CDCA concentration in the system, the percentage of aggregates decreases. The peak ΔA of the low energy aggregates ESA (820-880 nm) has lower intensity and the times that it maximizes (ET times), becomes slower. It is interesting that for the 1:50 and 1:100 DSSCs, after the total increase of the PA signal, there is no long time decay of the ESA, most probable due to the reduced aggregated species in the excited state. The slower ET times are accompanied by a slower GSB recovery, as it is expected. For the least aggregated 1:100 DSSC, in 10 ps the GSB decayed only 10 % of the initial signal. It is eye-catching that the GSB residual is higher in amplitude for the least aggregated samples, in comparison to the 1:0 one. This observation, as well as the elongation of the ET times upon de-aggregation, indicates that aggregates are non beneficial for the total electron injection in the **TB**-DSSCs too and most probably ET and injection are again, in a temporal competition, as they were for **VG20**.

The **TB423** TiO_2 [1:0] DSSC TAS, are presented in Figure 5.36.D. The general spectral features are similar, with a rise of the near-IR ESA of the aggregates and the PA peaking at 620 nm, already starting to form in sub-ps times. What is important to remind and highlight, is that the [1:0] **TB423** system, in terms of aggregate percentage, doesn't correspond to the [1:0] **TB207**. Its SSA features (e.g. A_{mono}/A_{agg}) that were described in the previous sections, reveal that the **TB423** 1:0 TiO_2 DSSC, is much less aggregated, due to the bulkier side group. Indeed, the near-IR aggregates ESA is much weaker in amplitude and the rising times, associated with ET are longer (50 ps), reminding more the 1:50 TiO_2 **TB207** DSSC. This observation establishes **TB423** as an appealing candidate for DSSC applications, with prospects to surpass the performance of **TB207**. However, it is noticeable that both the ET and PA exhibit similar dynamics and therefore a degree of ET and injection competition should be accounted for. In conclusion, from the TAS of both **TB207** and **TB423**, it is evident that the reaction scheme is similar to that described in detail for **VG20** and the detailed analysis of the dynamics should reveal the extent of ET and electron injection competition, resulting in higher or lower PCE.

5.5.2 Detailed determination of the injection and FRET rates and yields

In the previous section the spectral features that reveal ET, as well as the dye cation signal, were identified in the TAS spectral map. The complexity of the TAS gives rise to many overlapping spectral signals and the SE part cannot be purely isolated. Therefore the necessity raised for using FLUPS, in order to purely resolve the fluorescence dynamics that contain all the information relative to ET and injection dynamics. In Figure 5.37, the normalized fluorescence up-conversion kinetics are presented with the respective fit curves, for **TB207** in solution and in Al_2O_3 and TiO_2 DSSCs [2]. In a first inspection the Al_2O_3 kinetics (Figure 5.37.green) is strongly quenched, compared to solution and has already decayed in the 1 ns time window, due to monomer-to aggregate ET. Finally, the TiO_2 DSSCs kinetic (Figure 5.37.blue) decays even faster than in the Al_2O_3 DSSC, because of additional charge injection. A three-exponential fit is required to capture the main decay time scales and provide regular fit residuals. Their values as well as the relative amplitudes are given in table 5.21. A simple method of evaluating the carrier

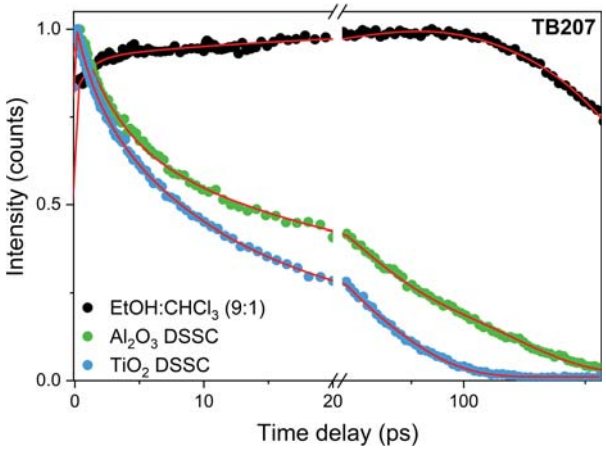

Figure 5.37: Normalized FLUPS kinetics with their respective fitting curved as red solid lines, of **TB207** in $EtOH : CHCl_3$ (9 : 1) solution, in Al_2O_3 and TiO_2 DSSCs, in the standard conditions. The solution samples were excited at 740 nm and the DSSCs at 730 nm, with an energy of 26 $\mu J/cm^2$. The standard conditions, relative to the dye:CDCA ratio for the Al_2O_3 DSSC is 1:0 and for the TiO_2 DSSC is 1:50.

injection efficiency is based on the average rates of carrier injection $\langle k_{inj} \rangle$, energy transfer $\langle k_{ET} \rangle$ and of isolated monomer excited state decay $\langle k_{mono} \rangle >$. The injection efficiency can

[2]For the **TB207** TiO_2 DSSCs the FLUPS traces for all CDCA concentrations are presented in Figure A.20 of the Appendix.

be expressed as:

$$\Phi_{inj} = \frac{\langle k_{inj} \rangle}{\langle k_{inj} \rangle + \langle k_{ET} \rangle + \langle k_{mono} \rangle} \tag{5.8}$$

$\langle k_{mono} \rangle \approx 1/3200\ ps^{-1}$, as it was found in solution is 10-100 times smaller than the ET and injection rates, which largely dominate (table 5.21). Consequently, eq. 5.8 can be simplified as:

$$\Phi_{inj} = \frac{\langle k_{inj} \rangle}{\langle k_{inj} \rangle + \langle k_{ET} \rangle} \tag{5.9}$$

Since $\langle k \rangle_{Al_2O_3} = \langle k_{ET} \rangle$ and $\langle k \rangle_{TiO_2} = \langle k_{ET} \rangle + \langle k_{inj} \rangle$ we find with the fit values from table 5.21 that $\langle k_{ET} \rangle = 0.0185\ ps^{-1}$ and $\langle k_{inj} \rangle = 0.037\ ps^{-1}$ and finally the injection efficiency is calculated to be $\Phi_{inj} \approx 67$ %, for **TB207**, i.e around two times higher than for the cyanine **VG20**. The main reasoning lies in the reduced **TB207** aggregate formation and the reduced ET amplitude and competition with charge injection. In addition, for **VG20**, the determination of the injection efficiency, was carried out by analysis of the TAS and it also possible that is underestimated. Both GSB and SE overlay and therefore it is possible that the ΔA amplitude, in early times, contains contribution from SE, resulting in underestimation of the injection efficiency value, as it was calculated, according to eq.5.7.

Table 5.21: Fitting values, of the FLUPS kinetics, of **TB207** in Al_2O_3 and TiO_2 DSSCs, prepared under the standard conditions*. The fits were made with a sum of 3 exponentials convoluted with a 150-fs Gaussian (temporal resolution). $\langle \tau \rangle$ and $\langle k \rangle$ refer to the average lifetime and the corresponding average rate.

DSSC	A_1%	$\tau_1(ps)$	A_2%	$\tau_2(ps)$	A_3%	$\tau_3(ps)$	$\langle \tau \rangle ps$	$\langle k \rangle ps^{-1}$
Al_2O_3	35	2.0	39	17	26	180	54.1	0.0185
TiO_2	16	1.5	43	8	41	35	18.0	0.055

*The standard dye:CDCA conditions for the Al_2O_3 DSSC are 1:0 and for the TiO_2 DSSC are 1:50.

An identical procedure was followed for the **TB423** DSSCs. In Figure 5.38, the normalized fluorescence up-conversion kinetics are presented for **TB423** in solution and in Al_2O_3 and TiO_2 DSSCs at the standard conditions [3]. Similar to **TB207**, the Al_2O_3 trace is much faster than in solution, due to quenching from the ET contribution. However, the kinetic it doesn't decay fully in the 1 ns time window, indicating that the ET contribution

[3]For the **TB423** TiO_2 DSSCs, the FLUPS traces for all CDCA concentrations are presented in Figure A.23 of the Appendix.

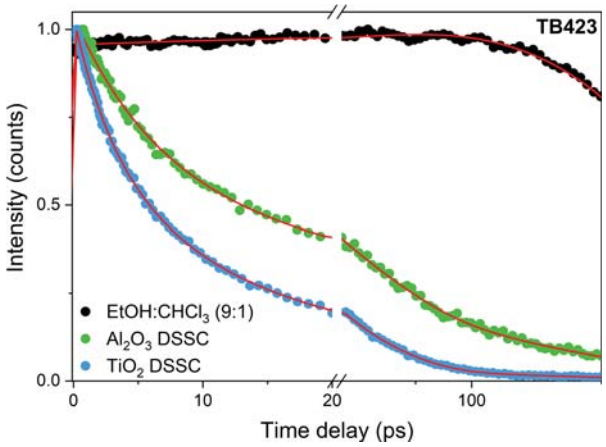

Figure 5.38: Normalized FLUPS kinetics with their respective fitting curves as red solid lines, of **TB423** in $EtOH : CHCl_3$ (9 : 1) solution, in Al_2O_3 and TiO_2 DSSCs, in the standard conditions. The solution samples was excited at 730 nm and the DSSCs at 7 20 nm, with an energy of 26 $\mu J/cm^2$. The standard conditions, relative to the dye:CDCA ratio for the Al_2O_3 DSSC is 1:0 and for the TiO_2 DSSC is 1:80.

is less than in the case of **TB207**. Moreover, the TiO_2 trace is even faster due to the additional injection process. For **TB207** the TiO_2 kinetic has decayed to the 1/3 of the total signal in only 20 ps, when for **TB423** the decay is even faster, indicating stronger quenching, due to more efficient electron injection. In table 5.22, the fitting parameters presented for the **TB423** DSSCs in the standard condition. It is evident that the first

Table 5.22: Fitting values, of the FLUPS kinetics, of **TB423** in Al_2O_3 and TiO_2 DSSCs, prepared under in standard conditions*. The fittings were made with a sum of 4 exponentials convoluted with a 150-fs Gaussian (temporal resolution). $\langle\tau\rangle$ and $\langle k\rangle$ refer to the average lifetime and the corresponding average rate.

DSSC	$A_1\%$	$\tau_1(ps)$	$A_2\%$	$\tau_2(ps)$	$A_3\%$	$\tau_3(ps)$	$A_4\%$	$\tau_4(ps)$	$\langle\tau\rangle ps$	$\langle k\rangle ps^{-1}$
Al_2O_3	45	6.2	35	29	10	103	11	740	100	0.01
TiO_2	31	2.8	39	8.2	28	27	2	338	17.7	0.056

*The standard dye:CDCA conditions for the Al_2O_3 DSSC are 1:0 and for the TiO_2 DSSC are 1:80.

two, faster, components are slower for **TB423**, in comparison to **TB207**, confirming that ET is slower for the bigger dye. It should be recalled that due to the inhomogeneity of the system, as ET and injection appear in a distribution of times. However, the general trend of slower ET dynamics is present. From the values of table 5.22 and considering that both ns components of the solution samples are many orders of magnitude longer

than the times obtained for the DSSCs, the same procedure as for **TB207** is applied. Therefore, the average rate for ET and injection are found to be $\langle k_{ET} \rangle = 0.01\ ps^{-1}$ and $\langle k_{inj} \rangle = 0.056\ ps^{-1}$ and the injection efficiency is calculated by eq.5.9, reaching the impressive value of $\Phi_{inj} \approx 82\ \%$. Therefore, **TB423** has been proven to be the best among the three dyes, in terms of injection efficiency, however, with the total PCE values yet to be optimized.

In a different approach the ET and injection rates can be identified via TAS (Figure A.21), which offers the unique advantage of visualizing the spectral responses for the various calculated time constants. In Figure B.12 the DADS are plotted for **TB207** in (A) Al_2O_3 and in (B) TiO_2 DSSCs, under standard conditions. To facilitate the interpre-

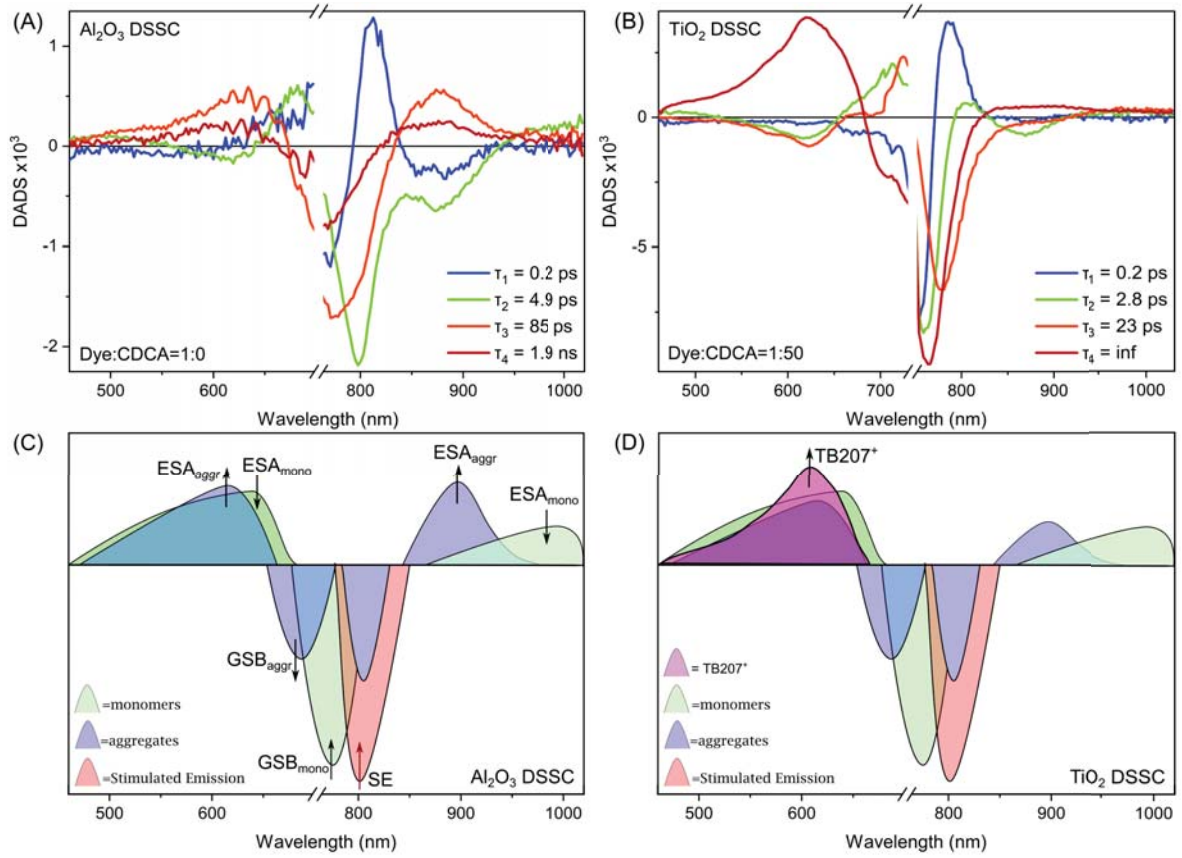

Figure 5.39: DADS, of **TB207** of (A) Al_2O_3 and (B) TiO_2 DSSCs, in the standard conditions. The samples was excited at 730 nm, with an energy of 26 $\mu J/cm^2$. The standard conditions, relative to the dye:CDCA ratio for the Al_2O_3 DSSC is 1:0 and for the TiO_2 DSSC is 1:50. (C) Al_2O_3, (D) TiO_2: A pictorial representation of the ΔA spectra, distinguishes the different ESA, GSB, SE and PA contributions, for both monomers and aggregates. The corresponding TAS are presented in Figure 5.32 (Al_2O_3) and 5.36 (TiO_2).

tation, a graphical illustration for (C) the Al_2O_3 and (D) TiO_2 DSSCs, of the major ΔA signals (GSB, ESA, SE, PA), in the TAS spectral region, are presented. With different colouration, the complicated ESA due the monomers and aggregates, as well the total GSB, can be distinguished, facilitating the interpretation of the DADS spectra. The global analysis approach was carried out with four wavelength-independent lifetimes. In agreement with the fluorescence decay times, $\tau 2$ and $\tau 3$ are shorter for TiO_2 than for Al_2O_3 DSSCs. The spectral features of the DADS allow to corroborate the excited state quenching mechanisms and the associated time constants i.e. cation formation and monomer-to-aggregate ET.

For Al_2O_3, the global decay constants obtained are 0.2 ps, 4.9 ps, 85 ps and 1.9 ns. The first and second components (0.2 ps, 4.9 ps) show ET character from the monomers to the aggregates, as it is revealed by the negative DADS at 630 nm and 880 nm, i.e. rise of the aggregate ESA. Moreover, the positive amplitudes in the 680-700 nm spectral range, where GSB dominates, highlight an increasing GSB in this wavelength range, where the aggregates high energy band prevails. On the other hand, the positive amplitude in the 0.15 ps DADS at 800 nm, is due to an ultrafast red-shift of the SE, attributed to excited state relaxation, also observed in the fluorescence up-conversion data (Figure 5.33). At 840-920 nm, the negative amplitude of both DADS is due to SE decay and rise of the aggregates ESA. In conclusion, and consistent with the fluorescence data, ET acts in a range of times from 0.15-5 ps, attributed to a distribution of monomer-to-aggregate distances and orientations on the SC nanoparticles. The DAD spectrum of the third time constant (85 ps), is positive at the aggregates ESA (630 & 880 nm), negative at the GSB of aggregates (690 & 800-820 nm) and therefore refers to the excited state decay of aggregates. The fluorescence is also in this range and monomers and aggregates coexist in this time scale. Furthermore, in τ_3, there is some contribution from SE and the low energy ESA of the monomers hasn't decayed completely, revealing a situation, identical to **VG20**, where aggregates and a percentage of neighbour monomers decay together to the ground state. The final DADS, at 2 ns component carries higher error in the time value, due to the limited experimentally accessible time-window. In 2 ns the low energy monomer ESA (955-1030 nm) has decayed and similar to the third component, the DADS is positive in the region of the two aggregates ESA, but with lower amplitude. In addition, the negative DADS, in the GSB region, is slightly blue-shifted compared to the case of τ_3. This observation, could indicate that pure aggregates that essentially have non-radiative character decay in the ns time scale.

Figure B.12.B, shows the DADS for TiO_2 with four time constants of 0.2, 2.8, and

23 ps and τ4 that has been fixed to a very long value to match the constant asymptotic signal. The spectral responses, differentiate from Al_2O_3 to TiO_2, where in the latter there is no indication of sub-ps ET and only the solvation features appear. In addition, for TiO_2, the 2.8 ps and 23 ps DADS are positive at the aggregate GSB region (690 nm) and negative at the SE and near-IR aggregates ESA (860-900 nm) regions. Likewise, the DADS are negative in the range 500-650 nm, which in the case of TiO_2, contains not only the aggregates ESA, but the **TB207** cation absorption spectrum, too. The rise of the absorption of **TB207** cation, corresponds directly, to the carrier injection process. This observation is in agreement with the proposal that both electron injection and ET take place in a distribution of times and not in a well-defined single time constant. Therefore, both the 2.8 ps and 23 ps correspond to the ET and injection process for TiO_2. The injection times are relatively slower than the faster ones reported for the benchmark Ru compounds, for which electron injection has been reported to start in sub-ps timescales [11]. The elongation of the injection times, can be attributed to the weaker driving force for injection, for the specific near-IR dyes, due to the smaller LUMO-CB energetic difference. It has been noted, from the DADS spectra for Al_2O_3 that ET starts acting in the sub-ps up to 4.9 ps time domain. However, detailed global analysis is a general approach and by probing individually the ESA of the aggregates no rise in the sub-ps time domain is found and the sub-ps component in the DADS, mostly corresponds to the solvation dynamics, but it is generalized to "catch" the kinetics in the whole spectral region. Moreover, the $Al2O_3$, DSSC, is slightly more aggregated than the TiO_2 (Figure 5.6) one, in the standard conditions. Therefore, when for the FLUPS analysis of the fluorescence kinetics, it is sufficient to compare the two DSSCs, for the detailed and in the whole TAS map, global analysis, the deviations of the ET times are present. It cannot be excluded that ET component is also present in 23 ps for the Al_2O_3 DSSC, while for the TiO_2 the positive band at the aggregates ESA at 720 nm constitutes a clear ET character. However, the much weaker negative signals at 850 nm (aggregates ESA of lower energy), indicate that injection mainly occurs in these times (see negative signal at 450-660 nm). The fourth DADS at fixed “infinitive” time, is identical to any selected transient spectrum at longer times giving the pure **TB207** cation absorption spectrum (500-690 nm) and the residual GSB of **TB207** (700-850 nm). The final reaction scheme of the injecting TiO_2 DSSC, is presented in Figure 5.40. The aggregate relaxation times were identified for Al_20_3, however in TiO_2 these contributions are not-detectable, due the ET quenching from the electron injection that occurs in similar times and therefore temporally competes.

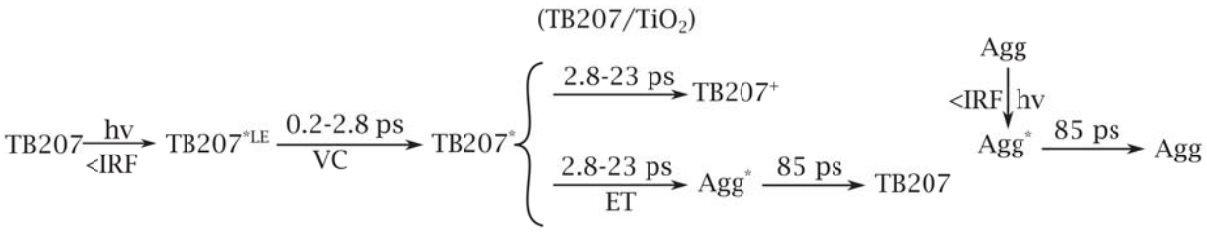

Figure 5.40: Excited state reaction scheme of TB207 TiO_2 DSSCs. The $\boldsymbol{TB207}^+$ cation, due to electron injection, can be formed and electron injection temporally competes with ET from monomers to aggregates.

The same comparison has been made for **TB423**. The DADS are presented in Figure 5.41.A.B, for both Al_2O_3 and TiO_2, respectively. The spectral position of the species and

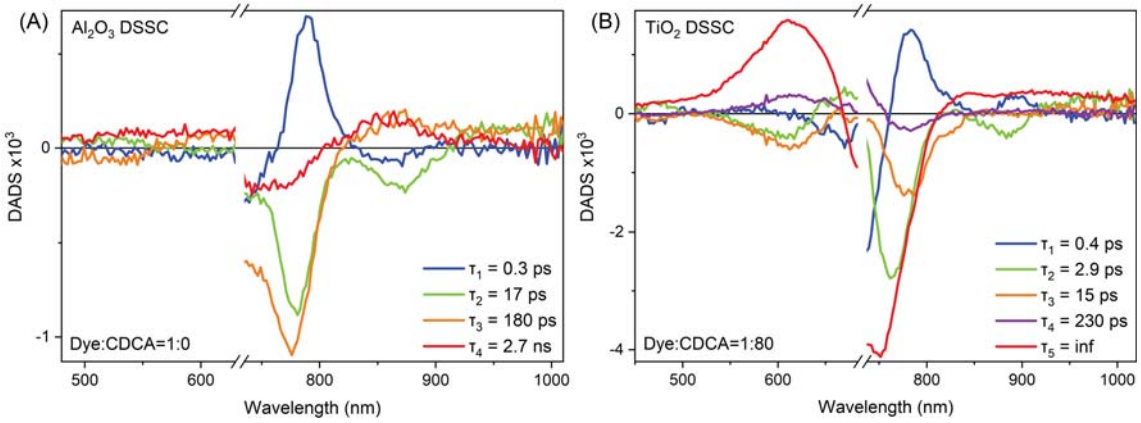

Figure 5.41: DADS of **TB423** of (A) Al_2O_3 and (B) TiO_2 DSSCs, in the standard conditions. The samples was excited at 830 nm, with an energy of 26 $\mu J/cm^2$. The standard conditions, relative to the dye:CDCA ratio for the Al_2O_3 DSSC is 1:0 and for the TiO_2 DSSC is 1:80.

processes are the same, as for **TB207**, with a general 10 nm blue-shift and therefore, in order to facilitate the interpretation, the pictorial representation of FigureB.12.C..D, can be used too. For Al_2O3 the times obtained by global analysis are 0.3 ps, 17 ps, 180 ps and 2.7 ns. The first component, similar to **TB207**, shows a positive signal at 780 nm, a trend that was attributed to ultrafast solvation of the monomer excited state. The negative feature at 870 nm (aggregates ESA), reveals that ET from monomers to aggregates, already starts in the sub-ps time domain. The visible part at 450-650 nm, has very low intensity and due to the low signal/noise ratio, no observations can be made, regarding the dynamic evolution of the ESA of monomers and aggregates. The last two components refer to the aggregate relaxation time, as it can be observed by the positive, aggregate ESA signals at 870 nm. In detail, similar to **TB207**, the faster, 180 ps component retains

a smaller SE contribution and monomers ESA (950-1030 nm) decay, indicating that in this times, in parallel with the aggregates, a percentage of neighbor monomer dyes are relaxing too. It is possible that this time refers to the pair of monomers/aggregates that interact and undergo ET. The last 2.7 ns component, shows only aggregates character and could refer to the rest of non-interactive aggregate. For the TiO_2 DSSC, 5 time constants describe the system best. The sub-ps component similarly to Al_2O3 and shows solvation character. The second, 2.9 ps and the third 15 ps refer to both ET and injection. Indeed, they both show negative DADS at the aggregate ESA at 630 nm and and positive DADS at the aggregate GSB at 700 nm. The near-IR, aggregate ESA amplitude at 870 nm is negative only for 2.9 ps, while for 15 ps it is compensated with a positive signal, probably of the monomer ESA decay. Therefore, ET and injection, both occur in the range of 2.9-15 ps, where the SE part (780-790 nm), also mainly decays. The times found by GA, are in a good agreement with the ones found via FLUPS, except the sub-ps that is absent in FLUPS, due to the longer IRF. The forth components (230 ps), has a smaller contribution and similarly to the third time component of the Al_2O_3 DSSC, it reflects the aggregate relaxation. Finally, the fifth component has been fixed to very long times, in order to account for the long time asymptotic signal, where positive, representing the **TB423** cation absorption and where negative, representing the GSB remaining, due to the reduced recovered monomers that injected and converted to cations. The corresponding reaction scheme is presented in Figure 5.42 and it is similar as for **TB207** with the respective aggregates/monomer and aggregates relaxation times (230 ps and 2.7 ns,respectively) to be significantly quenched in the data.

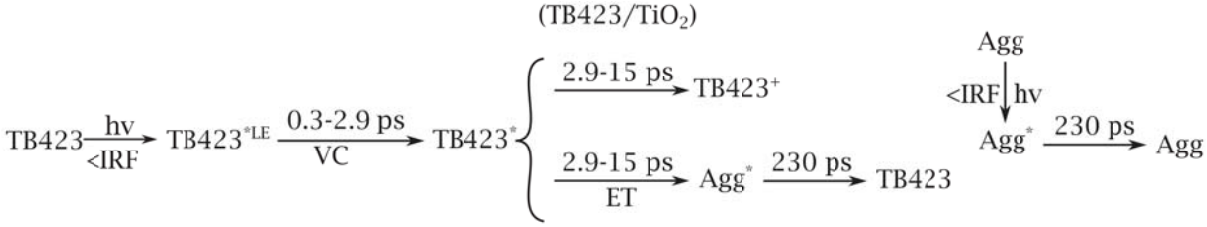

Figure 5.42: Excited state reaction scheme of TB423 TiO_2 DSSCs. The $\boldsymbol{TB423^+}$ cation, due to electron injection, can be formed and injection temporally competes with ET from monomers to aggregates.

Another important effect that has been examined for both **TB** dyes is the effect of CDCA and therefore of aggregates on injection. The photovoltaic measurements, revealed that **TB207** is sensitive to CDCA and more in detail, the PCE drops as the CDCA decreases (table 5.7), indicating that if aggregates inject, the process should be of much lower yield than monomers. For **TB423**, the trend is different, as there is no significant

effect of CDCA on the final PCE (table 5.7). However, no clear conclusion can be made about the injection efficiency from aggregates, as essentially, there is no great effect of CDCA on the **TB423** DSSC SSA spectra. It would be of interest, future experiments to be planned for analytical studies of pure aggregated **TB** DSSCs, in order to identify aggregate contribution in injection, with quantitative conclusions.

Finally, the injection efficiencies of the **TB207** and **TB423** TiO_2 DSSCs, as a function of CDCA have been calculated, in the same way as they were calculated for the **VG20** DSSCs (eq. 5.7), from the respective **TB207** and **TB423** TiO_2 transient spectra in Figures A.18, A.21 in the Appendix. Noted that the corresponding DADS for both **TB207** and **TB423** TiO_2 DSSCs are presented in the Appendix too (Figures A.19, A.22, respectively), as well as the tables with the kinetics parameters for both GA and single wavelength kinetic analysis, over various wavelengths (tables A.9, A.10, respectively). The calculated values are presented in table 5.23. For **TB207**, the injection efficiency increases from 39 %, for the CDCA-free system, up to 65 % for the 1:100 dye:CDCA case. This trend is in agreement with the photovoltaic measurements, as a function of CDCA

Table 5.23: Injection efficiencies (Φ_{inj}) of **TB207** and **TB423** TiO_2 DSSCs, increasing CDCA concentration with the electrolyte in standard conditions (1 M Li^+).

Dyes	**[Dye:CDCA]**	$\mathbf{\Phi_{inj}}$
TB207	1:0	39
	1:20	36
	1:50	43
	1:100	65
TB423	$1{:}0_{exc.690\ nm^*}$	60
	$1{:}0_{exc.790\ nm^*}$	51
	1:0	60
	1:50	65
	1:80	61

*All the **TB207** DSSCs were excited at 730 nm, when the **TB423** ones, where excited at 720 nm. The **TB423** DSSC in 1:0 conditions, was excited additionally at 690 nm and 790 nm, as it is indicated in the index.

(table 5.7), where the optimal PCE was found to be 1:50. While for 1:100 the injection efficiency increases, due to the minimized ET contribution, dye loading is sacrificed and therefore the PCE decreases. For **TB423**, both the injection efficiency and the PCE, aren't strongly affected by CDCA, as the system is in general optimal de-aggregated,

due to the bulkier nature of the dye. However, the injection efficiency is $\sim$ 20 %, higher for **TB423**, in comparison to **TB207** in optimal conditions, establishing it as a more appropriate DSSC candidate, of high PCE x AVT performance.

5.6 Summary and conclusions

In the experimental section of the current PhD Thesis, a complete spectroscopic investigation of three novel dye sensitizers was made. All three dyes (**VG20**, **TB207** and **TB423**), demonstrate excellent properties for transparent DSSC applications. After thorough optimization, the cyanine **VG20**, reaches PCE efficiencies over 3 %, while the **TB** dyes exhibit improved performances reaching for the dye-category the impressive, PCE of 3.9 %. The study was divided in two parts, the first refers to the cyanine **VG20** dyes and the second is related to the pyrrolopyrrole-cyanine dyes **TB207** and **TB423**. Analytical investigation of the dyes in solution phase was made, as well as, when they were incorporated in real DSSCs. The steady state absorption, directly showed that molecular aggregates are formed upon the dye attachment on the semiconductor and by using CDCA, the aggregates features greatly reduce. The aggregates spectrum was extracted, showed two peaks that according to the classic exciton theory, as described by Kasha, could refer to aggregates of an oblique geometry, with photophysical behavior that is related to a combination of both H and J-type aggregates. The fluorescence of the monomers overlays greatly with the lower aggregate band, indicating that interaction of energy transfer type, between the two species, can take place. Moreover, **VG20**, was identified to be the most notorious in terms of aggregates formation and without CDCA, the absorption broadly spans the visible spectral region. The second part of the experimental study focused on the time-resolved spectroscopy, in the fs, ps and ns time domain, in order to investigate the dynamic evolution of the system, for all dyes and important findings were retrieved.

Starting with **VG20**, in solution only monomers exist and therefore the excite state dynamics corresponds to their deactivation to the ground state. Continuing, the standard experimental strategy was organized by the individual study of the dye in both non-injecting, ZrO_2 and injecting, TiO_2, DSSCs. From the ZrO_2 studies, ET was found to occur in a distribution of times, from sub-ps up to 4 ps. Extending the study in the efficient TiO_2 DSSCs, the charge injection was determined to occur in similar time scales as ET. Therefore, ET and charge injection processes, dynamically compete, establishing

ET from monomers to aggregates, as the main loss channel for injection, as it has been reported in the reaction scheme in Figure 5.17. Additional TAS studies were performed, in various DSSCs, as a function of CDCA and it was found that ET becomes slightly slower, as the intermolecular distances of monomers and aggregates increase. The injection efficiency of the optimal CDCA conditions was determined to be around 30 %, revealing that aggregates are a major limitation for cyanine based DSSCs. The Li^+ additive in the electrolyte is of great importance, as it efficiently reduces the TiO_2 CB level, enhances the driving force for injection. Additional studies as a function of Li^+ concentration in the electrolyte, revealed that the charge injection times become faster, as the driving force optimizes. The optimal concentration was found to be 1 M.

The same experimental strategy was applied for **TB207** and **TB423**. Due to the increased complexity of the TAS spectra, because of the many overlaying signals, additional and complementary studies were performed via the FLUPS technique, in order to monitor exclusively the fluorescence dynamics. It was found that the reaction scheme is the same for both **TB** dyes, as for **VG20**. However, due to the bulkier structure of the **TB** dyes, the SSA spectra, showed weaker dependence on CDCA, with **TB423** to be almost independent of CDCA. For **TB207**, the ET and carrier injection times were found to be both in the range of 2.8-23 ps, acting in a competitive way. These injection times, are slower than for **VG20**, possible due to the weaker driving force for injection and charge separation in the excited state, towards the anchoring groups. The injection efficiency was calculated to be 40-60 %, already higher than for **VG20**, due to the reduced ET. For **TB423**, both ET and injection times are found, by global analysis, to be in the range of 2.9-15 ps, slightly faster than for **TB207**. Visualizing both contributions as distributions, the data showed that ET times are slower for **TB423**, as it is expected for a larger dye, when the ET contribution is also reduced, due to the reduced aggregate formation on these non-symmetric dyes that essentially have an even bulkier side group. Therefore, the injection efficiency is boosted compared to **TB207** and it was identified to take values in the range of 60-80 %, establishing this dye as the most promising for DSSC applications.

In summary, all three novel dyes have been synthesized to absorb in the near-IR with the highest possible efficiency, which is significantly limited, due to the low LUMO energy of the dyes. After thorough optimization, the **TB207** DSSCs were able to reach PCEs near 4 %, maintaining high AVT for transparent applications. The aggregates drawback, was tackled, in the new Pyrrolopyrrole Cyanine series of dyes, which carry bulkier structures and independent experiments show that **TB423** could surpass **TB207**. The future

study includes new dyes, with improved units of conjugated backbone, for example instead of Ph-groups, other electron rich moieties that boost the charge separation through the -COOH groups could be used, maintaining the bulkier possible structure, in order to reduce aggregates.

References

[1] W. Naim *et al.*, "Transparent and colorless dye-sensitized solar cells exceeding 75% average visible transmittance," *Jacs Au*, vol. 1, no. 4, pp. 409–426, 2021.

[2] V. Novelli, N. Barbero, C. Barolo, G. Viscardi, M. Sliwa, and F. Sauvage, "Electrolyte containing lithium cation in squaraine-sensitized solar cells: Interactions and consequences for performance and charge transfer dynamics," *Physical Chemistry Chemical Physics*, vol. 19, no. 40, pp. 27 670–27 681, 2017.

[3] V. Novelli, "Light harvesting in dye-sensitized solar cells: Challenges and perspectives of near-ir conversion," Ph.D. dissertation, Université de Picardie Jules Verne, 2017.

[4] T. Ono, T. Yamaguchi, and H. Arakawa, "Study on dye-sensitized solar cell using novel infrared dye," *Solar Energy Materials and Solar Cells*, vol. 93, no. 6-7, pp. 831–835, 2009.

[5] G. M. Fischer, E. Daltrozzo, and A. Zumbusch, *Selective nir chromophores: Bis (pyrrolopyrrole) cyanines*, 2011.

[6] G. M. Fischer, M. Isomäki-Krondahl, I. Göttker-Schnetmann, E. Daltrozzo, and A. Zumbusch, "Pyrrolopyrrole cyanine dyes: A new class of near-infrared dyes and fluorophores," *Chemistry–A European Journal*, vol. 15, no. 19, pp. 4857–4864, 2009.

[7] G. M. Fischer, A. P. Ehlers, A. Zumbusch, and E. Daltrozzo, "Near-infrared dyes and fluorophores based on diketopyrrolopyrroles," *Angewandte Chemie International Edition*, vol. 46, no. 20, pp. 3750–3753, 2007.

[8] G. M. Shalhoub, "Visible spectra conjugated dyes: Integrating quantum chemical concepts with experimental data," *Journal of chemical education*, vol. 74, no. 11, p. 1317, 1997.

[9] L. Zhang and J. M. Cole, "Dye aggregation in dye-sensitized solar cells," *Journal of Materials Chemistry A*, vol. 5, no. 37, pp. 19 541–19 559, 2017.

[10] M. Ziółek, J. Karolczak, M. Zalas, Y. Hao, H. Tian, and A. Douhal, "Aggregation and electrolyte composition effects on the efficiency of dye-sensitized solar cells. a case of a near-infrared absorbing dye for tandem cells," *The Journal of Physical Chemistry C*, vol. 118, no. 1, pp. 194–205, 2014.

[11] C. Martın, M. Ziółek, and A. Douhal, "Ultrafast and fast charge separation processes in real dye-sensitized solar cells," *Journal of Photochemistry and Photobiology C: Photochemistry Reviews*, vol. 26, pp. 1–30, 2016.

[12] K. Pydzińska and M. Ziółek, "Solar cells sensitized with near-infrared absorbing dye: Problems with sunlight conversion efficiency revealed in ultrafast laser spectroscopy studies," *Dyes and Pigments*, vol. 122, pp. 272–279, 2015.

[13] K. Virkki, E. Tervola, M. Medel, T. Torres, and N. V. Tkachenko, "Effect of coadsorbate and hole transporting layer on the photoinduced charge separation at the tio2–phthalocyanine interface," *ACS omega*, vol. 3, no. 5, pp. 4947–4958, 2018.

[14] A. R. Monahan and D. F. Blossey, "Aggregation of arylazonaphthols. i. dimerization of bonadur red in aqueous and methanolic systems," *The Journal of Physical Chemistry*, vol. 74, no. 23, pp. 4014–4021, 1970.

[15] P. Bojarski *et al.*, "Fluorescent dimers of rhodamine 6g in concentrated ethylene glycol solution," *Chemical physics*, vol. 210, no. 3, pp. 485–499, 1996.

[16] F. Del Monte, J. D. Mackenzie, and D. Levy, "Rhodamine fluorescent dimers adsorbed on the porous surface of silica gels," *Langmuir*, vol. 16, no. 19, pp. 7377–7382, 2000.

[17] T. Baranyaiová and J. Bujdák, "Effects of dye surface concentration on the molecular aggregation of xanthene dye in colloidal dispersions of montmorillonite," *Clays and Clay Minerals*, vol. 66, no. 2, pp. 114–126, 2018.

[18] C. M. Carbonaro, "Tuning the formation of aggregates in silica–rhodamine 6g hybrids by thermal treatment," *Journal of Photochemistry and Photobiology A: Chemistry*, vol. 222, no. 1, pp. 56–63, 2011.

[19] N. R. Reddy, S. Rhodes, Y. Ma, and J. Fang, "Davydov split aggregates of cyanine dyes on self-assembled nanotubes," *Langmuir*, vol. 36, no. 45, pp. 13 649–13 655, 2020.

[20] M. Y. Losytskyy, V. Yashchuk, S. Lukashov, and S. Yarmoluk, "Davydov splitting in spectra of cyanine dye j-aggregates, formed on the polynucleotides," *Journal of Fluorescence*, vol. 12, no. 1, pp. 109–112, 2002.

[21] S. L. Yefimova, G. V. Grygorova, V. K. Klochkov, I. A. Borovoy, A. V. Sorokin, and Y. V. Malyukin, "Molecular arrangement in cyanine dye j-aggregates formed on ceo2 nanoparticles," *The Journal of Physical Chemistry C*, vol. 122, no. 36, pp. 20 996–21 003, 2018.

[22] V. Novelli, "Light harvesting in dye-sensitized solar cells: Challenges and perspectives of near-ir conversion," Ph.D. dissertation, Université de Picardie Jules Verne, 2017.

[23] M. P. Williams *et al.*, "Synthesis, photophysical, electrochemical, tumor-imaging, and phototherapeutic properties of purpurinimide-n-substituted cyanine dyes joined with variable lengths of linkers," *Bioconjugate chemistry*, vol. 22, no. 11, pp. 2283–2295, 2011.

[24] F. Sauvage, S. Chhor, A. Marchioro, J.-E. Moser, and M. Graetzel, "Butyronitrile-based electrolyte for dye-sensitized solar cells," *Journal of the American Chemical Society*, vol. 133, no. 33, pp. 13 103–13 109, 2011.

[25] A. Y. Anderson, P. R. Barnes, J. R. Durrant, and B. C. O'Regan, "Quantifying regeneration in dye-sensitized solar cells," *The Journal of Physical Chemistry C*, vol. 115, no. 5, pp. 2439–2447, 2011.

[26] C. J. Traverse, R. Pandey, M. C. Barr, and R. R. Lunt, "Emergence of highly transparent photovoltaics for distributed applications," *Nature Energy*, vol. 2, no. 11, pp. 849–860, 2017.

[27] M. K. Nazeeruddin *et al.*, "Acid- base equilibria of (2, 2 '-bipyridyl-4, 4 '-dicarboxylic acid) ruthenium (ii) complexes and the effect of protonation on charge-transfer sensitization of nanocrystalline titania," *Inorganic Chemistry*, vol. 38, no. 26, pp. 6298–6305, 1999.

[28] A. Hagfeldt and M. Grätzel, "Molecular photovoltaics," *Accounts of chemical research*, vol. 33, no. 5, pp. 269–277, 2000.

[29] G. Paternò *et al.*, "Excited state photophysics of squaraine dyes for photovoltaic applications: An alternative deactivation scenario," *Journal of Materials Chemistry C*, vol. 6, no. 11, pp. 2778–2785, 2018.

[30] Q. Yu *et al.*, "High-efficiency dye-sensitized solar cells: The influence of lithium ions on exciton dissociation, charge recombination, and surface states," *ACS nano*, vol. 4, no. 10, pp. 6032–6038, 2010.

[31] J. C. Brauer, A. Marchioro, A. A. Paraecattil, A. A. Oskouei, and J.-E. Moser, "Dynamics of interfacial charge transfer states and carriers separation in dye-sensitized solar cells: A time-resolved terahertz spectroscopy study," *The Journal of Physical Chemistry C*, vol. 119, no. 47, pp. 26 266–26 274, 2015.

[32] F. R. Kohl, C. Grieco, and B. Kohler, "Ultrafast spectral hole burning reveals the distinct chromophores in eumelanin and their common photoresponse," *Chemical science*, vol. 11, no. 5, pp. 1248–1259, 2020.

[33] R. A. Nome, "Ultrafast dynamics of solvation: The story so far," *Journal of the Brazilian Chemical Society*, vol. 21, pp. 2189–2204, 2010.

Chapter 6

Conclusions and perspectives

The research took place in the framework of the current PhD Thesis, is part of a broader collaborating work in the scope of the VISION-NIR project. The main perspective of this collective work, is the production of next generation solar modules, falling into the category of wavelength selective DSSCs, which fulfill the following criteria: high power conversion efficiency, long run stability, low-cost production eco and human friendly characteristics and finally high levels of transparency and aesthetic view. To fulfill these criteria, novel dyes were synthesized that belong to the family of organic near-IR sensitizers, moving in a different scope from the Ru based DSSCs that owns the record in terms of efficiency. However they are more difficult and expensive to synthesize and not eco friendly, compared to their analogue organic dyes. The dyes that were investigated in the PhD Thesis, reached efficiencies above 3 %, which is very low compare to the record $\sim$ 15 %, however the maximum AVT that was achieved, secured the impressive value of 76 % [1]. In a different, but essential approach the important quantity for a general comparison, is the product $PCE \times AVT$. In this approach, the novel dyes that have been addressed in the Thesis, have also been reported in very recent and weighty works [2], to exhibit record values, as it can also be demonstrated in the updated Figure 5.10. The above mentioned novelties belong to the general framework of the collaborating project, from optimizing the dye structures, as well as the electrolyte composition, to finally improve and enhance the total photovoltaic performances.

Our contribution was focused on the ultrafast time-resolved characterization of the DSSCs. Important findings revealed, the drawbacks of the dyes, such as the aggregate formation and assisted, in this manner, the synthesis of the improved ones. Indeed, the experiments on **TB207** and **TB423** validate the design strategy aiming at reducing

monomer-to-aggregate ET. Moreover, two ultrafast techniques (FLUPS and TAS) were used, in a complementary way, for the same DSSC samples, which in our knowledge, has not been done before for DSSC studies of the complete solar cell modules. The relative times found by the two techniques exhibited differences that were reported and the combined use of both, allowed to identify the solvation, ET and charge injection times, in order to finally construct the reaction scheme. Investigation of the complete modules were made in great detail and the sample-to-sample reproducibility was examined in a wide range of DSSCs. In this manner the standard error was reported, offering a benchmark that should be taken into account in ultrafast measurements on these samples and when comparing differences of dynamics between samples. For **VG20** fs time-resolved spectroscopy has already been applied on complete DSSCs and reported in [3]. However in our knowledge in DSSCs based on the novel pyrrolopyrrole cyanine Dyes, such as **TB207** and **TB423**, ultrafast studies have been performed for the first time in the framework of the research of the present PhD Thesis. The injection times were identified in this first report, to be in a range of 2-20 ps, which are slower than the benchmark Ru based DSSCs, as for the latter, the CB/LUMO energy difference is higher and therefore the driving force for injection is enhanced. Furthermore, while for **VG20**, the injection starts to operate from the sub-ps domain the total injection efficiency was calculated to be higher for the **TB** dyes, as their bulkier structure prevent aggregate formation, minimizing the contribution of the ET. For all three dyes, the most promising was found to be **TB423**, which compared to its analogue **TB207**, possesses an even bulkier side group, reducing even further aggregation, without sacrificing dye loading with the additional use of de-aggregate dyes, as co-adsorbents. However, the total PCE appear lower (table 5.7) and further future optimization must be carried out . Relative to the dynamics, it has been confirmed that ET and injection times are represented not as distinguished values, but as distributions. These processes are very sensitive to the average intermolecular distances, which due to the inhomogeneity of the densely packed DSSC systems, come out as distributions too. Hereby, the effect of CDCA on increasing the intermolecular distances and reducing aggregates has been highlighted, as well as its effect on the ET times. Admittedly, CDCA dependence studies, on both injecting and non-injecting, as reference, DSSCs, via two complementary fs-techniques, have been proven excellent experimental methods to construct the reaction scheme of the dyes, in great detail.

In the end of the experimental studies, the current PhD Thesis addresses some open questions. First, whether aggregates inject, contributing in the total PCE. The complexity of the mechanisms made difficult the quantitative distinction of this lateral injection

process. Future experiments could be made using broadband excitation, provided by the improved 2D-TAS, in order to investigate possible aggregate injection. Second, with our experimental techniques we were able to identify the injection efficiency in a short timescale ($\sim$ 5 ns), however the degree of possible recombination on the SC surface, reducing the total PCE is yet to be determined. Future studies could utilizing more sophisticated techniques, such as X-ray TAS (section 2.3) probing directly the SC, could provided more direct observations and information, answering this open question. In conclusion, DSSCs have been proposed as one of the few, appealing and successful next generation photovoltaic technologies, promising for future, transparent energy harvesting applications and for the optimization, ultrafast spectroscopy has been proven to be a powerful tool of characterization.

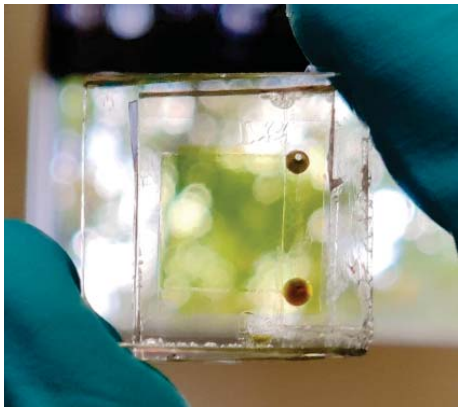

Figure 6.1: Image of a semi-transparent **TB207** TiO_2 DSSC, containing iodide based electrolyte.

References

[1] W. Naim *et al.*, "Transparent and colorless dye-sensitized solar cells exceeding 75% average visible transmittance," *Jacs Au*, vol. 1, no. 4, pp. 409–426, 2021.

[2] O. Almora *et al.*, "Device performance of emerging photovoltaic materials (version 2)," *Advanced Energy Materials*, vol. 11, no. 48, p. 2 102 526, 2021.

[3] K. Pydzińska and M. Ziółek, "Solar cells sensitized with near-infrared absorbing dye: Problems with sunlight conversion efficiency revealed in ultrafast laser spectroscopy studies," *Dyes and Pigments*, vol. 122, pp. 272–279, 2015.

Appendix A

Supporting information

The HOMO, LUMO and the difference EDD (S_0-S_1) were calculated by D. Jacquemin in the CEISAM laboratory (F. Odobel). The computational strategy relies on TD-DFT combined with the popular Polarizable Continuum Model (PCM) for simulating solvent effects (here DMF) and the computational software used is Gaussian16.A03.

The lowest bright transition corresponds to a HOMO-LUMO excitation, and we represent these two orbitals, as well as the associated electron density difference plot in Figure A.1. The HOMO is localized on the core of the dye, whereas the LUMO is slightly

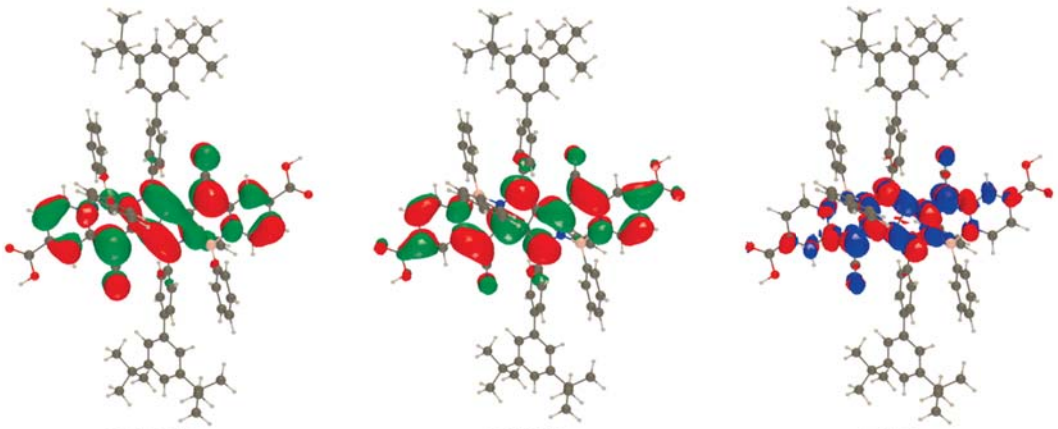

Figure A.1: From left to right: HOMO, LUMO and EDD ($S_0 - S_1$) representation for **TB207**. On the EDD, the blue and red regions represent regions of decrease and increase of electronic density upon excitation, respectively. Contour used: 0.02 (MOs) and 0.0006 (EDD).

more extended, showing contributions going up to the carboxylic anchoring groups. Nevertheless, the electronic excitation mostly induced changes in the central section of the compound, with rather limited geometrical reorganization, in line with the sharp absorp-

tion and emission bands and small Stokes shifts noted experimentally.

The 2D TAS profile, obtained via streak camera for **TB207** TiO_2 DSSC with inert electrolyte of just ACN and I_3^-/I^- redox couple in the electrolyte. In the first case, in the 2 μs time-window there is no decay of the photoproduct (**TB207** cation), because there is no redox couples. In this case any decay component refers to recombination mechanisms. In the second case, the iodide based electrolyte regenerates the dye cation, with efficiency near $\sim$ 100 %.

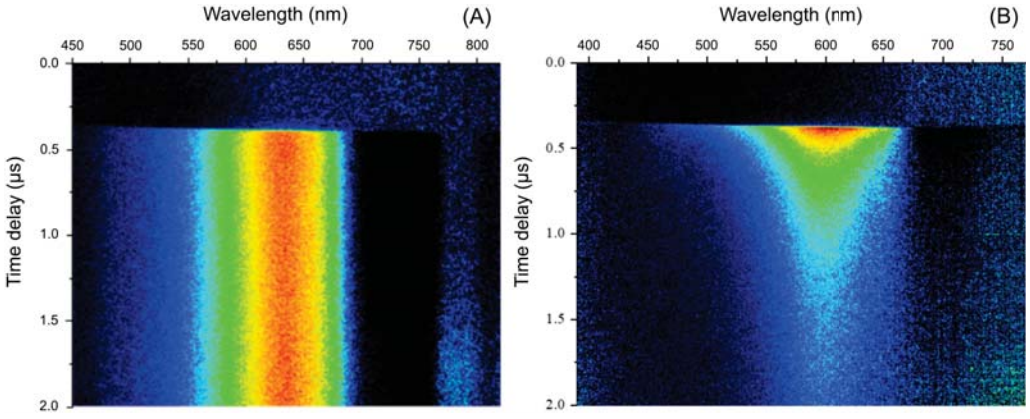

Figure A.2: 2D TAS profile, obtained via streak camera for **TB207** TiO_2 DSSC with (A) inert electrolyte of just ACN and (B) with I_3^-/I^- redox couple in the electrolyte.

Before measurements powertests were performed for all samples, both the solution and the DSSCs. When the energy density/pulse is too high, possible phenomena, such as Singlet-Singlet annihilation can occur, introducing in this way additional complexity in the reaction scheme. In addition, high powers can degrade and even destroy the samples, over long experimental times. The linearity of excitation is examined, by reporting the maximum intensity of the signal for a given energy density/pulse. Note, that for the calculation of the energy density/pulse, the beam profile was considered as circular and the diameter was considered at the $1/e^2$. For the **TB**-dyes, it is evident that in solution the non-linear regime is above 120 $\mu J/cm^2$, when for the DSSC is much lower $\sim$ 80 for TiO_2 and $\sim$ 40 for Al_2O_3. However, by overlaying the kinetics of the ESA or GSB signals, increasing the excitation energy density/pulse, no significant changes can be seen for the solution sample (Figure A.3.E), when for the DSSC the kinetics become significantly faster from 15 to 118 $\mu J/cm^2$ (Figure A.3.F). Therefore, for solution measurements $\sim$ 60 $\mu J/cm^2$ excitation energy density/pulse was chosen, when for the DSSCs $\sim$ 30 $\mu J/cm^2$. For the **VG20** DSSCs the samples were excited with $\sim$ 40 $\mu J/cm^2$, ensuring that the excitation is still in the linear regime. In general, the **VG20** samples are more aggregated than the **TB** and the ultrafast mechanisms (ET, electron injection) found to operate faster. Therefore, the threshold for the non-linear regime of excitation appears to be in smaller energy density/pulse ($\sim$ 50 $\mu J/cm^2$).

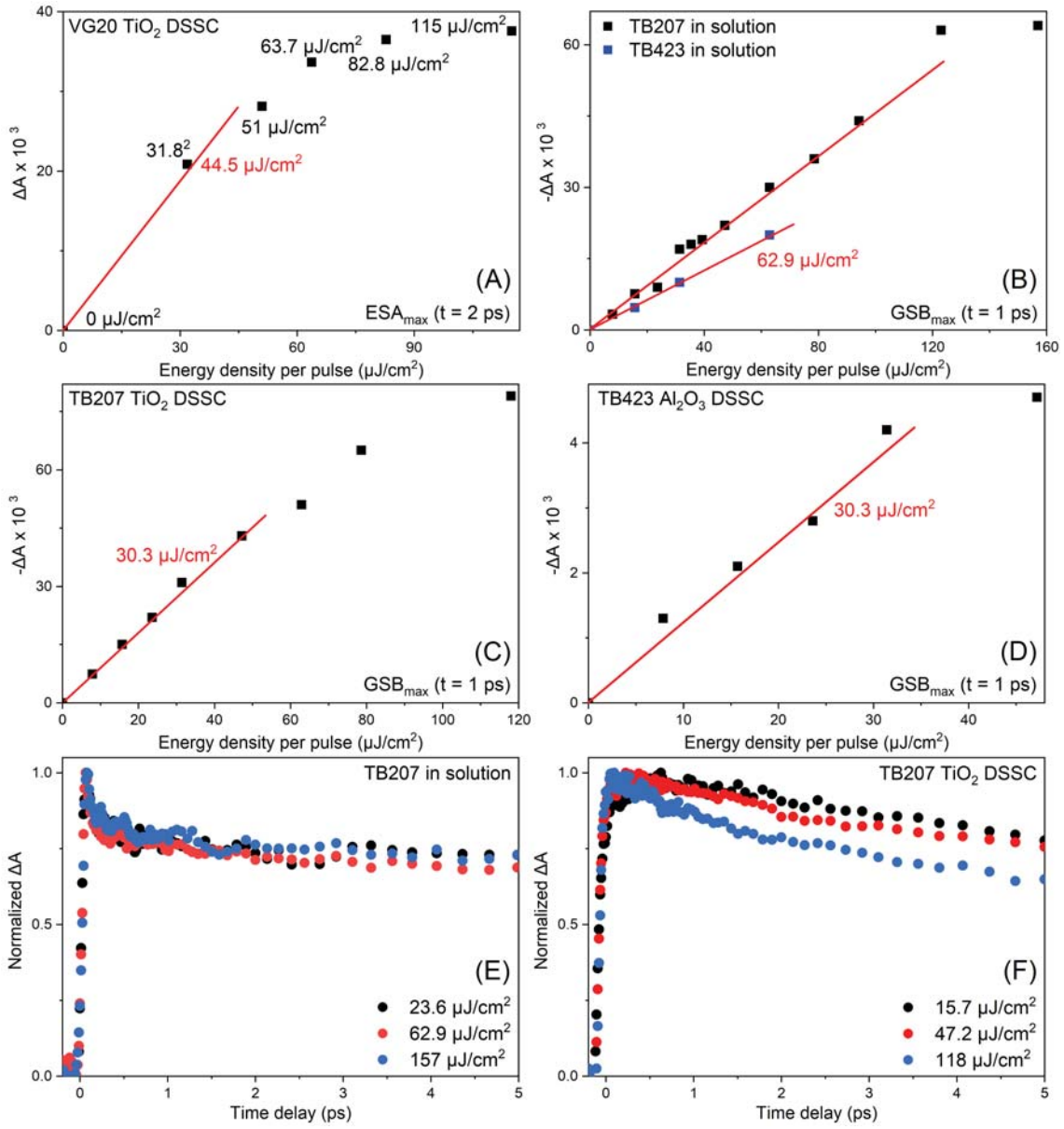

Figure A.3: Powertests of **VG20**, **TB207** and **TB423**, for both solution and DSSC samples.

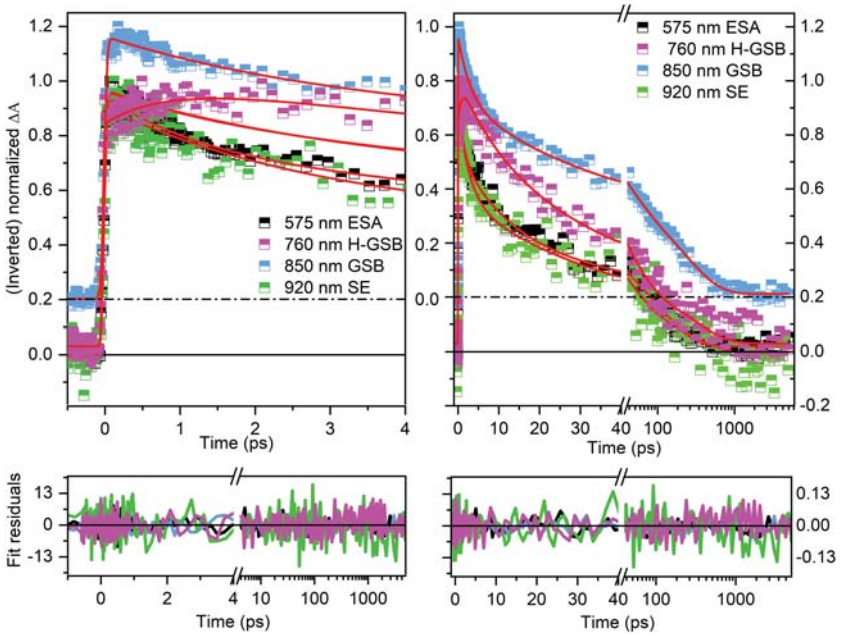

Figure A.4: TA kinetics of **VG20** ZrO_2 [1:500] dye:CDCA DSSC at different wavelengths. The left panel is restricted in the first 4 ps and the right in the whole 5 ns time-window, with a break at 40 ps and a logarithmic scale afterwards.

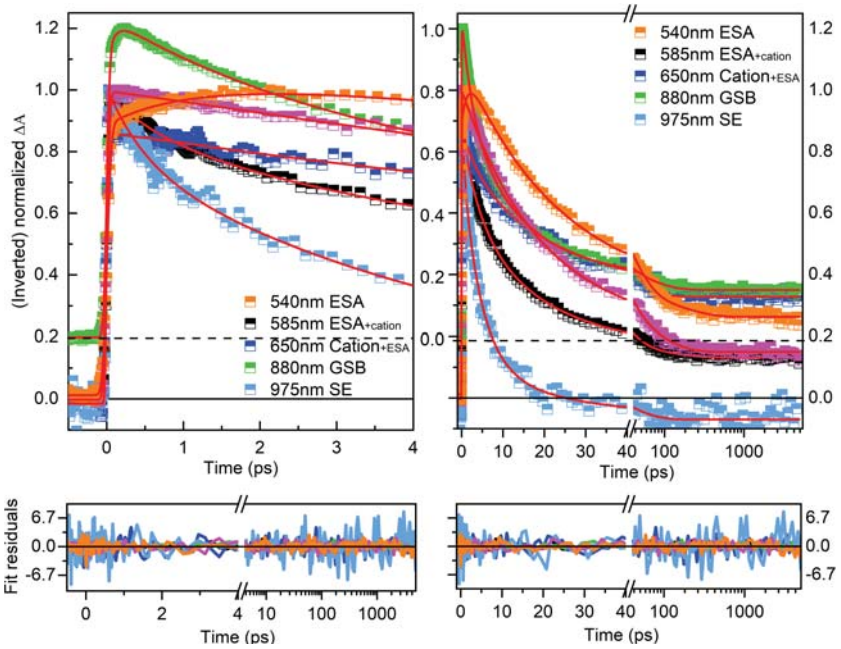

Figure A.5: TA kinetics of **VG20** TiO_2 [1:500] dye:CDCA DSSC at different wavelengths. The left panel is restricted in the first 4 ps and the right in the whole 5 ns time-window, with a break at 40 ps and a logarithmic scale afterwards.

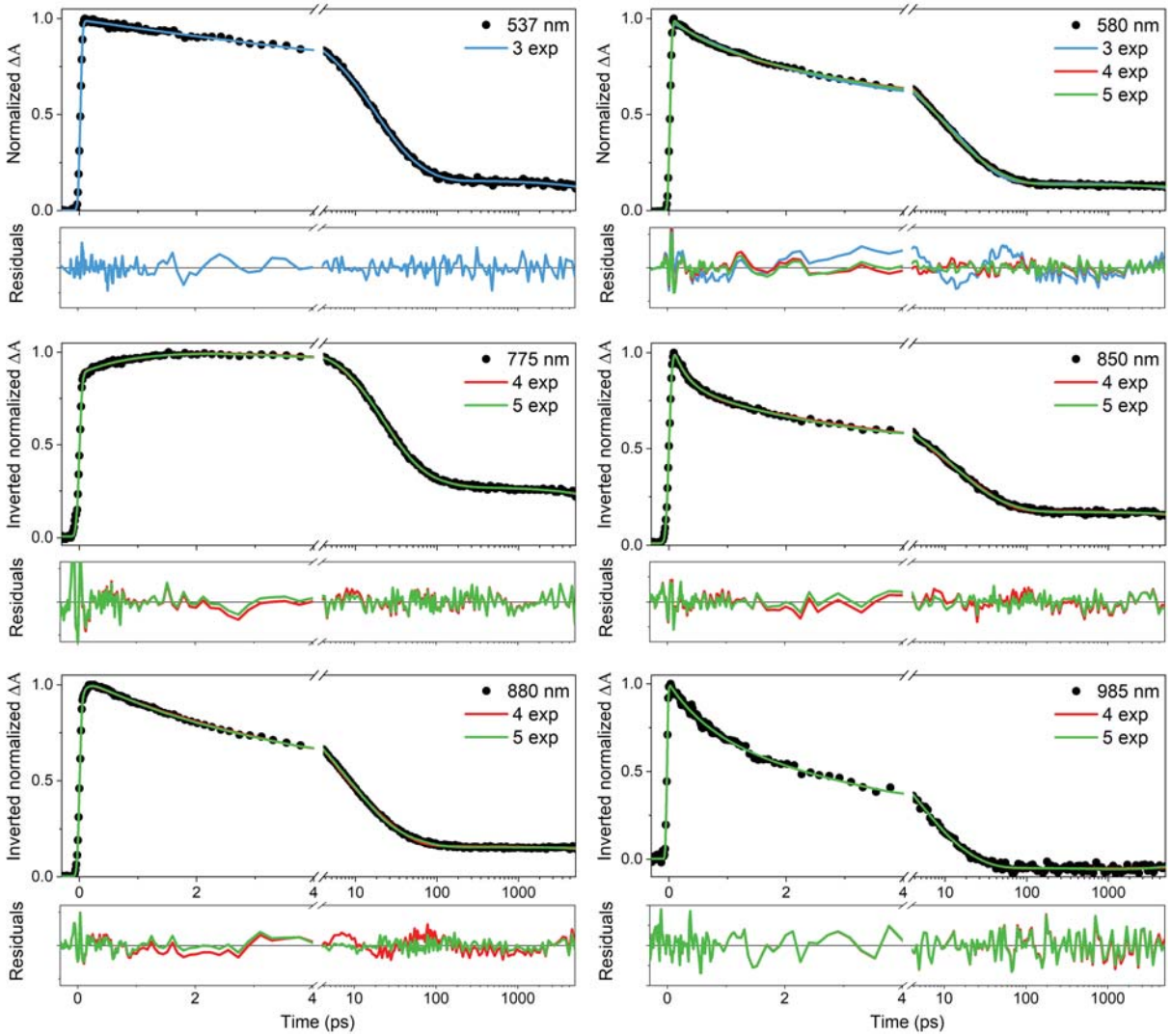

Figure A.6: TA kinetics with 3, 4 and 5 exponential fits, of **VG20** TiO_2 [1:500] dye:CDCA DSSC at different wavelengths. The scale is linear up to 4 ps, where there is a break and afterwards, up to 5 ns the scale is logarithmic.

Table A.1: Fitting values of VG20 ZrO_2 DSSCs of different CDCA concentrations obtained by TAS.

[Dye:CDCA]	**λ (nm)**	A_1 %	$\tau_1(ps)$	A_2 %	$\tau_2(ps)$	A_3 %	$\tau_3(ps)$	A_4 %	$\tau_4(ps)$
[1:0]	540	-9.5	1.1	68.4	13.2	27.1	59	5.1	inf
	580	6.1	0.8	91.4	10.0	2.2	68	0.4	inf
	670	-28.5	0.1	58.8.	14.2	22	60	9.3	inf
	720	-23.3	0.8	78.9	19.0	11.9	112	6.9	inf
	770	-7.6	0.7	66.8	13.8	24.7	60	7.8	inf
	845	29	0.4	35.4	4.9	32.5	28	4.5	inf
	880	31	0.9	42.6	5.7	22.7	31	2.8	inf
	920	45.5	1.6	44.5	8.6	11.9	49	-0.3	inf
	980	31	0.3	50.6	2.2	18.3	14	-4.5	inf
	GA	-	0.5	-	3.6	-	25.0	-	inf
[1:100]	540	20	9.8	64	27.5	17	123	2.8	inf
	580	24.8	0.7	49.3	10.0	27.3	52	1.8	inf
	670	-9	0.1	42	7.9	70.3	44	12.7	inf
	720	-20.4	1.2	71	23.0	18	97	6.5	inf
	770	-11.6	1.3	72.5	22.3	16.5	102	9.1	inf
	845	33.7	0.2	23.5	4.8	35.2	32	9.1	inf
	880	25.6	1.7	45.6	10.1	24.5	45	2	inf
	920	31.8	1.6	45.5	10.1	28.2	47	-1.7	inf
	980	28.7	0.5	50	4.1	22.3	32	-4.9	inf
	GA	-	0.3	-	4.1	-	31.0	-	inf
[1:500]	530	26.1	12.2	58.5	49.7	15.4	382	-1.9	inf
	570	22.8	1.0	38.9	13.3	37.1	114	1.31	inf
	650	14.2	1.7	50.2	39.3	21.7	208	13.9	inf
	760	-13.8	0.8	63.2	22.6	25	104	11.8	inf
	845	12.8	1.4	32.1	12.5	46.6	113	8.5	inf
	860	21.1	3.0	37.8	30.8	38.4	233	2.8	inf
	920	32.2	2.8	42.3	31.9	25.5	415	-6.5	inf
	960	36.4	1.2	41.5	20.0	32.1	383	-7.6	inf
	GA	-	1.7	-	21.4	-	193	-	inf
[1:1000]	530	-23.4	0.1	36.8	13.5	52.7	195	10.6	inf
	570	-0.4	3.7	41.4	20.1	56.3	276	2.2	inf
	650	22.6	4.2	29.2	38.4	47.2	323	1.0	inf
	770	1.0	0.7	44.8	22.7	39.8	144	14.6	inf
	840	19.5	0.9	25.8	28.8	53.1	254	3.4	inf
	870	15.2	8.8	28.6	57.3	56	384	0.2	inf
	920	17	2.7	29.1	37.7	52.5	252	1.3	inf
	970	21	1.4	36.2	70.7	40	217	3.0	inf
	GA	-	0.9	-	21.3	-	300	-	inf

Table A.2: Fitting values of **VG20** TiO_2 DSSCs of different CDCA concentrations obtained by TAS.

[Dye:CDCA]	**λ (nm)**	A_1 %	$\tau_1(ps)$	A_2 %	$\tau_2(ps)$	A_3 %	$\tau_3(ps)$	A_4 %	$\tau_4(ps)$
[1:0]	525	-13.5	0.9	70.3	11	21.7	59	8.1	inf
	555	25.2	0.4	40.8	5.6	26.2	30	7.8	inf
	650	-9.7	1	58.2	11	20.4	61	21.3	inf
	735	-34.3	0.5	74	11.8	16.7	70	9.3	inf
	920	46.2	0.7	25	5.2	12	32	17	inf
	1000	29.5	0.1	47	0.6	23.3	2.6	-5.4	inf
	GA	-	0.4	-	1.9	-	18	-	inf
[1:100]	540	-11	1.6	74	14.4	18.6	65	7.4	inf
	575	20	0.4	37	4.7	37	27	6.4	inf
	650	-12	1.3	60	18	10	173	30	inf
	775	-21	0.9	71	15	19	69	10	inf
	850	36	0.2	25	6	31	29	8.1	inf
	900	42	1	36	7.2	14	41	7.6	inf
	995	23	0.2	53	1.2	24	5.6	-5.2	inf
	GA	-	0.3	-	2	-	20	-	inf
[1:500]	540	48.5	13.3	35	40	-	-	16	inf
	580	15	0.8	40	6.5	32	29	14	inf
	650	-7.8	1.2	38.8	19.5	9.7	220	51.5	inf
	775	-20	1.4	65	22	12	87	24	inf
	850	25	0.3	25	3.8	35	26	15	inf
	880	15	0.1	42	3.7	42	20	16	inf
	985	25	0.7	44	4	31	15	-4.7	inf
	GA	-	0.4	-	4.2	-	24	-	inf
[1:1000]	540	9	1.4	38	14	29	58	24	inf
	585	37	1	34	9.2	28	46	21	inf
	650	-21.2	0.5	15.7	1.1	18.5	44	65.7	inf
	775	-6	1.2	41	24	12	37	47	inf
	850	13	0.7	26.5	6.3	30	37	31	inf
	870	7	0.1	33	4.7	43	34	25	inf
	990	22	1.2	42	7.9	36	39	-55	inf
	GA	-	0.5	-	5	-	36	-	inf

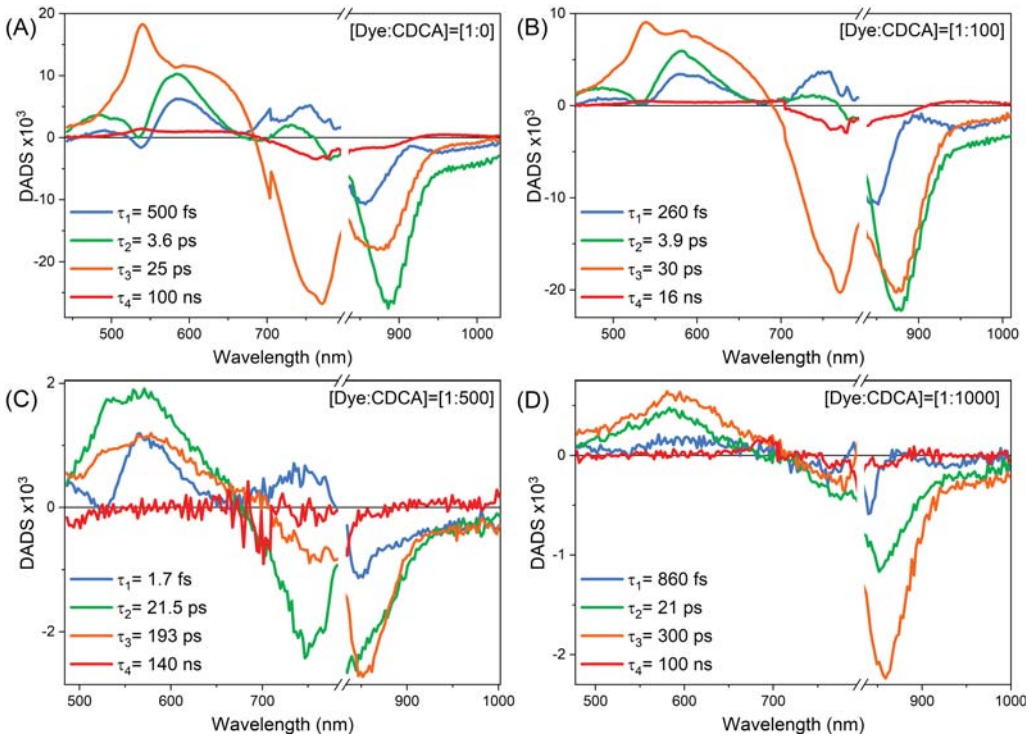

Figure A.7: DADS of VG20 ZrO_2 DSSCs, of (A) [1:0], (B) [1:100], (C) [1:500] and (D) [1:1000] dye:CDCA concentration ratios.

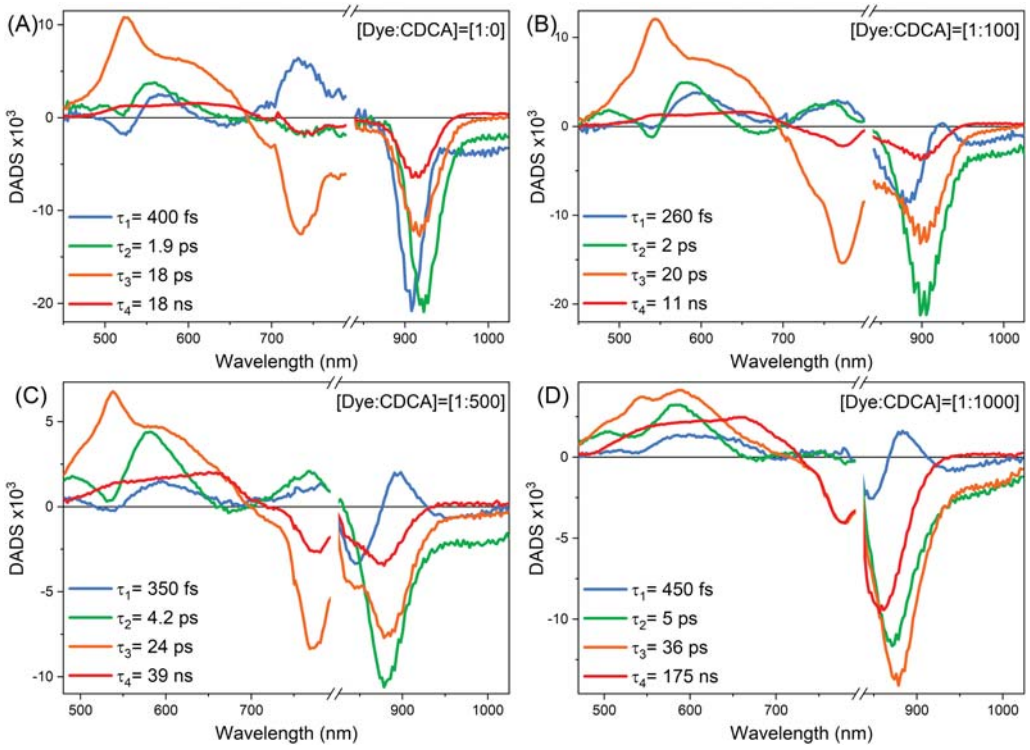

Figure A.8: DADS of VG20 TiO_2 DSSCs, of (A) [1:0], (B) [1:100], (C) [1:500] and (D) [1:1000] dye:CDCA concentration ratios.

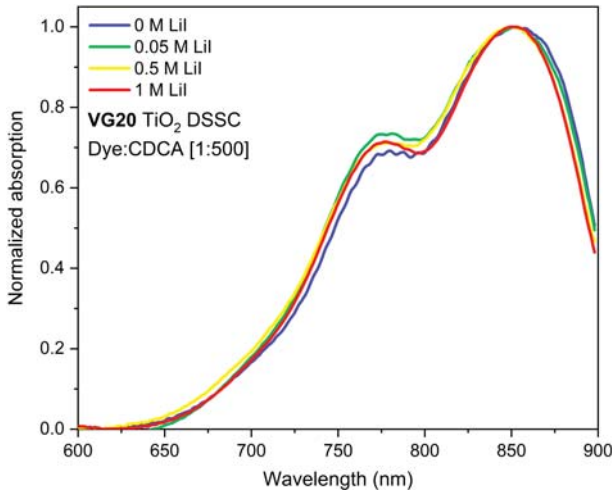

Figure A.9: SSA VG20 TiO_2 1:500 dye:CDCA DSSCs, of different Li^+ concentrations in the electrolyte.

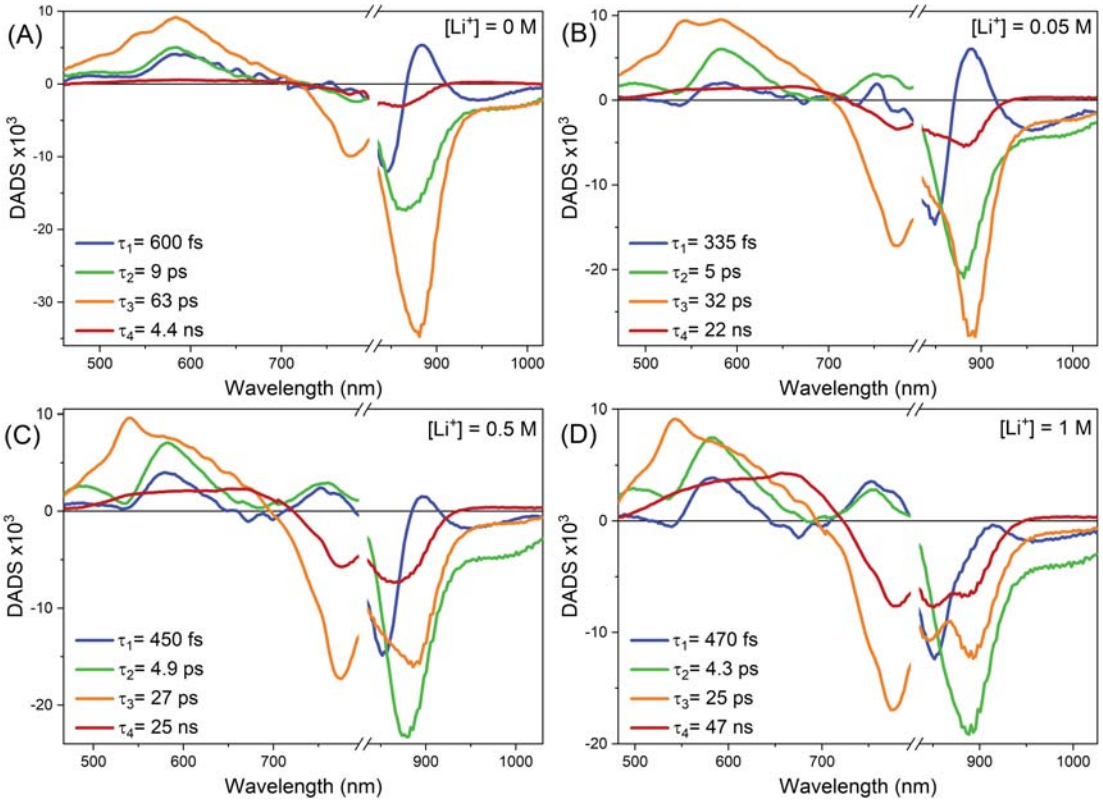

Figure A.10: DADS of VG20 TiO_2 DSSCs, of (A) 0 M, (B) 0.05 M, (C) 0.5 M and (D) 1 M, Li^+ concentration in the electrolyte.

Table A.3: Fitting values of **VG20** TiO_2 DSSCs of different Li^+ concentrations obtained by TAS.

$[Li^+]$	λ (nm)	A_1 %	$\tau_1(ps)$	A_2 %	$\tau_2(ps)$	A_3 %	$\tau_3(ps)$	A_4 %	$\tau_4(ps)$
	540	14	1	45	27	38	105	3	inf
	585	21	0.8	32	13	43	72	3	inf
	775	9	0.3	47	29	36	98	7	inf
0 M	850	23	0.8	31	9.9	41	71	5	inf
	875	-18	0.1	37	13	59	70	4	inf
	1000	17	1	44	11	40	71	-0.05	inf
	GA	-	0.6	-	9	-	63	-	inf
	540	9	0.4	52	20	32	66	9	inf
	580	20	0.5	32	7.2	42	38	7	inf
	775	-12	3.2	58	23	27	70	15	inf
0.05 M	855	28	0.4	30	4.3	35	33	11	inf
	885	-16	0.1	40	6.6	50	34	10	inf
	1000	23	0.9	49	6.6	28	32	-3.7	inf
	GA	-	0.4	-	5	-	32	-	inf
	540	6	0.3	60	17	20	65	12	inf
	585	23	0.6	39	7	30	33	10	inf
	775	-13	1.8	63	22	14	81	23	inf
0.5 M	865	21	0.5	37	4.5	33	25	15	inf
	875	24	1.7	44	9.3	20	36	14	inf
	1000	24	0.7	49	4	28	16	-3.8	inf
	GA	-	0.5	-	4.9	-	27	-	inf
	540	4	0.3	59	15	21	53	17	inf
	580	20	0.4	36	5	30	27	15	inf
	775	-16	1.4	50	18	20	61	30	inf
1 M	855	30	0.4	0.3	4.2	26	25	19	inf
	890	32	2.2	44	12	9	65	16	inf
	1000	28	0.6	46	3.7	26	14	-5.5	inf
	GA	-	0.5	-	4.3	-	25	-	inf

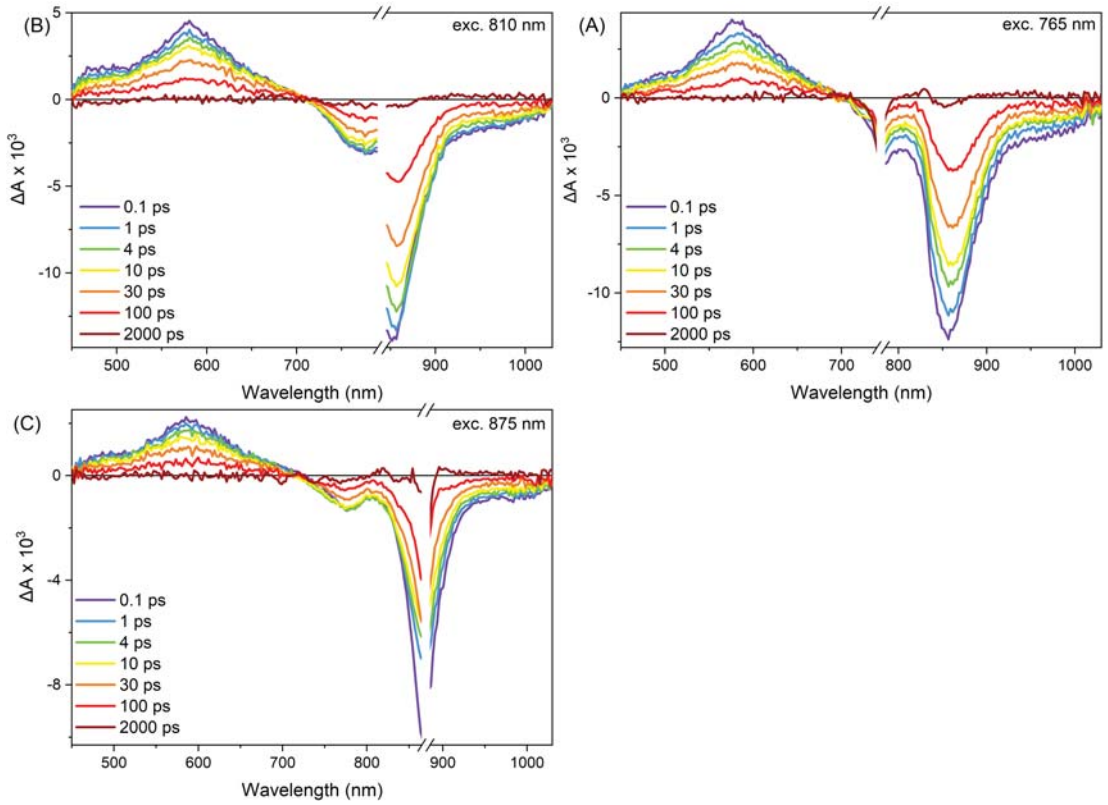

Figure A.11: TAS of a **VG20** ZrO_2 1:1000 DSSC, at (A) 765 nm, (B) 810 nm and (C) 875 nm excitation.

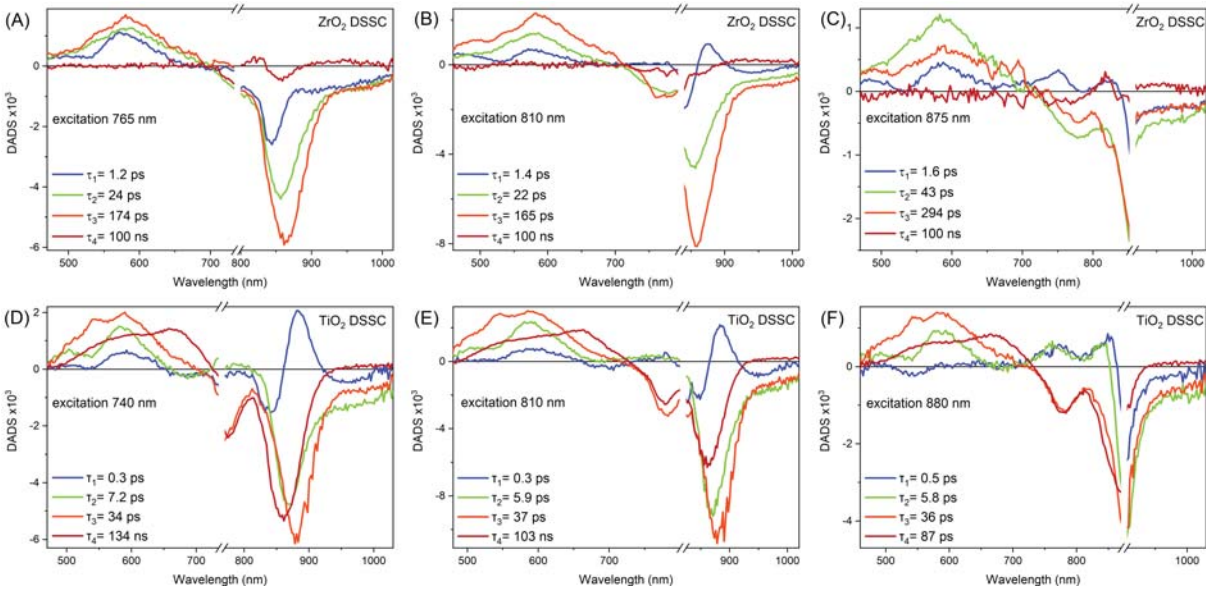

Figure A.12: DADS of a **VG20** (A-C) ZrO_2 and (D-F) TiO_2 1:1000 DSSC, at different excitation wavelengths.

Table A.4: Fitting values of **VG20** ZrO_2 DSSCs of different excitation wavelengths obtained by TAS.

$\boldsymbol{\lambda_{exc}}$	**λ (nm)**	$\boldsymbol{A_1}$ %	$\boldsymbol{\tau_1(ps)}$	$\boldsymbol{A_2}$ %	$\boldsymbol{\tau_2(ps)}$	$\boldsymbol{A_3}$ %	$\boldsymbol{\tau_3(ps)}$	$\boldsymbol{A_4}$ %	$\boldsymbol{\tau_4(ps)}$
	535	19	0.8	35	24	47	160	-0.23	inf
	580	21	0.7	33	21	41	173	0.4	inf
	785	25	0.7	37	24	24	162	11	inf
765 nm	855	19	1.0	32	21	46	160	3	inf
	895	16	1.6	37	30	47	204	-1.3	inf
	985	28	0.7	30	15	47	134	-4	inf
	GA	-	1.2	-	24	-	174	-	inf
	540	10	0.5	33	22	56	150	2	inf
	580	16	0.8	34	20	50	170	0.1	inf
	770	3.7	0.5	46	31	39	190	10	inf
810 nm	855	11	2	29	24	54	150	6.5	inf
	895	-18	0.1	40	36	61	187	-1	inf
	985	17	2.5	45	32	49	233	-10	inf
	GA	-	1.4	-	22	-	165	-	inf
	540	4	0.9	50	38	44	181	4	inf
	580	15	1	37	23	50	154	-1.4	inf
	775	-5	1.4	47	37	41	243	10	inf
875 nm	850	11	0.5	22	20	53	131	10	inf
	385	25	1.4	43	35	36	248	-11	inf
	GA	-	1.6	-	43	-	294	-	inf

Table A.5: Fitting values of **VG20** TiO_2 DSSCs of different excitation wavelength concentrations obtained by TAS.

$\boldsymbol{\lambda_{exc}}$	**λ (nm)**	$\boldsymbol{A_1}$ %	$\boldsymbol{\tau_1(ps)}$	$\boldsymbol{A_2}$ %	$\boldsymbol{\tau_2(ps)}$	$\boldsymbol{A_3}$ %	$\boldsymbol{\tau_3(ps)}$	$\boldsymbol{A_4}$ %	$\boldsymbol{\tau_4(ps)}$
	540	4	0.5	0.52	18	20	92	25	inf
	590	0.1	0.5	40	9	30	42	24	inf
	785	-0.03	2.6	40	0.04	40	33	50	inf
750 nm	840	30	0.4	13	14	30	29	37	inf
	870	-15	0.1	36	9	31	38	33	inf
	890	-20	0.2	50	14	46	46	25	inf
	985	10	0.8	40	5	50	27	-5	inf
	GA	-	0.3	-	7.2	-	34	-	inf
	540	7	1	45	18	27	66	22	inf
	590	15	1	40	11	30	50	20	inf
	780	-10	0.9	40	28	13	98	43	inf
810 nm	875	30	6.3	40	28	10	84	22	inf
	895	-18	0.1	42	8.5	43	44	16	inf
	985	13	0.9	52	6.4	40	39	-6	inf
	GA	-	0.3	-	5.9	-	37	-	inf
	540	-6	0.6	50	20	27	67	24	inf
	590	19	2.9	47	22	11	97	20	inf
	780	-30	1.6	37	29	15	97	54	inf
880 nm	840	-29	1.2	30	35	7	77	60	inf
	885	20	0.9	37	11	15	64	14	inf
	900	26	0.1	34	2.9	38	28	12	inf
	985	22	1	68	12	13	150	-7	inf
	GA	-	0.5	-	5.8	-	36	-	inf

The FLUPS 2D spectro-temporal maps, as well as the fluorescence spectra at early delays (upper inset), clearly demonstrate a gradual fluorescence ($\sim$ 10 nm) red-shift. In addition, there is no evidence of emission from aggregates.

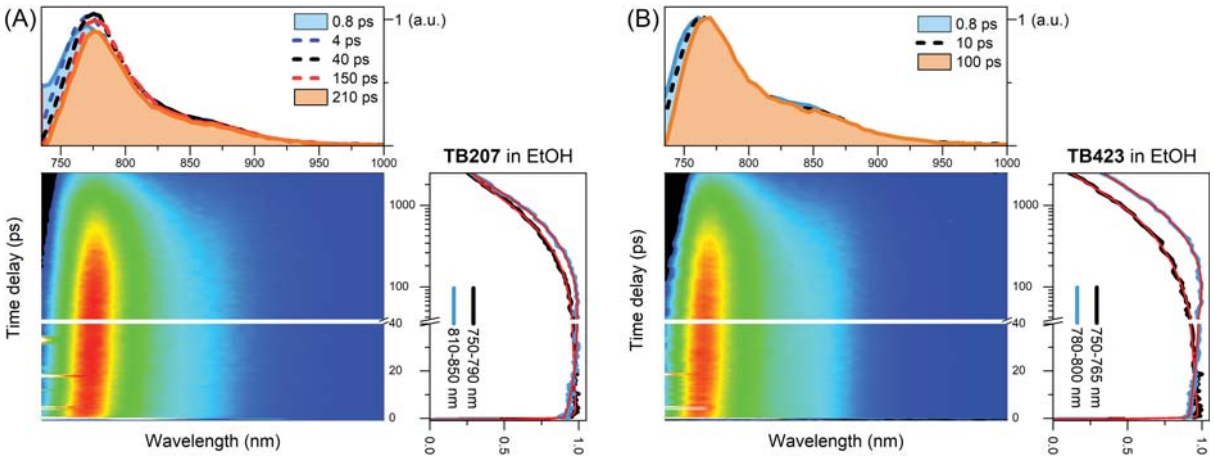

Figure A.13: FLUPS 2D spectro-temporal map of (A) TB207 and (B) TB423 TiO_2 DSSCs, in optimal DSSC conditions.

Table A.6: Fitting values of **TB207** and **TB423** in $EtOH$: $CHCl_3$ (9:1) solution obtained by TAS and FLUPS measurements.

[Dye:CDCA]	**λ (nm)**	$\boldsymbol{A_1}$ %	$\boldsymbol{\tau_1(ps)}$	$\boldsymbol{A_2}$ %	$\boldsymbol{\tau_2(ps)}$	$\boldsymbol{A_3}$ %	$\boldsymbol{\tau_3(ps)}$
TB207	610-630	16	1.7	16	380	69	4700
	670-700	4	4.2	19	500	77	5200
	780-800	13	1.9	-17	16	87	2400
	950-980	16	1.6	-9.3	6	84	2500
	GA	-	1.1	-	34	-	2700
	FLUPS	-18	1	-2	25	100	2000
TB423	540-580	-10	1	-17	77	100	4200
	GA	-	-	-	46	-	4200
	FLUPS	-10	0.5	-8	40	100	2100

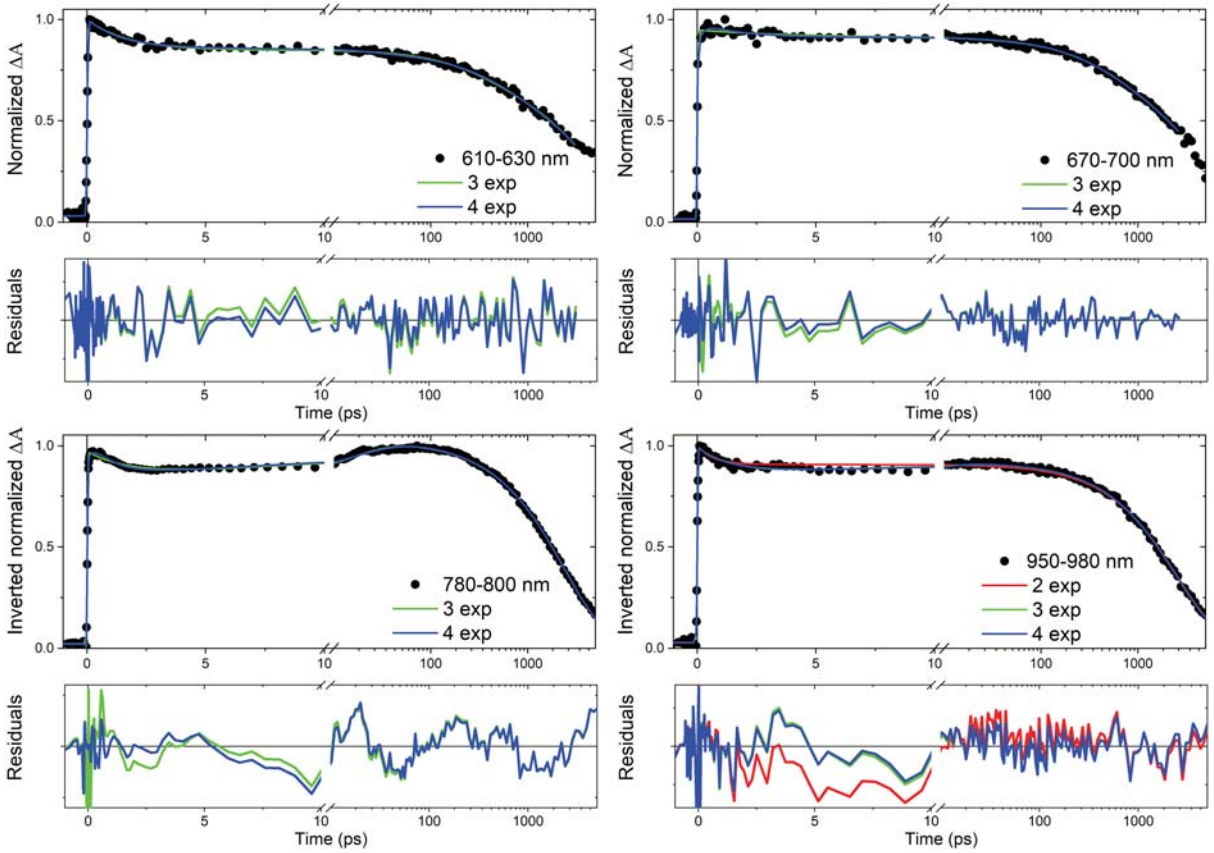

Figure A.14: TAS kinetics at different wavelengths and fittings, of TB207 in solution.

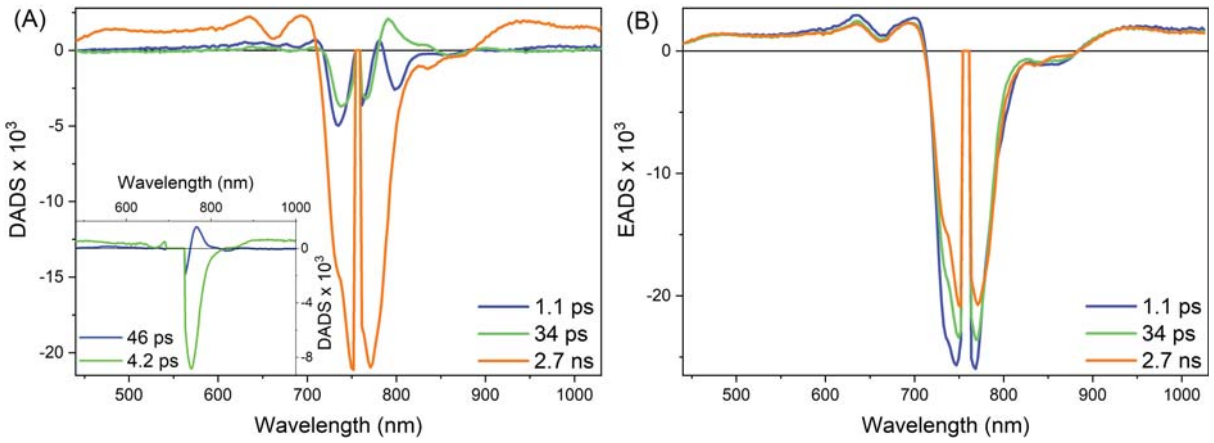

Figure A.15: (A) DADS of **TB207** in solution, obtained by GA, fitted with a 3 exponential function convoluted with the IRF. Inset: DADS of DADS and EADS of TB207 and TB423 in solution in solution. (B) The corresponding EADS of **TB207** in solution.

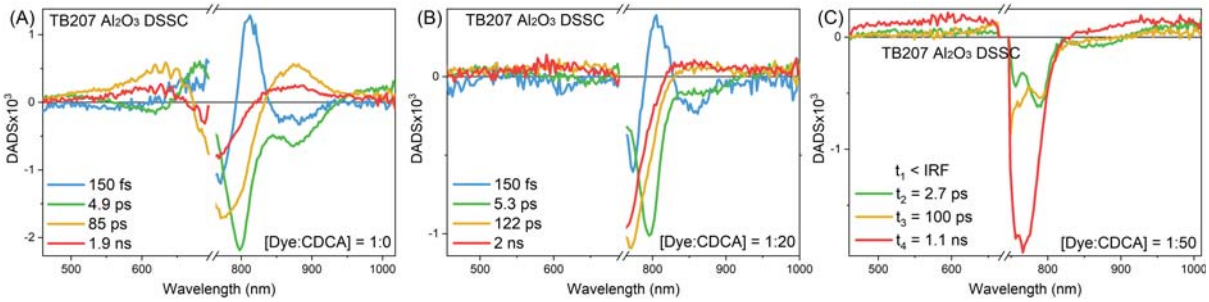

Figure A.16: DADS of **TB207** Al_2O_3 DSSCs, of (A) 1:0, (B) 1:20 and (C) 1:50 CDCA concentration.

Table A.7: Fitting values of **TB207** Al_2O_3 DSSCs of different CDCA concentrations obtained by TAS.

[Dye:CDCA]	**λ (nm)**	A_1 %	$\tau_1(ps)$	A_2 %	$\tau_2(ps)$	A_3 %	$\tau_3(ps)$	A_4 %	$\tau_4(ps)$
[1:0]	620	-22	0.2	-13	3.6	76	100	24	4400
	780	34	2.6	25	19	30	120	10	2600
	880	-10	0.8	-71	4.9	76	140	23	3400
	GA	-	0.2	-	5	-	85	-	2000
[1:20]	770	16	0.9	25	34	35	350	25	2500
	880	-27	1.3	-57	7.2	45	140	55	1800
	GA	-	0.2	-	5	-	120	-	2000
[1:50]	760	23	0.48	15	26	34	390	28	2600
	880	-80	0.14	-63	13	90	620	10	inf
	GA	-	<IRF	-	3	-	100	-	1100

In a different approach, instead of 3 exponential fits, we can use the stretched exponential, for the faster times as following:

$$I(t) = A_0 e^{-(t/\tau_0)^{\beta}} + A_1 e^{-t/\tau_1} \tag{A.1}$$

where β is a parameter defines the inhomogeneity of the system. From 1:0 to 1:50 dye:CDCA the β parameter increases from 0.29 to 0.7, indicating that CDCA may stabilize the anchored dyes.

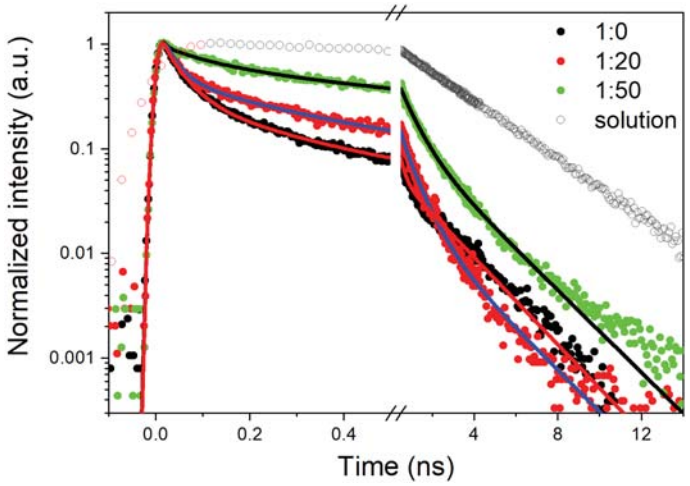

Figure A.17: Streak camera fluorescence kinetics of **TB207** Al_2O_3 DSSCs, increasing the CDCA concentration with a break at 0.5 ns. The **TB207** solution kinetic is presented as reference too.

Table A.8: Fitting values of **TB207** Al_2O_3 DSSC fluorescence kinetics, of different CDCA concentrations, obtained by streak camera measurements.

[Dye:CDCA]	$\boldsymbol{\tau_0(ps)/A_0}$	$\boldsymbol{\beta}$	$\boldsymbol{\tau_1(ns)/A_1}$
[1:0]	1.5/7.7	0.29	2.3/0.047
[1:20]	23/1.8	0.35	0.94/0.092
[1:50]	535/0.88	0.7	3.2/0.0448

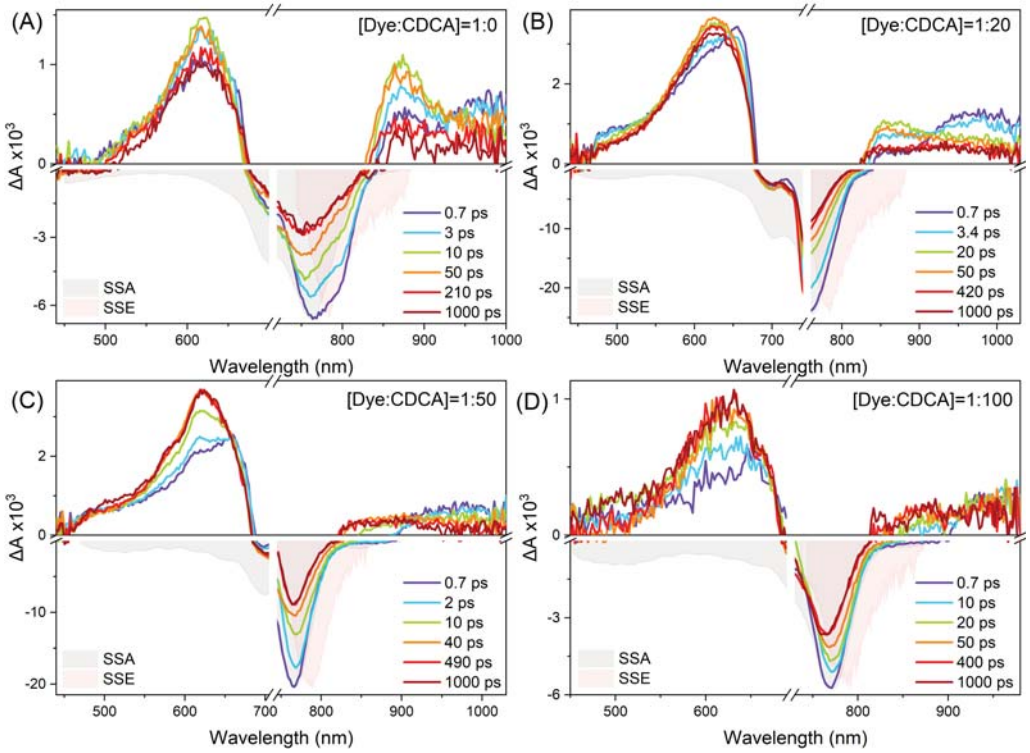

Figure A.18: TA spectra of **TB207** TiO_2 DSSCs, of (A) 1:0, (B) 1:20, (C) 1:50 and (D) 1:100 dye:CDCA concentration ratios.

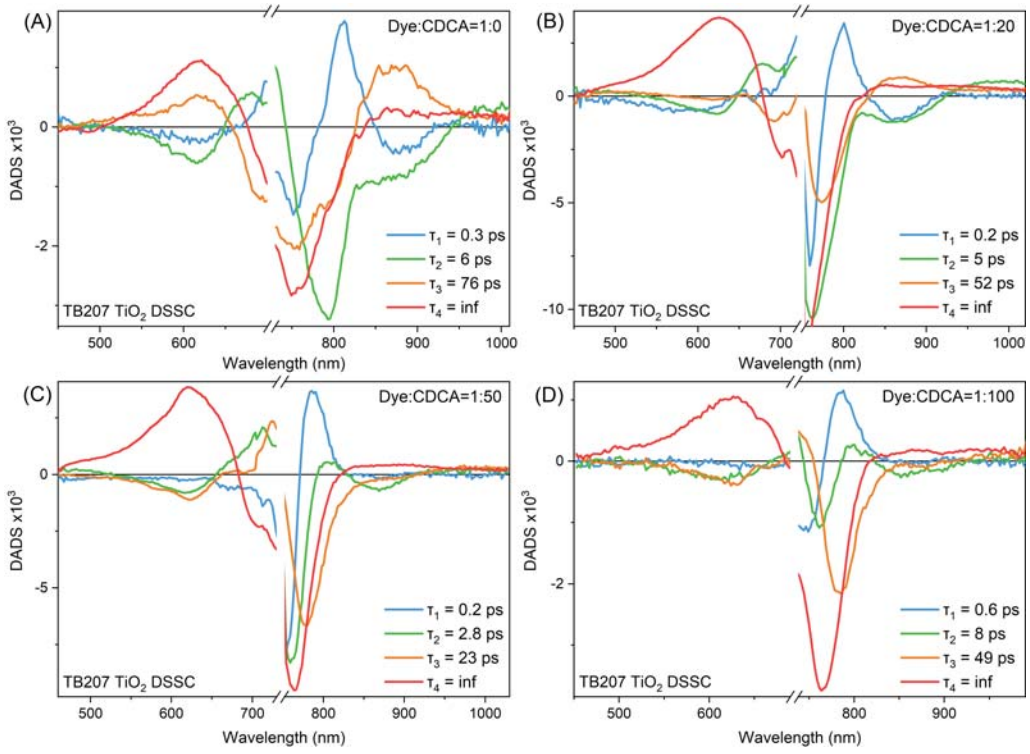

Figure A.19: DADS of **TB207** TiO_2 DSSCs, of (A) 1:0, (B) 1:20, (C) 1:50 and (D) 1:100 dye:CDCA concentration ratios.

Table A.9: Fitting values of **TB207** TiO_2 DSSCs of different CDCA concentrations obtained by TAS and FLUPS.

[Dye:CDCA]	λ (nm)	A_1 %	$\tau_1(ps)$	A_2 %	$\tau_2(ps)$	A_3 %	$\tau_3(ps)$	A_4 %	$\tau_4(ps)$
[1:0]	600-630	-15	0.2	-37	3	31	130	69	inf
	650-660	-7	0.5	26	5.9	8	460	66	inf
	780-790	24	2.8	28	23	20	72	27	inf
	855-880	-18	0.6	-63	4.8	80	110	20	inf
	GA	-	0.3	-	5.8	-	76	-	inf
	FLUPS	21	1.3	52	6	27	23	-	-
[1:20]	600-630	-9	0.8	-21	13	17	430	83	inf
	680-700	-25	2.5	-22	12	43	96	57	inf
	780-800	-44	0.1	50	6	26	110	24	inf
	850-880	-32	1.4	-51	6.8	69	96	31	inf
	GA	-	0.2	-	5	-	52	-	inf
[1:50]	610-630	-13	1.8	-35	16	5	300	95	inf
	780-800	-32	0.2	47	16	17	95	35	inf
	950-1000	25	2.4	37	23	11	600	26	inf
	GA	-	0.2	-	2.3	-	23	-	inf
	FLUPS	16	1.5	43	8	41	35	-	-
[1:100]	610-630	-9	0.4	-26	11	-32	36	100	inf
	780-790	-22	0.6	46	45	10	1200	43	inf
	855-880	6	0.3	63	9.1	34	47	-60	inf
	GA	-	0.6	-	8	-	49	-	inf
	FLUPS	13	1.5	42	9.4	45	42	-	-

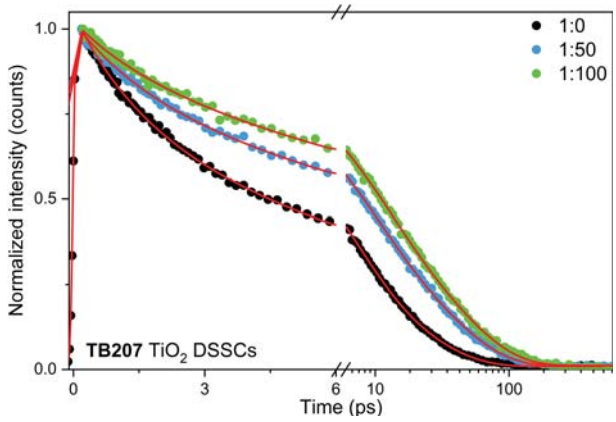

Figure A.20: FLUPS kinetics and fits of **TB207** TiO_2 DSSCs, of 1:0 (black), 1:50 (blue) and 1:500 (green) dye:CDCA concentration. In the time axis there is a break at 6 ps and afterwards a logarithmic scale has been set.

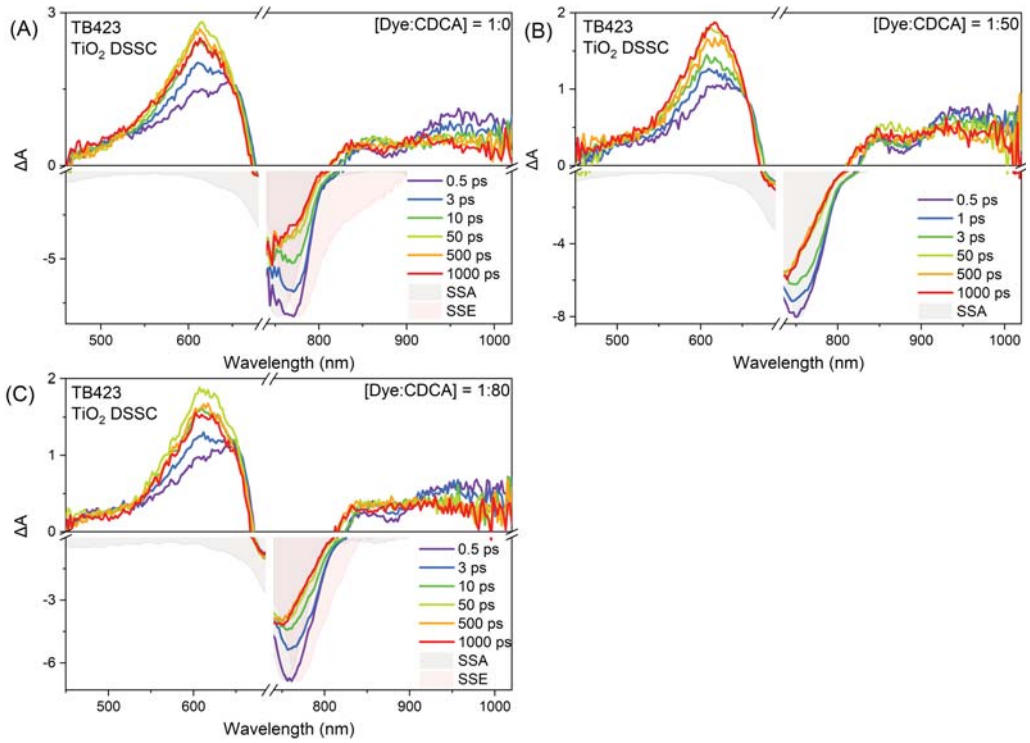

Figure A.21: TA spectra of **TB423** TiO_2 DSSCs, of (A) 1:0, (B) 1:50 and (C) 1:80 dye:CDCA concentration ratios.

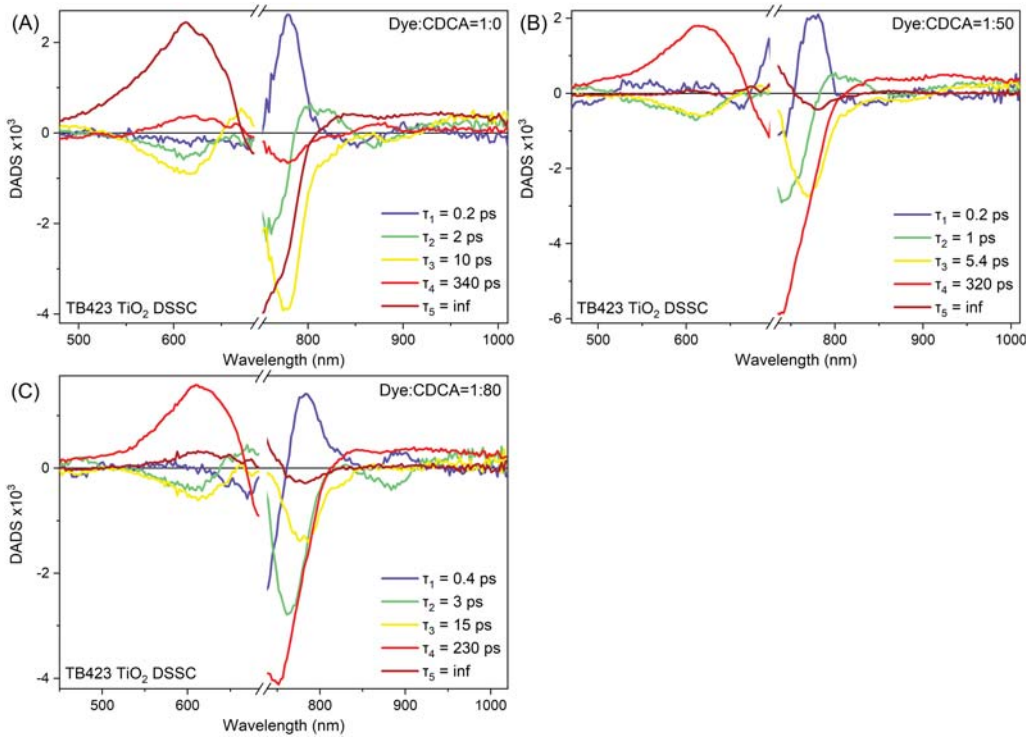

Figure A.22: DADS of **TB423** TiO_2 DSSCs, of (A) 1:0, (B) 1:50 and (C) 1:80 dye:CDCA concentration ratios.

Table A.10: Fitting values of **TB423** TiO_2 DSSCs of different CDCA concentrations obtained by TAS. The samples were excited at 720 nm.

[Dye:CDCA]	λ (nm)	A_1 %	$\tau_1(ps)$	A_2 %	$\tau_2(ps)$	A_3 %	$\tau_3(ps)$	A_4 %	$\tau_4(ps)$
[1:0]	610	-30	0.1	-13	1.9	-0.33	6.9	0.94	inf
	772	-30	0.1	54	7	10	188	35	inf
	950	18	0.1	35	4.4	12	77	35	inf
	GA	-	0.4	-	6.5	-	150	-	inf
[1:50]	610	-14	0.4	-35	2.4	-10	7	100	inf
	740	17	0.1	19	0.72	12	2	52	inf
	772	-36	0.1	47	3.9	10	66	44	inf
	950	-	-	43	2	4	110	53	inf
	GA	-	0.5	-	3.8	-	220	-	inf
[1:80]	610	-18	1.7	-35	13.5	16	270	84	inf
	760	20	2	25	6.2	5	100	48	inf
	950	12	0.34	29	4.8	6	58	43	inf
	GA	-	0.5	-	5	-	100	-	inf

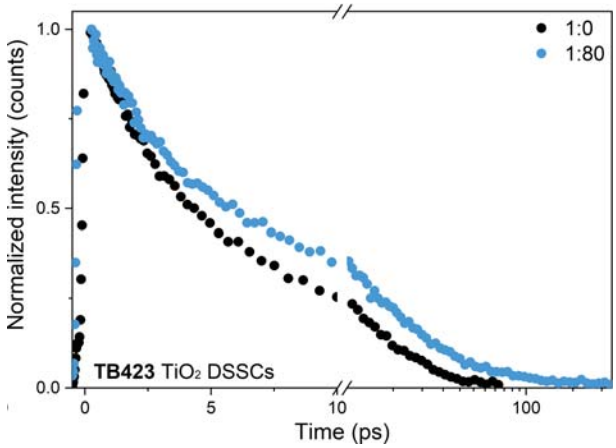

Figure A.23: FLUPS kinetics of **TB423** TiO_2 DSSCs, of 1:0 (black) and 1:50 (blue) dye:CDCA concentration. In the time axis there is a break at 10 ps afterwards a logarithmic scale has been set.

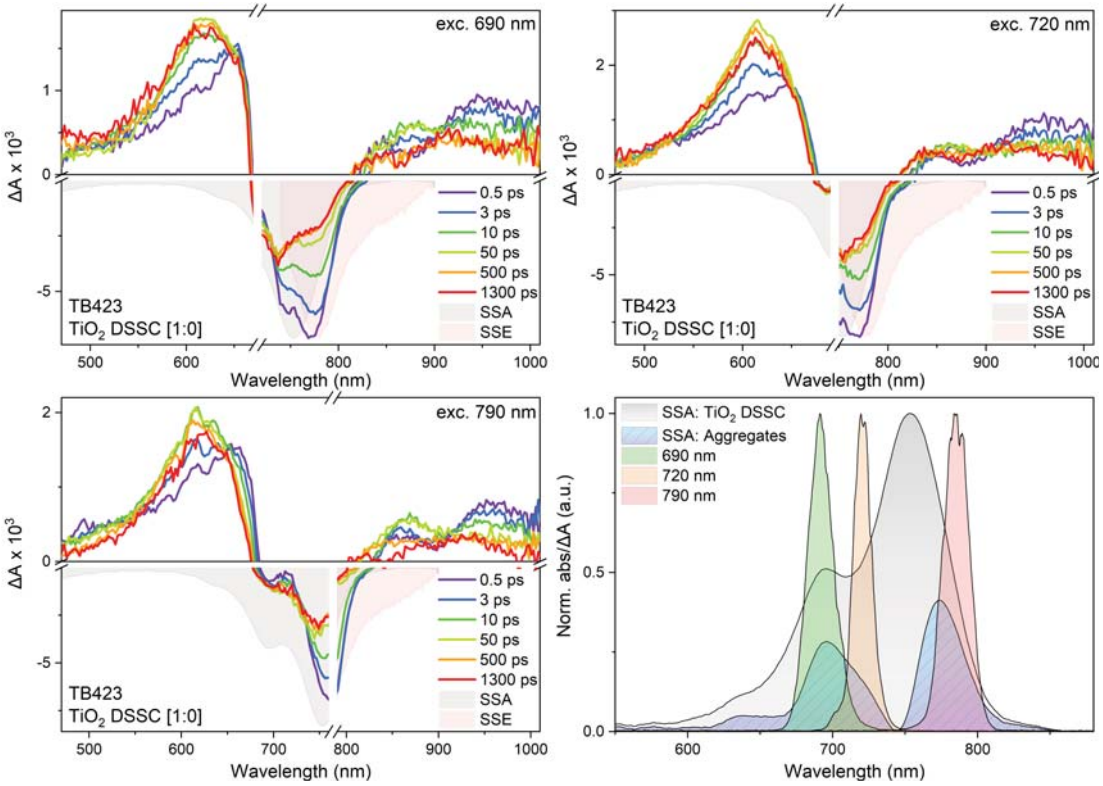

Figure A.24: TA spectra of a TB423 TiO_2 DSSC 1:0, excited at (A) 690 nm, (B) 720 nm and (C) 790 nm. In (D) the SSA spectrum of the DSSC is presented, as well as the extracted aggregates one, with the three excitation beam spectral profiles to overlay.

Table A.11: Fitting values of **TB423** 1:0 TiO_2 DSSCs at different excitation wavelengths obtained by TAS.

λ_{exc}	λ (nm)	A_1 %	$\tau_1(ps)$	A_2 %	$\tau_2(ps)$	A_3 %	$\tau_3(ps)$	A_4 %	$\tau_4(ps)$
690 nm	610	-13	1.4	27	13	11	80	62	inf
	740	24	0.15	19	2.1	14	13	52	inf
	772	-62	0.1	48	6.8	18	42	34	inf
	950	-	-	30	3.3	25	32	37	inf
	GA	-	0.5	-	7.4	-	80	-	inf
790 nm	740	-10	0.2	-5	8.2	20	58	66	inf
	950	5	0.6	28	7	23	34	43	inf
	GA	-	0.6	-	13	-	460	-	inf

JACS Au
AN OPEN ACCESS JOURNAL OF THE AMERICAN CHEMICAL SOCIETY

pubs.acs.org/jacsau Article

Transparent and Colorless Dye-Sensitized Solar Cells Exceeding 75% Average Visible Transmittance

Waad Naim, Vittoria Novelli, Ilias Nikolinakos, Nadia Barbero, Iva Dzeba, Fionnuala Grifoni, Yameng Ren, Thomas Alnasser, Amalia Velardo, Raffaele Borrelli, Stefan Haacke, Shaik M. Zakeeruddin, Michael Graetzel, Claudia Barolo, and Frédéric Sauvage*

Cite This: *JACS Au* 2021, 1, 409–426

Read Online

ACCESS | Metrics & More | Article Recommendations | Supporting Information

ABSTRACT: Most photovoltaic (PV) technologies are opaque to maximize visible light absorption. However, see-through solar cells open additional perspectives for PV integration. Looking beyond maximizing visible light harvesting, this work considers the human eye photopic response to optimize a selective near-infrared sensitizer based on a polymethine cyanine structure (VG20-C_x) to render dye-sensitized solar cells (DSSCs) fully transparent and colorless. This peculiarity was achieved by conferring to the dye the ability to strongly and sharply absorb beyond 800 nm (S_0–S_1 transition) while rejecting the upper S_0–S_n contributions far in the blue where the human retina is poorly sensitive. When associated with an aggregation-free anatase TiO_2 photoanode, the selective NIR-DSSC can display 3.1% power conversion efficiency, up to 76% average visible transmittance (AVT), a value approaching the 78% AVT value of a standard double glazing window while reaching a color rendering index (CRI) of 92.1%. The ultrafast and fast charge transfer processes are herein discussed, clarifying the different relaxation channels from the dye monomer excited states and highlighting the limiting steps to provide future directions to enhance the performances of this nonintrusive NIR-DSSC technology.

KEYWORDS: *transparent photovoltaic (TPV), dye-sensitized solar cells (DSSC), near-infrared sensitizers, cyanine dyes, time-resolved spectroscopies, high color rendering index TPV*

INTRODUCTION

Energy conversion from sunlight is a sustainable approach to solve long-term energy production, which is compatible with current and future energy needs. Photovoltaic (PV) modules are mostly based on silicon p–n junctions and installed on rooftops and in solar farms, representing ca. 4% of the energy production in Europe.[1] These two segments were specifically tailored in accordance with the strength of silicon PV technology. However, there are still plenty of opportunities to explore for reaching total independence from fossil fuels and nuclear energy. This is the case of see-through solar technologies, an old concept developed more than 30 years ago, which offers new integration possibilities such as building-integrated (BI) and automotive-integrated (AI) PV, electronic displays, autonomously powered electronic-glazing, etc.

The theoretical limit of power conversion efficiency (PCE) for a single junction NIR-selective transparent photovoltaic (TPV) technology with an average visible transmittance (AVT) of 100% is 20.5%.[2] In practice, only 10.8% can be expected after considering all optical losses. For the same AVT, the PCE is theoretically lower for nonselective broadband absorbing cells. Hence, selective TPV, i.e. selective conversion of either the UV or NIR part of the solar spectrum, represents an important stake for the advancement of such TPV technologies.

Two main approaches have been proposed to reach semi- to transparent PVs: (i) spatially segmented PV or broadband absorbing thin film opaque absorbers such as Si, CIGS, or perovskite solar cells[3−11] and (ii) wavelength selective thin film PVs through which only the nonvisible part of the solar spectrum is converted.

Lunt et al. were the first to propose a real selective TPV back in 2011 based on an organic planar heterojunction composed of a donor chloroaluminum phtalocyanine and C_{60} as an acceptor which achieved 1.3% PCE with an AVT of 65% and 1.7% PCE with 57% AVT when including a back-positioned NIR Bragg mirror.[12] This efficiency reached a PCE of 4% and an AVT of 64% by adopting a bulk heterojunction architecture based on PBDTT-DPP and PCBM polymers.[13] The American

Received: February 3, 2021
Published: March 29, 2021

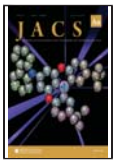

https://dx.doi.org/10.1021/jacsau.1c00045
JACS Au 2021, 1, 409–426

company Ubiquitous Energy, who has recently announced a TPV production line, achieved a Newport certification of 5.1% PCE and 51.5% AVT by means of a single junction NIR-selective excitonic semiconductors converting between 650 and 900 nm.[14] Conversion of near-UV light by combining a pair of wide-bandgap organic semiconductors has also been proposed recently reaching a PCE of ca. 1.2%.[15] A recent review on semitransparent polymer and perovskite solar cells provides state-of-the art progress in this field.[16] Today, luminescence solar concentrator technology reaches the highest level of AVT, up to 88.3%; however with only 0.4% PCE owing to the low cross-section absorption of NIR-light on glass edges.[17]

The optical rendering of dye-sensitized solar cell (DSSC) technology is particularly advantageous since both coloration and level of transparency can be finely adjusted through materials and electrode thickness. Extending the light absorption from visible toward the near-infrared (NIR) region was rapidly targeted to reach panchromatic light absorption for improving the PCE of DSSCs.[18−28] Differently, Han et al. reported in 2014 a green-colored see-through DSSC with a PCE of 3.66% and a peak maximum transmittance value of 60% at 560 nm. This green semitransparent technology is based on the cosensitization between two efficient dyes absorbing in the visible range, one short D−π−A dye (Y1) for blue-light conversion (λ = 400 nm) and a central-modified squaraine dye (HSQ5) absorbing in the red region (λ = 700 nm) leaving an absorption valley in the green.[29] A photochromic semitransparent DSSC was also proposed by Demadrille et al., who reported an AVT value of 59% in the dark without photovoltaic activity. The AVT value decreases to 27% under illumination affording the possibility to convert sunlight with a maximum of PCE of 3.7%.[30]

Semitransparent DSSCs based on a visible absorbing dye (N719) was also proposed recently by Mallick et al., who reported a maximum AVT of 44% depending on the photoanode thickness with an efficiency of 2.4%.[31,32] The authors introduced important metrics to assess the visual comfort of DSSCs for smart glazing applications, namely the color rendering index (CRI) and correlated color temperature (CCT) for which they reported CRI values between 83 and 93%, and CCT values between 4647 and 5500 K in their different publications on semitransparent DSSC technology.

Toward the development of a selective NIR sensitizer with absorption going well-beyond 700 nm, metal-free organic polymethine dyes are the most promising, ranging from squaraines,[33−45] croconines,[46,47] to cyanines.[48−52] The most remarkable achievement has been reported by Arakawa et al., who proposed a heptamethine cyanine dye decorated with a benzo-condensed heteroaromatic unit allowing the singlet-to-singlet absorption to be shifted to 822 nm with a high molar extinction coefficient (ε) of 146 000 L/mol·cm.[50] The final device reached a record PCE of 2.3%, however requiring an opaque photoanode of 25 μm thickness to reach this level of efficiency.

In this work, a series is reported of new symmetrical NIR-selective heptamethine cyanine dyes, coded VG20-C_x, inspired by the seminal work of Arakawa et al.[50] The originality in these new dyes lies in two aspects. First, it bears two carboxylic acid anchoring groups conjugated to the condensed benzo-indolenine lateral unit for stronger binding to the surface of TiO_2 nanocrystals. Second, longer side alkyl chains are introduced to impede the formation of H-type aggregation which are harmful not only for device performance but also for strengthening the cell coloration, thus reducing both cell transmittance and color rendering. As a result, a PCE record of 3.1% for selective NIR-DSSC was achieved and a maximum of 76% AVT is demonstrated thanks to a holistic reduction of optical losses and a further red-shifted conversion maximum at 850 nm, that goes well beyond our cones' sensitivity limit. The rate-limiting processes and the future challenges to level up the performances of this class of selective NIR-DSSCs are herein discussed based on ultrafast time-resolved spectroscopies.

RESULTS AND DISCUSSION

Synthesis and Characterization of VG20-C_{16} in Solution

This work relies on the synthesis of a series of symmetrical heptamethine dyes, coded VG20-C_x, with x values varying from 2 to 16 carbons on the alkyl chain (Figure 1). The trans

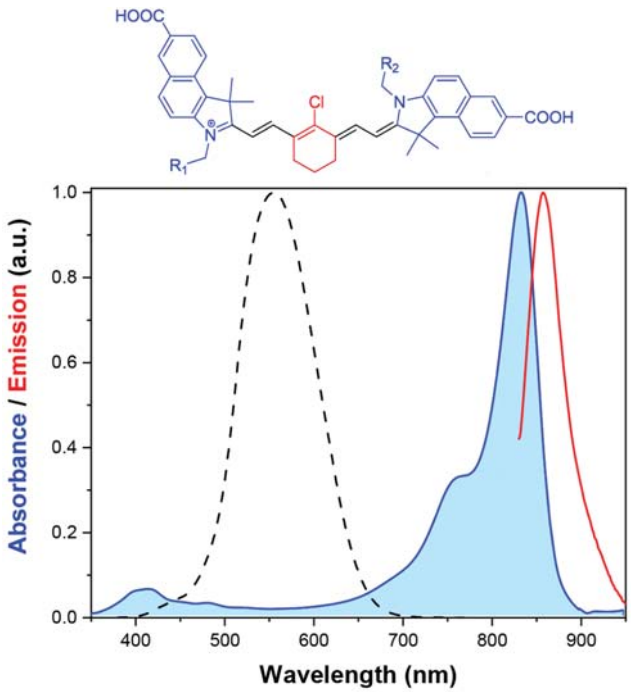

Figure 1. General chemical structure of VG20-C_x dye with R_1 = R_2 = C_2H_5, C_8H_{17}, or $C_{16}H_{33}$ investigated in this study. Normalized UV−visible absorption spectrum of VG20-C_{16} in solution (blue curve) and steady-state photoluminescence (red curve) in 9/1 (v/v) ethanol/DMSO solvent mixture (dye concentration 100 μmol/L, CDCA concentration 50 mmol/L). The photopic response of the human eye is represented as a black dashed line for comparison.

configuration of the polymethine bridge is stabilized by a classical cyclohexene moiety, substituted by a chlorine atom. The two 1*H*-benzo[*e*]indole end units, different from the analogous dyes reported by Arakawa et al.,[50] are decorated with a carboxylic acid in position 7. The central chlorine has an electron withdrawing property and contributes to pulling electrons from the polymethine chain causing the dye's absorbance to shift in the NIR region. Besides facilitating the ability to scale up syntheses, the rationale behind the synthesis of symmetrical dyes, in which the anchoring groups are directly conjugated on the lateral heteroaromatic groups, is also to further red-shift the absorption maxima as previously demonstrated on symmetrical squaraines.[42,45,53] This molec-

https://dx.doi.org/10.1021/jacsau.1c00045
JACS Au 2021, 1, 409−426

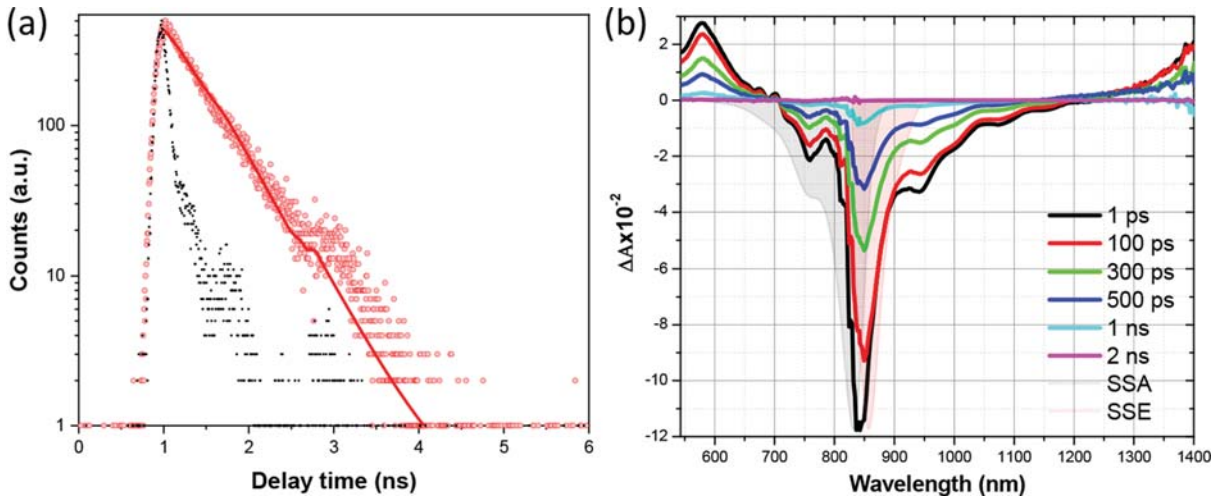

Figure 2. Time-resolved study of VG20-C_{16} dye (100 μmol/L) in 9/1 ethanol/DMSO solvent mixture including 50 mmol/L of CDCA by (a) time-correlated single photon counting with an excitation at 640 nm, emission probed at 860 nm, and (b) femtosecond pump−probe transient absorption spectra at different delays. The excitation was at 810 nm with a 90 μJ/cm^2 pulse energy.

ular design, inspired by Arakawa's work and our previous work on squaraines, affords a better overlap between the lowest unoccupied molecular orbital (LUMO) of the dye and the conduction band (CB) of TiO_2 to favor charge injection.[42]

VG20-C_{16} in solution exhibits a sharp and intense absorption band in the NIR region with a maximum at λ_{max} = 834 nm (ε = 154 000 L/mol·cm) corresponding to the S_0−S_1 electronic transition (Figure 1). The shoulder at 765 nm principally relates to vibronic states in the molecule. However, as it will be discussed in the following, H-aggregation of molecules composing the self-assembled monolayer also influences the relative intensity ratio of this shoulder with respect to the main electronic transition. Higher energy singlet transitions (S_0−S_n) only lead to a residual broad and relatively weak absorption in the blue region (ca. 410 nm), thus suitable for light transparency purposes. The fluorescence of VG20-C_{16} exhibits a sharp emission band at λ_{max} = 850 nm leading to a narrow Stokes shift of 225 cm^{-1}. The vertical excitation energy is E_{0-0} = 1.47 eV, a value remarkably close to the optical bandgap (E_g = 1.49 eV) which means that VG20-type dyes in solution undergo negligible structural rearrangements in the excited-state, thus limiting intramolecular energy losses. It has a high photoluminescence quantum yield (PLQY) of 47%, which makes this class of cyanine dyes also attractive for NIR fluorescent labeling.[54−56]

The systematic increase of the chenodeoxycholic acid (CDCA) concentration into VG20 dye solution has no influence either on the shoulder amplitude or on the width of the absorption band (Figure S1). This indicates that H-type aggregates are unlikely to form in the EtOH/DMSO solvent mixture (9/1 ratio, v/v) at a dye concentration of 100 μmol/L.

Electronic structure calculations point out that the VG20 dye can coexist in two stable conformational isomers (cis and trans) given by the double bonds of the polymethine chain. The trans-conformation is 1.3 kcal·mol^{-1} higher in energy than the cis-isomer. Hence, the latter represents more than 90% of the entire population in solution at room temperature. The electronic spectrum in vacuum of the cis-VG20 has been computed using the second-order algebraic-diagrammatic-construction ADC(2) level of theory. It shows a strong absorption at 832 nm corresponding to the first excited singlet state $S_0 \rightarrow S_1$ in agreement with the experimental data. The S_1 singlet state is assigned to a π−π* HOMO to LUMO transition. The calculated molecular frontier orbitals involve almost exclusively the polymethine chain (Figure S2). The theoretical analysis does not show any additional electronic transition at around 750 nm, in agreement with the above assignment of a vibronic transition. Computational details and further spectral assignments are provided in Table S1. The HOMO and LUMO energy positions were determined by cyclic voltammetry (Figure S3). The two quasi-reversible peaks at +0.24 V (vs Fc^+/Fc) and +0.57 V (vs Fc^+/Fc) are attributed to the HOMO and HOMO + 1 energy levels. The LUMO level is situated at −1.06 V (vs Fc^+/Fc). These values lead to the HOMO and HOMO + 1 at +0.87 and +1.20 V (vs NHE), respectively, and the LUMO level at −0.43 V (vs NHE), considering the Fc^+/Fc redox potential at +0.63 V vs NHE.[57] The dye regeneration is thus thermodynamically favorable with both I_3^-/I^- (+0.35 V vs NHE) and $Co(bpy)_3^{3+/2+}$ (+0.56 V vs NHE) redox couples. However, we can postulate more difficulties for the electron injection step ($E_{CB,TiO2} \approx -0.45$ V vs NHE[58]) owing to a lack of an energetic driving force.

The photodynamic study of VG20-C_{16} in solution has been carried out combining picosecond time-correlated single photon counting (TCSPC) and femtosecond time-resolved transient absorption spectroscopy (TAS) to assess the kinetics of both radiative and nonradiative deactivation processes (Figure 2). The photoluminescence (PL) decay shows two subnanosecond components: τ_1 = 391 ps (f = 93%) and τ_2 = 925 ps attributed to the coexistence between the cis (τ_1) and trans (τ_2) forms in solution (Figure 2a). These values are significantly faster compared to the benchmark ruthenium or organic dyes used in DSSCs which lie between 2 and 100 ns.[45,59−61] This is due to the highly bound Frenkel excitons in the cyanine backbone structure leading to a comparatively poorer electron/hole delocalization in the excited states as it is also indicated by the calculation of the molecular frontier orbitals. The side-alkyl chain length and the CDCA content in solution have no noticeable influence on the excited-state dynamics (Figures S4−S5). Similar kinetics were measured by fs-TAS. Upon excitation with a 50 fs pulse at 810 nm, VG20-C_{16} exhibits pronounced excited state signatures, such as

https://dx.doi.org/10.1021/jacsau.1c00045
JACS Au 2021, 1, 409−426

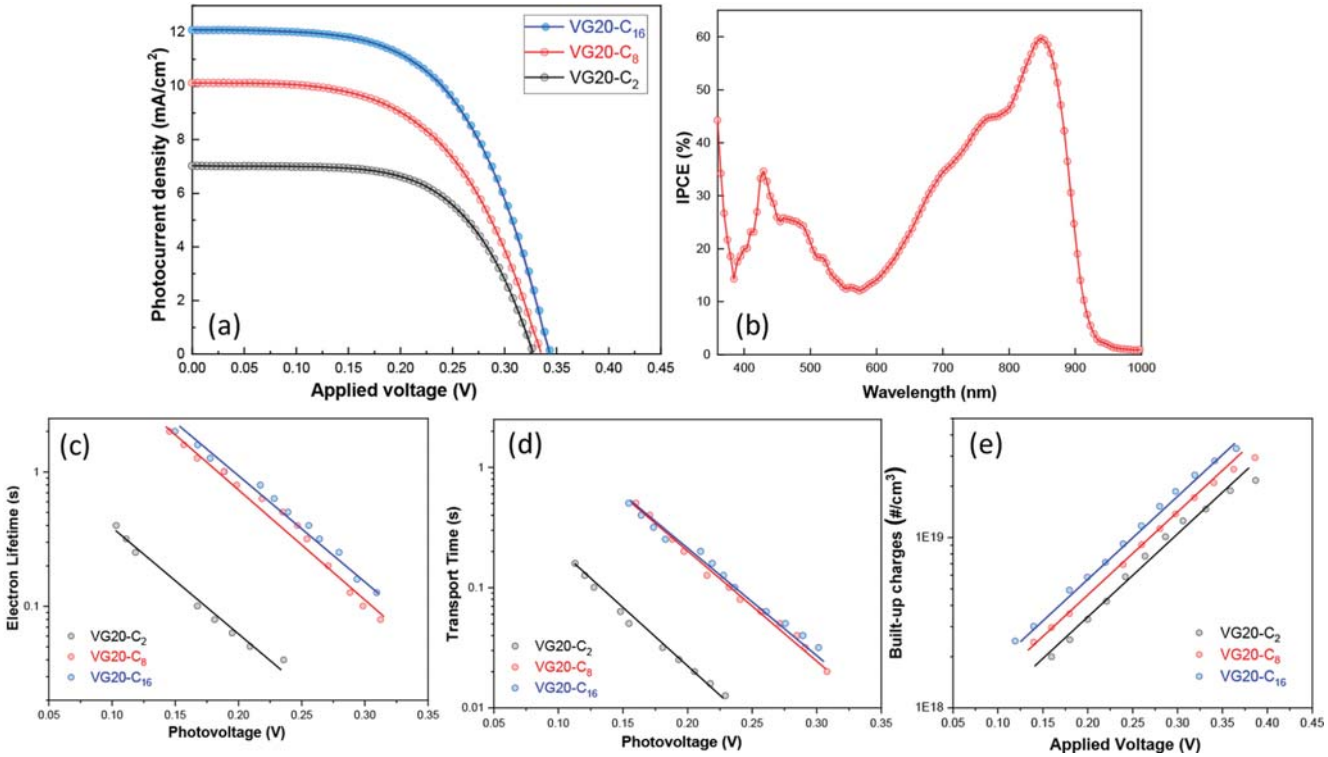

Figure 3. (a) $J-V$ curve under illumination at A.M. 1.5G conditions of VG20 dye as a function of the alkyl chain length for C_2 (black curve), C_8 (red curve), and C_{16} (blue curve). (b) IPCE spectrum of a VG20-C_{16} based DSSC and (c) IMVS, (d) IMPS, and (e) dark charge extraction measurements of VG20 dye as a function of the alkyl chain length for C_2 (black curves), C_8 (red curves), and C_{16} (blue curves) (the electrolyte composition is 1 mol/L DMII, 0.03 mol/L I_2, and 1 mol/L LiI in the acetonitrile/valeronitrile solvent mixture (85/15 v/v), and the devices are made of 8 μm thick 20 nm-based TiO_2 nanoparticles sheltered by 5.5 μm thick 400 nm TiO_2 particles).

excited state absorption (ESA) below 670 nm and beyond 1.3 μm (positive signal) and stimulated emission (SE) between 850 and 1100 nm, partially overlapping with ground state bleach (GSB) in the 700−900 nm range (Figures 2b, S6). Kinetic traces taken in the maximum of ESA, SE, and GSB decay in parallel, and individual wavelength fits give decay times in the range of 360 to 410 ps (Table S2). An additional rise component, in the range of 1−2 ps is also observed, most likely due to intramolecular relaxation and solvation dynamics in the EtOH/DMSO (9/1) mixture.

Rational Optimization of the Device Performance and Transparency

Since cyanines molecules are notorious for forming aggregates, the above results indicating the absence of aggregation in solution when combining ethanol/DMSO solvent mixture and low dye concentration of 100 μmol/L is important. However, the addition of CDCA as a deaggregating agent in the dyeing solution remains compulsory for the device performance to avoid quenching of the excited states that penalizes high yield of electron injection[62−64] and to maintain a colorless aspect of the photoanode (Figure S7). This work raises multiple points of evidence that strong H-type and J-type aggregates are formed within the self-assembled monolayer (SAM). This constitutes a major limitation not only for the device performance but also for the aesthetic as will be further discussed. The best conversion performances are obtained using a highly diluted dye solution (100 μmol/L) including 50 mmol/L of CDCA (1/500 ratio). Increasing the CDCA concentration to such an extent reduces the level of aggregation but also decreases the dye loading because the dye chemisorption enters into competition with CDCA coadsorption.[65]

Different alkyl chain lengths from C_2 to C_{16} were synthesized to hamper tail-to-tail dye aggregation.[66] It has no influence on the energy positions of both HOMO and LUMO orbitals. However, the longer the alkyl chain, the higher the molar extinction coefficient. A very slight red-shift by 6 nm of the singlet-to-singlet transition is also noticed (Figure S8). Optimizing the alkyl chain length contributes noticeably to the device performance, i.e., from 1.5% PCE for VG20-C_2, 1.9% for VG20-C_8, and 2.5% PCE for VG20-C_{16} (Figure 3a, Table S3). This improvement stems mainly from the photocurrent, increasing from 7.1 to 12.0 mA/cm^2, and to the cell photovoltage to a lower extent. To achieve these performances, the typical Lewis acid 4-*tert*-butylpyridine (4-TBP) and the guanidinium thiocyanate (GuSCN) are removed from the electrolyte to downshift the TiO_2 conduction band edge.[67−70] The electrolyte also includes a high concentration of lithium (1 mol/L) as will be discussed in the following. The incident photon to current efficiency (IPCE) spectrum shows a maximum of 60% at 850 nm leading after integration to a maximum J_{sc} value of 11.6 mA/cm^2 (Figure 3b). Although the S_0-S_n transitions are only weakly absorbing, they still provide ca. 30% IPCE indicating that conversion of high energy photons is an efficient process within this type of dye.

Intensity modulated photovoltage/photocurrent spectroscopy (IMVS/PS) experiments highlight that the alkyl chain length affects both nongeminate recombination and electron transport (Figure 3c, d). Indeed, whereas C_8 and C_{16} behave very comparably, reducing the number of carbon to C_2 leads to

https://dx.doi.org/10.1021/jacsau.1c00045
JACS Au 2021, 1, 409−426

a shortening of electron lifetime by ca. 1 order of magnitude and the transport time to a lesser extent. The electron transport is affected since the surface trapped electrons and the chemisorbed lithium are forming a quasi-particle contributing to an ambipolar transport of carriers toward the collection.[71,72] The charge collection efficiency (η_{cc}), expressed as the time ratio between the electron lifetime and the sum of electron lifetime and transport time, is enhanced by extending the length of the alkyl chain, from η_{cc} = 70% for C_2 to η_{cc} = 80% for C_8 and C_{16}. These results suggest, in agreement with previous literature, that longer alkyl chain length helps to repel tri-iodide species from the TiO_2 surface. Additional charge extraction experiments confirm that it modifies the SAM molecular packing based on the movement of the trap state energy driven by a different interfacial electric field strength (Figure 3e). The 15 mV gain in photovoltage experimentally observed is thus the result of the combination between the 1 order of magnitude longer electron lifetime (+59 mV expected) and 40 mV energy downshift of the traps.

Small alkali cations, such as Li^+, are known for their specific adsorption properties upon TiO_2 surfaces. Its Coulombic interaction with the surface of TiO_2 nanocrystals increases the flat band potential value, which moves the conduction band edge and surface traps down proportionally to the Nernst equation, i.e. 59 mV per decade of concentration.[45,71,72] In the case of the VG20-C_{16} dye, a high concentration of 1 mol/L of Li^+ in the electrolyte is required to reach a short-circuit current density of 12.1 mA/cm^2 (Figure S9, Table 1). Nevertheless,

Table 1. Cell Characteristics Depending on the Lithium Concentration in the Electrolyte for VG20-C_{16}-Based DSSCs[a]

Li^+ concentration	V_{oc} (mV)	J_{sc} (mA/cm^2)	fill factor (%)	PCE (%)
0.1 mol/L	395	5.5	66	1.6
0.25 mol/L	375	8.4	58	1.9
0.5 mol/L	368	9.6	56	2.2
1.0 mol/L	347	12.1	58	2.5

[a]Electrolyte composition is 1 mol/L DMII, 0.03 mol/L I_2, and 1 mol/L LiI in acetonitrile/valeronitrile solvent mixture 85/15 v/v.

this enhancement is at the expense of the cell photovoltage, which decreases by a value close to the 59 mV expected thermodynamically from Nernst equation (from 395 to 347 mV).

In addition to the CDCA and the alkyl chain length, the sensitization temperature modifies the dye packing as previously demonstrated on ruthenium-based complexes and also showed here by different data.[73] Three different temperatures have been investigated: room-temperature (RT), 4, and −20 °C. To compensate for the slower dye chemisorption, the sensitization time has been prolonged from 12 h to 7 days at −20 °C to maintain similar dye loading on the photoanode (Figure S10). Without dramatically losing the cell photocurrent, it increases both the fill factor and the cell photovoltage, thanks to a reduction of the nongeminate recombination kinetics (Figures 4 and S11). A PCE maximum of 3.1% can be achieved after sensitizing the electrodes at −20 °C while applying rigorously all aforementioned optimization steps (Table 2).

The stability of polymethine-based sensitizers has never been demonstrated so far in the literature. This is one drawback of this family of dyes. We identified water molecules

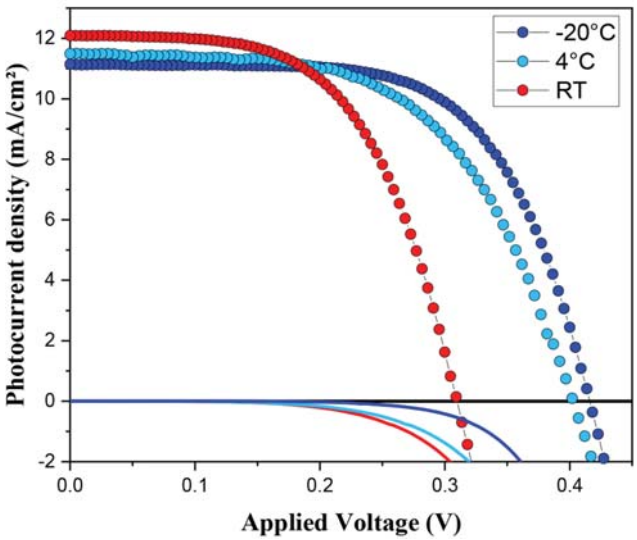

Figure 4. $J-V$ curve under illumination at A.M. 1.5G conditions of the VG20-C_{16}-based DSSC as a function of the temperature of sensitization, RT (red), 4 °C (light blue), and −20 °C (blue dark) (the electrolyte composition is 1 mol/L DMII, 0.03 mol/L I_2, and 1 mol/L LiI in the acetonitrile/valeronitrile solvent mixture (85/15 v/v), and the devices are made of 8 μm thick 20 nm-based TiO_2 nanoparticles sheltered by 5.5 μm thick 400 nm TiO_2 particles).

Table 2. Cell Characteristics Depending on the Sensitization Temperature VG20-C_{16}-Based DSSCs

temperature	V_{oc} (mV)	J_{sc} (mA/cm^2)	fill factor (%)	PCE (%)
RT	343	12.0	58	2.5
4 °C	402	11.5	58	2.6
−20 °C	422	11.2	65	3.1

as one major factor impacting the device stability. An enhancement of shelf life stability can be attained by assembling the devices in dry room (dew point temperature below −75 °C), drying solvents and electrolyte components carefully before using. Replacing the EtOH/DMSO solvent mixture for sensitization by DCM/DMSO affords improvement in the devices shelf life stability with a PCE retention over 92% for 400 h (Figure S12).

Replacing the tri-iodide/iodide redox mediator by Co(+III/+II) complexes affords reducing energy losses for the dye regeneration and circumventing the device orange coloration.[74−80] NIR photosensitizers associated with cobalt-based electrolytes have not been explored so far. Using a $Co(bpy)_3^{3+/2+}$ redox couple, the optimized concentration of lithium for the device performance can be reduced down to 0.1 mol/L of LiTFSI (Table S4). This has the further advantage that, while maintaining the J_{SC} constant, the open circuit photovoltage (V_{OC}) increases from 358 to 387 mV. As a result, the best PCE is obtained with 0.1 mol/L LiTFSI in the electrolyte leading to 1.9%. However, one drawback in the utilization of cobalt(+III/+II) complexes stems from the faster nongeminate recombination kinetics which herein limit the possible gain in photovoltage.[81−84] To alleviate this issue, atomic layer deposition (ALD) has been employed to retard loss reactions at the TiO_2/dye/electrolyte interfaces.[81,84−86] In this case, the best performances were obtained with an optimized subnanometric-thick Ga_2O_3 overlayer which acts as a tunnelling barrier to effectively balance injection and

https://dx.doi.org/10.1021/jacsau.1c00045
JACS Au 2021, 1, 409−426

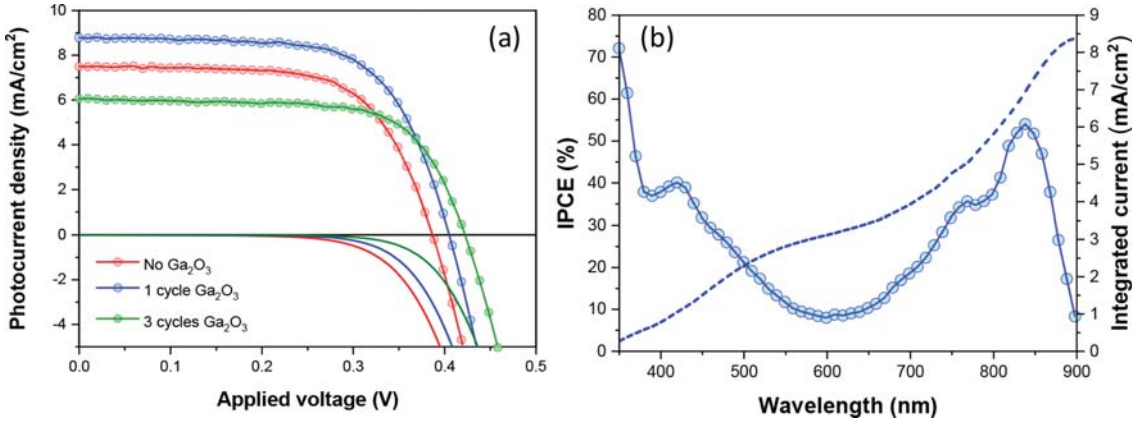

Figure 5. (a) $J-V$ curves for DSSC photoanodes subjected to different numbers of Ga_2O_3 ALD cycles under A.M. 1.5G conditions. (b) IPCE spectrum and integrated current density. (the electrolyte composition is 0.25 mol/L $Co(bpy)_3^{2+}$, 0.05 mol/L $Co(bpy)_3^{3+}$, and 0.1 mol/L LiTFSI in the acetonitrile/valeronitrile solvent mixture (85/15 v/v), and the devices are made of 8 μm thick 20 nm-based TiO_2 nanoparticles sheltered by 5.5 μm thick 400 nm TiO_2 particles).

recombination (Figure 5a).[86] As a result, production of dark current is significantly blocked due to the kinetic hindrance of nongeminate recombination. With the deposition of a single layer, both the photovoltage and the photocurrent values are increased to V_{OC} = 406 mV, J_{SC} = 8.6 mA/cm^2 leading to a PCE of 2.3%. The IPCE spectrum is very similar to tri-iodide/iodide redox mediator with a maximum of 54% at 840 nm. This latter is slightly blue-shifted due to existing electrostatic interactions between the dye and the redox mediator (Figure 5b). Thicker Ga_2O_3 deposition led to an increase of the photovoltage to 423 mV; however, the photocurrent dropped dramatically to 5.9 mA/cm^2 after 3 cycles, leading to a PCE of 1.7% (Table S5).

Average Visible Transmittance and Color Rendering

The level of device transparency was evaluated based on the average visible transmittance (AVT) considering not only the transmittance spectrum (T) but also the visual perception of human eyes through the photopic response (P) and the solar photon flux (S) in A.M. 1.5G conditions according to the following equation:[87]

$$\mathrm{AVT} = \frac{\int T(\lambda)P(\lambda)S(\lambda)\,\mathrm{d}(\lambda)}{\int P(\lambda)S(\lambda)\,\mathrm{d}(\lambda)}$$

AVT is the most recommended assessment by the windows industry to evaluate the transparency level of TPVs. Figure 6a shows the total transmittance spectrum of full devices without dye and electrolyte (black curve) and with VG20-C_{16} dye in either I_3^-/I^- or $Co(bpy)_3^{3+/2+}$ redox mediators. Taking advantage of VG20-C_{16} design, we matched remarkably the higher cell transmittance region to the maximum of the human eye's photopic response leading for the first time to completely transparent and colorless DSSC devices (Figure 6a). The electrolyte absorption shows up in the UV and blue region (<500 nm): a region in which the human cones are much less sensitive. On the other hand, dye aggregation, featured by a broadening of the S_0-S_1 transition, has a slight effect in the red part tail of the photopic response (Figures S7, S13). The AVT of the reference device, i.e. complete cell without the dye, reaches a maximum value of 74% without subtraction of glass reflections; this latter accounts for 9.5−11% depending on the incident wavelength (Figure S14). The sensitization of the photoanode decreases the AVT value to 65% as a result of the aggregation-induced broadening of the S_0-S_1 transition and the S_0-S_n transition in the blue part competing with the electrolyte absorption (Figure S13).

Devices based on tri-iodide/iodide redox couple has x,y coordinates of 0.370 and 0.416 in the CIE1931 chromaticity diagram (Figure 6b). It corresponds to the light yellowish part of the color space in agreement with the visual aspect of the device reported in the inset of Figure 6a. It reaches a color rendering index (CRI) value of 88%, and the correlated color temperature (CCT) is 5612 K. The CRI is also an important metric to consider in TPV applications as it describes the quantitative accuracy of the color rendered through a transparent medium. A value greater than 85% is considered excellent for TPV technologies applied to building facades.

The utilization of cobalt complexes avoids this slight orange coloration of the electrolyte given by tri-iodide. It leads to a noticeable shift of the x,y coordinates in the chromaticity diagram toward the center corresponding to the colorless region, i.e. x = 0.349 and y = 0.360 (Figure 6b). The CRI value increases to 92.1%, and the CCT value is 5553 K. The change to cobalt complexes influences a little of the absorption fingerprint of the dye. The S_0-S_1 maximum shifts from 848 nm for an I_3^-/I^--based electrolyte to 844 nm for $Co(bpy)_3^{3+/2+}$. The main absorption band becomes narrower, and the shoulder containing the spectroscopic signature of the H-aggregates is less pronounced. These results suggest that the dye interacts very intimately with the redox mediator, influencing the SAM geometry and packing. Consequently, the AVT of devices based on $Co(bpy)_3^{3+/2+}$ reaches a value of 68% up to an electrode thickness of 4 μm. With this AVT value, our devices appear totally transparent and close to colorless, in agreement with that found by Lunt et al., who pointed out that an AVT value of 60% constitutes a threshold value from which the PV device becomes clear.[14,88] Following a spin-coated layer of SiO_2 nanoparticles as an antireflecting coating (ARC), we achieved an AVT value of 76% (Figure S15). Such a number achieved with a selective NIR-DSSC lies well beyond the values reported so far in semitransparent visible DSSCs.[29−32] It approaches very closely the AVT characteristic of a standard double glazed window which is 78%.[32] Optimizing the number of layers of SiO_2 depositing

https://dx.doi.org/10.1021/jacsau.1c00045
JACS Au 2021, 1, 409−426

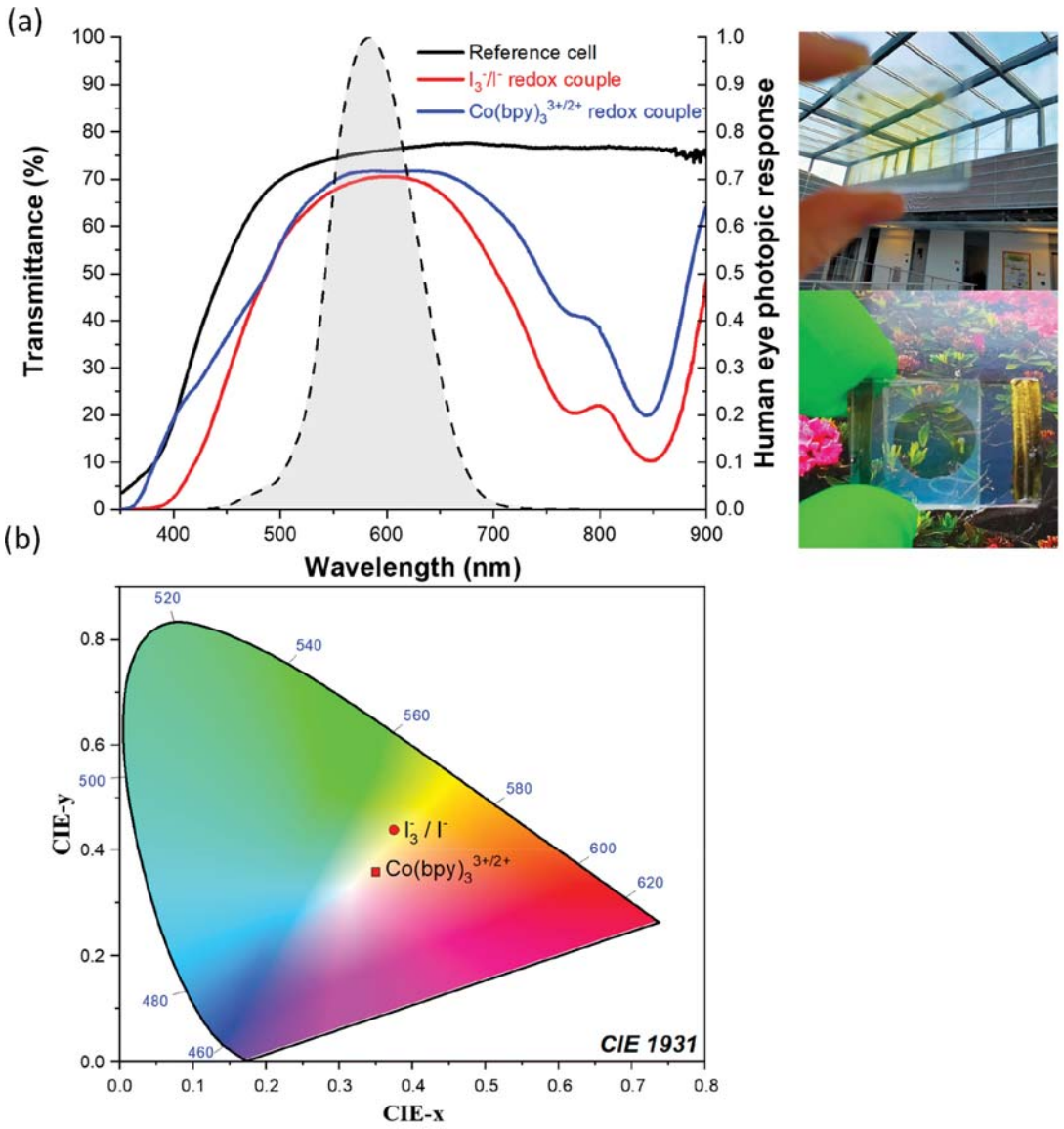

Figure 6. (a) Comparison of total cell transmittance measured using an integration sphere of a reference cell without dye and with an optimized electrolyte based on I_3^-/I^- redox couple (black curve) and VG20-C_{16} based devices constituted by an optimized electrolyte formulation based on the I_3^-/I^- redox couple (red curve) and $Co(bpy)_3^{3+/2+}$ redox couple (blue curve) with the aforementioned composition. The photoanode thickness is 4.0 μm. The human eye photopic response is included for comparison with the eye's sensitivity. Two pictures of the transparent NIR-DSSC are also provided: (top) with the I_3^-/I^- redox couple and (bottom) with the $Co(bpy)_3^{3+/2+}$ redox couple. (b) CIE 1931 color space diagram for VG20-C_{16} devices based on the I_3^-/I^- or $Co(bpy)_3^{3+/2+}$ redox couples in the electrolyte.

allows increased cell transmittance in the NIR region and, therefore, a gain 0.2% PCE in the final device performance.

Dye Regeneration and Electron Injection Kinetics

Dye regeneration kinetics have been evaluated using transient absorption spectroscopy associated with a streak camera for both spectral and temporal resolution of the transient dye radical cation. Figure 7 depicts the kinetic evolution depending on the electrolyte composition: i.e. I_3^-/I^- redox mediator (Figure 7a), $Co(bpy)_3^{3+/2+}$ (Figure 7b), or for a redox couple-free electrolyte (Figure 7c). The VG20-C_{16} radical cation absorbs in the visible range in agreement with the literature.[89] It shows up as a broad absorption spectrum between ca. 500 and 720 nm (Figure 7, Figure S16) for which the kinetics differ for the two redox mediators. The molar absorption coefficient of the dye radical cation in solution is about 25 times weaker compared to the reduced form in the same solution ($\varepsilon \approx 6200$ L/mol·cm) (Figure S17).

The related transient decay corresponds to the depopulation of the dye radical cation after a 30 ps pump pulse at 830 nm (Figure 8). The exponential decay requires systematically two components to account for fast and slower processes in regeneration involving HOMO and HOMO + 1 levels. For a I_3^-/I^- redox couple, dye regeneration takes place within τ_1 = 1.5 μs ($\pm$0.09 μs) and τ_2 = 19.4 μs ($\pm$1.3 μs). These values are the same order of magnitude as those reported for conventional ruthenium and D–π–A dyes.[45,90−92] Although the cobalt complex is a fast one-electron redox couple, the halftime for dye regeneration is about 1 order of magnitude longer, i.e. τ_1 = 15.6 μs ($\pm$0.4 μs) and τ_2 = 100.7 μs ($\pm$4.2 μs) as a result of the reduced driving force for the hole transfer, i.e. $-\Delta G^\circ_{reg}$ = 520 mV for I_3^-/I^- and $-\Delta G^\circ_{reg}$ = 310 mV for $Co(bpy)_3^{3+/2+}$.

https://dx.doi.org/10.1021/jacsau.1c00045
JACS Au 2021, 1, 409−426

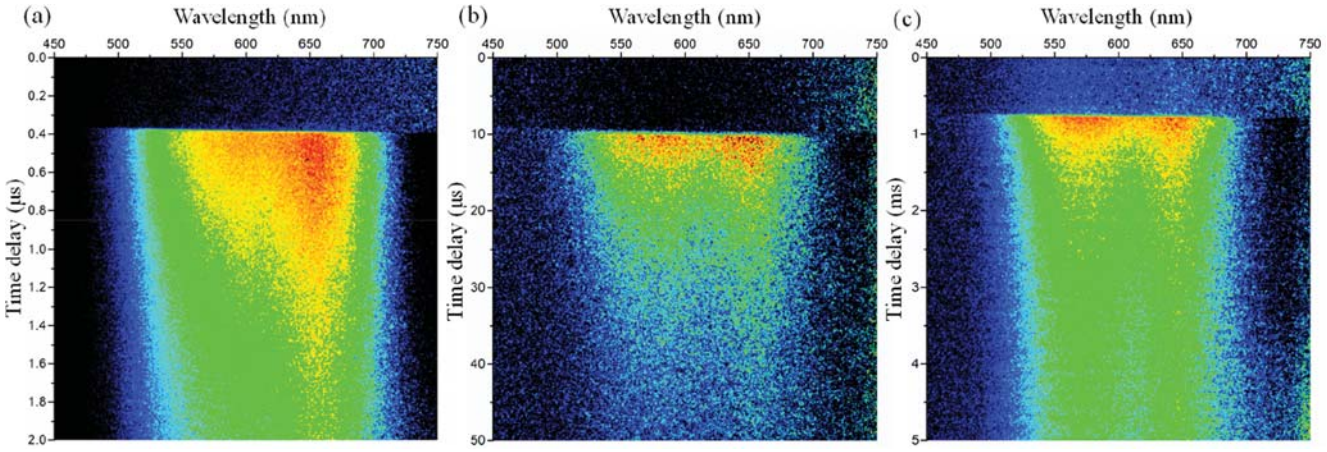

Figure 7. Time-resolved transient absorption spectral streak image of the VG20-C_{16} based DSSC for (a) the I_3^-/I^- redox couple, (b) the $Co(bpy)_3^{3+/2+}$ redox couple, and (c) the redox couple-free electrolyte. Note the difference of time delay between the different electrolytes.

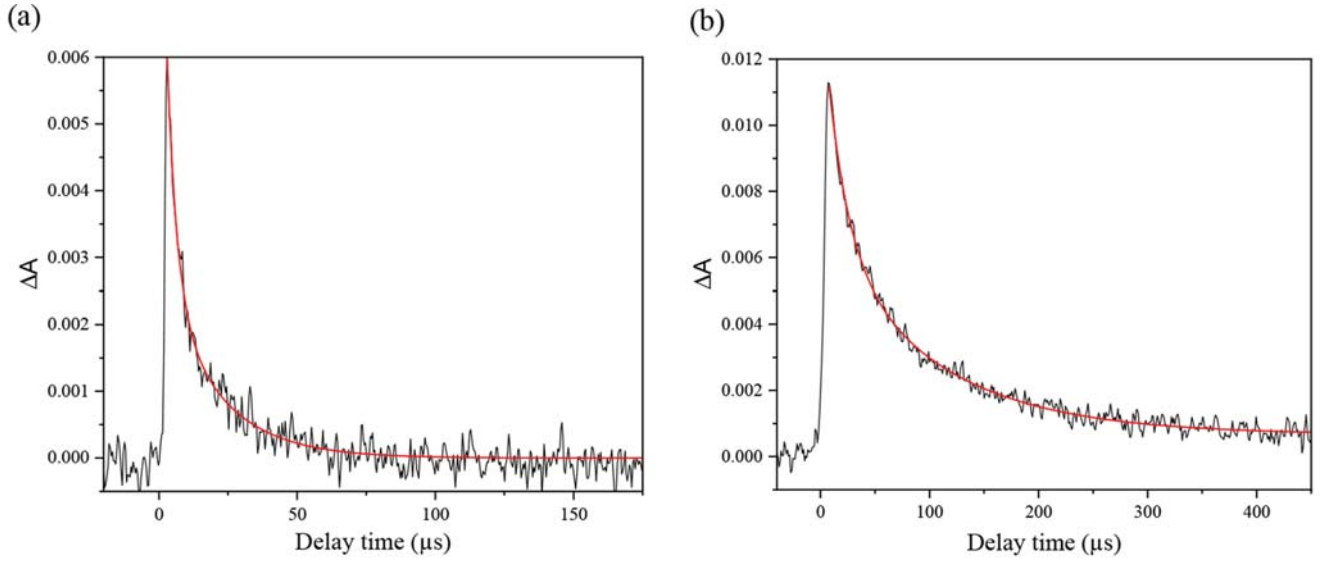

Figure 8. Transient absorption kinetics of the VG20-C_{16} based DSSC: (a) at 650 nm in the presence of the I_3^-/I^- redox couple and (b) at 550 nm in the presence the $Co(bpy)_3^{3+/2+}$ redox couple ($E_{810\ nm} \approx 0.18$ mJ/cm^2).

This range of values is also in agreement with the typical kinetics reported in the literature.[93] On the other hand, a long-lived radical dye cation is observed for an electrolyte free of redox couple (Figures 7c and S18). The geminate recombination takes place within 0.94 ms (± 0.02 ms) and does not totally decay even beyond the technical limit of the 5 ms time scale of the streak camera. Based on these results, we can conclude that dye regeneration yield is close to being quantitative and does not constitute the step limiting the IPCE, i.e. $\Phi_{reg} > 98\%$ in I_3^-/I^- and $\Phi_{reg} > 90\%$ in $Co(bpy)_3^{3+/2+}$.

The femtosecond dynamics of the excited state of VG20-C_{16} has also been investigated. Figure 9a shows the differential absorption spectra obtained in an average-representing data set characteristic for TiO_2 devices. The transient absorption kinetics are presented for selected wavelengths in Figure S19. These spectra are characterized by a prominent ESA peaking at 580 nm, which, unlike the data obtained in solution, decays rapidly within 25 ps leaving behind a broad, red-shifted absorption with a maximum at 660 nm and a long tail spanning the visible part of the spectrum (cf. 100 ps delay). Such a residual long-lived signature is assigned to the absorption of the VG20-C_{16} radical cation ($VG20^+$) in good agreement with the transient spectra measured using the picosecond TAS experiment (Figures 7 and S16).

In the near-IR part, SE is observed in the 850−1030 nm range, which decays on a picosecond time scale up to 25 ps. The GSB signal, between 730 and 900 nm, shows a double peak structure, akin to the steady-state absorption spectra due to monomers and aggregates. According to the ground state absorption spectra (SSA) of VG20-C_{16} in solution and on TiO_2 (Figures 2b and S7), one infers that the high-energy band at 770 nm is dominated by aggregates, while the low-energy band is a combination of GSB bleach of monomers and aggregates and SE from monomers. The 880 nm band has decayed by half its amplitude within 10 ps and reaches a stable level of ≈20% of the initial value by 100 ps. While the fast decay is due to SE decay and partial ground state recovery, the long-time asymptote is due to the radical dye cation.

The 770 nm band shows different kinetics. A small rise of this aggregate-dominated band is observed until 2 ps (Figure S19), which is a clear signature of excitation of aggregates due

https://dx.doi.org/10.1021/jacsau.1c00045
JACS Au 2021, 1, 409−426

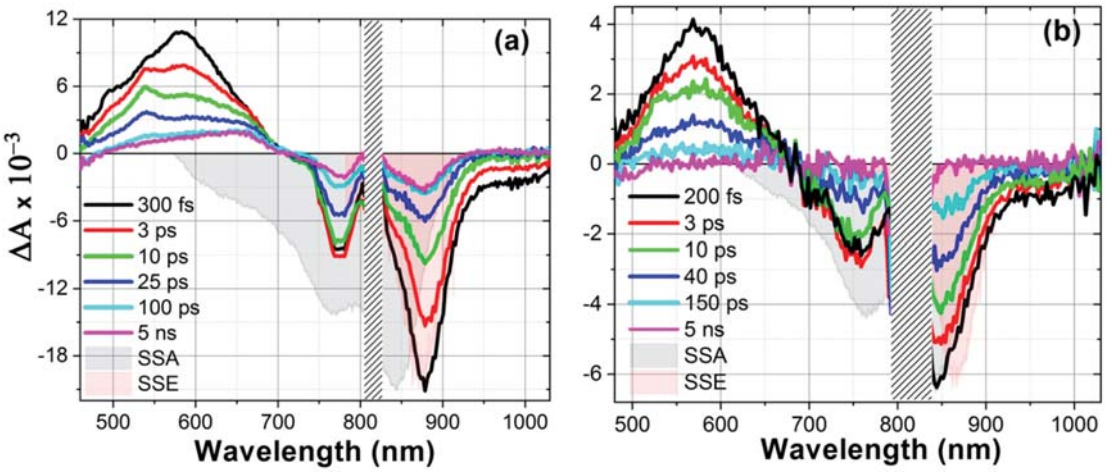

Figure 9. Transient spectra of VG20-C_{16} dye anchored on (a) injecting TiO_2 nanocrystals and (b) noninjecting ZrO_2 nanocrystals. The devices were pumped at 800 nm with an energy of 90 $\mu J/cm^2$. The electrolyte is composed of 1 mol/L DMII, 30 mmol/L I_2, and 1 mol/L LiI in acetonitrile. SSA and SSE are steady-state absorption and emission spectra arbitrarily scaled for comparison and allow identification of the regions where ground state bleach (GSB) and stimulated emission (SE) dominate the signal. The SSE spectrum is available only for $\lambda < 920$ nm, due to the limited sensitivity of the fluorimeter used.

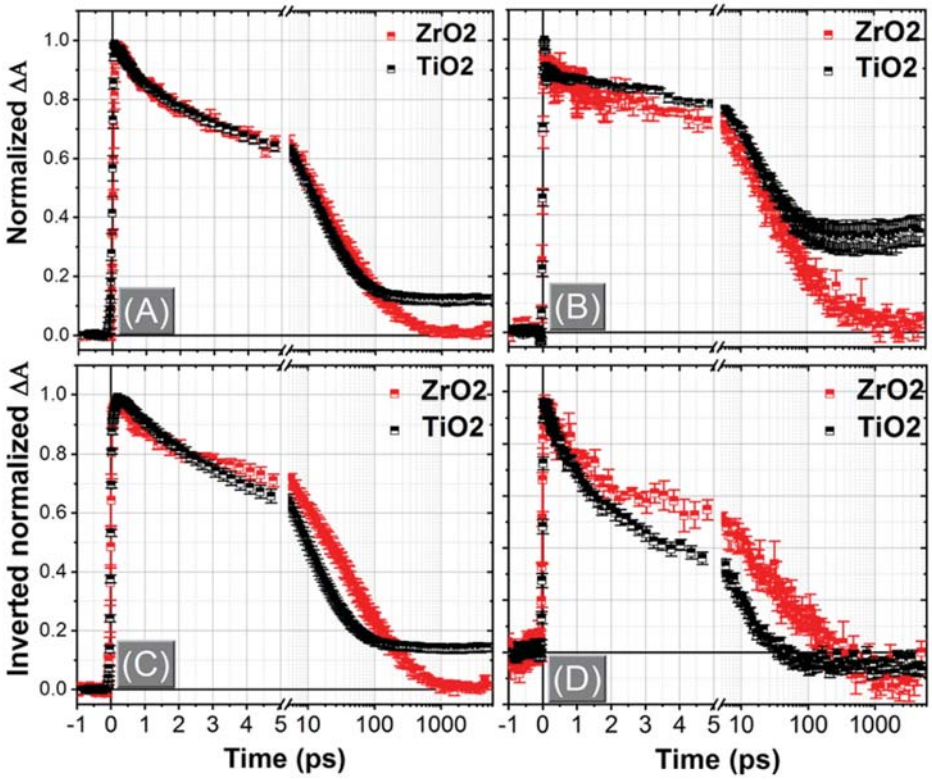

Figure 10. Comparison of normalized transient absorption kinetic profiles for the VG20-C_{16}-based DSSC using either ZrO_2 or TiO_2 nanocrystals at (a) 570 nm (ZrO_2) and 585 nm (TiO_2), (b) 640 nm (ZrO_2) and 650 nm (TiO_2), (c) 860 nm (ZrO_2) and 880 nm (TiO_2), and (d) 960 nm (ZrO_2) and 975 nm (TiO_2). All DSSC devices were excited at 800 nm with 90 $\mu J/cm^2$. The kinetics are averaged over seven samples for TiO_2 and three samples for ZrO_2. Error bars indicate the statistical standard error.

to energy transfer (ET) from monomers. In addition, a sharp absorption feature develops at $\lambda \approx 535$ nm on a 2 ps time scale. Since it is not observed in monomers, it is attributed to ESA of aggregates, rising according to the monomer−aggregate energy transfer process.

If all molecules (monomers and aggregates) became photo-oxidized, and since the cation absorption is negligible in the region of dominant GSB (800−900 nm), the negative ΔA signal should not decay with time, contrary to what is herein observed, meaning that the carrier injection yield (Φ_{inj}) is well-below 100%. Hence, the ratio GSB(t = 0.2 ps)/GSB(t = 5 ns) provides an estimate of Φ_{inj}. However, part of ΔA is due to SE, thus making the determination of the pure GSB component difficult. Nevertheless, analyzing the $\Delta A(t = 0)/\Delta A(t = 5$ ns) ratio at different wavelengths (770−850 nm) provides an upper limit of $\Phi_{inj} \approx 30$−35%. Although lower, this value is

https://dx.doi.org/10.1021/jacsau.1c00045
JACS Au 2021, 1, 409−426

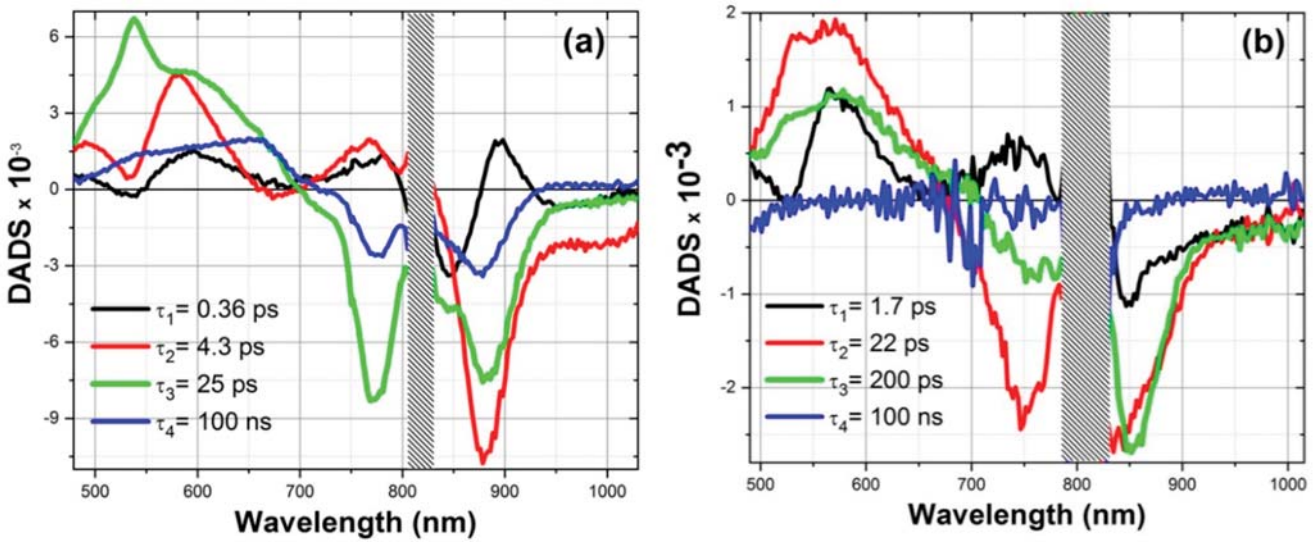

Figure 11. Wavelength-dependent amplitudes of VG20-C_{16}-based devices including (a) injecting TiO_2 nanocrystals and (b) noninjecting ZrO_2 nanocrystals. The devices were pumped at 800 nm with an energy of 90 $\mu J/cm^2$. The electrolyte is composed of 1 mol/L DMII, 30 mmol/L I_2, and 1 mol/L LiI in acetonitrile

relatively consistent with the IPCE at 810 nm (≈40−45%) (Figure 3b). The discrepancy is explained first by the TAS experimental conditions which are different than those of the IPCE and $J-V$ experiments in terms of excitation power (i.e. nonlinear response of DSSCs between cell photocurrent and incident light power) and the absence of a scattering layer in the device made for TAS measurements.

We have also studied the excited state dynamics in noninjecting ZrO_2-based devices, which serve as a reference to identify excited state processes, e.g. energy transfer which may be in kinetic competition with the electron injection in TiO_2 devices with an equivalent degree of aggregation. The differential spectra for ZrO_2-based devices show clear differences compared with TiO_2 (Figure 9b). Indeed, the radical cation signature is absent and the GSB fully recovers (zero signal) by ca. 1 ns. The SE (>900 nm) decays slower than in TiO_2 devices, since a weak signature can still be observed at a delay of 150 ps. The monomer-to-aggregate energy transfer (ET) is also observed for ZrO_2, as a small increase of the bleach band at 760 nm. Plots of kinetic traces and detailed multiexponential fits are gathered in Figures S19−21.

In order to highlight the carrier injection processes and their kinetics, Figure 10 shows kinetic traces obtained by averaging seven TiO_2-based and three ZrO_2-based devices. Selected wavelengths represent the monomer ESA (A), dye radical cation absorption (B), the low-energy GSB band (C), and SE (D). The prominent long-time signal for TiO_2 is due to the VG20-C_{16} radical cation absorption (580 and 650 nm) and incomplete GSB recovery (880 nm). Note a small positive absorption in the SE trace of TiO_2 ($\lambda \approx 975$ nm) most likely due to absorption by free carriers in TiO_2 or to a near-IR tail of the radical cation absorption.

The data suggest two distinct reaction scenarios for VG20-C_{16} on TiO_2 and ZrO_2, as summarized in Scheme S1 starting from photoexcited monomers (VG20*) and aggregates (Agg*).

As summarized in Tables S6−S7, characteristic lifetimes for TiO_2 are in the 0.5−1, 4−8, and 20−40 ps range, in addition to a fixed 100 ns time accounting for the nondecaying signals at long delays. In order to identify the most relevant characteristic lifetimes and processes, a global fit approach was carried out, i.e. the wavelength-dependent decay times are approximated by four wavelength-independent values. For TiO_2 (Figure 11a), the global decay constants obtained are 0.4 ps, 4.3 ps, 25 ps, and 100 ns, this latter value being fixed for the fit. Special features in the decay-associated difference spectra (DADS) allow identifying the main excited state processes, i.e. monomer-to-aggregate energy transfer and carrier injection/radical cation formation and their respective lifetimes. For the former, and as discussed above, the rise of the 770 nm GSB band and the 530 nm aggregate−ESA peak are the fingerprint, reflected in the DADS with dominating positive and negative signals, respectively. Hence, the energy transfer with rate k_{ET} is operative during the subpicosecond (0.4 ps) and the ≈4 ps phases (Figure 11a). Charge injection/radical cation formation is best identified as a rise of the absorption at the radical cation peak wavelength (660−670 nm) and monomer excited state decay, i.e. the decay of SE (>950 nm). The DADS of Figure 11a shows that charge injection, rate k_{inj}, occurs concomitantly with the energy transfer, dominantly during the ≈4 ps time scale and to a lesser extent at shorter times (0.4 ps DADS). The 25 ps DADS is characterized by SE and ESA decay both for monomers and aggregates (peak at 530 nm), but these decay amplitudes hide possibly weaker signatures of radical cation formation since the 25 ps DADS at 660 nm is purely positive (i.e., ESA decay).

The same global analysis on ZrO_2 is reported in Figure 11b. It reveals four time constants: 1.7, 22, and 200 ps in addition to a long-lived but almost vanishing 100 ns, used for consistency with fits of the TiO_2 data, its amplitude being in the noise level. The fastest 1.7 ps component (black line) displays a DADS very similar to that of TiO_2, with all the features consistent with monomer-to-aggregate energy transfer (k_{ET}). The ca. 24 ps component (red curve) displays signatures of both monomer and aggregate excited state decay: monomer SE > 850 nm, monomer and aggregate ESA decay (450−680 nm), with the weak sharp feature at 530 nm already identified for TiO_2 as due to aggregate ESA (k_{agg}). Note that the fast sub-10

https://dx.doi.org/10.1021/jacsau.1c00045
JACS Au 2021, 1, 409−426

ps component observed for electron injection (DADS negative at 660−680 nm) is absent as expected. Remarkably, the longer ≈200 ps component (blue curve) is due to a second slower monomer excited state decay (k_{nr}), since it displays SE, ESA, and GSB recovery very similarly, although with a shorter lifetime, to VG20-C_{16} in solution (Figure 2).

In summary, the comparison of VG20-C_{16} on TiO_2 and ZrO_2 allows to identify the kinetic signatures of electron injection within dominantly 4 ps most probably from monomers (k_{inj}), competing with monomer-to-aggregate energy transfer (k_{ET}) identified already on a 0.4 ps time scale, but also on the slower 4 ps lifetime (Table 3). This kinetic competition limits the electron injection efficiency from the monomer to ca. 30%. Injection from the monomers and aggregates may also take place on the 25 ps time scale since prominent excited state decay is observed, but a clear radical cation formation signature is missing possibly due to compensating for ESA decay/radical cation formation. Based on all of these important results, we can clearly confirm that aggregate formation and the related energy transfer from monomer to the aggregates limits the injection efficiency and the performances of this type of NIR-DSSC using polymethine cyanine dyes.

Table 3. Average Lifetimes Characterizing the Main Photophysical Processes for VG20-C_{16} on ZrO_2 and TiO_2 DSSCs Obtained from Femtosecond Transient Absorption Studies[a]

VG20-C_{16} DSSCs	τ_1 (ps)	τ_2 (ps)	τ_3 (ps)	τ_4 (ns)
TiO_2 + 50 mM CDCA	0.4	4.3	25	100
ZrO_2 + 50 mM CDCA	1.7	22	200	100

[a] τ_1 is dominated by monomer-to-aggregate energy transfer. For TiO_2 devices, electron injection occurs on both the τ_1 and τ_2 time scales.

CONCLUSIONS

In this work, a family of NIR-selective polymethine cyanine dyes coded as VG20-C_x was developed. The main attribute of VG20-C_x is its strong and sharp S_0−S_1 transition in the near-infrared region (λ = 832 nm) and a minimized S_0−S_n contribution in the far blue where the human retina is poorly sensitive. By bringing the NIR-selective dye-sensitized solar cell transmittance in the maximum region of the photopic response, we herein demonstrated a never reached level of aesthetic performance with an AVT value of 76%, CRI of 92.1%, and CCT of 4223 K when associated with Co-$(bpy)_3^{3+/2+}$ redox mediator in the electrolyte.

After a carefully led optimization of the dye structure and all device fabrication parameters, we demonstrated a PCE as high as 3.1% under A.M. 1.5G conditions. As a result of the absorber bandgap narrowing, making less overpotential for both injection and dye regeneration, we revealed that the electron injection is in kinetic competition with nonproductive monomer-to-aggregate energy transfer which limits the device performance based on such polymethine cyanine dyes.[43,94] Nevertheless, this first proof-of-concept of selective NIR-dye-sensitized solar cells opens up new scientific and technological directions for the field of transparent PVs filling the gap between organic photovoltaic (OPV) having high performances with relatively lower AVT in the range of 50% and LSC reaching above 80% AVT but with very poor performances. Based on this first work, we estimate that NIR-DSSCs can reach (i) AVT values greater than 80% by developing more transparent redox mediators and by abating molecular aggregation in the SAM and (ii) power conversion efficiencies greater than 7% can rapidly obtained after a complete redesign of all the DSSC components to reduce internal energy losses during the photon-to-electron conversion and once again by limiting the formation of harmful aggregates in the SAM thus turning the unproductive monomer-to-aggregate energy transfer into useful electron injection from reactive monomer excited states.

EXPERIMENTAL SECTION

The synthetic procedure to obtain the symmetrical heptamethine cyanine dyes, VG20, is reported in Scheme 1. It involves the condensation of the quaternary heterocyclic salts (**2**), bearing an activated methyl group, with the Vilsmeier−Haack reagent **3**.[95]

The 1,1,2-trimethyl-1*H*-benzo[e]indole-7-carboxylic acid (**1**) was readily obtained exploiting the Fischer indole synthesis, as previously described.[96] The subsequent quaternization of the benzoindolenine ring, performed under microwave irradiation,[97] led to increased acidity of the methyl group which enabled the cyanine bridge formation (see the first step in Scheme 1). All the symmetrical cyanine dyes were synthesized in a one-step reaction under microwave heating by reacting 2 equiv of quaternary heterocyclic salts **2** with the Vilsmeier−Haack reagent **3** in the presence of potassium acetate and ethanol (see Scheme 1). The brownish solid in the reaction mixture was filtered and washed with diethyl ether. Unreacted potassium acetate crystals were then removed by DCM. Finally, a recrystallization in acetonitrile was performed, and once all the precipitate was dissolved, a few drops of acetic acid were added to completely protonate the carboxylic moieties.

All microwave reactions were performed in a single-mode Biotage Initiator 2.5. TLC was performed on silica gel 60 F254 plates. GC-MS spectra were recorded on a Thermo Finnigan Trace GC with a cross-linked methyl silicone capillary column, coupled to a Thermo

Scheme 1. Synthesis of the VG20 Cyanine Series[a]

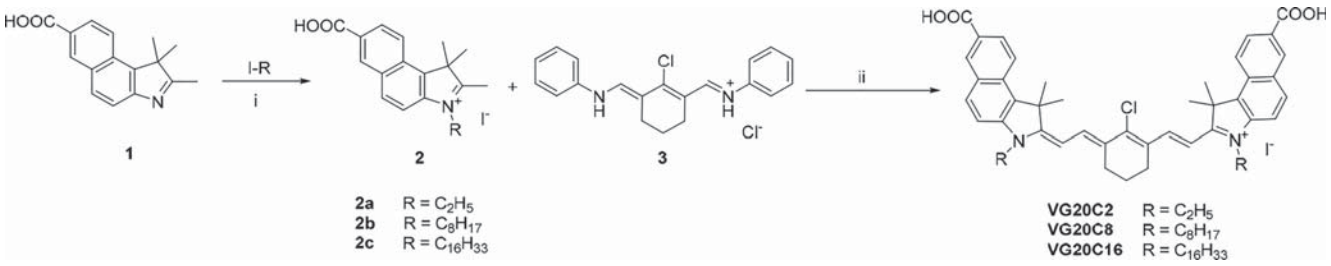

[a] Experimental conditions: (i) anhydrous acetonitrile, iodoalkane, MW, 40 min, 155 °C; (ii) potassium acetate, absolute ethanol, MW, 10 min, 120 °C.

https://dx.doi.org/10.1021/jacsau.1c00045
JACS Au 2021, 1, 409−426

Finnigan Trace MS mass spectrometer equipped with an electronic impact source (EI). UV−visible absorption spectra were recorded on a Shimadzu UV-1700 spectrometer. ^{1}H NMR spectra were recorded on a Jeol ECZR 600 MHz NMR. The purity of the final compounds was evaluated through HPLC using a Shimadzu LC 10 AD equipped with a C18 Altech C18 250 × 4. Each VG20 dye was dissolved in methanol and 20 μL of the solution was injected. The mobile phase (water/methanol) was used in gradient concentration: 80−20 at time 0 min, 80−20 at time 5 min, 0−100 at time 20 min, and 0−100 at time 30 min. It was pumped at a flow rate of 1 mL/min. The temperature of the column was set at 35 °C. The UV detector was set at the maximum absorbance wavelength of the sample.

All the chemicals were purchased from Sigma-Aldrich, except for the Vilsmeier−Haack reagent **3** which was obtained from Cyanine Technologies and was used without any further purification. The intermediate 1,1,2-trimethyl-1*H*-benzo[e]indole-7-carboxylic acid was prepared as described in the literature. The 7-carboxy-1,1,2-trimethyl-1*H*-benzo[e]indol-3-ium salts **2a** and **2b** are known compounds and were prepared as reported in the literature.[95,96] The carboxy-1*H*-benzo[e]indol-3-ium salt **2c** was synthesized according to the previously reported method.[97]

Synthesis of 7-Carboxy-1,1,2-trimethyl-3-hexadecyl-1*H*-benzo[e]-indol-3-ium Iodide 2c

1,1,2-Trimethyl-1*H*-benzo[e]indole-7-carboxylic **1** (1g, 3.95 mmol), 1-iodohexadecane (4.97 mL, 5.57 g, 15.8 mmol), and 8 mL of CH_3CN were introduced in a 10−20 mL microwave reaction vial. The reaction is carried out at 155 °C for 40 min under microwave irradiation. The resulting mixture was evaporated under vacuum, and the raw material was repeatedly washed under stirring with diethyl ether (3 × 100 mL), filtered, and then crystallized with acetonitrile. **2c** was obtained as a yellow powder (50 mg, 21%).

^{1}H NMR (600 MHz, DMSO-d_6) δ 8.88 (d, J = 1.7 Hz, 1H), 8.50 (dd, J = 16.9, 8.9 Hz, 2H), 8.24 (d, J = 9.0 Hz, 1H), 8.20 (dd, J = 8.8, 1.8 Hz, 1H), 4.57 (t, J = 7.8 Hz, 2H), 2.96 (s, 3H), 1.88 (p, J = 7.9 Hz, 2H), 1.77 (s, 6H), 1.27−1.14 (m, 26H), 0.84 (t, J = 7.0 Hz, 3H).

ESI $[M^+]$: 478.34 m/z.

ESI $[M - I - M]^+$: 1082.54 m/z.

General Synthetic Procedure of VG20 Dyes

7-Carboxy-1,1,2-trimethyl-1*H*-benzo[e]indol-3-ium salt **2**, Vilsmeier−Haack reagent **3**, and potassium acetate in a 2:1:2 ratio were introduced with absolute ethanol in a microwave reaction vial. The reaction was carried out at 120 °C for 10 min under microwave irradiation until TLC and UV showed reaction completion. At the end of the reaction a brownish precipitate and a dark green solution was observed. The precipitate was then filtered and washed with diethyl ether. The crude was dissolved in dichloromethane to remove the potassium acetate. Then, a recrystallization was performed with acetonitrile and a few drops of acetic acid were added. The precipitate was then filtered and washed several times with diethyl ether to obtain a dark powder.

VG20-C_2

7-Carboxy-3-ethyl-1,1,2-trimethyl-1*H*-benzo[e]indol-3-ium iodide **2a** (500 mg, 1.22 mmol), Vilsmeier−Haack reagent **3** (176 mg, 0.49 mmol), potassium acetate (119 mg, 1.22 mmol), and 5 mL of absolute ethanol were reacted as described in the general procedure. VG20-C_2 was obtained as a bronze precipitate (81 mg, 20%).

MS (ESI) m/z calculated for $[M - I]^+$ 699.2984, found 699.30.

^{1}H NMR (600 MHz, DMSO-d_6): δ 8.73 (s, 2H), 8.41−8.38 (m, 4H), 8.33 (d, J = 6 Hz, 2H), 8.10 (dd, J = 6 Hz, J = 1.68 Hz, 2H), 7.88 (d, J = 6, 2H), 6.43 (d, J = 18 Hz, 2H), 4.41 (m, 4H), 2.78 (m, 4H), 1.96 (s, 12H), 1.91 (m, 2H), 1.37 (t, J = 6 Hz, 6H).

The compound solubility was too low to record a ^{13}C NMR spectrum.

λ_{max} = 825 nm, λ_{em} = 839 nm, ε = 118 000 1/M·cm (measured in absolute ethanol).

VG20-C_8

7-Carboxy-1,1,2-trimethyl-3-octyl-1*H*-benzo[e]indol-3-ium iodide **2b** (500 mg, 1.01 mmol), *N*-(((*E*)-2-chloro-3-((phenylamino)-methylene)cyclohex-1-en-1-yl)methylene)benzenaminium chloride **3** (145 mg, 0.40 mmol), potassium acetate (99 mg, 1.01 mmol), and absolute ethanol (5 mL) were introduced in a microwave vial and reacted as described in the general procedure.

MS (ESI) m/z calculated for $[M - I]^+$ 867.4862, found 867.57.

The final compound VG20-C_8 was obtained as a brown-dark red solid (223 mg, 56%).

^{1}H NMR (600 MHz, DMSO-d_6): δ 8.72 (s, 2H), 8.38 (d, J = 12 Hz, 4H), 8.31 (d, J = 6 Hz, 2H), 8.10 (d, J = 6 Hz, 2H), 7.87 (d, J = 6 Hz, 2H), 6.41 (d, J = 12 Hz, 2H), 4.36 (m, 4H), 2.78 (m, 4H), 1.96 (s, 12H), 1.89 (m, 2H), 1.79 (m, 4H), 1.41 (m, 4H), 1.34 (m, 4H), 1.24 (m, 12H), 0.83 (t, J = 6 Hz, 6H).

The compound solubility was too low to record a ^{13}C NMR spectrum.

λ_{max} = 829 nm, λ_{em} = 845 nm, ε = 136 000 1/M·cm (measured in absolute ethanol).

VG20-C_{16}

7-Carboxy-3-hexadecyl-1,1,2-trimethyl-1*H*-benzo[e]indol-3-ium iodide **2c** (500 mg, 0.82 mmol), Vilsmeier−Haack reagent **3** (119 mg, 0.33 mmol), potassium acetate (81 mg, 0.82 mmol), and 5 mL of absolute ethanol were reacted as described in the general procedure. A bronze precipitate was obtained (96 mg, yield: 24%).

MS (ESI) m/z calculated for $[M - I]^+$ m/z: 1091.7366, found 1091.695.

^{1}H NMR (600 MHz, DMSO) δ 8.69 (s, 2H), 8.40 (d, J = 12 Hz, 2H), 8.32 (d, J = 6 Hz, 2H), 8.24 (d, J = 6 Hz, 2H), 8.09 (dd, J = 12 Hz, 2H), 7.79 (d, J = 6 Hz, 2H), 6.36 (d, J = 12 Hz, 2H), 4.32 (t, J = 6 Hz, 4H), 2.72 (m, 4H), 1.95 (s, 12H), 1.89 (m, 2H) 1.79 (m, 4H), 1.39 (m, 4H), 1.32 (m, 4H), 1.16 (m, 42H), 0.78 (t, J = 6 Hz, 6H).

The compound solubility was too low to record a ^{13}C NMR spectrum.

λ_{max} = 831 nm, λ_{em} = 848 nm, ε = 154 000 M·cm (measured in absolute ethanol).

Determination of Molar Extinction Coefficient

A concentrated solution of each dye was prepared by weighting the dye (5−7 mg) and dissolving it into 10 mL of absolute ethanol (EtOH). Three diluted solution (25 mL) of EtOH were prepared by taking aliquots (0.2, 0.1, and 0.05 mL) of the stock solution. The diluted solutions were measured by steady-state UV−visible absorption spectroscopy (Shimadzu UV-1700) using a quartz cuvette (1 cm pathway length). The absorbance intensities of each solution at the λ_{max} were plotted versus the sample concentration. A linear fit was applied to determine the molar extinction coefficient (ε) using the Beer−Lambert equation. The analysis was duplicated. The obtained data were considered acceptable when the difference between the determined log ε was less or equal to 0.02 in respect to their average. Otherwise, new concentrated dye stock solution in absolute EtOH was prepared and the protocol repeated.

Materials. Dimethyl sulfoxide (DMSO), ethanol (EtOH), acetonitrile (ACN), chenodeoxycholic acid (CDCA), and lithium bis(trifuoromethanesulfonyl)imide (LiTFSI) were purchased from Sigma-Aldrich. Tris(2,2′-bipyridine)cobalt(II) di[bis(trifluoromethanesulfonyl)imide] and tris(2,2′-bipyridine)cobalt(III) tris[bis-(trifluoromethanesulfonyl)imide] were purchased from Dyenamo AB.

Fabrication of Solar Cells. The mesoporous TiO_2 electrodes are prepared as previously described yielding 8 μm thick transparent electrode.[98] For the device performance it was sheltered with a 5 μm thick 400 nm-based TiO_2 scattering layer. The fluorine-doped SnO_2 (FTO) conducting glass (NSG-10, Nippon Sheet Glass) was thoroughly cleaned with a detergent solution, acetone, and ethanol solvents. The initial step was followed by an 18 min ultraviolet/O_3 treatment. Then the substrates were treated with 40 mM $TiCl_4$ aqueous solution at 70 °C for 45 min in order to make a thin and compact TiO_2 underlayer. The colloidal TiO_2 paste of Dyenamo DN-EP03 was used in conjunction with tri-iodide/iodide redox couple

https://dx.doi.org/10.1021/jacsau.1c00045
JACS Au 2021, 1, 409−426

and DSL30 NR-D (Greatcell Solar) with cobalt complexes. The layers were sequentially deposited on the $TiCl_4$ solution-treated FTO glass via screen printing technology, which results in a different thickness of TiO_2. The TiO_2 film was sintered at 500 °C under dry air flow and cooled down to room temperature to a obtain mesoporous, electronic conductive film. The mesoporous TiO_2 film was treated in $TiCl_4$ (40 mmol/L) and kept at 70 °C in an oven for 30 min. After sintering at 500 °C in air and cooled down to 80 °C, the mesoporous TiO_2 electrodes were stained by immersing them into the dye solution at room temperature or 4 °C for 12 h and 7 days for experiments at −20 °C. The Ga_2O_3 passivated mesoporous TiO_2 electrodes were made according to prior literature.[85] The growth rate of Ga_2O_3 was estimated to be ∼1 Å per cycle as deduced from ellipsometry on the Si wafer. The dye solution is composed of VG20-C_{16} (100 μmol/L) and CDCA (50 mmol/L) in DMSO/EtOH (1:9, v/v). The dye-coated TiO_2 film working electrode and thermally low-concentrated platinized conducting glass counter electrode were assembled using a 25 μm thick Surlyn hot-melt ring (DuPont, USA) heated at 125 °C. The internal space was filled with electrolyte using a vacuum pump through a predrilled hole on the counter electrode. The hole was sealed with a Bynel sheet and a thin glass cover by heating. All fabrication and assembling devices using the tri-iodide/iodide redox couple were carried out in a dry room (dew point of ca. −75 °C). The Co(III/II)tris(bipyridyl)-based redox electrolyte is made from tris(2,2′-bipyridine)cobalt(II) di[bis(trifluoromethanesulfonyl)imide] (0.25 mol/L), tris(2,2′-bipyridine)cobalt(III) tris[bis(trifluoromethanesulfonyl)imide] (0.05 mol/L), and LiTFSI (0.1, 0.5, or 1.0 mol/L) in acetonitrile. All PCE values have been reproduced. The reproducibility over cells is in the range of 0.1% in power conversion efficiencies. W.N., F.G., and V.N. reproduced the 3.1% PCE record.

Optical and Electrical Characterization of Solar Cells. During the photovoltaic performance measurements, a black metal mask with an aperture area of 0.158 cm^2 covered the solar cells. The solar cells were measured under radiation at 100 mW/cm^2 provided by a 450 W xenon lamp of the Oriel solar simulator (USA). The spectral output of the lamp passed a Schott K113 Tempax sunlight filter (Präzisions Glas & Optik GmbH, Germany) reducing the mismatch between the simulated and true solar spectra to less than 2%. The light intensity was determined using a calibrated Si reference diode equipped with an infrared cutoff filter (KG-3, Schott). The $J-V$ curves were recorded by a Keithley 2400 source meter. The voltage scan rate was set to 20 mV/s. IPCE spectra were measured with a lock-in amplifier (Stanford Research System SR830 DSP) under chopped monochromatic light (2 Hz) generated by a white light source from a 300W xenon lamp passing through a Gemini-180 double monochromator (Jobin Yvon Ltd.). The optical properties of the dye in solution and in the device were measured using an Agilent Cary 5000 spectrophotometer. A quartz cuvette with 1 cm light path was used for solution in dual beam transmission mode. For devices, all measurements were carried out in total transmittance mode using a 150 mm integration sphere. Background and zero were corrected, however without subtracting any external contributions such as glass absorption and reflection. All AVT measurements therefore correspond to a complete device assessment. CRI and CCT values were determined accordingly to the literature.[99,100]

Picosecond Pump−Probe Transient Absorption Spectroscopy (TAS) Measurements. The picosecond setup for the TAS measurements was used to investigate regeneration and recombination kinetics of the dye radical cation. The setup is composed of (1) a Nd:YAG laser (EKSPLA, PL2550, 10 Hz repetition rate, 30 ps pulse duration, 532 or 355 nm excitation) in combination with an optical parametric generator (EKSPLA, PG400 with broad excitation range 420−2300 nm) which is pumped by the third harmonic of Nd:YAG; (2) three different probe systems (Hamamatsu Photonics): Xe breakdown cell for the shortest 0.5−20 ns time scale; Xe Flash lamp for the 50 ns to 2 μs time scale; and continuous 150 W Xe lamp for the 5 μs to 10 ms time scale; (3) detector part: spectrograph (Princeton Instruments, SP2300), high dynamic range streak camera (Hamamatsu Photonics, C13410) with digital readout camera (Hamamatsu Photonics, ORCA Flash4, C11440); (4) delay generator (Stanford Research Systems, DG645), delay unit, and shutters control unit (Hamamatsu Photonics) to synchronize all the setup parts controlled by computer through the HPD-TA software (Hamamatsu Phonics); and (5) white light input optics, excitation optics, pump and probe shutters, moving sample holder, and motorized 12-position optical density filter wheel for attenuation of laser excitation pulse energy.

For the TAS measurements of the DSSC, the probe light was focused perpendicular to the sample and the pump light was focused 45° to the sample. The probe light was attenuated with different optical density filters (Newport or Thorlabs) and transmitted through the sample. The resulting light was introduced into the spectrograph and analyzed by the streak camera. The energy of the pump pulse in the excitation wavelength range 810−830 nm was set to ca. 0.2 mJ. A 750 nm short pass cutoff filter (Thorlabs) was placed before the spectrograph to cut scattering light from the pump. Transient absorption is calculated from four streak images according to the equation:

$$\Delta A = -\log\left(\frac{\text{data} - \text{emission}}{\text{monitor} - \text{dark}}\right)$$

where data is the intensity of the image obtained where both pump and probe are on, emission where only pump is on, monitor where only probe is on, and dark when both pump and probe are off in order to subtract the contribution of stray light. Each of these four images consisted of N integrated camera images. Measurements are performed in the sequence, data, emission, monitor, dark, and this sequence is repeated M times. In order to obtain a satisfactory signal-to-noise ratio, N was 500 and M = 5−10.

Femtosecond Pump−Probe Transient Absorption Spectroscopy (TAS) Measurements. The experimental pump−probe setup was already described in detail in previous papers.[101,102] To record the TA spectra, a home-built setup fs-TA spectrometer was utilized based on a Ti:sapphire regenerative amplifier laser system (Pulsar, Amplitude Technology) delivering 40 fs-long pulses, at 5 kHz, centered at 800 nm. One portion of the 800 nm beam is used directly as the pump beam, and the second for the white light generation (460−1030 nm) utilizing a 3 mm sapphire crystal. The residual fundamental at 800 nm was filtered by a conveniently concentrated solution of the IR125 dye (Lambda Physik) in EtOH in a 1 mm quartz cell. The relative linear polarization between pump and probe beams is set at the magic angle (54.7°), and the fwhm of the instrument response function (IRF) is 35 fs. To ensure sufficient reduction of the noise level, for every time point 200 spectra are averaged and the final data result from averaging 8 different scans in solution and 6−8 in the DSSC samples, changing the 2 mm long excitation line every 3−4 scans to avoid degradation. Every individual scan lasts 7 min and over 4−5 scans no change of the kinetics is observed due to possible degradation. For solution samples, in order to avoid re-exciting the same molecules in the 0.5 mm quartz cuvette, we sufficiently circulate the sample using a peristaltic pump. The pump pulse intensity was set so as to ensure a linear dependence of the ground state bleach signals in all experiments reported here. A 90 μJ/cm^2 pump energy fluence was used both on the solution samples, as well as on the complete DSSC samples. The DSSC samples for the TA measurements were prepared under similar conditions as described above, restricted on single-TiO_2 or ZrO_2 layers and sensitization was carried out overnight (14 h) using the same composition of the dye solution. The optical density (OD) of TiO_2 DSSCs was ∼0.4, and it was ∼0.2 for ZrO_2. The concentration of the solution sample was 5×10^{-5} M and the OD/mm = 0.75.

Data are processed to correct the effects of group velocity dispersion (chirp) in the white light continuum and to subtract the nonlinear signal from the solvent and the presence of any delay-independent background.[101,102] All transient spectra presented in this work are obtained by appending two data sets covering two adjacent spectral windows, from 460 to 1030 nm. After chirp correction, the zero time-delay is defined with an error bar of 30 fs over the entire observation spectral window. Single wavelength fits are made with

https://dx.doi.org/10.1021/jacsau.1c00045
JACS Au 2021, 1, 409−426

ORIGIN (eq 1), and global analysis, with the GLOTARAN software.[103]

$$\Delta A(\lambda, t) = \sum_i A_i(\lambda) e^{-t/\tau_i} \otimes \mathrm{IRF} \quad (1)$$

Time-Correlated Single Photon Counting Measurements. Excited state lifetimes were monitored using a time-correlated single photon counting (TCSPC) technique using an Edinburgh Instrument FLS980 spectrometer. The same spectrometer was used for steady-state measurements using a continuous Xe light source and double excitation/emission monochromator. TCSPC experiments were carried out using a 70 ps width laser diode as an excitation source (20 MHz repetition rate, 5 pJ/cm^2 average energy, instrument response in the range of 90−100 ps fwhm) and a microchannel plate photomultiplier tube (MCP-PMT) Hamamatsu detector set after the first emission monochromator. A 780 nm long pass filter was used in emission to reject light scattering from the glass of the device. The emission was monitored at 840 nm with a slit opening of 10 nm in the emission monochromator. The numerical analysis of the excited-state lifetime has been determined after reconvolution of the photoluminescence decay considering the instrumental response function (IRF). The PLQY was measured with an integration sphere based on indirect and direct method.

Note for Device Optimization. All PCEs presented in this work include a scattering layer of 5.5 μm thickness in the device to determine the maximum power conversion efficiency which can be obtained for this type of dye (transparent layer thickness is 8 μm). Comparison with a scattering layer (J_{sc} = 11.6 mA/cm^2, V_{oc} = 359 mV, ff = 0.62, PCE = 2.6%) and without scattering layer (J_{sc} = 9.7 mA/cm^2, V_{oc} = 348 mV, ff = 0.61, PCE = 2.1%) provides the reader the information that the scattering layer enhances the photocurrent by ca. 2 mA/cm^2. Most of this additional current originates from an enhancement in the blue region for which the particles scatter the most. Scattering of the TiO_2 particles decreases substantially beyond 800 nm in accordance with Mie scattering theory. The J−V and IPCE comparison based on the VG20-C_8 DSSC is reported in Figure S22.

■ ASSOCIATED CONTENT

Supporting Information

The Supporting Information is available free of charge at https://pubs.acs.org/doi/10.1021/jacsau.1c00045.

Further UV−visible absorption spectroscopy experiments in solution and on mesoscopic TiO_2 film, distribution of the molecular frontier orbitals, cyclic voltamperometry, additional PL and TA decays in solution or devices, additional J−V curves under illumination, IPCE and IMVS/IMPS of NIR-DSSC devices, and tabulated values of additional results (PDF)

■ AUTHOR INFORMATION

Corresponding Author

Frédéric Sauvage − *Laboratoire de Réactivité et Chimie des Solides, Université de Picardie Jules Verne (UPJV), CNRS UMR 7314, 80039 Amiens, France;* orcid.org/0000-0002-7740-3209; Email: frederic.sauvage@u-picardie.fr

Authors

Waad Naim − *Laboratoire de Réactivité et Chimie des Solides, Université de Picardie Jules Verne (UPJV), CNRS UMR 7314, 80039 Amiens, France*

Vittoria Novelli − *Laboratoire de Réactivité et Chimie des Solides, Université de Picardie Jules Verne (UPJV), CNRS UMR 7314, 80039 Amiens, France*

Ilias Nikolinakos − *IPCMS, UMR 7504, 67034 Strasbourg, France*

Nadia Barbero − *Laboratoire de Réactivité et Chimie des Solides, Université de Picardie Jules Verne (UPJV), CNRS UMR 7314, 80039 Amiens, France; Department of Chemistry, NIS Interdepartmental and INSTM Reference Centre, University of Torino, 10125 Torino, Italy*

Iva Dzeba − *Laboratoire de Réactivité et Chimie des Solides, Université de Picardie Jules Verne (UPJV), CNRS UMR 7314, 80039 Amiens, France*

Fionnuala Grifoni − *Laboratoire de Réactivité et Chimie des Solides, Université de Picardie Jules Verne (UPJV), CNRS UMR 7314, 80039 Amiens, France*

Yameng Ren − *Laboratory of Photonics and Interfaces, Ecole Polytechnique Fédérale de Lausanne (EPFL), 1015 Lausanne, Switzerland;* orcid.org/0000-0002-9362-9988

Thomas Alnasser − *Laboratoire de Réactivité et Chimie des Solides, Université de Picardie Jules Verne (UPJV), CNRS UMR 7314, 80039 Amiens, France*

Amalia Velardo − *Dipartimento di Scienze Agrarie, Forestali e Alimentari, University of Torino, Grugliasco 10095, Italy;* orcid.org/0000-0002-8028-6779

Raffaele Borrelli − *Dipartimento di Scienze Agrarie, Forestali e Alimentari, University of Torino, Grugliasco 10095, Italy;* orcid.org/0000-0002-0060-4520

Stefan Haacke − *IPCMS, UMR 7504, 67034 Strasbourg, France*

Shaik M. Zakeeruddin − *Laboratory of Photonics and Interfaces, Ecole Polytechnique Fédérale de Lausanne (EPFL), 1015 Lausanne, Switzerland*

Michael Graetzel − *Laboratory of Photonics and Interfaces, Ecole Polytechnique Fédérale de Lausanne (EPFL), 1015 Lausanne, Switzerland;* orcid.org/0000-0002-0068-0195

Claudia Barolo − *Department of Chemistry, NIS Interdepartmental and INSTM Reference Centre, University of Torino, 10125 Torino, Italy;* orcid.org/0000-0003-0627-2579

Complete contact information is available at: https://pubs.acs.org/10.1021/jacsau.1c00045

Author Contributions

W.N., V.N., Y.R., and F.G. have fabricated devices in addition to optimization and characterization. I.D. performed the ps-TAS experiments. T.A. carried out TiO_2 nanocrystals synthesis and antireflective coating work. I.N. and S.H. designed and performed all the fs-TAS experiments. N.B. and C.B. designed the dye synthesis. A.V. and R.B. performed the DFT calculations. S.M.Z. and M.G. supervised the work of Y.R. and participated in the discussions. F.S. designed the initial concept and experiments, supervised W.N., V.N., F.G., I.D., and T.A. in their work, coordinated the projects on the NIR-DSSC, and wrote the first version of the manuscript.

Notes

The authors declare no competing financial interest.

■ ACKNOWLEDGMENTS

W.N., I.N., I.D., S.H. and F.S. wish to thank the Agence National de la Recherche (ANR) "VISION-NIR" program under grant agreement number ANR-17-CE05-0037 for financial support. N.B., F.G., T.A., Y.R., R.B., S.M.Z., M.G., C.B., and F.S. acknowledge the "IMPRESSIVE" project which received funding from the European Union's Horizon2020 research and innovation program under grant agreement number no. 826013. S.H. acknowledges funding from the ANR

Labex NIE (ANR-11-LABX-0058_NIE). V.N. is indebted to the French Ministry of Recherche for financial support of her Ph.D. grant. F.S. wishes to thank Dr. Matteo Bonomo (UNITO) for fruitful discussions and comments. W.N. and F.S. wish also to thank Prof. A. Di Carlo, Dr. F. Matteocci, and Dr. D. Rossi from University Tor Vegata for fruitful discussion on AVT, CRI, and CCT assessment. Mrs. Daphné Boursier (LRCS) is acknowledged for proof-reading the manuscript.

REFERENCES

(1) Electricity production from wind and solar photovoltaic power in the EU, Feb. 2018, https://eca.europa.eu/Lists/ECADocuments/BP_WIND_SOLAR/BP_WIND_SOLAR_EN.pdf.
(2) Lunt, R. R. Theoretical limits for visibly transparent photovoltaics. *Appl. Phys. Lett.* **2012**, *101*, 043902.
(3) Yoon, J.; Baca, A. J.; Park, S. I.; Elvikis, P.; Geddes, J. B.; Li, L.; Kim, R. H.; Xiao, J.; Wang, S.; Kim, T. H.; et al. Ultrathin silicon solar microcells for semitransparent, mechanically flexible and microconcentrator module designs. *Nat. Mater.* **2008**, *7*, 907−915.
(4) Eperon, G. E.; Bryant, D.; Troughton, J.; Stranks, S. D.; Johnston, M. B.; Watson, T.; Worsley, D. A.; Snaith, H. J. Efficient, semitransparent neutral-colored solar cells based on microstructured formamidinium lead trihalide perovskite. *J. Phys. Chem. Lett.* **2015**, *6*, 129−138.
(5) Eperon, G. E.; Burkalov, V. M.; Goriely, A.; Snaith, H. J. Neutral color semi-transparent microstructured perovskite solar cells. *ACS Nano* **2014**, *8*, 591.
(6) Zhang, X.; Eperon, G. E.; Liu, J.; Johansson, E. M. J. Semitransparent quantum dot solar cell. *Nano Energy* **2016**, *22*, 70−78.
(7) Saifullah, M.; Ahn, S. J.; Gwak, J.; Ahn, S.; Kim, K.; Cho, J.; Park, J. H.; Eo, Y. J.; Cho, A.; Yoo, J. S.; et al. Development of semitransparent CIGS thin-film solar cells modified with a sulfurized-AgGa layer for building applications. *J. Mater. Chem. A* **2016**, *4*, 10542−10551.
(8) Karsthof, R.; Racke, P.; von Wenckstern, H.; Grundmann, M. Semi-transparent NiO/ZnO UV photovoltaic cells. *Phys. Status Solidi A* **2016**, *213*, 30−27.
(9) Lim, J. W.; Lee, D. J.; Yun, S. J. Semi-transparent amorphous silicon solar cells using a thin p-Si layer and a buffer layer. *ECS Solid State Lett.* **2013**, *2*, Q47−Q49.
(10) Guo, F.; Azimi, H.; Hou, Y.; Przybilla, T.; Hu, M.; Bronnbauer, C.; Langner, S.; Spiecker, E.; Forberich, K.; Brabec, C. J. High-performance semi-transparent perovskite solar cells with solution-processed silver nanowires as top electrodes. *Nanoscale* **2015**, *7*, 1642−1649.
(11) Della Gaspera, E.; Peng, Y.; Hou, Q.; Spiccia, L.; Bach, U.; Jasieniak, J. J.; Cheng, Y.-B. Ultra-thin high efficiency semi-transparent perovskite solar cells. *Nano Energy* **2015**, *13*, 249−257.
(12) Lunt, R. R.; Bulovic, V. Transparent, near-infrared organic photovoltaic solar cells for window and energy-scavenging applications. *Appl. Phys. Lett.* **2011**, *98*, 113305.
(13) Chen, C. C.; Dou, L.; Zhu, R.; Chung, C. H.; Song, T. B.; Zheng, Y. B.; Hawks, S.; Li, G.; Weiss, P. S.; Yang, Y. Visibly transparent polymer solar cells produced by solution processing. *ACS Nano* **2012**, *6*, 7185−7190.
(14) Traverse, C. J.; Pandey, R.; Barr, M. C.; Lunt, R. R. Emergence of highly transparent photovoltaics for distributed applications. *Nat. Energy* **2017**, *2*, 849−860.
(15) Davy, N. C.; Sezen-Edmonds, M.; Gao, J.; Lin, X.; Liu, A.; Yao, N.; Kahn, A.; Loo, Y. L. Pairing of near-ultraviolet solar cells with electrochromic windows for smart management of the solar spectrum. *Nat. Energy* **2017**, *2*, 17104.
(16) Xue, Q.; Xia, R.; Brabec, C. J.; Yip, H. L. Recent advances in semi-transparent polymer and perovskite solar cells for power generating window applications. *Energy Environ. Sci.* **2018**, *11*, 1688.
(17) Zhao, Y.; Meek, G. A.; Levine, B. G.; Lunt, R. R. Near-infrared harvesting transparent luminescent solar concentrators. *Adv. Opt. Mater.* **2014**, *2*, 606−611.
(18) Nazeeruddin, Md. K.; Pechy, P.; Renouard, T.; Zakeeruddin, S. M.; Humphry-Baker, R.; Comte, P.; Liska, P.; Cevey, L.; Costa, E.; Shklover, V.; et al. Engineering of efficient panchromatic sensitizers for nanocrystalline TiO_2-based solar cells. *J. Am. Chem. Soc.* **2001**, *123*, 1613−1624.
(19) Yella, A.; Lee, H. W.; Tsao, H. N.; Yi, C.; Chandiran, A. K.; Nazeeruddin, Md. K.; Diau, E. W. G.; Yeh, C. Y.; Zakeeruddin, S. M.; Graetzel, M. Porphyrin-sensitized solar cells with cobalt (II/III)-based redox electrolyte exceed 12% efficiency. *Science* **2011**, *334*, 629−634.
(20) Kakiage, K.; Aoyama, Y.; Yano, T.; Oya, K.; Fujisawa, J. I.; Hanaya, M. Highly-efficient dye-sensitized solar cells with collaborative sensitization by silyl-anchor and carboxy-anchor dyes. *Chem. Commun.* **2015**, *51*, 15894−15897.
(21) Holliman, P. J.; Mohsen, M.; Connell, A.; Davies, M. L.; Al-Salihi, K.; Pitak, M. B.; Tizzard, G. J.; Coles, S. J.; Harrington, R. W.; Clegg, W.; et al. Ultra-fast co-sensitization and tri-sensitization of dye-sensitized solar cells with N719, SQ1 and triarylamine dyes. *J. Mater. Chem.* **2012**, *22*, 13318−13327.
(22) Yum, J.-H.; Jang, S. R.; Walter, P.; Geiger, T.; Nüesch, F.; Kim, S.; Ko, J.; Grätzel, M.; Nazeeruddin, Md. K. Efficient co-sensitization of nanocrystalline TiO_2 films by organic sensitizers. *Chem. Commun.* **2007**, *44*, 4680−4682.
(23) Shiu, J.-W.; Chang, Y.-C.; Chan, C.-Y.; Wu, H.-P.; Hsu, H.-Y.; Wang, C.-L.; Lin, C.-Y.; Diau, E. W. G. Panchromatic co-sensitization of porphyrin-sensitized solar cells to harvest near-infrared light beyond 900 nm. *J. Mater. Chem. A* **2015**, *3*, 1417−1420.
(24) Islam, A.; Akhtaruzzaman, M.; Chowdhury, T. H.; Qin, C.; Han, L.; Bedja, I. M.; Stalder, R.; Schanze, K. S.; Reynolds, J. R. Enhanced photovoltaic performances of dye-sensitized solar cells by co-sensitization of benzothiadiazole and squaraine-based dyes. *ACS Appl. Mater. Interfaces* **2016**, *8*, 4616−4623.
(25) Ogura, R. Y.; Nakane, S.; Morooka, M.; Orihashi, M.; Suzuki, Y.; Noda, K. High-performance dye-sensitized solar cell with a multiple dye system. *Appl. Phys. Lett.* **2009**, *94*, 073308.
(26) Qin, C. J.; Numata, Y.; Zhang, S. F.; Islam, A.; Yang, X. D.; Sodeyama, K.; Tateyama, Y.; Han, L. Y. A Near-Infrared cis-configured squaraine co-sensitizer for high efficiency dye-sensitized solar cells. *Adv. Funct. Mater.* **2013**, *23*, 3782−3789.
(27) Chang, S.; Wang, H.; Lin Lee, L. T.; Zheng, S.; Li, Q.; Wong, K. Y.; Wong, W.-K.; Zhu, X.; Wong, W.-Y.; Xiao, X.; Chen, T. Panchromatic light harvesting by N719 with a porphyrin molecule for high-performance dye-sensitized solar cells. *J. Mater. Chem. C* **2014**, *2*, 3521−3526.
(28) Dong, L. H.; Zheng, Z. W.; Wang, Y. F.; Li, X.; Hua, J. L.; Hu, A. G. Co-sensitization of N719 with polyphenylenes from the Bergman cyclization of maleimide-based enediynes for dye-sensitized solar cells. *J. Mater. Chem. A* **2015**, *3*, 11607−11614.
(29) Zhang, K.; Qin, C.; Yang, X.; Islam, A.; Zhang, S.; Chen, H.; Han, L. High performance, transparent, dye-sensitized solar cells for see-through photovoltaic windows. *Adv. Energy. Mater.* **2014**, *4*, 1301966.
(30) Huaulmé, Q.; Mwalukuku, V. M.; Joly, D.; Liotier, J.; Kervella, Y.; Maldivi, P.; Narbey, S.; Oswald, F.; Riquelme, A. J.; Anta, J. A.; Demadrille, R. Photochromic dye-sensitized solar cells with light-driven adjustable optical transmission and power conversion efficiency. *Nat. Energy* **2020**, *5*, 468−477.
(31) Roy, A.; Ghosh, A.; Bhandari, S.; Selvaraj, P.; Sundaram, S.; Mallick, T. K. Color comfort evaluation of dye-sensitized solar cell (DSSC) based Building-Integrated Photovoltaic (BIPV) glazing after 2 years of ambient exposure. *J. Phys. Chem. C* **2019**, *123*, 23834−23837.
(32) Ghosh, A.; Selvaraj, P.; Sundaram, S.; Mallick, T. K. The colour rendering index and correlated colour temperature of dye-sensitized solar cell for adaptive glazing application. *Sol. Energy* **2018**, *163*, 537−44.
(33) Zhao, W.; Jun Hou, Y.; Song Wang, X.; Wen Zhang, B.; Cao, Y.; Yang, R.; Bo Wang, W.; Rui Xiao, X. Study on squarylium cyanine dyes for photoelectric conversion. *Sol. Energy Mater. Sol. Cells* **1999**, *58*, 173−183.

https://dx.doi.org/10.1021/jacsau.1c00045
JACS Au 2021, 1, 409−426

(34) Alex, S.; Santhosh, U.; Das, S. Dye sensitization of nanocrystalline TiO_2: enhanced efficiency of unsymmetrical versus symmetrical squaraine dyes. *J. Photochem. Photobiol., A* **2005**, *172*, 63−71.
(35) Yum, J.-H.; Walter, P.; Huber, S.; Rentsch, D.; Geiger, T.; Nuesch, F.; De Angelis, F.; Gratzel, M.; Nazeeruddin, M. K. Efficient far red sensitization of nanocrystalline TiO_2 films by an unsymmetrical squaraine dye. *J. Am. Chem. Soc.* **2007**, *129*, 10320−10321.
(36) Geiger, T.; Kuster, S.; Yum, J.-H.; Moon, S.-J.; Nazeeruddin, M. K.; Gratzel, M.; Nuesch, F. Molecular design of unsymmetrical squaraine dyes for high efficiency conversion of low energy photons into electrons using TiO_2 nanocrystalline films. *Adv. Funct. Mater.* **2009**, *19*, 2720−2727.
(37) Park, J.; Barolo, C.; Sauvage, F.; Barbero, N.; Benzi, C.; Quagliotto, P.; Coluccia, S.; Di, Censo D.; Grätzel, M.; Nazeeruddin, Md. K.; Viscardi, G. Symmetric vs. asymmetric squaraines as photosensitisers in mesoscopic injection solar cells: a structure-property relationship study. *Chem. Commun.* **2012**, *48*, 2782−2784.
(38) Kuster, S.; Sauvage, F.; Nazeeruddin, Md. K.; Graetzel, M.; Nuesch, F.; Geiger, T. Unsymmetrical squaraine dimer with an extended π-electron framework: An approach in harvesting near infrared photons for energy conversion. *Dyes Pigm.* **2010**, *87*, 30−38.
(39) Magistris, C.; Martiniani, S.; Barbero, N.; Park, J.; Benzi, C.; Anderson, A.; Law, C.; Barolo, C.; O'Regan, B. Near-infrared absorbing squaraine dye with extended π conjugation for dye-sensitized solar cells. *Renewable Energy* **2013**, *60*, 672−678.
(40) Maeda, T.; Arikawa, S.; Nakao, H.; Yagi, S.; Nakazumi, H. Linearly π-extended squaraine dyes enable the spectral response of dye-sensitized solar cells in the NIR region over 800 nm. *New J. Chem.* **2013**, *37*, 701−708.
(41) Maeda, T.; Hamamura, Y.; Miyanaga, K.; Shima, N.; Yagi, S.; Nakazumi, H. Near-infrared absorbing squarylium dyes with linearly extended π-conjugated structure for dye-sensitized solar cell applications. *Org. Lett.* **2011**, *13*, 5994−5997.
(42) Park, J.; Barbero, N.; Yoon, J.; Dell'Orto, E.; Galliano, S.; Borrelli, R.; Yum, J.-H.; Di Censo, D.; Gratzel, M.; Nazeeruddin, M. K.; Barolo, C.; Viscardi, G. Panchromatic symmetrical squaraines: a step forward in the molecular engineering of low cost blue-greenish sensitizers for dye-sensitized solar cells. *Phys. Chem. Chem. Phys.* **2014**, *16*, 24173−24177.
(43) Pandey, S. S.; Inoue, T.; Fujikawa, N.; Yamaguchi, Y.; Hayase, S. Substituent effect in direct ring functionalized squaraine dyes on near infra-red sensitization of nanocrystalline TiO_2 for molecular photovoltaics. *Thin Solid Films* **2010**, *519*, 1066−1073.
(44) Qin, C.; Numata, Y.; Zhang, S.; Yang, X.; Islam, A.; Zhang, K.; Chen, H.; Han, L. Novel near-infrared squaraine sensitizers for stable and efficient dye-sensitized solar cells. *Adv. Funct. Mater.* **2014**, *24*, 3059−3066.
(45) Novelli, V.; Barbero, N.; Barolo, C.; Viscardi, G.; Sliwa, M.; Sauvage, F. Electrolyte containing lithium cation in squaraine-sensitized solar cells: interactions and consequences for performance and charge transfer dynamics. *Phys. Chem. Chem. Phys.* **2017**, *19*, 27670−27681.
(46) Tian, M.; Tatsuura, S.; Furuki, M.; Sato, Y.; Iwasa, I.; Pu, L. S. Discovery of novel dyes with absorption maxima at 1.1 μm. *J. Am. Chem. Soc.* **2003**, *125*, 348−349.
(47) Keil, D.; Hartmann, H.; Reichardt, C. Synthesis and spectroscopic characterization of new NIR absorbing (2-thienyl) and (4-dialkylaminoaryl)-substituted croconic acid dyes. *Liebigs Ann. Chem.* **1993**, *9*, 935−939.
(48) Ehret, A.; Stuhl, L.; Spitler, M. T. Spectral sensitization of TiO_2 nanocrystalline electrodes with aggregated cyanine dyes. *J. Phys. Chem. B* **2001**, *105*, 9960−9965.
(49) Sayama, K.; Tsukagoshi, S.; Mori, T.; Hara, K.; Ohga, Y.; Shinpou, A.; Abe, Y.; Suga, S.; Arakawa, H. Efficient sensitization of nanocrystalline TiO_2 films with cyanine and merocyanine organic dyes. *Sol. Energy Mater. Sol. Cells* **2003**, *80*, 47−71.
(50) Ono, T.; Yamaguchi, T.; Arakawa, H. Study on dye-sensitized solar cell using novel infrared dye. *Sol. Energy Mater. Sol. Cells* **2009**, *93*, 831−835.
(51) Funabiki, K.; Mase, H.; Hibino, A.; Tanaka, N.; Mizuhata, N.; Sakuragi, Y.; Nakashima, A.; Yoshida, T.; Kubota, Y.; Matsui, M. Synthesis of a novel heptamethine-cyanine dye for use in near-infrared active dye-sensitized solar cells with porous zinc oxide prepared at low temperature. *Energy Environ. Sci.* **2011**, *4*, 2186.
(52) Geiger, T.; Schoger, I.; Rentsch, D.; Veron, A. C.; Oswald, F.; Meyer, T.; Nuesch, F. Unsymmetrical heptamethine dyes for NIR dye-sensitized solar cells. *Int. J. Photoenergy* **2014**, 258984.
(53) Galliano, S.; Novelli, V.; Barbero, N.; Smarra, A.; Viscardi, G.; Borrelli, R.; Sauvage, F.; Barolo, C. Dicyanovinyl and cyano-ester benzoindolenine squaraine dyes: The effect of the central functionalization on dye-sensitized solar cell performance. *Energies* **2016**, *9*, 486.
(54) Encinas, C.; Otazo, E.; Rivera, L.; Miltsov, S.; Alonso, J. Croconines: new acidochromic dyes for the near infrared region. *Tetrahedron Lett.* **2002**, *43*, 8391−8393.
(55) Li, Z.; Jin, Z.; Kasatani, K.; Okamoto, H. Resonant third-order optical nonlinearities of 1, 3-bis [(3, 3-dimethylindolin-2-ylidene) methyl] croconine. *Phys. B* **2006**, *382*, 229−234.
(56) Ciubini, B.; Visentin, S.; Serpe, L.; Canaparo, R.; Fin, A.; Barbero, N. Design and synthesis of symmetrical pentamethine cyanine dyes as NIR photosensitizers for PDT. *Dyes Pigm.* **2019**, *160*, 806−813.
(57) Hagberg, D. P.; Yum, J.-H.; Lee, H.; De Angelis, F.; Marinado, T.; Karlsson, K. M.; Humphry-Baker, R.; Sun, L.; Hagfeldt, A.; Gratzel, M.; Nazeeruddin, M.. K. Molecular engineering of organic sensitizers for dye-sensitized solar cell applications. *J. Am. Chem. Soc.* **2008**, *130*, 6259−6266.
(58) Grätzel, M. Photoelectrochemical cells. *Nature* **2001**, *414*, 338−344.
(59) Nazeeruddin, Md. K.; Zakeeruddin, S. M.; Humphry-Baker, R.; Jirousek, M.; Liska, P.; Vlachopoulos, N.; Shklover, V.; Fischer, C.-H.; Grätzel, M. Acid-base equilibria of (2,2'-bipyridyl-4,4'-dicarboxylic acid) ruthenium(II) complexes and the effect of protonation on charge-transfer sensitization of nanocrystalline titania. *Inorg. Chem.* **1999**, *38*, 6298−6305.
(60) Hagfeldt, A.; Grätzel, M. Molecular photovoltaics. *Acc. Chem. Res.* **2000**, *33*, 269−277.
(61) Paternò, G. M.; Barbero, N.; Galliano, S.; Barolo, C.; Lanzani, G.; Scotognella, F.; Borrelli, R. Excited state photophysics of squaraine dyes for photovoltaic applications: an alternative deactivation scenario. *J. Mater. Chem. C* **2018**, *6*, 2778−2785.
(62) Kay, A.; Graetzel, M. Artificial photosynthesis. 1. Photosensitization of titania solar cells with chlorophyll derivatives and related natural porphyrins. *J. Phys. Chem.* **1993**, *97*, 6272−6277.
(63) Salvatori, P.; Marotta, G.; Cinti, A.; Anselmi, C.; Mosconi, E.; De Angelis, F. Supramolecular interactions of chenodeoxycholic acid increase the efficiency of dye-sensitized solar cells based on a cobalt electrolyte. *J. Phys. Chem. C* **2013**, *117*, 3874−3887.
(64) Zhang, L.; Cole, J. Dye aggregation in dye-sensitized solar cells. *J. Mater. Chem. A* **2017**, *5*, 19541−19559.
(65) Chandiran, A. K.; Zakeeruddin, S. M.; Humphry-Baker, R.; Nazeeruddin, Md. K.; Grätzel, M.; Sauvage, F. Investigation on the interface modification of TiO_2 surfaces by functional co-adsorbents for high-efficiency dye-sensitized solar cells. *ChemPhysChem* **2017**, *18*, 2724−2731.
(66) Kroeze, J.; Hirata, N.; Koops, S.; Nazeeruddin, Md.K.; Schmidt-Mende, L.; Grätzel, M.; Durrant, J. Alkyl chain barriers for kinetic optimization in dye-sensitized solar cells. *J. Am. Chem. Soc.* **2006**, *128*, 16376−16383.
(67) Katoh, R.; Kasuya, M.; Kodate, S.; Furube, A.; Fuke, N.; Koide, N. Effects of 4-tert-butylpyridine and Li-ions on photoinduced electron injection efficiency in black dye-sensitized nanocrystalline TiO_2 films. *J. Phys. Chem. C* **2009**, *113*, 20738−20744.

https://dx.doi.org/10.1021/jacsau.1c00045
JACS Au 2021, 1, 409−426

(68) Koops, S. E.; O'Regan, B.; Barnes, P. R. F.; Durrant, J. R. Parameters influencing the efficiency of electron injection in dye-sensitized solar cells. *J. Am. Chem. Soc.* **2009**, *131*, 4808−4818.
(69) Boschloo, G.; Haggman, L.; Hagfeldt, A. Quantification of the effect of 4-tert-butylpyridine addition to I^-/I_3^- redox electrolytes in dye-sensitized nanostructured TiO_2 solar cells. *J. Phys. Chem. B* **2006**, *110*, 13144−13150.
(70) Katoh, R.; Fuke, N.; Furube, A.; Koide, N. Effect of dye coverage on photo-induced electron injection efficiency in N719-sensitized nanocrystalline TiO_2 films. *Chem. Phys. Lett.* **2010**, *489*, 202−206.
(71) Kelly, C. A.; Farzad, F.; Thompson, D. W.; Stipkala, J. M.; Meyer, G. J. Cation-controlled interfacial charge injection in sensitized nanocrystalline TiO_2. *Langmuir* **1999**, *15*, 7047−7054.
(72) Park, N.-G.; Chang, S.-H.; van de Lagemaat, J.; Kimand, K.-J.; Frank, A. J. Effect of cations on the open-circuit photovoltage and the charge injection efficiency of dye-sensitized nanocrystalline rutile TiO_2 films. *Bull. Korean Chem. Soc.* **2000**, *21*, 985−988.
(73) Sauvage, F.; Decoppet, J.-D.; Zhang, M.; Zakeeruddin, S. M.; Comte, P.; Nazeeruddin, Md. K.; Wang, P.; Grätzel, M. Effect of sensitizer adsorption temperature on the performance of dye-sensitized solar cells. *J. Am. Chem. Soc.* **2011**, *133*, 9304−9310.
(74) Feldt, S. M.; Gibson, E. A.; Gabrielsson, E.; Sun, L.; Boschloo, G.; Hagfeldt, A. Design of organic dyes and cobalt polypyridine redox mediators for high-efficiency dye-sensitized solar cells. *J. Am. Chem. Soc.* **2010**, *132*, 16714−16724.
(75) Yella, A.; Lee, H.-W.; Tsao, H. N.; Yi, C.; Chandiran, A. K.; Nazeeruddin, Md. K.; Diau, E.W.-G.; Yeh, C.-Y.; Zakeeruddin, S. M.; Grätzel, M. Porphyrin-sensitized solar cells with cobalt (II/III)-based redox electrolyte exceed 12% efficiency. *Science* **2011**, *334*, 629−634.
(76) Yum, J.-H.; Baranoff, E.; Kessler, F.; Moehl, T.; Ahmad, S.; Bessho, T.; Marchioro, A.; Ghadiri, E.; Moser, J.-E.; Yi, C.; Nazeeruddin, Md. K.; Graetzel, M. A cobalt complex redox shuttle for dye-sensitized solar cells with high open-circuit potentials. *Nat. Commun.* **2012**, *3*, 631.
(77) Mosconi, E.; Yum, J.-H.; Kessler, F.; Gomez Garcia, C. J.; Zuccaccia, C.; Cinti, A.; Nazeeruddin, M. K.; Gratzel, M.; De Angelis, F. Cobalt electrolyte/dye interactions in dye-sensitized solar cells: a combined computational and experimental study. *J. Am. Chem. Soc.* **2012**, *134*, 19438−19453.
(78) Mathew, S.; Yella, A.; Gao, P.; Humphry-Baker, R.; Curchod, B. F. E.; Ashari-Astani, N.; Tavernelli, I.; Rothlisberger, U.; Nazeeruddin, Md. K.; Gratzel, M. Dye-sensitized solar cells with 13% efficiency achieved through the molecular engineering of porphyrin sensitizers. *Nat. Chem.* **2014**, *6*, 242−247.
(79) Yao, Z.; Wu, H.; Li, Y.; Wang, J.; Zhang, J.; Zhang, M.; Guo, Y.; Wang, P. Dithienopicenocarbazole as the kernel module of low-energy-gap organic dyes for efficient conversion of sunlight to electricity. *Energy Environ. Sci.* **2015**, *8*, 3192.
(80) Ren, Y.; Sun, D.; Cao, Y.; Tsao, H. N.; Yuan, Y.; Zakeeruddin, S. M.; Wang, P.; Grätzel, M. A stable blue photosensitizer for color palette of dye-sensitized solar cells reaching 12.6% efficiency. *J. Am. Chem. Soc.* **2018**, *140*, 2405−2408.
(81) Gregg, B. A.; Pichot, F.; Ferrere, S.; Fields, C. L. Interfacial recombination processes in dye-sensitized solar cells and methods to passivate the interfaces. *J. Phys. Chem. B* **2001**, *105*, 1422−1429.
(82) Klahr, B. M.; Hamann, T. W. Performance enhancement and limitations of cobalt bipyridyl redox shuttles in dye-sensitized solar cells. *J. Phys. Chem. C* **2009**, *113*, 14040−14045.
(83) Feldt, S. M.; Cappel, U. B.; Johansson, E. M. J.; Boschloo, G.; Hagfeldt, A. Characterization of surface passivation by poly(methylsiloxane) for dye-sensitized solar cells employing the ferrocene redox couple. *J. Phys. Chem. C* **2010**, *114*, 10551−10558.
(84) Nelson, J. J.; Amick, T. J.; Elliott, C. M. Mass transport of polypyridyl cobalt complexes in dye-sensitized solar cells with mesoporous TiO_2 photoanodes. *J. Phys. Chem. C* **2008**, *112*, 18255−18263.
(85) Antila, L. J.; Heikkila, M. J.; Aumanen, V.; Kemell, M.; Myllyperkio, P.; Leskela, M.; Korppi-Tommola, J. E. I. Suppression of forward electron injection from $Ru(dcbpy)_2(NCS)_2$ to nanocrystalline TiO_2 film as a result of an interfacial Al_2O_3 barrier layer prepared with Atomic Layer Deposition. *J. Phys. Chem. Lett.* **2010**, *1*, 536.
(86) Chandiran, A. K.; Tetreault, N.; Humphry-Baker, R.; Kessler, F.; Baranoff, E.; Yi, C.; Nazeeruddin, Md. K.; Gratzel, M. Subnanometer Ga_2O_3 tunnelling layer by atomic layer deposition to achieve 1.1 V open-circuit potential in dye-sensitized solar cells. *Nano Lett.* **2012**, *12*, 3941−3947.
(87) Finlayson, E. U., Arasteh, D. K., Huizenga, C., Rubin, M. D., Reilly, M. S. *WINDOW 4.0: Documentation of calculation procedures report no. LBL-33943*; Lawrence Berkeley Laboratory and Enermodal Engineering, Inc., 1993.
(88) Fisette, P. *Windows: Understanding energy efficient performance*; University of Massachusetts, 2003; https://bct.eco.umass.edu/publications/articles/windows-understanding-energy-efficient-performance/ (accessed on 01/18/2021).
(89) Williams, M. P. A.; Ethirajan, M.; Ohkubo, K.; Chen, P.; Pera, P.; Morgan, J.; White, W. H.; Shibata, M.; Fukuzumi, S.; Kadish, K. M.; Pandey, R. K. Synthesis, Photophysical, electrochemical, tumor-Imaging, and phototherapeutic properties of purpurinimide-N-substituted cyanine dyes joined with variable lengths of linkers. *Bioconjugate Chem.* **2011**, *22*, 2283−2295.
(90) Sauvage, F.; Chhor, S.; Marchioro, A.; Moser, J. E.; Graetzel, M. Butyronitrile-based electrolyte for dye-sensitized solar cells. *J. Am. Chem. Soc.* **2011**, *133*, 13103−13109.
(91) Anderson, A. Y.; Barnes, P. R. F.; Durrant, J. R.; O'Regan, B. Quantifying regeneration in dye-sensitized solar cells. *J. Phys. Chem. C* **2011**, *115*, 2439−2447.
(92) Flasque, M.; Nhien, A. N. V.; Moia, D.; Barnes, P. R. F.; Sauvage, F. Consequences of solid electrolyte interphase (SEI) Formation upon aging on charge-transfer processes in dye-sensitized solar cells. *J. Phys. Chem. C* **2016**, *120*, 18991−18998.
(93) Feldt, S. M.; Lohse, P. W.; Kessler, F.; Nazeeruddin, Md. K.; Grätzel, M.; Boschloo, G.; Hagfeldt, A. Regeneration and recombination kinetics in cobalt polypyridine based dye-sensitized solar cells, explained using Marcus theory. *Phys. Chem. Chem. Phys.* **2013**, *15*, 7087.
(94) Pydzińska, K.; Ziółek, M. Solar cells sensitized with near-infrared absorbing dye: Problems with sunlight conversion efficiency revealed in ultrafast laser spectroscopy studies. *Dyes Pigm.* **2015**, *122*, 272−279.
(95) Sinibaldi, A.; Fieramosca, A.; Rizzo, R.; Anopchenko, A.; Danz, N.; Munzert, P.; Magistris, C.; Barolo, C.; Michelotti, F. Combining label-free and fluorescence operation of Bloch surface wave optical sensors. *Opt. Lett.* **2014**, *39*, 2947−2950.
(96) Park, J.; Barbero, N.; Yoon, J.; Dell'Orto, E.; Galliano, S.; Borrelli, R.; Yum, J.-H.; Di Censo, D.; Gratzel, M.; Nazeeruddin, M.. K.; Barolo, C.; Viscardi, G. Panchromatic symmetrical squaraines: a step forward in the molecular engineering of low cost bluegreenish sensitizers for dye-sensitized solar cells. *Phys. Chem. Chem. Phys.* **2014**, *16*, 24173−24177.
(97) Barbero, N.; Magistris, C.; Park, J.; Saccone, D.; Quagliotto, P.; Buscaino, R.; Medana, C.; Barolo, C.; Viscardi, G. Microwave-assisted synthesis of near-infrared fluorescent indole-based squaraines. *Org. Lett.* **2015**, *17*, 3306−3309.
(98) Ito, S.; Murakami, T. N.; Comte, P.; Liska, P.; Grätzel, C.; Nazeeruddin, Md. K.; Grätzel, M. Fabrication of thin film dye sensitized solar cells with solar to electric power conversion efficiency over 10%. *Thin Solid Films* **2008**, *516*, 4613.
(99) McCamy, C. S. Correlated color temperature as an explicit function of chromaticity coordinates. *Color Res. Appl.* **1992**, *17*, 142−144.
(100) Commission Internationale de l'Eclairage. *CIE 1988, 2° spectral luminous efficiency function for photopic vision*, CIE 086-1990; 1990.
(101) Liu, L.; Eisenbrandt, P.; Roland, T.; Polkehn, M.; Schwartz, P. O.; Bruchlos, K.; Omiecienski, B.; Ludwigs, S.; Leclerc, N.; Zaborova, E.; Léonard, J.; Méry, S.; Burghardt, I.; Haacke, S. Controlling charge

https://dx.doi.org/10.1021/jacsau.1c00045
JACS Au 2021, 1, 409−426

separation and recombination by chemical design in donor-acceptor dyads. *Phys. Chem. Chem. Phys.* **2016**, *18*, 18536.
(102) Roland, T.; Leonard, J.; Hernandez Ramirez, G.; Mery, S.; Yurchenko, O.; Ludwigs, S.; Haacke, S. Sub-100 fs charge transfer in a novel donor-acceptor-donor triad organized in a smectic film. *Phys. Chem. Chem. Phys.* **2012**, *14*, 273−279.
(103) Snellenburg, J. J.; Laptenok, S. P.; Seger, R.; Mullen, K. M.; Stokkum, I. H. M. v. Glotaran : A Java-Based Graphical User Interface for the R Package TIMP. *J. Stat. Soft.* **2012**, *49*, 1−22. http://www.jstatsoft.org/.

https://dx.doi.org/10.1021/jacsau.1c00045
JACS Au 2021, 1, 409−426

Appendix B

Thèse résumée en français

B.1 Introduction générale

L'augmentation de la consommation énergétique mondiale exige une plus grande variété de sources d'énergie propres et durables. Dans ce contexte, la technologie photovoltaïque est sans aucun doute une réponse attrayante et applicable à ce défi, car l'énergie solaire peut répondre aux besoins énergétiques mondiaux croissants. Selon de récentes enquêtes statistiques, depuis 2010, le taux de production des énergies nouvelles et renouvelables a connu une croissance rapide, passant de 1,24 %, à 8,88 % en 2018, et au cours de la même période, la production d'énergie solaire a présenté une croissance impressionnante de 1200 % [1]. Aujourd'hui, les cellules solaires à base de silicium représentent plus de 90 % des installations actuelles et environ 4 % de la production d'énergie en Europe, ils ont réussi l'exploit impressionnant de produire plusieurs dixièmes de GW d'électricité. Les inconvénients des cellules photovoltaïques en silice, tels que leur coût de production et de conservation élevé, leur faible rendement et leur conception encombrante et non flexible, peuvent être surmontés par des solutions encore plus "vertes", comme les cellules photovoltaïques de troisième génération. Dans cette catégorie figurent les dispositifs photovoltaïques organiques (OPV), les dispositifs photovoltaïques en pérovkites, les dispositifs photovoltaïques à boîtes quantiques et les cellules solaires à colorants (DSSC en anglais). Tous présentent des avantages et des inconvénients, principalement liés aux performances photovoltaïques en termes de rendement [2], la stabilité à long terme, les propriétés respectueuses de l'environnement et de l'homme, la production à faible coût et donc la durabilité de la production. L'intérêt croissant de la recherche multidisciplinaire pour ces technologies prometteuses, qui donnent lieu à des records d'efficacité successifs, incite de nombreuses entreprises (Great Cell Energy, Ubiquitous Energy, Solaronix, etc.)

à les commercialiser.

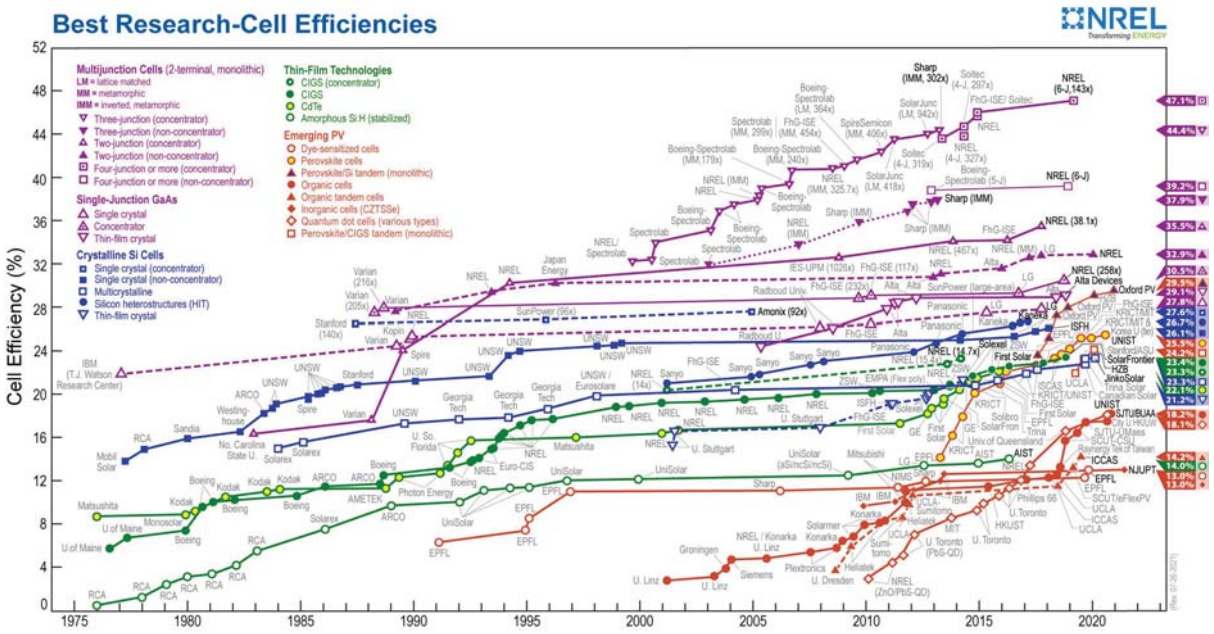

Figure B.1: Résumé des meilleurs résultats des différentes technologies cellulaires par année (source: www.nrel.gov/pv/cell-efficiency). De manière impressionnante, de nouvelles solutions d'applications photovoltaïques sont apparues au cours des dernières décennies (graphiques rouges) avec des rendements de cellules atteignant 26 %.

Notre projet collaboratif est axé sur la technologie des DSSC, reconnaissant leurs avantages uniques pour diverses applications. Celles-ci s'inscrivent dans le cadre de la technologie des dispositifs transparents qui peuvent être intégrés dans des bâtiments, des écrans électroniques, des vitrages électroniques alimentés de manière autonome, etc. Notre objectif est la création, la caractérisation et l'optimisation de ces nouveaux dispositifs DSSC transparents ou semi-transparents. L'effort réunit quatre groupes de recherche dans le cadre du projet VISION-NIR et d'autres groupes internationaux collaborateurs. La conception de la synthèse du premier colorant étudié dans cette thèse (cyanine -**VG20**) a été réalisée par le groupe de C. Barolo à l'Université de Turin et les deux derniers (pyrrolopyrrole cyanines - **TB207**,**TB423**) par le groupe de F. Odobel au laboratoire CEISAM de l'Université de Nantes. L'optimisation complète des cellules solaires et les mesures des performances photovoltaïques ont été réalisées par le groupe de F Sauvage au sein du groupe LRCS de l'Université de Picardie Jules Verne à Amiens. La croissance et la caractérisation des nanoparticules de semi-conducteurs (SC) est le domaine d'étude du groupe de C. Sassoye à l'Université de la Sorbonne à Paris.

Ce travail de doctorat a eu lieu dans le groupe BIODYN du Département d'Optique

Ultra-rapide et de Nanophotonique (DON) de l'Institut de Physique et de Chimie des Matériaux (IPCMS) sous la tutelle du Centre National de la Recherche Scientifique (CNRS) et de l'Université de Strasbourg. Notre étude se concentre sur l'identification des processus ultrarapides qui se produisent dans un DSSC suite à lors de la photoexcitation à l'échelle de temps fs-ps et ns. Grâce à des techniques expérimentales de pointe à résolution temporelle fs, qui excitent et sondent le proche UV, le visible et le proche IR, nous sommes en mesure de déterminer les taux cinétiques des processus radiatifs et non radiatifs qui limitent ou améliorent les performances photovoltaïques des cellules solaires, en particulier l'efficacité de l'injection des électrons dans la bande de conduction du semi-conducteur, qui se produit à l'échelle de temps ps. La description détaillée des montages expérimentaux est présentée au chapitre 4 et la démonstration, l'analyse et la discussion des résultats expérimentaux au chapitre 5.

B.2 Photovoltaïque transparente

Si l'on s'intéresse aux dispositifs photovoltaïques de troisième génération, avec les cellules photovoltaïques organiques à hétérojonction (OPV), les cellules solaires à boîtes quantiques et les cellules solaires perovskites à halogénure organique-inorganique, les DSSC, initialement inventées en 1991 par B. O'Regan et M. Grätzel, constituent une technologie très importante.

L'architecture élémentaire des DSSCs contient les composants suivants, tels qu'ils sont illustrés dans la Figure B.2. Outre les sensibilisateurs de colorants déposés sur les nanoparticules semi-conductrices, de TiO_2, les éléments supplémentaires sont les deux électrodes, à savoir la photoanode et la photocathode, qui sont essentiellement des films de verre, dont les parties de connexion sont recouvertes d'un oxyde conducteur transparent (TCO). De plus, les nanoparticules semi-conductrices (SC) sont recouvertes d'une couche transparente du côté de la conduction de la photoanode, et enfin l'électrolyte entre les deux films. Le colorant, chimiquement adsorbé sur le semi-conducteur, absorbe un photon et passe instantanément à son état excité. L'injection d'électrons dans la SC est un processus rapide, plus rapide que la vitesse de désactivation du colorant à son état fondamental et laisse le colorant sous sa forme cationique. Ensuite, les électrons se transportent à travers la couche nanostructurée de l'anode et sont finalement extraits dans le circuit externe. Après l'injection, le colorant est régénéré par l'électrolyte et, entre les deux, des processus de recombinaison des charges peuvent se produire, ce qui limite l'efficacité. Le schéma temporel de ces processus s'étend de ∼100 fs à ms. Dans

cette thèse, pour les DSSCs étudiés, une optimisation approfondie a été réalisée par nos collaborateurs dans toutes les différentes "sections" individuelles et nos études se concentrent précisément sur les processus ultrarapides. Plus précisément, nos études incluent l'examen du taux d'injection et de l'efficacité, ainsi que des interactions plus spécifiques entre différentes espèces moléculaires et, en général, l'étude photophysique du système.

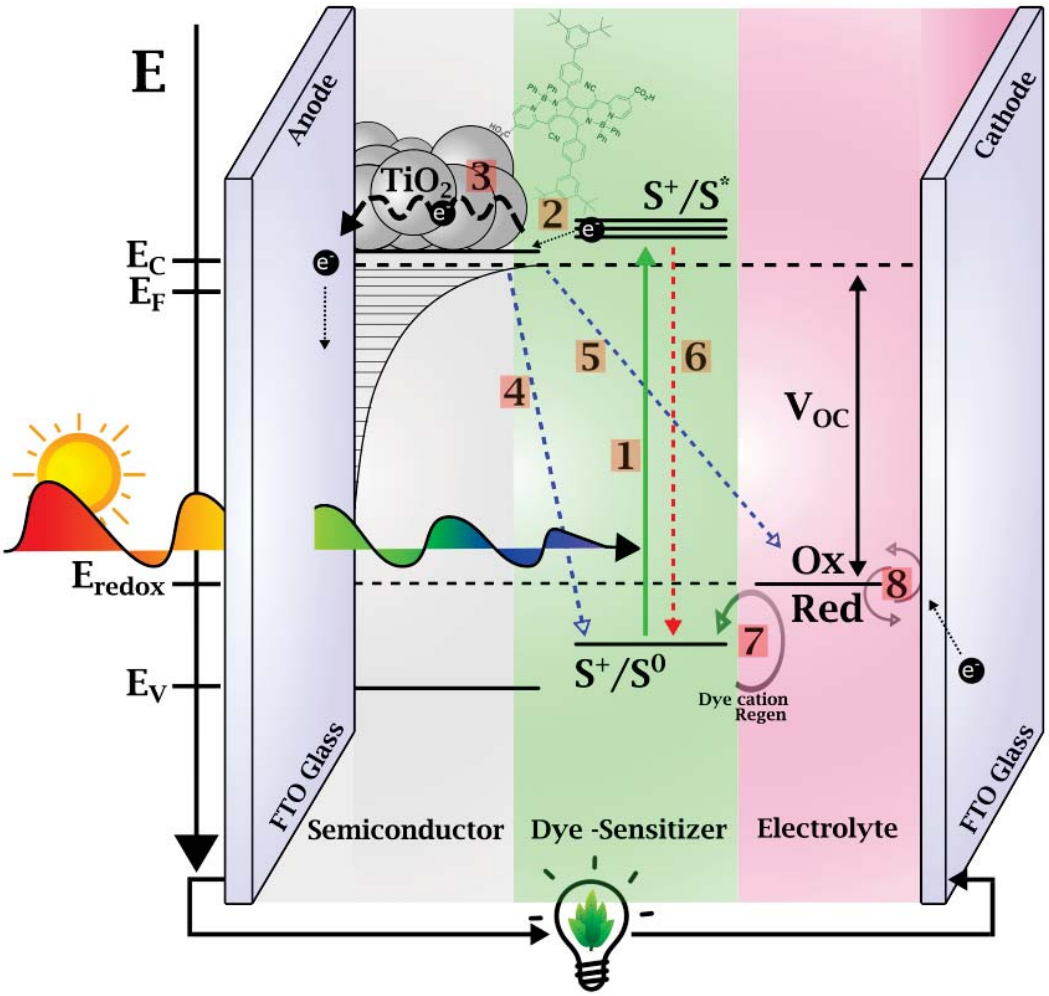

Figure B.2: Le principe des DSSC et les différents composants du dispositif. (1) Absorption du colorant. (2) Injection dans le SC. (3) Transport de charge. (4) Recombinaison entre le SC et le cation du colorant (transfert d'électrons inverse). (5) Recombinaison à partir du SC-électrolyte (recombinaison indirecte). (6) Désactivation du premier état excité. (7) Régénération du colorant. (8) Régénération du couple redox

Les technologies transparentes avec transmission partielle de la lumière sont un domaine d'étude depuis trois décennies. Ils peuvent s'intégrer dans l'espace de vie quantidien, ce que ne peuvent pas faire les systèmes photovoltaïques conventionnels plus encombrants. L'utilisation efficace de l'espace architectural en fait des candidats parfaits pour les fenêtres intégrées des bâtiments, les applications automobiles, les affichages électroniques et les infrastructures urbaines et autres. Ils nécessitent moins d'espace, offrant plus de surface active à utiliser et par conséquent augmentent le gain total. Actuellement, il existe diverses technologies TPV qui peuvent être classées en fonction de la longueur d'onde sélective et de la non-sélectivité [3]. Les DSSCs transparents de notre étude appartiennent à la catégorie des PVs sélectifs en longueur d'onde, récoltant la partie proche IR du spectre solaire. Pour cette raison, nous étudions les DSSCs avec des sensibilisateurs explicites pour le proche IR.

Il existe plusieurs approches pour déterminer le niveau de transparence des TPVs. Une approche générale, acceptée par l'industrie, consiste à introduire le facteur de transmission visible moyen (AVT), qui est défini comme le rapport entre l'intégration du spectre de transmission et la réponse de l'œil humain phototopique. De plus, une métrique plus complète, représente l'efficacité globale du système en rationalisant AVT et PCE en tant que tels:

$$LUE = PCE \times AVT \tag{B.1}$$

B.3 Photophysique

Dans cette thèse de doctorat, l'étude s'est concentrée sur l'examen des mécanismes ultrarapides des colorants incorporés dans de véritables DSSC. Toutes les propriétés photophysiques mesurées des colorants-sensibilisateurs en solution commencent par la photoexcitation/absorption et se terminent par la fluorescence. Les processus généraux qui se produisent peuvent être décrits par le diagramme de Perrin-Jablonski. Dans les DSSC, lors de la fixation au SC, différentes espèces telles que des agrégats moléculaires de colorants, peuvent être formées et des processus intra/intermoléculaires de transfert d'énergie et d'électrons peuvent avoir lieu. La photophysique fondamentale des monomères et des agrégats est bien connue depuis plusieurs décennies.

Dans les systèmes spectroscopiques de base tels que les colorants en phase de solution ou les interfaces simples des DSSC où aucune configuration moléculaire plus large n'est formée, la prédiction basée sur les agrégats H et J est couramment utilisée et reproduit

les résultats expérimentaux. En général, l'énergie d'interaction V définira l'écartement des états d'énergie excités des agrégats par rapport aux monomères (écart de Davidov = 2V). En principe, les agrégats H sont énergétiquement décalés vers le bleu avec un taux radiatif réduit par rapport aux monomères, tandis que les agrégats J sont décalés vers le rouge avec un rendement de taux radiatif accru. Il est intéressant de noter que les deux transitions peuvent être peuplées et être actives avec un moment dipolaire de transition non-nul, pour une géométrie oblique (Figure: B.3), où:

$$V = \frac{\overline{\mu_1}^2}{\overline{R}^3}(cos\alpha + 3cos^2\theta) \tag{B.2}$$

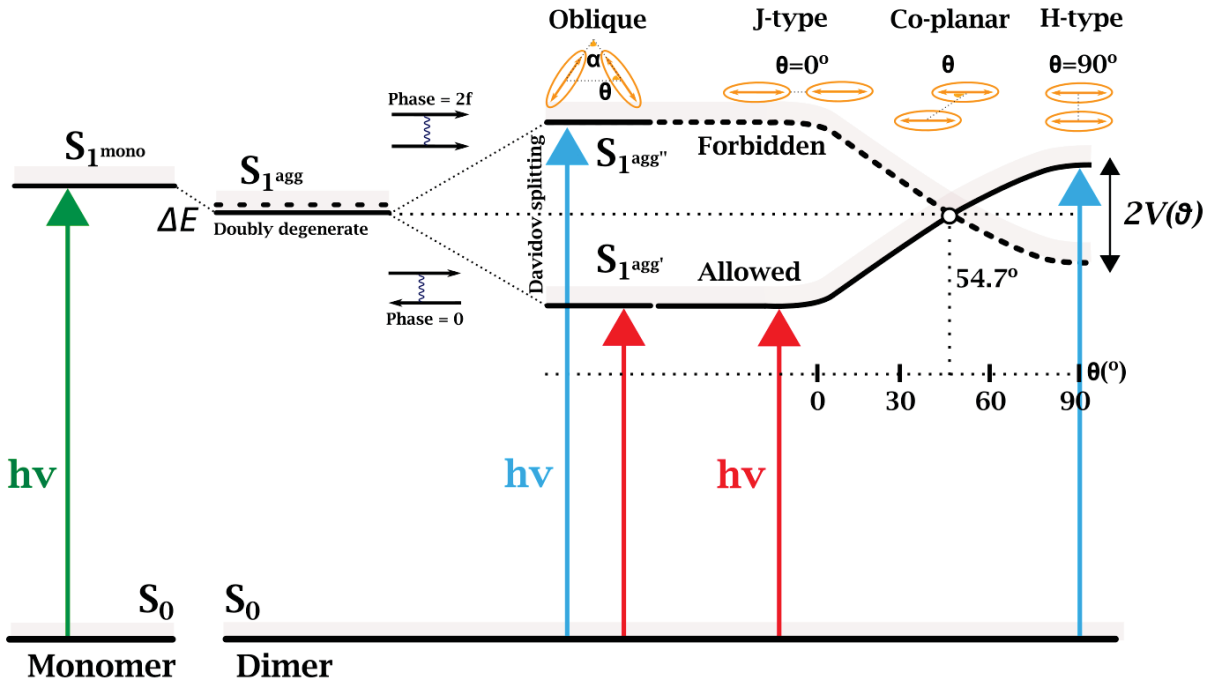

Figure B.3: Représentation schématique de la transition moléculaire autorisée en fonction du type d'agrégats et par rapport au niveau d'énergie du monomère.

L'un des processus les plus importants dans les DSSC est l'injection de charge des colorants vers le SC. La vitesse de transfert des électrons peut être bien décrite par la théorie classique de Marcus. [4–14] as:

$$K_{ET} = \frac{2\pi}{\hbar}V^2(\frac{1}{2\pi\lambda kT})^{1/2}\exp[-\frac{(\lambda + \Delta G_0)^2}{4\lambda kT}] \tag{B.3}$$

où V est le couplage électronique du donneur (D) et de l'accepteur (A) qui dépend du chevauchement des fonctions d'onde électroniques et qui décroît de manière exponentielle avec la distance D-A. Dans les DSSC, les colorants ont le rôle de D et le SC est le A. Le régime non-adiabatique domine lorsque le couplage entre D et A est faible et se réfère à des transitions directes d'un niveau vibronique de D à un niveau vibronique de A. Dans une forte approximation, on peut supposer que l'état excité du colorant est dans une position optimale avec une gamme d' états dans la bande de conduction du collecteur et donc (pour la limite de haute température) il n'y a pas besoin de mécanisme de relaxation de l'énergie par des vibrations moléculaires. Ainsi, le K_{ET} dépend uniquement du couplage électronique. [11, 15, 16].

B.4 Méthodes expérimentales

L'étude des DSSCs est un domaine multidisciplinaire et de nombreuses techniques expérimentales sont utilisées pour une analyse détaillée. Dans le cadre de la présente thèse de doctorat, la spectroscopie d'absorption et de fluorescence est utilisée, tant en régime stationnaire qu'en régime résolu dans le temps, de quelques dizaines de fs à plusieurs ns.

Le spectromètre d'absorption qui a été utilisé est le modèle LAMBDA 950 UV/Vis de PerkinElmer. Il offre la possibilité de sonder le domaine du proche UV jusqu'au proche IR. Il y a deux positions d'échantillon, l'une pour l'échantillon étudié et la seconde pour la référence, dont l'absorption est généralement soustraite (par exemple, le solvant pour les échantillons de solution). Pour les DSSC, nous effectuons deux mesures à la fois du dispositif DSSC complet et du " demi-DSSC " sans sensibilisateurs, afin de contrôler et de soustraire, si nécessaire, l'absorption de fond de l'électrolyte, des substrats en verre et du SC. Pour obtenir les spectres de fluorescence à l'état stationnaire, un fluorimètre modèle HORIBA (Fluoromax 4) a été utilisé. De même, il offre la possibilité d'une excitation par lampe de la partie proche UV à la partie proche IR du spectre et la détection est fiable jusqu'à l'IR (900nm). Les échantillons étudiés sont les colorants soit en solution, dans des solvants spécifiques avec des cuvettes de 0,1 cm d'épaisseur, soit dans des dispositifs DSSC complets.

Les principales techniques résolues en temps utilisées dans la thèse sont la caméra à balayage de fente, la Fluorescence Up-Conversion (FLUPS) et l'absorption transitoire fs (TA). Mesurer la fluorescence sur différentes échelles de temps peut être avantageux par rapport à d'autres techniques sans fond, comme la TA. Le modèle de caméra à balayage utilisé dans nos expériences est la HAMAMATSU C10627 dont le principe de fonction-

nement est bien connu [17] (Figure B.4). La résolution temporelle est un paramètre

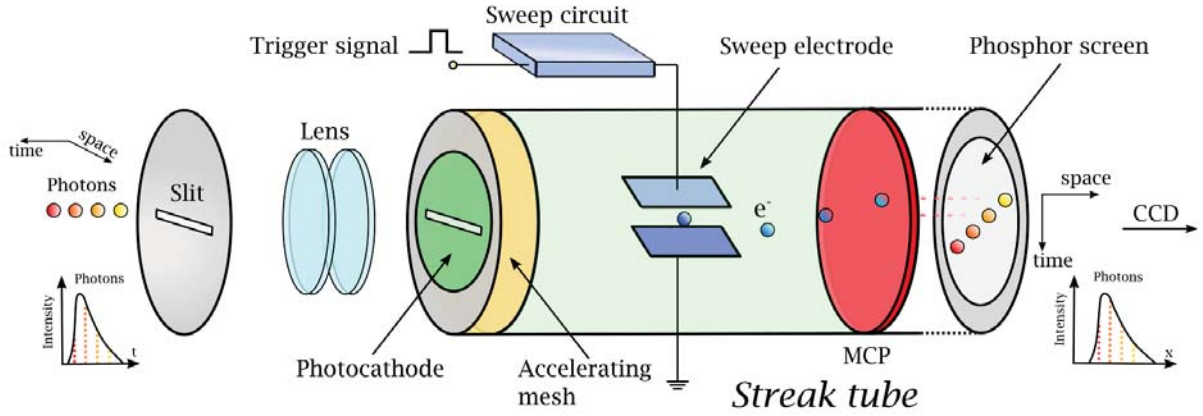

Figure B.4: Représentation schématique de la caméra à balayage de fente (Streak camera). *La figure a été modifiée sur la base de la référence [17].

critique et, dans le cas de la caméra à balayage de fente, elle est limitée par plusieurs facteurs [18] en fonction des différents signaux électriques et surtout de la réponse de la tension de balayage. Par conséquent, la meilleure résolution temporelle offerte par la caméra à balayage est limitée à $\sim$ 10 ps. Pour obtenir une résolution temporelle plus courte, de l'ordre de $\sim$ 200 fs on utilise une technique de pointe, appelée "up-conversion", par génération de somme de fréquence (SFG), qui utilise essentiellement un second faisceau laser comme porte optique et, dans ce cas, la résolution temporelle dépend de la durée d'impulsion du faisceau.

La figure B.5 présente le dispositif expérimental de manière schématique et concise, ainsi qu'un système d'imagerie "1-1" (en bas à droite) du centre du cristal BBO. Notre système laser est une source Ti:Sapphire (FemtoLasers Synergy 20) avec une longueur d'onde centrale à 800 nm, produisant des impulsions d'une résolution temporelle de 20 fs et une fréquence de répétition de 80 MHz. Le faisceau fondamental passe par un système d'amplification pulsée chirpée (CPA-Amplitude Technology Pulsar) pour produire finalement des impulsions d'une énergie de 0.5 mJ, d'une résolution temporelle de 40 fs à 5 kHz. La longueur d'onde d'excitation est finement réglée par de multiples processus non linéaires dans la boîte TOPAS-Prime. La fluorescence et le faisceau de la porte sont focalisés sur un cristal β-BBO dans lequel les conditions de superposition temporel et spatial doivent être remplies pour que le signal de somme de fréquence généré (correspondance de phase de type II). Après le temps zéro, les impulsions de la porte arrivent avec un retard τ et les courbes de décroissance pour les longueurs d'onde de fluorescence sont reconstruites à partir de l'intensité de SFG, on "up-conversion" (I_{UP}) en fonction

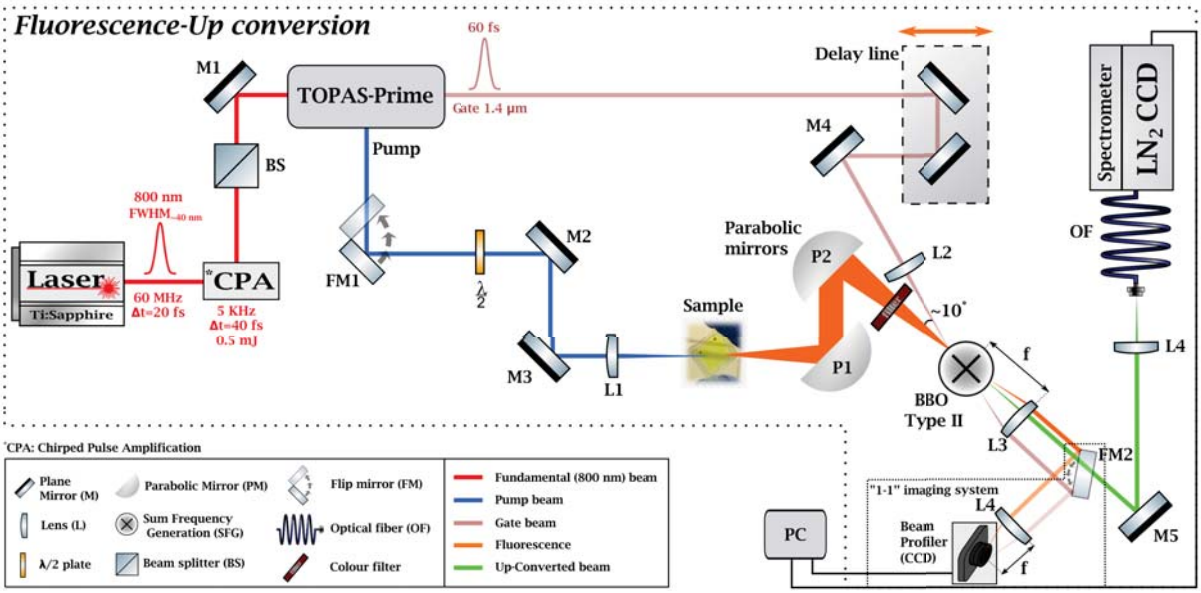

Figure B.5: Représentation schématique simplifiée du dispositif de Fluorescence-Up-Conversion (FLUPS) à large bande. Le système d'imagerie "1-1" du centre du cristal BBO est illustré à droite (cadre en pointillés).

de τ comme :

$$I_{UP}(\tau) = \int_{-\infty}^{\infty} I_{FL}(t) I_G(t-\tau) dt \tag{B.4}$$

La technique pompe-sonde la plus courante, basée sur la spectroscopie non linéaire du troisième ordre [19, 20] est la spectroscopie d'absorption transitoire (TAS). Le dispositif expérimental utilisé pour cette thèse a été décrit en détail ailleurs [21] et est présenté schématiquement dans la figure B.6. FLUPS et TA partagent la même source laser produisant des impulsions à 800 nm et une fréquence de répétition de 5 kHz. Les spectres d'absorption différentielle ΔA (pompe on/off) sont obtenus pour différents délais entre la pompe et la sonde. Ainsi, expérimentalement et en rappelant la loi de Beer-Lambert (équation 3.1), le $\Delta A(\lambda, t)$ mesuré peut être exprimé comme suit:

$$\Delta A(\lambda, t) = A(\lambda, t)_{pump,on} - A(\lambda, t)_{pump,off} = -\log \frac{I(\lambda, t)_{pump,on}}{I(\lambda, t)_{pump,off}} \tag{B.5}$$

où $A(\lambda, t)_{pump,off}$ est l'absorbance du WL et $I(\lambda, t)_{pump,off}$ l'intensité du WL transmis au délai t sans présence de la pompe. De même, $A(\lambda, t)_{pump,on}$ et $I(\lambda, t)_{pump,on}$ désignent l'absorbance et l'intensité de la sonde transmise lorsque la pompe est présente et excite l'échantillon. La TAS est avantageuse car elle offre la possibilité de localiser et de suivre

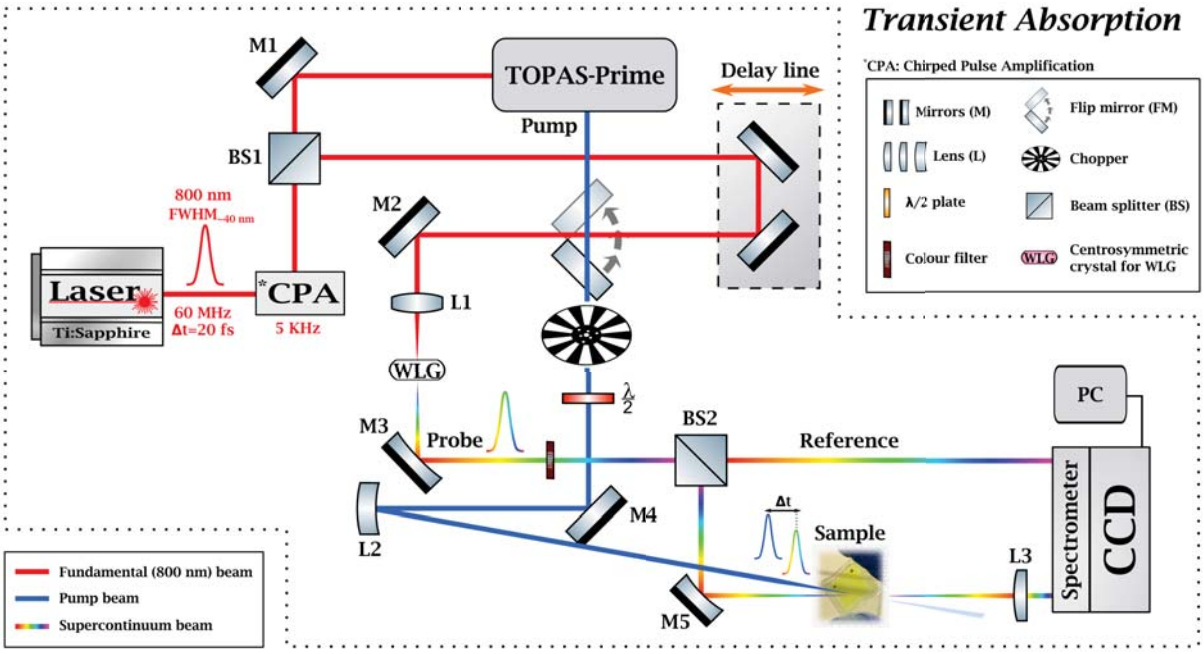

Figure B.6: Représentation schématique simplifiée de l'installation d'absorption transitoire fs.

diverses caractéristiques spectrales sur une large plage de longeurs d'onde. Les contributions de base qui seront discutées sont le blanchiment de l'état fondamental (GSB), l'émission stimulée (SE), l'absorption à l'état excité (ESA) et l'absorption de photoproduits (PA) [22].

Dans de nombreux systèmes, tels que les colorants pyrrolocyanines que nous étudions pour les applications DSSC, le SE recouvre spectralement partiellement le GSB et donc, pour les études analytiques des composantes cinétiques de la fluorescence, des mesures supplémentaires ont été effectuées avec FLUPS. La dernière composante spectrale est le PA qui se réfère généralement à la formation de nouvelles espèces, généralement à durée de vie longue, comme les colorants isomérisés ou la formation de radicaux de colorants, par exemple en raison de l'oxydation ou de la protonation. Elle apparaît comme un signal positif. Il est très important de souligner que dans les DSSC opérationnels, après une photo-injection efficace, le sensibilisateur est laissé sous forme cationique et la formation de la nouvelle espèce suit l'évolution du PA dans les spectres TAS.

B.5 Résultats expérimentaux

Il existe de nombreux colorants dans l'infrarouge qui produ conviennent aux applications DSSC transparentes. Pour les études relatives à cette thèse, nous avons étudié trois colorants portant les noms de code suivants : **VG20-C16** (ou simplement **VG20**), **TB207** et **TB423**. Lorsque **VG20** est la seule cyanine linéaire dans cette étude, **TB207** et **TB423** sont étroitement liés, en appartenant à la même classe de colorants. Le **TB423** possède une structure identique à celle du **TB207**, à l'exception du groupe latéral qui est plus volumineux et d'un seul groupe carboxylique (voir B.7).

La structure chimique de **VG20**, est présentée dans la figure B.7 (en haut). **VG20** a été synthétisé par le groupe de Claudia Barolo à l'Université de Turin et la procédure de synthèse analytique a été décrite ailleurs [23]. La nouveauté de ce colorant réside dans la position des groupes d'ancrage et la longueur des chaînes latérales hydrocarbonées. Plus en détail, **VG20** appartient à la catégorie des colorants à longue chaîne polyméthinique et plus particulièrement aux heptaméthines. La longueur étendue de la chaîne avec l'ajout d'un chlorocyclohexényle au centre, déplace considérablement l'absorption dans le proche IR. Le chlorocyclohexényle, dont l'atome de chlorure se trouve en position méso du cycle, réduit la densité des électrons sur la chaîne, dont l'absorption est essentiellement associée à la longueur de la π-conjugaison. En augmentant la longueur de la chaîne alkyle, le coefficient d'extinction molaire du colorant devient également plus élevé et, pour la configuration C16, il a été calculé qu'il est égal à $\varepsilon = 154'000 M^{-1} cm^{-1}$ dans l'éthanol. Enfin, la longue durée de vie de l'état excité, l'absorption dans l'infrarouge proche avec de faibles contributions de la partie visible de la région spectrale et le coefficient d'extinction molaire élevé, fait de **VG20-C16** un candidat prometteur pour les applications DSSC (semi-)-transparentes.

La deuxième série de colorants est constituée de **TB207** et de **TB423**, dont les structures chimiques sont illustrées dans la figure B.7. Les deux colorants **TB** ont été synthétisés par le groupe de F. Odobel au laboratoire CEISAM de l'Université de Nantes. Ils appartiennent tous deux à la sous-catégorie des colorants pyrrolopyrrole-cyanine (PPCys) qui a été rapportée pour la première fois par Daltrozzo et al [24–26] et, comme pour les cyanines classiques et les colorants pyrrolopyrroliques, leur maximum d'absorption ($\varepsilon = 134'000 - 138'000 M^{-1} cm^{-1}$ dans DCM) est décalé dans la partie proche IR du spectre (> 700 nm). Par rapport à **VG20** Les colorants ont été synthétisés pour minimiser les agrégats dans le système. Ceci est possible grâce à l'incorporation de groupes phényles qui rendent les structures plus volumineuses. Cependant, les agrégats sont toujours présents mais à plus faible concentration (Fig. B.8). La version améliorée du **TB207** est le **TB423** non symétrique, dans lequel un côté est remplacé par une partie

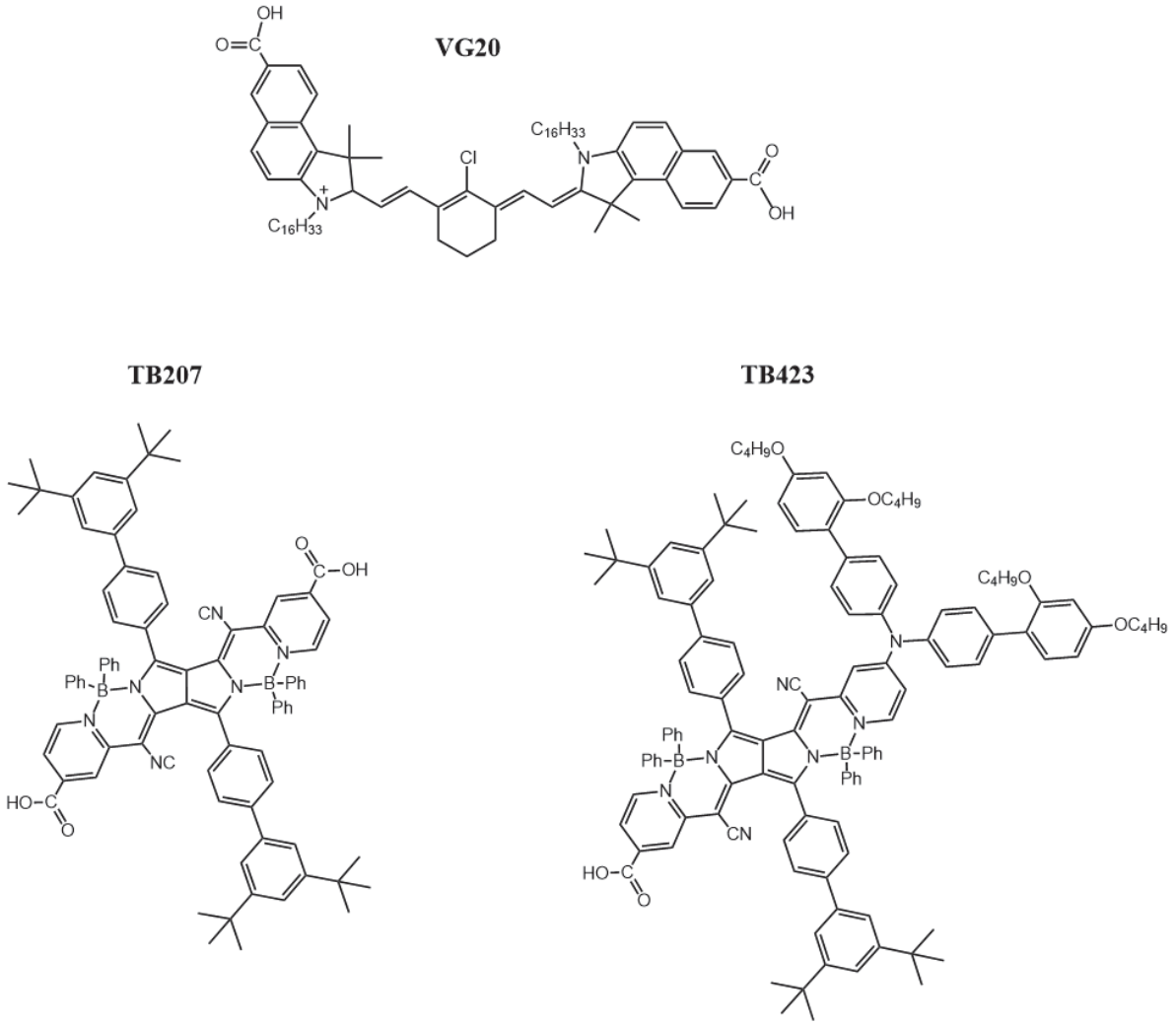

Figure B.7: Structures chimiques des molécules étudiées portant les noms de code **VG20**, **TB207** et **TB423**.

plus volumineuse réduisant encore plus la formation d' agrégats.

Ces trois colorants ont montré des avantages considérables pour le développement des DSSC dans le domaine des technologies transparentes. Ils présentent tous des coefficients d'extinction molaire élevés dans le proche infrarouge et faibles dans le visible et le proche ultraviolet, ce qui améliore considérablement le niveau d'AVT et, dans le même temps, ils présentent les valeurs PCE actuelles les plus élevées pour les colorants du proche infrarouge. Leurs différences spectroscopiques en régime permanent et résolues dans le temps sont présentées dans cette thèse, sondant divers effets avec un intérêt particulier pour l'effet des agrégats sur la séparation des charges à l'interface colorant-SC.

Les spectres d'absorption (SSA) des trois colorants incorporés dans des DSSC réels sont présentés dans la Figure B.8. Nous avons étudié les semiconducteurs ZrO_2 ou Al_2O_3

(E_g>6 eV), sans injection et TiO_2 (E_g=3.2 eV). L'effet des agrégats se manifeste par un

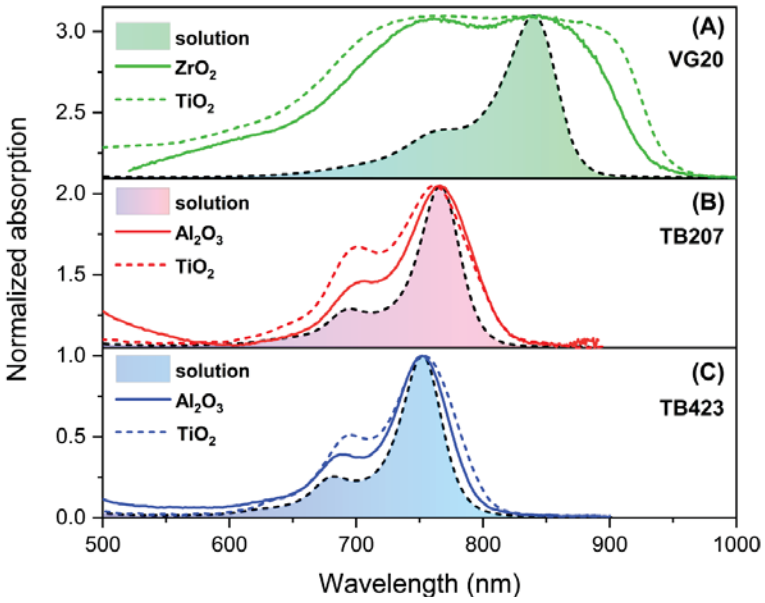

Figure B.8: Spectres d'absorption en régime permanent de (A) **VG20**, (B) **TB207** et (C) **TB423** dans des dispositifs DSSC réels, sans ajout d'agent de désagrégation. Les lignes pleines correspondent aux spectres d'absorption des DSSC à grand gap (ZrO_2 et Al_2O_3) et les pointillés aux DSSC TiO_2, tandis que les spectres remplis et pointillés représentent l'absorption en solution, décalée vers le rouge de 10 nm (A), 6 nm (B) et 4 nm (C) comme référence.

élargissement du spectre d'absorption ainsi que par une augmentation de l'intensité de l'épaulement d'absorption à haute énergie (à 720 nm pour les colorants **VG20** et à 690-700 nm pour le colorant **TB**). En solution, il correspond à un niveau vibronique, mais dans les DSSC, il inclut également l'absorption des agrégats.

Les agrégats dans les DSSC ont été signalés comme ayant un effet négatif sur les performances photovoltaïques totales en réduisant l'efficacité de l'injection du colorant dans le SC [27–32] et ils réduisent également l'AVT, en raison de leur contribution à l'absorption dans le visible [33]. Pour cette raison, diverses stratégies ont été utilisées pour réduire les agrégats, la plus courante étant l'utilisation de l'acide chénodésoxycholique (CDCA, Sigma Aldrich), qui est essentiellement un acide biliaire, comme agent de désagrégation. En ajoutant du CDCA, les distances intermoléculaires augmentent et le pourcentage d'agrégats diminue. (Figure B.9). Les performances photovoltaïques en fonction du CDCA ont été rapportées (tableau 5.7) montrant des conditions optimales de 1:500 colorant:CDCA pour **VG20**, 1:50 pour **TB207** et 1:5 pour **TB423**.

L'un des principaux points clés de notre étude est d'identifier les taux d'injection, qui se produisent dans le domaine temporel ps et les processus concurrentiels à celui-ci.

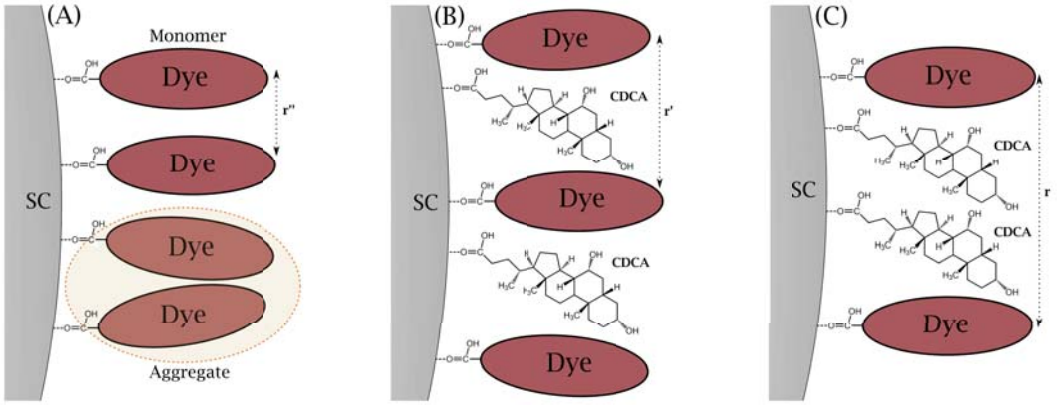

Figure B.9: Illustration schématique de l'interface colorant-SC pour trois cas différents, en augmentant la concentration de CDCA de (A) à (C). En ajoutant le CDCA, la distance intermoléculaire, de A à C, augmente ($r'' < r' < r$).

Par conséquent, la stratégie expérimentale est l'étude individuelle des DSSCs de TiO_2 avec injection et de ZrO_2 ou Al_2O_3 sans injection comme référence. Les études de fluorescence à résolution temporelle des molécules en solution ont montré que les durées de vie des états excités étaient suffisamment longues pour ne pas entrer en compétition avec l'injection (360 ps pour le **VG20**, 3.2 ns pour le **TB207** et >1 ns pour le **TB423**). Les figures B.10.A.B présentent les amplitudes de **VG20** en fonction de la longueur d'onde dans des DSSC ZrO_2 sans injection et TiO_2 avec injection, respectivement. Les figures B.10C.D montrent une représentation schématique des spectres ΔA correspondant aux différentes espèces (monomères, agrégats et cations de colorant) et SE, pour les DSSCs ZrO_2 et TiO_2, respectivement. Ces graphiques ont été réalisés pour faciliter l'interprétation des spectres DADS. Pour le DSSC ZrO_2, le signal positif à haute énergie (450-700 nm) contient l'ESA des monomères et des agrégats, alors que dans la même région, pour le DSSC TiO_2 l'absorption des cations est également présente. La montée de ce signal doit apparaître comme une caractéristique négative dans le DADS et le temps de montée correspond au temps d'injection. Quatre constantes de temps décrivent les systèmes au mieux par une approche d'analyse globale. L'absence de la composante sub-ps dans le DSSC ZrO_2 indique que l'injection commence à partir de 0,4 ps et s'étend jusqu'à 4.3 ps. Le signal négatif de l'agrégat ESA (520 nm) et le signal positif de l'agrégat GSB (760 nm) en parallèle avec la décroissance de l'agrégat monomère ESA (620 nm) et GSB (850 nm) révèle le transfer d' énergie (ET) des monomères aux agrégats. Il est essentiel de souligner que l'ET et l'injection se produisent à des moments similaires et se font concurrence, ce qui révèle que l'ET est le principal canal de perte pour l'injection. En outre, en raison de l'inhomogénéité du système (distribution des distances entre les

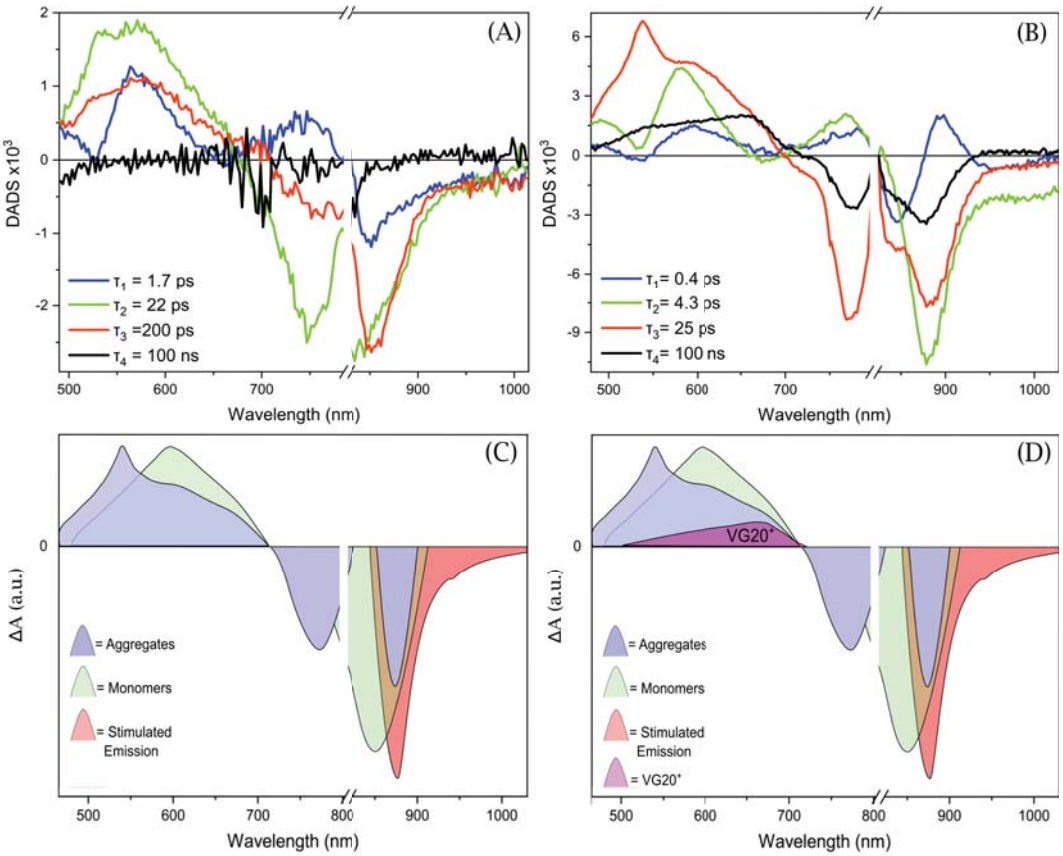

Figure B.10: Amplitudes de **VG20** en fonction de la longueur d'onde dans (A) des DSSCS ZrO_2 non injectés et (B) TiO_2 injectés. (C), (D) Représentation graphique des spectres ΔA correspondant aux différentes espèces (monomères, agrégats et cations de colorant) et SE, pour les DSSCs Zr_{O2} et TiO_2, respectivement. Les dispositifs ont été pompés à 800 nm avec une énergie de 90 $\mu J/cm^2$.

monomères et les agrégats), les temps de l' ET se présentent également sous forme de distribution, tout comme les temps d'injection. Le diagramme simplifié des états excités photophysiques pour les monomères et les agrégats à l'interface colorant-SC se trouve dans la Figure B.11. L'efficacité de l'injection peut être calculée à partir des spectres TA comme suit:

$$\Phi_{inj} = \frac{-\Delta C_{t_0}}{-\Delta C_{t\to\inf}} = \frac{C_{VG20^+}}{C_{VG20^*}} = \frac{\Delta A_{GSB_{max},t\to\infty}}{\Delta A_{GSB_{max},t=0}} \tag{B.6}$$

Pour le **VG20**, dans les conditions optimales, il s'est avéré être de ∼30 % pour une concentration de CDCA optimale. Deux séries d'expériences supplémentaires ont été menées. L'étude TAS des DSSC augmentant le [CDCA] a confirmé les caractéristiques spectrales des monomères et des agrégats telles qu'elles ont été attribuées ci-dessus. De plus, comme il a été prédit, l'efficacité de l'injection augmente avec l'augmentation de [CDCA] (tableau

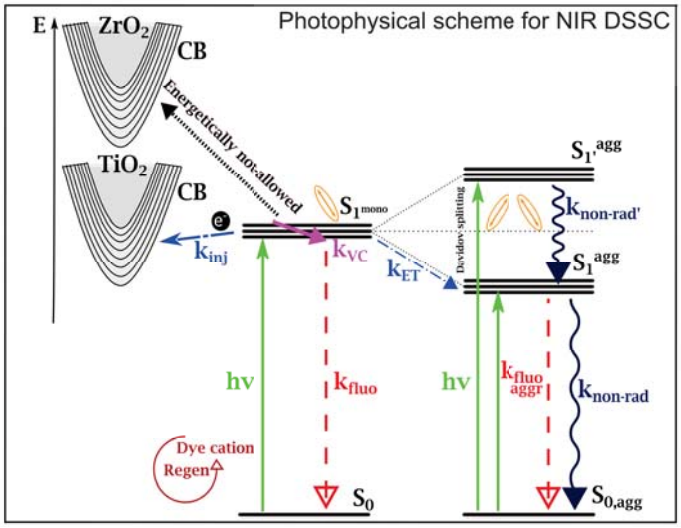

Figure B.11: Diagramme simplifié des états excités photophysiques pour les monomères et les agrégats dans l'interface colorant-SC.

5.13). En outre, l'analyse cinétique a révélé qu'en allongeant les distances intermoléculaires, les temps d'ET deviennent plus rapides, comme le prédit la théorie de l'ET, sans changement des temps d'injection. Dans une approche différente, en augmentant le $[Li^+]$ dans l'électrolyte, l'énergie du CB diminue et la différence d'énergie optimale CB/LUMO est approchée. Les conditions optimales sont trouvées pour 1 M $[Li^+]$. L'augmentation de la force motrice pour l'injection a entraîné des temps d'injection plus rapides et des efficacités d'injection plus élevées (tableau 5.14).

Le modèle proposé dans la figure B.11 est également valable pour **TB207** et **TB423**. Les DADS pour **TB207** sont présentés sur la figure B.12. Comme pour **VG20**, l'absorption des cations se superpose largement à l'ESA des monomères et des agrégats. En outre, deux signaux ESA correspondants apparaissent dans le proche IR, se superposant aux signaux SE et GSB, ce qui complique l'interprétation visuelle. Les temps d'injection sont plus lents que ceux de **VG20** à partir de 2.8 ps et s'étendent jusqu'à 23 ps. Cette observation pourrait être le résultat d'une force motrice plus faible pour l'injection, en raison des conditions non optimisées. Cependant, le pourcentage d'agrégats minimisé dans ce système permet d'obtenir des efficacités d'injection de 40-60%. Des études supplémentaires sur les DSSC de différents [CDCA] ont montré des résultats similaires à ceux de **VG20**, l'efficacité augmentant avec l'augmentation de [CDCA] (tableau 5.23).

Il est intéressant de mentionner que pour le **TB423**, l'effet du CDCA est négligeable, en raison de la structure encore plus volumineuse que celle du **TB207**. Le colorant est plus long et donc les distances intermoléculaires aussi, ce qui entraîne des temps d'ET plus longs. Ainsi, l'efficacité d'injection s'est avérée être encore plus élevée (60-80 %), ce

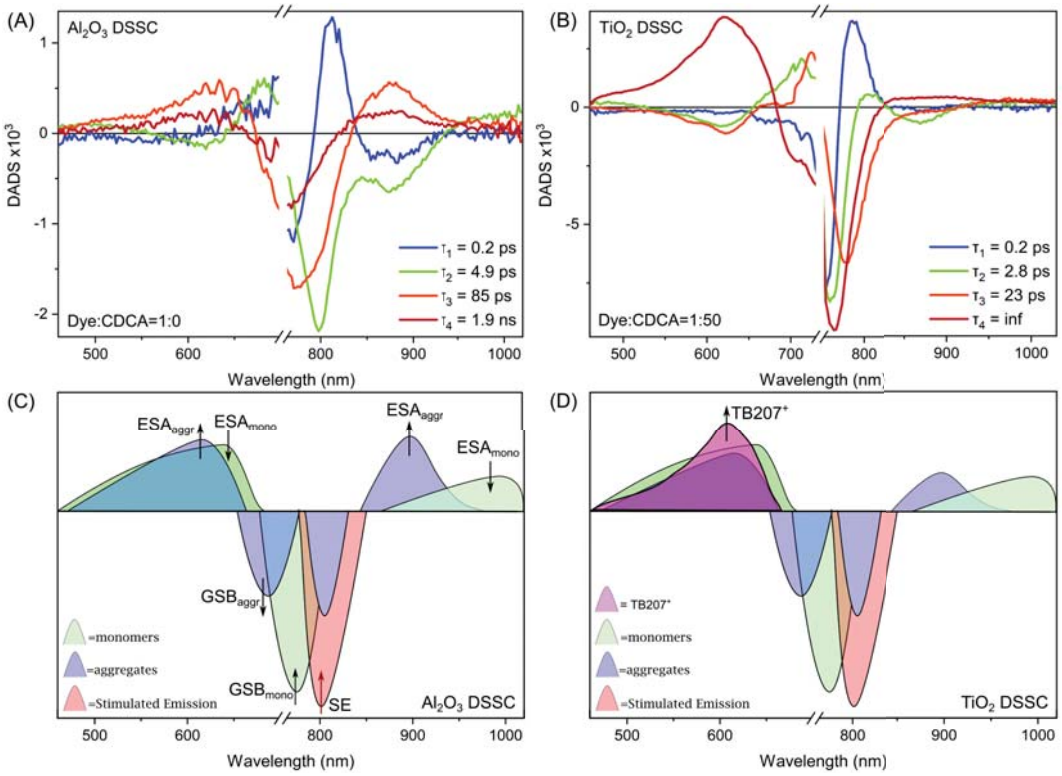

Figure B.12: DADS, de **TB207** de (A) Al_2O_3 et (B) TiO_2 DSSCs, dans les conditions standard. Les échantillons ont été excités à 730 nm, avec une énergie de $26\mu J/cm^2$. Les conditions standard, relatives au rapport colorant:CDCA pour le DSSC Al_2O_3 est de 1:0 et pour le DSSC TiO_2 est de 1:50. (C) Al_2O_3, (D) TiO_2 : Une représentation imagée des spectres ΔA, distingue les différentes contributions ESA, GSB, SE et PA, pour les monomères et les agrégats. Les TAS correspondants sont présentés dans la Figure 5.32 (Al_2O_3) et 5.36 (TiO_2).

qui fait de ce colorant un candidat intéressant pour des applications DSSC efficaces et transparentes. Cependant, le PCE n'a pas dépassé la valeur record de 3.9 % de **TB207** et des études supplémentaires doivent être effectuées.

Il est important de souligner que pour la série de colorants **TB**, en raison de la complexité des caractéristiques spectrales du TAS, FLUPS a été utilisé comme méthode complémentaire. La figure B.13 montre la cinétique FLUPS avec les ajustements de **TB207** et **TB423** en solution, dans des DSSCs de Al_2O_3 et TiO_2, dans les conditions standard. La trace cinétique de Al_2O_3 (vert) est plus rapide que la solution (noir) pour les deux cas, due au mécanisme ET, qui est essentiellement un processus non radiatif. De plus, les traces cinétiques de TiO_2 (bleu) sont encore plus rapides que celles de Al_2O_3, en raison de l'injection de charge. L'efficacité de l'injection peut être évaluée alternativement

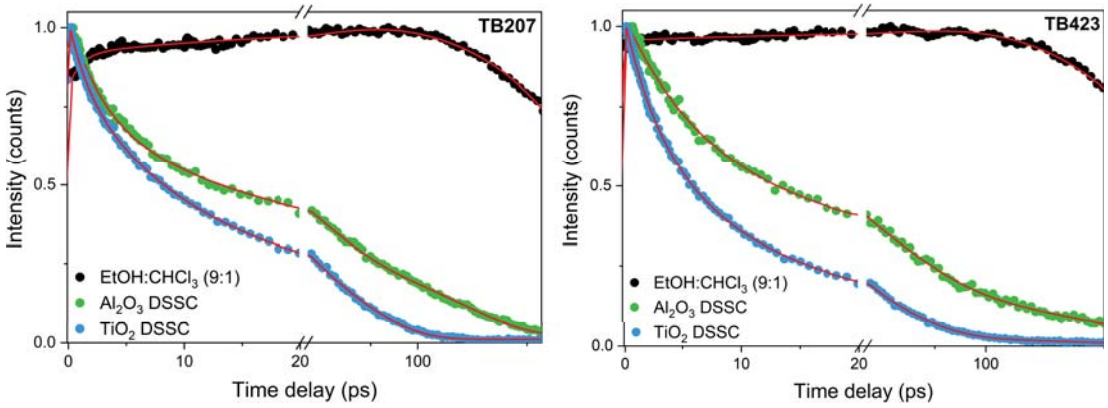

Figure B.13: Cinétique FLUPS normalisée avec leurs ajustements respectifs courbés en lignes solides rouges, de **TB207** et **TB423** dans une solution $EtOH : CHCl_3$ (9 : 1), dans des DSSCs Al_2O_3 et TiO_2, dans les conditions standard. Les échantillons de solution ont été excités à 730-740 nm et les DSSCs à 720-730 nm, avec une énergie de $26\mu J/cm^2$. Les conditions standard, relatives au rapport colorant:CDCA pour le DSSC Al_2O_3 est de 1:0 et pour le DSSC TiO_2 est de 1:50 pour **TB207** et 1:80 pour **TB423**.

à partir de la cinétique de fluorescence comme:

$$\Phi_{inj} = \frac{\langle k_{inj} \rangle}{\langle k_{inj} \rangle + \langle k_{ET} \rangle + \langle k_{mono} \rangle} \tag{B.7}$$

à partir des taux cinétiques (k), évalués par l'ajustement. Pour **TB207** le rendement d'injection a été calculé à 60 %, alors que pour **TB423** il est de 80 %. Ces valeurs sont relativement plus élevées que celles calculées par TAS, dans lequel l'émission de SE dans les premiers temps pourrait sous-estimer le rendement d'injection. Cependant, en cohérence avec TAS, **TB423** s'avère être plus efficace que **TB207**, en raison de l'agrégation minimisée du système.

En conclusion, en termes d'efficacité d'injection, le colorant le plus prometteur semble être le **TB423**, possédant le groupe latéral le plus volumineux, établissant ces nouveaux colorants pyrrolopyrrole cyanine comme des candidats attrayants pour des dispositifs photovoltaïques transparents et efficaces.

Appendix C

Conclusions et perspectives

Les recherches menées au cours de cette thèse de doctorat font partie d'une collaboration plus large dans le cadre du projet ANR VISION-NIR. La perspective à long terme de ce travail collectif est la production de modules solaires de nouvelle génération, entrant dans la catégorie des DSSCs sélectifs en longueur d'onde, qui remplissent les critères suivants : haut rendement de conversion de puissance, stabilité à long terme, production à faible coût, caractéristiques écologiques et humaines et enfin hauts niveaux de transparence et d'esthétique. Pour répondre à ces critères, de nouveaux colorants ont été synthétisés. Ils appartiennent à la famille des sensibilisateurs organiques dams l'infrarouge probe et se situent dans une perspective différente de celle des DSSC à base de Ru on photosynthétiser organiques pour le VIS qui détiennent le record en termes d'efficacité. Les colorants étudiés dans le cadre de la thèse ont atteint des rendements supérieurs à 3 %, ce qui est très faible par rapport au record de 15 %. Cependant, l'AVT maximum atteint a obtenu la valeur impressionnante de 76 % [1]. Dans une approche différente, mais essentielle, la quantité importante pour une comparaison générale, est le produit $PCE \times AVT$. Dans cette approche, les nouveaux colorants qui ont été abordés dans la thèse, ont également été cités dans des travaux très récents et importants [2], pour présenter des valeurs record, comme il peut également être démontré dans la figure 5.10 (p.113). Les nouveautés mentionnées ci-dessus s'inscrivent dans le cadre général du projet de collaboration, de l'optimisation des structures des colorants, ainsi que de la composition de l'électrolyte, pour finalement améliorer et renforcer les performances photovoltaïques totales.

Notre contribution s'est concentrée sur la caractérisation ultrarapide résolue en temps des DSSCs. Des résultats importants ont révélé les inconvénients des colorants, tels que la

formation d'agrégats, et ont aidé, de cette manière, à la synthèse de colorants améliorés. En effet, les expériences sur le **TB207** et le **TB423** valident la stratégie de conception visant à réduire la formation d'agrégats par rapport au monomère ET. De plus, deux techniques ultrarapides (FLUPS et TAS) ont été utilisées, de manière complémentaire, pour les mêmes échantillons de DSSC, ce qui, à notre connaissance, n'a jamais été fait auparavant pour des études de DSSC de modules complets de cellules solaires. Les temps relatifs trouvés par les deux techniques présentaient des différences qui ont été rapportées et l'utilisation combinée des deux a permis d'identifier les temps de solvatation, d'ET et d'injection de charge, afin de construire finalement le schéma de réaction. Les modules complets ont été étudiés en détail et la reproductibilité d'échantillon à échantillon a été examinée dans une large gamme de DSSC. De cette manière, l'erreur standard a été rapportée, offrant un point de référence qui devrait être pris en compte dans les mesures ultrarapides sur ces échantillons et lors de la comparaison des différences de dynamique entre les échantillons. Pour **VG20** la spectroscopie résolue en temps fs a déjà été appliquée sur des DSSCs complets et rapportée dans [3]. Cependant, à notre connaissance, des études ultrarapides ont été réalisées pour la première fois dans les DSSCs basés sur les nouveaux colorants pyrrolopyrrole cyanine, tels que **TB207** et **TB423**, dans le cadre des recherches de la présente thèse de doctorat. Les temps d'injection ont été identifiés dans ce premier rapport comme étant dans une gamme de 2-20 ps, ce qui est plus lent que les DSSCs basés sur le Ru, car pour ces derniers, la différence d'énergie CB/LUMO est plus élevée et donc la force motrice pour l'injection est accrue. De plus, alors que pour le colorant **VG20**, l'injection commence à fonctionner à partir du domaine sub-ps, l'efficacité totale de l'injection a été calculée comme étant plus élevée pour les colorants **TB**, car leur structure plus volumineuse empêche la formation d'agrégats, minimisant ainsi la contribution de l'ET. Pour les trois colorants, le plus prometteur s'est avéré être le **TB423**, qui, comparé à son analogue **TB207**, possède un groupe latéral encore plus volumineux, réduisant encore plus l'agrégation, sans sacrifier la charge en colorants avec l'utilisation supplémentaire de CDCA, comme co-adsorbants. Cependant, le PCE total semble inférieur (tableau 5.7) et une optimisation future doit être effectuée. En ce qui concerne la dynamique, il a été confirmé que les temps d'ET et d'injection sont représentés non pas comme des valeurs distinctes, mais comme des distributions. Ces processus sont très sensibles aux distances intermoléculaires moyennes, qui, en raison de l'inhomogénéité structurale des systèmes DSSC aux interfaces SC-colorants densément emballés, apparaissent également comme des distributions. L'effet du CDCA sur l'augmentation des distances intermoléculaires et la réduction des agrégats a été mis en évidence, ainsi que

son effet sur les temps d'ET. Les études en fonction de la concentration de CDCA, sur des DSSCs avec et sans injection, comme référence, via deux techniques fs complémentaires, se sont avérées être d'excellentes méthodes expérimentales pour construire le schéma de réaction des colorants, de manière très détaillée.

À l'issue des études expérimentales, la présente thèse de doctorat aborde certaines questions ouvertes. La première est de savoir, si les agrégats injectent, contribuant ainsi au PCE total. Malheureusement la complexité des mécanismes a rendu difficile la distinction quantitative de ce processus d'injection parallèle. De futures expériences pourraient être réalisées en utilisant une excitation à large bande, fournie par le 2D-TAS amélioré, afin d'étudier l'injection possible d'agrégats. Deuxièmement, avec nos techniques expérimentales, nous avons pu identifier l'efficacité de l'injection dans une échelle de temps courte ($\sim$ 5 ns), cependant le degré de recombinaison possible sur la surface du SC, réduisant le PCE total, reste à déterminer. Les études futures pourraient utiliser des techniques plus sophistiquées, telles que le TAS avec une soinde de rayons X ou UV sondant directement le SC, pourraient fournir des observations et des informations plus directes, répondant à cette question ouverte. En conclusion, les DSSC se démarquent comme une des rares technologies photovoltaïques de nouvelle génération, qui a fait ses preuves et qui reste, prometteuse pour les futures applications de production d'énergie par des dispotifs transparent. Pour l'optimisation des colorants la spectroscopie ultrarapide s'est avérée être un outil de caractérisation puissant.

References

[1] W. Naim *et al.*, "Transparent and colorless dye-sensitized solar cells exceeding 75% average visible transmittance," *Jacs Au*, vol. 1, no. 4, pp. 409–426, 2021.

[2] O. Almora *et al.*, "Device performance of emerging photovoltaic materials (version 2)," *Advanced Energy Materials*, vol. 11, no. 48, p. 2 102 526, 2021.

[3] K. Pydzińska and M. Ziółek, "Solar cells sensitized with near-infrared absorbing dye: Problems with sunlight conversion efficiency revealed in ultrafast laser spectroscopy studies," *Dyes and Pigments*, vol. 122, pp. 272–279, 2015.

Ilias Nikolinakos

Ultrafast Spectroscopy of Transparent Dye Sensitized Solar Cells designed for the near-Infrared

Résumé

Les cellules solaires à colorant (DSSC) sont un des candidats les plus prometteurs pour les applications de conversion d'énergie. L'objectif du projet est de créer des DSSCs efficaces et transparentes. Dans le cadre de la thèse de doctorat, nous avons appliqué la spectroscopie ultrarapide UV-Vis-IR proche proche dans l'échelle de temps fs-ps-ns, afin de construire le schéma photophysique des colorants, lorsqu'ils seront incorporés dans des dispositifs DSSC réels. Deux catégories de colorants organiques ont été examinées, de type cyanine et pyrrolopyrrole cyanine, présentant une forte absorption dans le proche IR et une faible absorption dans le visible, ainsi qu'une efficacité de conversion de puissance record de 4% et une transmittance moyenne dans le visible de 75%. Il a été démontré que des agrégats de colorants se forment sur la nanocouche. Le transfert d'énergie (monomères vers agrégats) se produit dans des temps allant de sub-ps à des dizaines de ps et sa compétition cinétique avec l'injection de charge (colorant vers semi-conducteur) en fait le principal canal de perte pour l'injection.

Résumé en anglais

Dye-sensitized solar cells (DSSCs) are one of the most promising candidates for energy harvesting applications. The aim of the project is the creation of efficient and transparent DSSCs. In the context of the PhD Thesis we applied UV-Vis ultrafast spectroscopy in the fs-ps-ns time scale, in order to construct the photophysical scheme of the dyes, when incorporated in real DSSC devices. Two categories of organic dyes were examined, of cyanine and pyrrolopyrrole cyanine type, exhibiting strong absorption in the near-IR and weak in the visible, as well as record Power-Conversion Efficiency 4% and Average Visible Transmittance 75%. It was shown that dye aggregates are formed on the nanolayer. Energy Transfer (monomers-to-aggregates) occurs in sub-ps to tens of ps times and its kinetic competition with charge injection (dye-to-semiconductor) constitutes it the main loss channel for injection.